Forschungsbericht 2016-01

Including Coarse Mode Aerosol Microphysics in a Climate Model: Model Development and First Application

Christopher Kaiser

Deutsches Zentrum für Luft- und Raumfahrt
Institut für Physik der Atmosphäre
Oberpfaffenhofen

Dissertation
an der Fakultät für Physik
der Ludwig-Maximilians-Universität
München

ISSN 1434-8454

ISRN DLR-FB--2016-01

ISRN DLR-FB--2016-01

C. Kaiser

DLR Deutsches Zentrum für Luft- und Raumfahrt

Herausgeber
Deutsches Zentrum
für Luft- und Raumfahrt e.V.
Bibliotheks- und
Informationswesen
D-51170 Köln
Porz-Wahnheide
Linder Höhe
D-51147 Köln

Telefon (0 22 03) 6 01- 44 44
Telefax (0 22 03) 6 01- 47 47

ISSN 1434-8454

Forschungsbericht 2016-1

Including Coarse Mode Aerosol Microphysics in a Climate Model: Model Development and First Application

Christopher Kaiser

Deutsches Zentrum für Luft- und Raumfahrt
Institut für Physik der Atmosphäre
Oberpfaffenhofen

Dissertation
an der Fakultät für Physik
der Ludwig-Maximilians-Universität
München

171 Seiten
42 Bilder
11 Tabellen
485 Literaturstellen

DLR **Deutsches Zentrum für Luft- und Raumfahrt**

Erstgutachter: Prof. Dr. Robert Sausen
Zweitgutachter: Prof. Dr. George Craig
Tag der mündlichen Prüfung: 15.12.2015

Including Coarse Mode Aerosol Microphysics in a Climate Model: Model Development and First Application

Christopher Kaiser

Dissertation
an der Fakultät für Physik
der Ludwig–Maximilians–Universität
München

vorgelegt von
Christopher Kaiser
aus Vechta

München, im Februar 2016

Contents

Abstract **xi**

Kurzfassung **xiii**

1 Introduction **1**

1.1 Motivation . . . 1

1.2 Scientific questions . . . 2

1.3 Method . . . 2

2 Background and state of the science **5**

2.1 The atmospheric aerosol . . . 5

2.1.1 Relevance . . . 6

2.1.2 Aerosol processes . . . 8

2.1.3 Aerosol properties . . . 10

2.2 The influence of ship emissions . . . 15

2.3 Aerosol modeling . . . 16

2.3.1 Selected results . . . 16

2.3.2 Motivation to expand on previous work . . . 19

2.3.3 The computational approach . . . 20

2.3.4 Existing aerosol microphysics submodels . . . 22

2.3.5 MADE3 as a successor of MADE and MADE-in . . . 24

3 The aerosol submodel MADE3 **25**

3.1 Aerosol characteristics . . . 25

3.1.1 Modes . . . 25

3.1.2 Species . . . 25

3.1.3 Mathematical representation of aerosol characteristics . . . 28

3.2 Aerosol processes . . . 28

3.2.1 Gas–particle partitioning . . . 29

3.2.2 Condensation of H_2SO_4 and organic vapors . . . 29

3.2.3 New particle formation . . . 31

3.2.4 Coagulation . . . 32

3.2.5 Renaming . . . 34

3.2.6 Aging of insoluble particles . . . 34

4 Box model tests **37**
4.1 Model description: MADE vs. MADE3 . . . 37
4.2 Model description: PartMC-MOSAIC . . . 38
4.3 Test case scenario . . . 39
4.4 Results: MADE3 vs. MADE . . . 42
4.4.1 Size distributions . . . 42
4.4.2 Composition . . . 43
4.5 Results: MADE3 vs. PartMC-MOSAIC . . . 44
4.5.1 Size distributions . . . 44
4.5.2 Composition . . . 46
4.6 Summary and conclusions . . . 47

5 MADE3 in the atmospheric chemistry general circulation model EMAC **49**
5.1 Basic settings . . . 50
5.2 Emissions . . . 52
5.3 Transport . . . 54
5.4 Gas phase chemistry . . . 56
5.5 Cloud formation . . . 56
5.5.1 Stratiform clouds . . . 56
5.5.2 Convective clouds . . . 57
5.6 Cloud and precipitation processing of the aerosol . . . 57
5.7 Wet deposition . . . 60
5.8 Dry deposition . . . 60
5.9 Sedimentation . . . 61
5.10 Optical properties . . . 62

6 Evaluation of simulated tropospheric aerosol properties **65**
6.1 Data comparability . . . 65
6.2 The MADE3 aerosol within EMAC . . . 66
6.2.1 Near-surface mass concentrations . . . 66
6.2.2 Vertical distributions . . . 72
6.2.3 Size distributions . . . 75
6.2.4 Aerosol optical depth . . . 80
6.2.5 Global tropospheric burdens and residence times . . . 82
6.2.6 Summary and conclusions . . . 83
6.3 Comparison to MADE . . . 84
6.4 New features of MADE3 . . . 85

7 Effects of oceanic ship emissions on atmospheric aerosol particles **89**
7.1 Effects of year 2000 emissions . . . 89
7.1.1 Near-surface concentrations . . . 90
7.1.2 Near-surface size distributions . . . 92
7.1.3 Tropospheric burdens . . . 94
7.2 Effects of an idealized fuel sulfur content reduction . . . 95
7.3 Summary and conclusions . . . 97

8 Summary, conclusions, and outlook **99**

Appendix **103**
A.1 Particle evolution in the box model study . . . 103
A.2 Gas phase chemical mechanism . . . 104
A.3 Liquid phase chemical mechanism . . . 114
A.4 Mode assignment of cloud residual aerosol . . . 119
A.4.1 Terminology . . . 119
A.4.2 Basic assumptions . . . 119
A.4.3 Algorithm for residual assignment . . . 120
A.5 Year 2000 aerosol in EMAC with MADE3 . . . 125
A.6 Near-surface mass concentration evaluation . . . 130

References **133**

Acronyms, symbols, and species names **166**
Acronyms . . . 166
Symbols . . . 166
Tracers and chemical species . . . 169

Danksagung **171**

List of Figures

2.1 Transmission electron microscopy images of ambient particles 5
2.2 Aerosol processes 8
2.3 Aerosol particle nucleation and growth 9
2.4 Measured aerosol volume size distributions 11

3.1 MADE3 modes and aerosol composition 26

4.1 Box model test: initial size distribution and composition 40
4.2 Box model test: MADE3 vs. MADE (size distributions) 42
4.3 Box model test: MADE3 vs. MADE (composition) 44
4.4 Box model test: MADE3 vs. PartMC-MOSAIC (size distributions) 45
4.5 Box model test: MADE3 vs. PartMC-MOSAIC (composition) 46

5.1 Aerosol dynamics processes and corresponding MESSy submodels 50

6.1 EMAC (MADE3) vs. station measurements: secondary inorganic aerosol 69
6.2 EMAC (MADE3) vs. station measurements: sea spray aerosol 70
6.3 EMAC (MADE3) vs. station measurements: mineral dust 71
6.4 EMAC (MADE3) vs. station measurements: carbonaceous aerosol 71
6.5 EMAC (MADE3) vs. airborne measurements: mass mixing ratios 74
6.6 EMAC (MADE3) vs. airborne measurements: particle number concentrations . . 76
6.7 EMAC (MADE3) vs. measured size distributions: changes with altitude 77
6.8 EMAC (MADE3) vs. measured size distributions: changes with season 79
6.9 EMAC (MADE3) vs. radiometer data: aerosol optical depth 81
6.10 EMAC (MADE3) vs. electron microscopy data: size-resolved aerosol composition 87
6.11 EMAC (MADE3) vs. electron microscopy data: variability 87

7.1 Ship emissions effect on near-surface sulfate (SO_4) concentration 90
7.2 Ship emissions effect on near-surface nitrate (NO_3) concentration 91
7.3 Ship emissions effect on near-surface aerosol size distributions (standard fuel) . . 93
7.4 Ship emissions effect on near-surface SO_4 and NO_3 concentrations (low-sulfur fuel) 96
7.5 Ship emissions effect on near-surface aerosol size distributions (low-sulfur fuel) . 97

A.1 Evolution of size-resolved aerosol composition in the box model 103
A.2 Transfer of soluble accumulation mode particles to residual modes 121
A.3 Soluble Aitken mode in the MADE3 reference simulation 125
A.4 Mixed Aitken mode in the MADE3 reference simulation 126
A.5 Insoluble Aitken mode in the MADE3 reference simulation 126
A.6 Soluble accumulation mode in the MADE3 reference simulation 127
A.7 Mixed accumulation mode in the MADE3 reference simulation 127
A.8 Insoluble accumulation mode in the MADE3 reference simulation 128
A.9 Soluble coarse mode in the MADE3 reference simulation 128

A.10 Mixed coarse mode in the MADE3 reference simulation 129
A.11 Insoluble coarse mode in the MADE3 reference simulation 129
A.12 Evaluation of near-surface aerosol mass concentrations: IMPROVE 130
A.13 Evaluation of near-surface aerosol mass concentrations: CASTNET 131
A.14 Evaluation of near-surface aerosol mass concentrations: EMEP 131
A.15 Evaluation of near-surface aerosol mass concentrations: EANET 132

List of Tables

2.1 Available aerosol microphysics submodels for global atmospheric models 23

3.1 MADE3 parameter values 27
3.2 Coagulated particle assignment matrix 33

4.1 Box model test: initial concentrations 41
4.2 Box model test: emissions and formation rates 41

5.1 Applied MESSy submodels 51
5.2 Particle emissions size distributions 55

6.1 Near-surface concentrations: simulation–observations comparison statistics . . . 68
6.2 Aircraft measurement datasets used in the evaluation of vertical profiles 73
6.3 Global tropospheric aerosol burdens and residence times 82

7.1 Changes in aerosol burdens due to ship traffic 94

Abstract

Recent climate model simulations indicated that sulfate (SO_4) formed from ship emissions may be one of the major contributors to the negative anthropogenic aerosol radiative forcing. Due to increasingly stringent regulations on the maximum sulfur content of ship fuels this contribution is expected to decrease strongly in the future. Possibly, nitrate (NO_3) formation will compensate for part of the reduction, but measurements indicate that it may be crucial to include coarse mode particle interactions with condensable trace gases in order to quantify this effect. However, none of the aerosol (sub)models previously used for such assessments accounted for the coarse mode particle effects. This provided the motivation to extend one of those submodels, namely MADE, in the present work.

The new submodel, MADE3, is based on the second generation of MADE, called MADE-in. It includes nine lognormal modes to represent three size ranges with three types of aerosol particles each. The associated increase in complexity w.r.t. to MADE and MADE-in required a complete revision of the code and careful reexamination of the underlying physical assumptions, as only the fine modes had been considered in the gas–particle interactions in the predecessor submodels. The main new features of MADE3 are the ability of coarse mode particles to take up condensing vapors and to coagulate with fine mode particles, and the gas–particle partitioning of chlorine, which is mainly contained in sea spray (SS) particles.

In order to test the algorithms used in the new submodel it was run in a box model setup and the results were compared to those obtained in an analogous setup with the much more detailed, particle-resolved aerosol model PartMC-MOSAIC. The comparison was performed for an idealized marine boundary layer test case and showed improved performance of MADE3 over MADE in the representation of coarse mode particles and total aerosol composition.

Subsequently, MADE3 was implemented into the atmospheric chemistry general circulation model EMAC. Due to the new mode structure this required extensive adaptations to other submodels, specifically to the one used for cloud and precipitation processing of aerosol particles. EMAC does not track interstitial aerosol particles separately from those immersed in cloud droplets, ice crystals, or precipitation. Hence, a sophisticated scheme was devised and implemented for the assignment of the in-cloud or in-precipitation aerosol to one of four possible modes, instead of just one possible mode in the MADE case.

The coupled model, EMAC with MADE3, was thoroughly evaluated by comparison of simulation output to station network measurements of near-surface aerosol component mass concentrations, to airborne measurements of vertical aerosol mass mixing ratio and number concentration profiles, to ground-based and airborne measurements of particle size distributions, and to station network and satellite measurements of aerosol optical depth. Satisfactory agreement with the observations was obtained and it was thus shown that MADE3 is ready for application within EMAC. The results from an identically designed simulation with the predecessor submodel MADE led to the conclusion that a fraction of the secondary aerosol species partitions to the coarse modes in MADE3 and is thus removed more quickly from the atmosphere. Furthermore, a new evaluation method was developed, which allows for comparison of model output to size-resolved electron microscopy measurements of particle composition.

Both submodels, MADE3 and MADE, were finally used in EMAC simulations of the effect of ship emissions on the atmospheric aerosol. As in previous studies for year 2000 conditions, SO_4 was found to be the dominant species in the fine modes in this context. In contrast to SO_4, the major fraction of ship emissions-induced near-surface NO_3 was found to partition to the coarse modes in the MADE3 simulations. A similar amount of fine mode NO_3 as in the present

and former MADE simulations was also formed. Hence, fine mode particle growth due to ship emissions was also similar, and was reduced in idealized simulations of a future low-sulfur fuel scenario. Particle volume concentration decreased by about 1 % due to ship emissions in the MADE3 simulations, but not in the MADE simulations. This finding was independent of the fuel sulfur content. In summary, the inclusion of coarse mode particle interactions and the gas–particle partitioning of chlorine could alter prior conclusions on the climate effect of ship emissions-induced aerosol perturbations, mainly due to the differences in NO_3 formation.

This climate effect will be re-quantified in a follow-up study by coupling the MADE3 aerosol to a two-moment cloud microphysics scheme. Further planned applications of the new submodel include the quantification of climate effects of aerosol perturbations via their influence on ice clouds as well as simulations with boundary conditions specific to measurement campaigns. Results from the latter may lead to further model improvements and can also provide guidance for the interpretation of measurement results.

Kurzfassung

Laut jüngeren Klimamodellstudien könnte Sulfat (SO_4) aus Schiffsabgasen einen der größten Beiträge zum negativen anthropogenen Strahlungsantrieb durch Aerosole liefern. Aufgrund strengerer Grenzwerte für den maximalen Schwefelgehalt in Schiffstreibstoffen erwartet man für die Zukunft einen starken Rückgang dieses Beitrags. Ein Teil der Reduktion könnte durch Bildung von Nitrat (NO_3) kompensiert werden. Allerdings deuten Messungen darauf hin, dass zur Quantifizierung dieses Effekts die Wechselwirkung von Partikeln der Grobmode mit kondensierbaren Spurengasen zu berücksichtigen ist, was in bisherigen Studien zu diesem Thema nicht der Fall war. Die vorliegende Arbeit befasst sich aufgrund dieses Defizits mit der Erweiterung eines der in den früheren Studien verwendeten Aerosol-Submodelle, nämlich MADE.

Das neue Submodell, MADE3, basiert auf MADE-in, der zweiten Generation von MADE. Mit seinen neun Moden werden je drei Partikeltypen in drei Größenklassen dargestellt. Die damit verbundene erhöhte Komplexität gegenüber MADE und MADE-in machte eine vollständige Überarbeitung des Modell-Quelltexts erforderlich. Zudem mussten grundlegende Annahmen überdacht werden, da in den Vorgänger-Submodellen nur die feinen Moden in der Gas-Aerosol-Wechselwirkung berücksichtigt wurden. Neben der Einbeziehung der groben Moden in diesen Prozess sind die wesentlichen Neuerungen in MADE3 die Berücksichtigung von Koagulation zwischen Partikeln der feinen und groben Moden und die Partitionierung von Chlor, hauptsächlich aus Seesalz, zwischen Gas und Aerosol.

Um die Algorithmen des neuen Submodells zu prüfen, wurde eine idealisierte Boxmodell-Simulation der marinen Grenzschicht durchgeführt, deren Resultate mit denjenigen einer analogen Simulation mit dem sehr viel detaillierteren, partikelaufgelösten Aerosolmodell PartMC-MOSAIC verglichen wurden. Der Vergleich zeigte eine Verbesserung von MADE3 gegenüber MADE in der Darstellung von Partikeln der groben Mode und der Gesamtaerosol-Zusammensetzung.

Anschließend wurde MADE3 in das globale Chemie-Zirkulationsmodell EMAC implementiert. Durch die neue Modenstruktur waren hierfür umfangreiche Eingriffe in andere Submodelle erforderlich, speziell in dasjenige, das Wolken- und Niederschlagseffekte auf das Aerosol berechnet. Da EMAC interstitielles und in Wolkentröpfchen, Eiskristallen oder Niederschlag enthaltenes Aerosol nicht separat beschreibt, wurde ein ausgeklügeltes Schema entworfen, um letzteres den vier möglichen Moden – statt einer im Fall von MADE – zuzuordnen.

Das gekoppelte Modell wurde sorgfältig evaluiert. Hierzu diente der Vergleich von Simulationsdaten mit Stationsnetzwerkmessungen von oberflächennahen Massenkonzentrationen von Aerosolkomponenten, mit Flugzeugmessungen von Vertikalprofilen der Anzahlkonzentration und des Aerosolmassenmischungsverhältnisses, mit bodengebundenen und flugzeuggetragenen Messungen von Partikelgrößenverteilungen sowie mit Stationsnetzwerk- und Satellitenmessungen der optischen Dicke des Aerosols. Durch eine zufriedenstellende Übereinstimmung konnte gezeigt werden, dass MADE3 als Teil von EMAC einsatzreif ist. Aus einer identisch aufgesetzten Simulation mit MADE ergab sich, dass ein Teil des sekundären Aerosols bei Verwendung von MADE3 in die groben Moden gelangt und so schneller aus der Atmosphäre entfernt wird. Zudem wurde eine neue Evaluationsmethode entwickelt, die es erlaubt, Simulationsdaten mit größenaufgelösten Elektronenmikroskopie-Messungen der Partikelzusammensetzung zu vergleichen.

Schließlich wurde sowohl MADE3 als auch MADE in EMAC-Simulationen des Effekts von Schiffsemissionen auf das atmosphärische Aerosol verwendet. Wie in früheren Studien stellte sich dabei für die Bedingungen im Jahr 2000 SO_4 als wichtigster Beitrag zu den feinen Moden

heraus. Im Gegensatz zu SO_4 gelangte NO_3 in den Simulationen mit MADE3 zu einem großen Teil in die groben Moden. In den feinen Moden bildete sich eine ähnliche Menge NO_3 wie in der hier durchgeführten und früheren Simulationen mit MADE. Partikel der feinen Moden vergrößerten sich daher durch Schiffsemissionen ebenfalls ähnlich, auch in einem idealisierten Zukunftsszenario mit geringerem Schwefelgehalt im Treibstoff. Die Volumenkonzentration von Partikeln verringerte sich aufgrund der Schiffsemissionen in den MADE3-Simulationen um etwa 1 %, in den MADE-Simulationen hingegen nicht – unabhängig von dem Schwefelgehalt des Treibstoffs. Zusammenfassend lässt sich feststellen, dass die Berücksichtigung von Wechselwirkungen der Grobmodenpartikel und der Gas-Aerosol-Partitionierung von Chlor auch Folgen für die Bestimmung der Klimawirkung von durch Schiffsemissionen verursachten Aerosolstörungen haben könnte, speziell durch den Effekt auf die NO_3-Bildung.

Diese Klimawirkung wird in einer Folgestudie neu quantifiziert werden, indem das MADE3-Aerosol an ein Zwei-Momenten-Schema für Wolkenmikrophysik gekoppelt wird. Darüber hinaus sind Anwendungen des neuen Submodells zur Bestimmung der Klimawirkung von Aerosolstörungen durch deren Einfluss auf Eiswolken geplant sowie Simulationen mit den spezifischen Randbedingungen von Messkampagnen. Letztere können sowohl dazu dienen das Modell weiter zu verbessern als auch dabei helfen Messergebnisse zu interpretieren.

Chapter 1

Introduction[1]

1.1 Motivation

Aerosol particles affect the energy balance of the earth both directly by scattering or absorbing radiation and indirectly by acting as cloud condensation nuclei. The present-day global annual average net effect of these processes is probably a negative radiative forcing (RF), i.e., a cooling effect, with respect to preindustrial times (e.g., Forster et al., 2007; Bellouin et al., 2013b; Boucher et al., 2013; Naik et al., 2013). Hence, the concurrent positive forcing by long-lived greenhouse gases may be partly offset by the aerosol forcing.

Global model simulations indicated that the emissions from ocean ship traffic may be one of the largest contributors to the anthropogenic aerosol forcing (Capaldo et al., 1999; Lauer et al., 2007, 2009; Righi et al., 2011, 2013; Olivié et al., 2012; Peters et al., 2012, 2013). This contribution is mainly caused by the sulfur in the ship exhaust plumes that leads to the formation of aerosol sulfate (SO_4). Nucleation of new particles, condensation of sulfuric acid (H_2SO_4) vapor on emitted as well as on background particles, and chemical reactions of sulfur dioxide (SO_2) dissolved in cloud droplets all contribute to SO_4 formation.

In addition to their potential climate impact, ship emissions may also affect human health. Due to increased regulation on other emitters and due to a growing ship traffic volume, ship emissions have become one of the major sources of pollution in coastal areas and port cities (Lu et al., 2013; González & Rodríguez, 2013). For instance, Nie et al. (2013) reported an increase of SO_2 and reactive nitrogen oxides (NO_x) emissions by ships over the South China Sea of 19 % and 15 %, respectively, during little more than a decade. The concentrations of pollutants emitted by ships are highest in the vicinity of major harbors (e.g., Johansson et al., 2013) and can contribute several 10 % to fine particle mass concentrations in coastal areas (Ault et al., 2009; Kotchenruther, 2013; Yau et al., 2013; Zhao et al., 2013c; Viana et al., 2014; Kivekäs et al., 2014).

The International Maritime Organization (IMO) has therefore set limits on allowed ship fuel sulfur content that will be further tightened in the future (IMO, 2011) in order to improve air quality in port cities and along coasts. Such air quality improvement strategies also influence the climatic effects of pollutants (Eyring et al., 2010; Péré et al., 2012; Baker et al., 2015). In this case, on the one hand, the sulfur reduction leads to a decrease of SO_2 and, thus, aerosol SO_4 concentrations (Lauer et al., 2009; Righi et al., 2011; Schembari et al., 2012; Johansson et al., 2013; Jonson et al., 2015). On the other hand, the reduced SO_4 concentrations allow more aerosol nitrate (NO_3) to be formed by condensation of nitric acid (HNO_3) from the gas phase. Increased NO_3 content was shown to make up for a substantial fraction of the SO_4 reduction (Lauer et al., 2009; Bellouin et al., 2011; Righi et al., 2011). The aerosol RF and total particulate mass concentrations may therefore not be reduced as much as the SO_4 concentrations.

A number of measurements suggest that aerosol NO_3 primarily partitions to coarse mode particles ($\gtrsim 2\,\mu m$) both under clean marine conditions and when marine aerosol is affected by anthropogenic pollution (Kerminen et al., 1997; Hara et al., 1999; Yeatman et al., 2001; Cavalli et al., 2004; Nolte et al., 2008). Specifically, the measurements presented by Prabhakar

[1] Parts of this chapter appeared in similar form in a recent publication (Kaiser et al., The MESSy aerosol submodel MADE3 (v2.0b): description and a box model test, Geosci. Model Dev., 7(3), 1137–1157).

et al. (2014) indicate that ship-induced NO_3 is mainly associated with coarse mode sea spray particles. However, in the assessments of the ship emissions-induced aerosol effects on climate by Olivié et al. (2012) and Peters et al. (2012, 2013) NO_3 formation was not included at all, and the low-sulfur ship fuel studies by Lauer et al. (2009) and Righi et al. (2011) did not include interactions of condensable gases with coarse mode particles (except for water vapor). These deficiencies may have led to errors in the quantification of shipping effects on the atmospheric aerosol. The role that coarse mode particles and aerosol NO_3 formation play for the impact of ship emissions on the global aerosol is therefore unclear, which provides the motivation for the present work.

1.2 Scientific questions

In order to reassess the aerosol perturbations caused by global ship traffic a more detailed microphysical treatment of coarse mode particles has to be included in a global model. This will of course have wider consequences on the atmospheric aerosol as a whole. For instance, since a major fraction of the natural aerosol mass burden is associated with coarse mode particles, one may also expect to see an effect on the simulated properties of the natural aerosol. This work is therefore motivated by a general question about the global aerosol and two specific ones concerning ship emissions:

1. How, where, and by how much do simulated size-resolved aerosol species mass and number concentrations change if interactions of coarse mode particles with fine particles and condensable gases are included?

2. Does the inclusion of the above-mentioned coarse mode particle interactions change the simulated effect of year 2000 emissions by ocean-going ships on the aerosol composition and/or distribution?

3. Does it change the simulated response to anticipated future reductions in ship fuel sulfur content?

1.3 Method

To improve on previous aerosol modeling studies a new aerosol submodel was developed as part of the present work: MADE3, the 3rd generation of the Modal Aerosol Dynamics model for Europe, adapted for global applications (Chap. 3). Designed as an extension to a global atmospheric chemistry general circulation model (AC-GCM), MADE3 is based on MADE (Ackermann et al., 1998; Lauer et al., 2005) and MADE-in (Aquila et al., 2011), but for the first time includes interactions of coarse mode particles with both condensable gases and other particles. To enable the further extension major parts of the submodel code were restructured and improved.

In a box model test, simulations with MADE3, its predecessor MADE, and the much more detailed stand-alone aerosol box model PartMC-MOSAIC were compared in order to test the algorithms applied in the new submodel (Chap. 4). As the results of this intercomparison were encouraging, MADE3 was subsequently implemented within the MESSy framework (Jöckel et al., 2005, 2010). Thus, it can be coupled to an atmospheric chemistry scheme and to the general circulation model ECHAM5 (Roeckner et al., 2006). Together with a few others, these (sub)models form the AC-GCM EMAC (ECHAM5/MESSy2 atmospheric chemistry model).

The new model, i.e., EMAC with MADE3 (Chap. 5), was evaluated against multiple observational datasets (Chap. 6). These include measurements of aerosol species concentrations,

particle size distributions, and aerosol optical depth from ground-based station networks, vertical profiles of particle number concentrations and (species) mass mixing ratios measured by airborne instruments, aerosol optical depth data derived from satellite observations, and electron microscopy measurements of size-resolved particle composition.

Different model setups were designed for simulations that specifically address the questions raised in the previous section (Chaps. 6 and 7). Separate EMAC simulations were run using either MADE or MADE3 with a reference model setup that had been used in similar form in previous simulations with the old submodel MADE. Thus, it was possible to assess differences in the simulated global aerosol composition and distribution due to inclusion of the coarse mode particle interactions with condensable gases and fine particles (Question 1; Sect. 6.3). On the basis of the reference setup, a model configuration was developed that allowed for a re-quantification of the ship emission effects on the global aerosol for year 2000 conditions (Question 2; Sect. 7.1). A further setup was used to assess potential effects of a future ship fuel sulfur reduction (Question 3; Sect. 7.2). These simulations were again run with both the old submodel MADE and the new submodel MADE3. Thus, they allowed for a discussion of differences to previous assessments that were caused by the inclusion of the coarse mode particle interactions.

Chapter 2

Background and state of the science

This chapter provides the context in which the present work should be viewed. The first two sections focus on measurements and observations of atmospheric aerosol particles and their implications, and contain some general information on the relevant physics and chemistry. In the third section, background knowledge on modeling the atmospheric aerosol is presented and the most relevant results of past studies are summarized.

2.1 The atmospheric aerosol

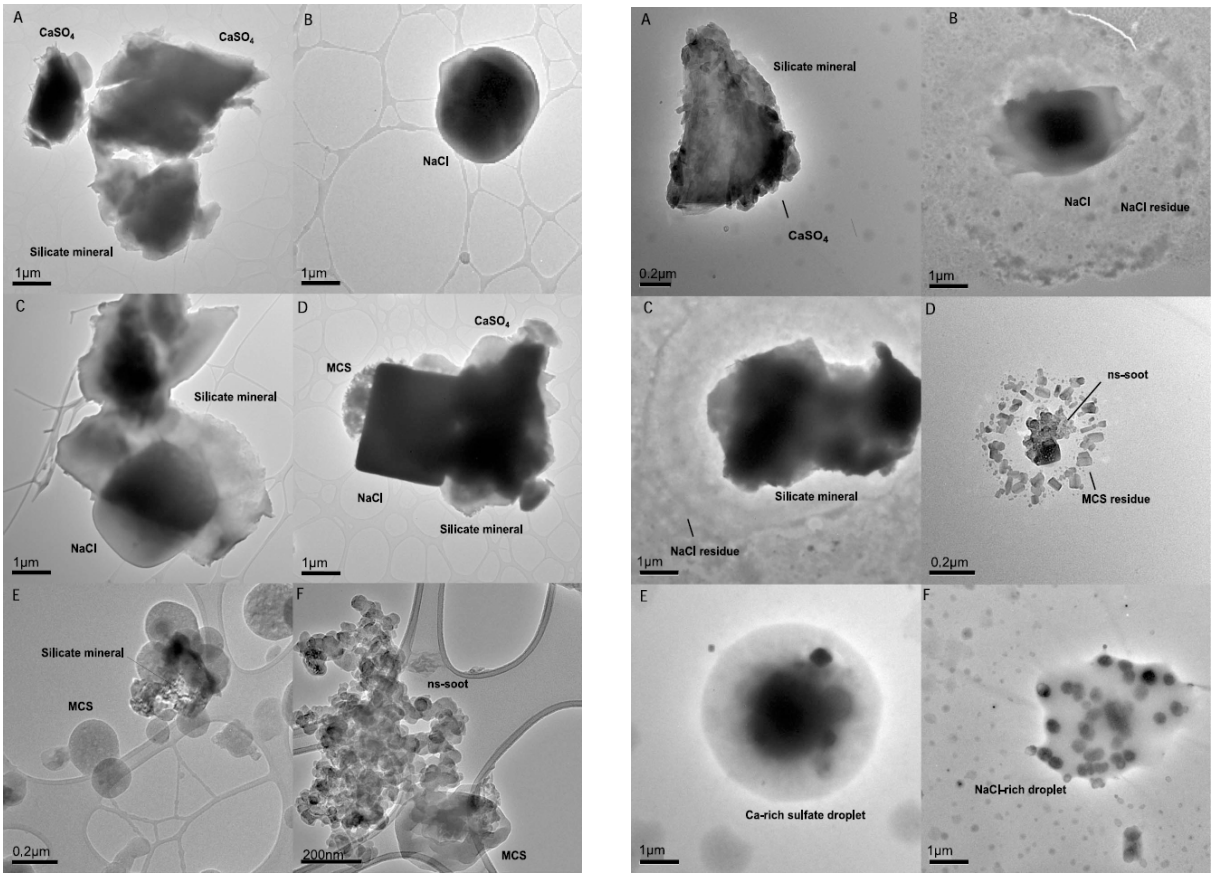

Figure 2.1: Transmission electron microscopy images of dried ambient aerosol particles sampled in the Oman mountain region (Semeniuk et al., 2014, their Figs. 5 and 6)

Aerosol particles, i.e., suspended solid particles or liquid droplets that are smaller than a few tens of micrometers, are a ubiquitous and essential component of the earth's atmosphere (Pöschl, 2005). Some example particles that were collected during aircraft measurements in the Oman mountain region are shown in Fig. 2.1. Although the actual definition of an aerosol includes both the particles and the gas in which they are suspended, the atmospheric science community often uses the term to refer to the particulate phase only. This section aims to

provide the motivation for studying aerosol particles—with a focus on the troposphere—and their atmospheric processing, some basic background knowledge on the subject, and an overview of the current state of the science. It is tailored to the scope of the present work. For a more comprehensive review of the state of the science the reader is referred to the recent review by Fuzzi et al. (2015), who put a special focus on policy implications.

2.1.1 Relevance

Aerosol particles play an essential role in weather and climate due to their interactions with radiation and clouds (Boucher et al., 2013). Locally, the induced modifications can be quite substantial, as shown, for instance, by the 10 K temperature drop due to agricultural burning and fossil fuel combustion found in a study by Ding et al. (2013). On the regional scale, Makar et al. (2015) showed that weather forecast skill can be improved when including aerosol effects. This is also evident from the study by Chen et al. (2015a), who found improved predictive skill for a hurricane track when including the aerosol–radiation interaction of mineral dust in their model. On a different note, aerosol particles also influence air quality, i.e., they can impair visual range, and, depending on their concentration, size, and composition, they also affect human health (Chow et al., 2006; Arden Pope III & Dockery, 2006). Fang et al. (2013), for example, associated an annual average of about 1.5 million premature deaths with increases in aerosol concentrations over the period of industrialization. Furthermore, the particles influence tropospheric chemistry, e.g. directly via condensation and evaporation of semi-volatile vapors, and indirectly via enhanced lightning activity that influences ozone chemistry (Yuan et al., 2012). Atmospheric chemistry can also be affected by aerosol particles in the tropopause region and in the stratosphere, for instance via heterogeneous chemical reactions on their surfaces (e.g., Hendricks et al., 1999; Kärcher & Solomon, 1999, and references therein), which can lead to strong ozone depletion after volcanic eruptions (Telford et al., 2009). Additionally, the particles can serve as a means of transport for both toxic chemicals (e.g., deposition of Pb from road traffic onto soils; Catinon et al., 2013) and nutrients (e.g., deposition of iron into the oceans, or phosphorus from Africa in the Amazon basin; Fan et al., 2006; Yu et al., 2015). Finally, many of the proposed options for climate geoengineering via solar radiation management rely on the addition of aerosol particles to the atmosphere (Vaughan & Lenton, 2011).

In this thesis the emphasis is on the aerosol particle-induced effects on climate-relevant processes. To put the present work into context and as part of the motivation this section contains a selection of observational evidence for such phenomena.

Frequently used measures for the aerosol impact on the climate are the radiative effect (RE) and the radiative forcing (RF). Both measures describe differences in the radiation budget of the earth that can be attributed to a forcing agent, in this case the aerosol. The term “radiative forcing” (RF) is normally used when discussing the net change of radiative flux (units: $\mathrm{W\,m^{-2}}$) at the tropopause due to a perturbation with respect to a reference year, which is usually assumed to be representative of preindustrial times. Adjustment of the stratosphere to the perturbation is sometimes allowed, whereas tropospheric conditions are held fixed at their unperturbed state. The term “radiative effect” (RE) is often used when referring to a flux difference at the top of the atmosphere between two different (assumed) atmospheric states at the same instant in time. For a quantitative comparison of the two measures see the article by Heald et al. (2014). The main influence of aerosol particles on the radiation budget of the earth is due to tropospheric aerosol rather than stratospheric particles, except after major volcanic eruptions (Deshler, 2008).

In publications on aerosol radiative effects or forcings, a distinction is often made between the so-called direct and indirect effects or forcings. The term “direct” refers to the radiation that is directly scattered or absorbed by the aerosol particles. The term “indirect” is used for

the perturbation to the radiation budget that is caused by aerosol–cloud interactions and the associated modification of cloud (optical) properties.

Both RF and RE are typically quantified using computer models (see Sect. 2.3). However, a few studies have also attempted to derive them from observations. For instance, Loeb & Manalo-Smith (2005) compared two methods to derive the direct aerosol RE over oceans from satellite data, while Sundström et al. (2015) focused on a retrieval over land that is based on data from the same instruments. Cherian et al. (2014) used observed trends in solar radiation that reaches the ground over Europe in combination with modeled correlations of this trend with the global RE of anthropogenic aerosol particles to estimate a value of $(-1.3 \pm 0.4)\,\mathrm{W\,m^{-2}}$ for the latter. Bellouin et al. (2013b), using satellite retrievals combined with numerical modeling, arrived at a global average direct aerosol RF of $(-0.7 \pm 0.3)\,\mathrm{W\,m^{-2}}$ and an indirect RF of $(-0.6 \pm 0.4)\,\mathrm{W\,m^{-2}}$, which is compatible with the results from a similar study by Ma et al. (2014), where a different reference scenario was used: $-0.59\,\mathrm{W\,m^{-2}}$ and $-0.34\,\mathrm{W\,m^{-2}}$, respectively.

The direct aerosol-induced perturbation of the earth's radiation budget is determined by the interplay of absorption and scattering of solar and terrestrial radiation by the particles with other physical climate factors such as clouds, albedo, and relative humidity (Ocko et al., 2012). For example, the effect of aerosol–radiation interactions strongly depends on the relative altitude of clouds and aerosol layers (e.g., Vuolo et al., 2014). Put simply, aerosol particles below a cloud will have a different effect than the same particles above a cloud. Aerosol water uptake can also strongly modify this effect via changes in the particles' optical properties (e.g., Rastak et al., 2014). Furthermore, the vertical profile of aerosol mass concentrations was also shown to be an important factor for the aerosol impact on climate (e.g., Ban-Weiss et al., 2012).

The indirect contribution to the radiation budget perturbations by aerosols is due to their interactions with clouds. Clouds would not exist in the form that we are used to without aerosol particles (Seinfeld & Pandis, 2006). It is therefore reasonable to assume that particle composition and size, as well as varying levels of particle concentrations may affect cloud formation or cloud properties. For instance, a cloud's reflectivity is largely determined by the cloud droplet number concentration (CDNC) and the radii of the cloud droplets. At constant cloud liquid water content it increases with increasing CDNC, as cloud droplet radii decrease. In clean air masses, CDNC is mainly driven by the cloud condensation nuclei (CCN) number concentration, which is in turn driven by the number concentration of aerosol particles with diameters greater than $\sim$100 nm (Anttila et al., 2012). This finding is in line with a number of other measurement reports (Lu et al., 2007; Christensen & Stephens, 2011), which concluded that increased aerosol loading, at least up to an asymptotic upper limit (Ahmad et al., 2013), increases CDNC and decreases the cloud droplet radius. The associated brightening of the cloud is called the Twomey effect (Twomey, 1977), which was also observed by Werner et al. (2014), for instance.

Other effects of aerosol particles on clouds are also conceivable. Wang et al. (2012), for instance, using satellite observations, analyzed the effect on cloud lifetime through an increase in liquid water path (i.e., the vertical integral of cloud liquid water content), but found it to be small. It should also be noted that the aerosol effect of enhanced cloud formation may not exclusively be due to additional CCN. An absorbing aerosol layer may also enhance cloud formation below by influencing meteorological parameters such as the temperature gradient (Costantino & Bréon, 2013; Doherty & Evan, 2014). However, such a layer can also have a significant direct RE (Meyer et al., 2013, and references therein) and may thus offset the below- and in-cloud aerosol-induced cloud brightening.

Due to couplings and feedbacks in the climate system the aerosol influence on climate can be strongly non-local. For example, Clarke et al. (2013) found that a major fraction of CCN in the equatorial Pacific marine boundary layer (MBL) could be derived from aerosol particles that have been transported over thousands of kilometers in the free troposphere above the

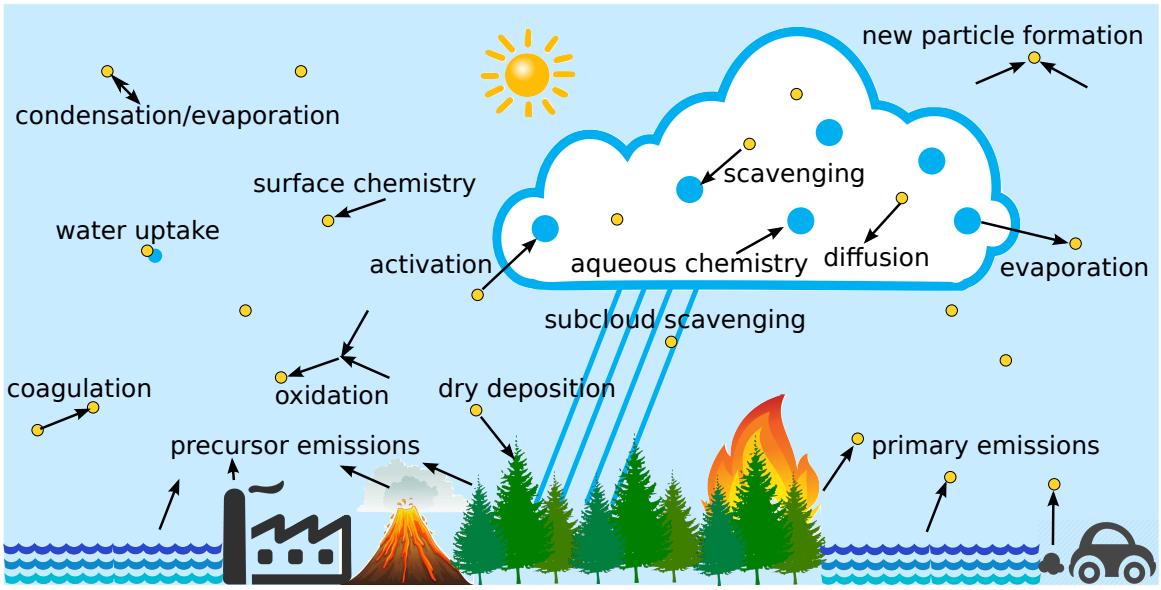

Figure 2.2: Processes relevant for aerosol dynamics in the atmosphere (adapted from Ghan & Schwartz, 2007, their Fig. 1).

planetary boundary layer (typically the lowest 0.5 to 2 km of the atmosphere). Another such example is the reduction in snow albedo at high latitudes that is caused by soot particles (e.g., Warren & Wiscombe, 1980; Boucher et al., 2013) which are mostly emitted in the midlatitudes and tropics.

2.1.2 Aerosol processes

Figure 2.2 provides an overview of all the processes relevant for the dynamics of the atmospheric aerosol. These processes are briefly described in this subsection.

Aerosol particles can enter the atmosphere either by direct emission, both from natural and anthropogenic sources, or by in-situ nucleation of molecular clusters formed from low-volatility vapors. Favorable sites for nucleation include the free troposphere, the forested continental boundary layer, and coastal areas (Kulmala & Kerminen, 2008). Possibly, the clean MBL should also be added to this list (Clarke et al., 1998). Furthermore, nucleation occurs within or close to the tail pipes of vehicles powered by fossil fuels and in the vicinity of industrial chimneys (Kulmala & Kerminen, 2008), and may also take place in biomass burning plumes (Hennigan et al., 2012). The process of new particle formation (NPF), i.e., nucleation and initial growth to detectable aerosol particle sizes (Fig. 2.3), is one of the least understood parts of the atmospheric aerosol life cycle. It is now an established fact that sulfuric acid (H_2SO_4) plays a major role in this context (Kulmala et al., 2004), but it may not be the only required ingredient (Rose et al., 2015). The degree to which other species such as ammonia (NH_3) and other bases (e.g., Almeida et al., 2013; Neitola et al., 2014; Schobesberger et al., 2015; Glasoe et al., 2015), ions (e.g., Yu et al., 2012; Gonser et al., 2014), organic compounds (e.g., Karl et al., 2012; Bzdek et al., 2014; Riccobono et al., 2014; Wong et al., 2014; Olin et al., 2015; Wang et al., 2015; Patoulias et al., 2015), radicals (e.g., Bonn et al., 2014), and other components (e.g. iodine; Allan et al., 2015) are involved is still an area of active research. Gaseous H_2SO_4 is produced in the atmosphere by oxidation of sulfur dioxide (SO_2). SO_2, in turn, is directly emitted in anthropogenic activities such as coal burning as well as by volcanoes, and also produced in situ from dimethyl sulfide (DMS), which is emitted by phytoplankton in the oceans. While nucleation is an important source of CCN (Merikanto et al., 2009; Westervelt et al., 2013), the exact concentrations of CCN are generally not very sensitive to the rate of NPF (Lee et al., 2013a,c; Westervelt et al., 2013).

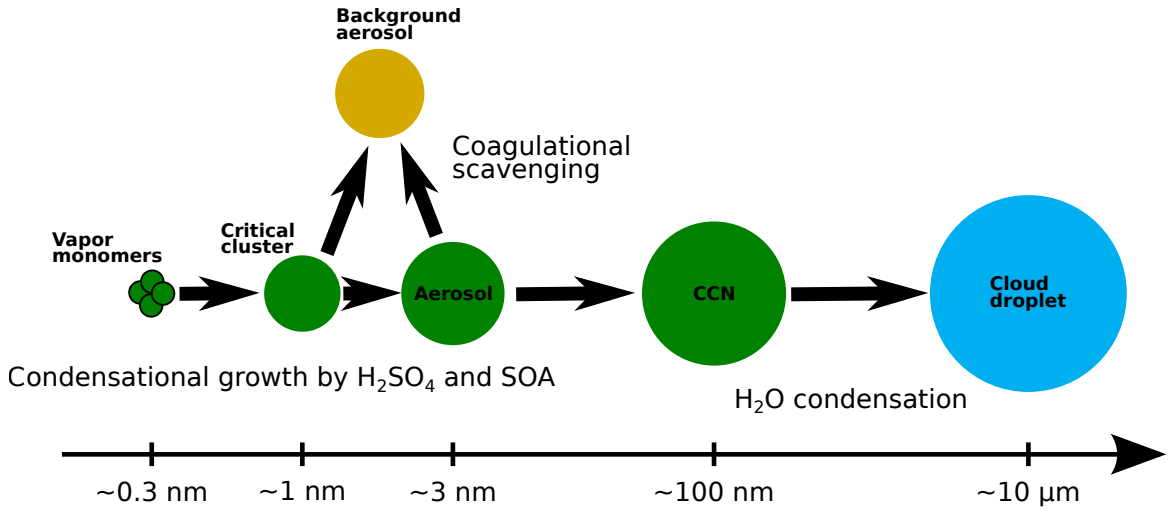

Figure 2.3: Nucleation and growth of aerosol particles (adapted from Westervelt et al., 2013, their Fig. 1).

After entering the atmosphere aerosol particles are transported with the air that surrounds them. Thus, they are subject to advection, convective up- and downdrafts, as well as lofting by the vertical wind components inside cyclones and along mountain slopes. During transport they undergo various processes that affect their mass and number concentrations and their size distribution.

As mentioned above, some particles, i.e., the CCN, can be "activated" to form cloud or fog droplets. The process of activation is triggered when the water vapor supersaturation surpasses a critical value. This threshold is determined by the Gibbs free energy of the gas–particle system (Seinfeld & Pandis, 2006). The magnitude of the Gibbs free energy reduction by transfer of water molecules from the gas to the condensed phase is determined by the supersaturation. If this reduction outweighs the Gibbs free energy increase that is associated with the transfer due to the particle's surface tension, the particle will grow into a cloud or fog droplet. The ability of aerosol particles to act as CCN depends on their size and composition. Besides, particle morphology may also play a role (e.g., Giordano et al., 2015). While Dusek et al. (2006) claimed that size mattered more than composition for the activation behavior of CCN, this may not be the case for low supersaturations (e.g., Zhang et al., 2014a) and for all aerosol size ranges. Studies by Twohy & Anderson (2008) and Almeida et al. (2014) indicated that composition will matter less for larger particles, but can still play the dominant role at smaller particle sizes. The threshold diameter between these two regimes increases with decreasing supersaturation (Twohy & Anderson, 2008). Hence, in marine stratocumulus clouds, for example, where high supersaturations are rare due to the shallow convection that does not lead to high updraft velocities, composition may play the more important role. Furthermore, measurements by Crosbie et al. (2015) showed that much variability in aerosol CCN activity is also associated with environmental parameters such as meteorology, aerosol precursor emissions, and their atmospheric processing. In their study, for instance, particle size was the dominant driver of CCN activation behavior during winter, but could not explain CCN variability satisfactorily during summer.

Once they have formed, cloud and fog droplets can serve as chemical "reactors", where reactions of dissolved gases can lead to formation of substances that will partition to the aerosol phase upon droplet evaporation. Furthermore, interstitial particles may be taken up by cloud or fog droplets, which reduces the aerosol number concentration.

If cloud droplets do not re-evaporate, they remove aerosol particles from the atmosphere by precipitation, or wet deposition. For CCN-sized particles ($\gtrsim 100$ nm) nucleation scavenging, i.e., activation and subsequent rain-out, is the most efficient removal process, whereas for smaller

particles scavenging by impaction of falling hydrometeors is more efficient. Generally, wet deposition of particle mass is increasingly efficient as particle size increases (e.g., Moteki et al., 2012; Bègue et al., 2012). Dry deposition, i.e., loss of particles from the atmosphere by contact with soils, canopies, or water bodies, is another important particle removal process, at least in the lowest atmospheric layer. Furthermore, large particles ($\gtrsim 1\,\mu m$) are also removed from the atmosphere to a significant degree by gravitational settling (sedimentation). Finally, aerosol particles may freeze or act as ice nuclei (IN) and thus contribute to ice cloud formation. Again, their fate then depends on whether the ice crystals sublimate (or melt and evaporate) or if they reach the ground in the form of precipitation.

Condensation of low- and semi-volatile vapors on pre-existing particles can be another source of aerosol mass in addition to primary emissions and cloud processing. Conversely, evaporation of semi-volatile vapors can reduce the atmospheric aerosol mass burden. These processes, and which one of them dominates, depend on environmental parameters such as temperature and relative humidity (RH) (e.g., Aan de Brugh et al., 2013).

A sink that only affects aerosol particle numbers is coagulation of particles. Coagulation rates increase with an increasing difference in the sizes of the involved particles. Hence, this process most strongly affects the number concentrations of the smallest particles.

Aerosol particles absorb and/or scatter both solar and terrestrial radiation during atmospheric transport and processing. Typically, the shortwave part of the spectrum provides the more relevant contribution to these effects (Zhou & Savijärvi, 2014). Scattering of solar radiation cools the atmospheric layers below the scatterers, while absorption heats the layer that contains the absorbers. The latter can also lead to "cloud burn-off" if the particles are located inside a cloud, or even inside cloud droplets (e.g., Wang et al., 2013b). The ratio of scattered and absorbed radiative fluxes depends on the composition of the particles, especially on their mixing state (e.g., Matsui et al., 2013, see also Sect. 5.10).

2.1.3 Aerosol properties

Both the impact and the atmospheric fate of aerosol particles are mainly influenced by their size and composition. These properties depend on the particles' sources and are in turn affected by their atmospheric processing. This subsection provides a brief overview of relevant aerosol properties as derived from measurements.

Size and lifetime

Aerosol particle measurements often refer to the so-called dry aerosol mass, i.e., all particle components except water. Although aerosol particles are not necessarily spherical in shape (especially dry particles, see Fig. 2.1), their size is typically reported in terms of a radius or diameter. It is therefore important in measurement reports to define how the (equivalent) diameter was derived (e.g., volumetric vs. aerodynamic diameter) because different techniques yield different numerical values. However, for the overview presented here, the differences are small enough to be ignored.

Due to the different processes acting on particles of different sizes the atmospheric aerosol often appears in three distinct size ranges, or modes, namely the Aitken (tens of nanometers), accumulation (hundreds of nanometers), and coarse modes (micrometers and greater). In some cases an additional nucleation mode (less than about 10 nm) may be present at the small end of the scale. Another distinction that is often made is that between fine particles, which include the nucleation, Aitken, and accumulation modes, and coarse particles, i.e., the coarse mode. Especially in the context of air quality research and policymaking, the term PM2.5 is also used frequently. It describes the mass of all particles smaller than 2.5 µm and thus roughly

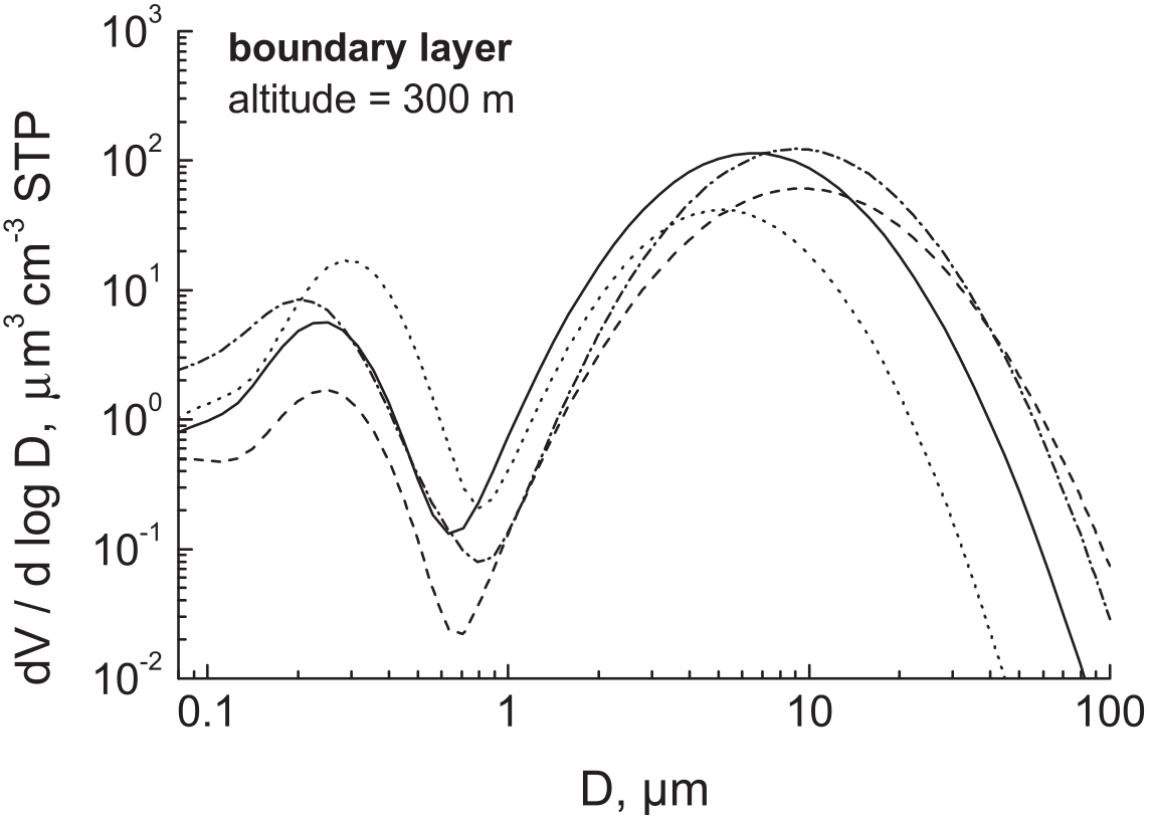

Figure 2.4: Aerosol volume size distributions (accumulation and coarse modes) measured over north-eastern Germany on different days during an aircraft campaign in July and August 1998 (adapted from Petzold et al., 2002, their Fig. 6).

corresponds to the integral mass of the fine modes. Similarly, PM1 describes particles with diameters $< 1\,\mu m$, often called ultrafine particles, and PM10 stands for the mass of all particles smaller than $10\,\mu m$, i.e., it essentially also includes the coarse mode.

Coarse mode aerosol mass and number concentrations predominantly stem from natural emissions because most particles emitted by human activities generally fall in the size range of the fine modes (exceptions include dust emissions due to land use, for example). For PM2.5, however, the anthropogenic contribution may actually be dominant, at least in the Northern Hemisphere, where most people live. Zare et al. (2014) found a natural contribution of 34 % to Northern Hemispheric PM2.5.

Particles of sizes up to a few tens of micrometers can be transported over long distances (e.g., Jeong et al., 2014). Thus, they participate in the processes outlined in Sect. 2.1.2. Larger particles settle too quickly upon emission to make a relevant impact and particles smaller than the nucleation mode have to be treated as molecular clusters rather than as aerosol.

The nucleation (if existent) and Aitken modes typically dominate the aerosol number concentration, sometimes reaching up to a few $10^5\,cm^{-3}$. The accumulation mode typically provides the largest contribution to particle surface area concentration, and the coarse mode often contributes the largest fraction to volume or mass concentration, up to a few $mg\,m^{-3}$. As an example, Figure 2.4 shows volume size distributions, i.e., the particle volume concentration per logarithmic size interval, from an aircraft campaign targeted at measuring optical and microphysical aerosol properties.

With an atmospheric residence time of a few weeks at most, tropospheric aerosol particles are considered a short-lived climate forcing agent. Hence, they react rather quickly to changes in emissions (e.g., Kompalli et al., 2014). Accumulation mode particles are those with the longest atmospheric residence time. Due to their larger size coarse mode particles are removed

more quickly by sedimentation. Nucleation and Aitken mode particles typically only exist for a couple of hours or days at most because they are efficiently collected by larger particles via coagulation and quickly grow into the accumulation mode via uptake of condensable vapors.

Composition

With respect to climatic effects, the chemical components of atmospheric aerosol particles that play a major role are sea spray (SS); mineral dust (DU); black carbon (BC); organic aerosol (OA); sulfate (SO_4); ammonium (NH_4); nitrate (NO_3); and water (H_2O). Note that ion charges are omitted in these abbreviations because different oxidation states of the aerosol components are not distinguished here. Based on composition, particles can be classified into various different categories, e.g., natural vs. anthropogenic, oceanic vs. continental, or primary vs. secondary.

Natural emissions of primary aerosol particles include the two largest contributors to atmospheric aerosol mass, namely DU from deserts and SS from the oceans' surface. The major fraction of these particles' mass resides in the coarse mode. DU particles mainly consist of chemically inert, insoluble silicates, but often also contain calcium (Ca) and other metal ions that can undergo reactions in the atmosphere. While there are ongoing debates about which particles or particle components serve as efficient IN and which do not, there has long been agreement that DU particles are important for ice cloud formation (e.g., Murray et al., 2012). This was confirmed again by the recent studies by Sakai et al. (2014), Tan et al. (2014), and Zhang et al. (2015).

The aerosol in the MBL is dominated by SS particles, whose major component is sodium chloride (NaCl) (Heintzenberg et al., 2000). In addition to NaCl, the marine aerosol contains SO_4, which is part of the SS aerosol itself, but also stems from oxidation of gaseous DMS that is emitted from the ocean's surface during biologically active periods, and from long-range transport (Simpson et al., 2014). Substitution of the chloride (Cl) in the SS particles, mainly by SO_4 and NO_3 formed from precursor gases, leads to the release of hydrochloric acid (HCl) to the gas phase. Depending on biological activity, OA can also make up a fraction of several 10 % of the SS, or more generally, the marine aerosol mass, especially in fine mode particles (e.g., Cavalli et al., 2004; Gantt & Meskhidze, 2013; Schmale et al., 2013). While the organic component of marine aerosol was found to be mainly primary material (O'Dowd et al., 2004), biological activity can also entail secondary organic aerosol (SOA) formation from the gas phase (Bikkina et al., 2014). Concerning marine aerosol–cloud interactions, the role of NaCl is clear: it forms efficient CCN as it easily takes up water. Larger uncertainties are associated with the contribution of organics to the MBL CCN budget (e.g., Meskhidze et al., 2011). Possibly, marine organic aerosol particles also act as IN and thus contribute further to the natural aerosol RE (e.g., Knopf et al., 2011; Yun & Penner, 2013, and references therein).

Other natural emitters include forest fires, which mainly add BC and OA to the atmosphere, and volcanic eruptions, which are responsible for the episodically significant concentrations of ash particles. Furthermore, volcanoes inject SO_2 into both the troposphere and the stratosphere and thus also add to the SO_4 that dominates the stratospheric aerosol (e.g., Murphy et al., 2014b, and references therein). Another significant natural source of aerosol mass in the troposphere is the formation of SOA from gaseous precursors that are emitted from the continental biosphere and the oceans. A similar, or even greater, fraction of SOA precursors, however, appears to be man-made (Hallquist et al., 2009, and references therein).

Anthropogenic emissions, like the natural ones, also include primary particles and precursors of secondary aerosol species. Among the former, the major component is BC, which is emitted in all kinds of combustion processes, e.g., in road, air, and ship traffic, industrial activities, domestic heating and cooking, or electric power generation from coal and gas. It is the major light-absorbing aerosol component; other components typically scatter more of the incoming

radiation than they absorb (e.g., Zhao et al., 2013b). Furthermore, BC particles may be the dominant IN during formation of contrails and contrail cirrus clouds (e.g., Petzold et al., 1998). Many other species, especially aerosol precursor gases, are co-emitted with BC to varying degrees in the combustion processes.

Only a small amount of SO_4 is emitted directly. The major SO_4 production occurs via oxidation of emitted SO_2 to H_2SO_4, which has a very low volatility. Globally, SO_2 mainly stems from anthropogenic sources, e.g., power plants, but over the remote ocean oxidation of DMS emissions can provide the largest contribution (e.g., Lin et al., 2012). Oxidation of SO_2 can occur in the gas phase, in cloud droplets, or on particle surfaces (e.g., Harris et al., 2014; Huang et al., 2014; Ueda et al., 2014). Similarly, NO_3, Cl, and NH_4 are produced from their precursor gases nitric acid (HNO_3), HCl, and NH_3 via condensation or via dissolution in aerosol particles or in cloud or fog droplets (e.g., Shrivastava et al., 2013; Yao & Zhang, 2012). HNO_3 is an oxidation product of reactive nitrogen oxides (NO_x), of which the dominant fraction is anthropogenically produced during combustion processes. Natural NO_x sources include biomass burning and lightning activity. The major source of HCl is the evaporation of Cl from SS particles. NH_3 plays a special role because it is the only base in the atmosphere with concentrations that affect aerosol composition. In many regions, anion uptake, i.e., uptake of NO_3 and Cl, depends on the availability of NH_3 (e.g., Kharol et al., 2013; Squizzato et al., 2013; Banzhaf et al., 2013). Its main source are agricultural activities.

Temperature is also a crucial factor in the gas–particle partitioning of NH_3/NH_4, HNO_3/NO_3, and HCl/Cl. Ammonium salts other than ammonium sulfate ($(NH_4)_2SO_4$), i.e., ammonium nitrate (NH_4NO_3) and ammonium chloride (NH_4Cl), readily evaporate at high temperatures. Hence, NO_3 and Cl concentrations are not necessarily elevated, even if NH_3 concentrations would permit additional formation of the ammonium salts (Gong et al., 2013).

Particulate organic matter (POM) is arguably the least well characterized component of the atmospheric aerosol, and it is the subject of a very active field of research. One major problem is the sheer number of different chemical species that contribute to POM and their classification into a useful number of groups, in which individual compounds have similar properties (e.g., Crippa et al., 2014; Murphy et al., 2014a). Regionally, up to ∼80 % of the fine particle mass can be POM (e.g., Murphy et al., 2006). In analogy to the inorganic species the organic aerosol mass is often separated into primary and secondary components, where the former stem from direct emissions and the latter are generated by oxidation of precursor vapors within the atmosphere. However, due to the semi-volatile nature of many organic compounds this distinction is not always straightforward (Donahue et al., 2009). Global estimates of organic aerosol mass formation by direct emission and SOA condensation vary by more than an order of magnitude (Hallquist et al., 2009).

The interaction of insoluble aerosol particles with other components of the climate system, especially with radiation and clouds, depends on their mixing state. A particle ensemble is said to be internally mixed if individual particles contain different chemical components; it is said to be externally mixed if each particle consists of only one specific component, but the ensemble contains multiple species. For example, the optical and CCN activation properties of soot/SO_4 mixtures depend on the mixing state of the particle ensemble (e.g., Ackerman & Toon, 1981; Fiebig et al., 2003; Liu et al., 2013). Furthermore, DU particles may become less efficient as IN if they acquire inorganic coatings (e.g., Chernoff & Bertram, 2010; Sullivan et al., 2010; Tan et al., 2014; Augustin-Bauditz et al., 2014), i.e., if they are transformed into an internal mixture. The ice nucleation efficiency of other potential IN, e.g., BC-containing soot particles, may also be affected by such coatings (e.g., Kärcher et al., 2007, and references therein).

Water uptake

Another ubiquitous component of atmospheric aerosol particles is H_2O. Its concentration in the particulate phase is generally regarded as a function of both RH and the so-called "dry" aerosol composition, i.e., the contributions of all non-H_2O components. Furthermore, aerosol water content also depends on the RH history due to hysteresis in the water uptake and expulsion process, and can also depend on the phase state of a particle's components (e.g., Gupta et al., 2015; Hodas et al., 2015).

Aerosol water content has several important implications for the fate and climatic impacts of aerosol particles. Through its contribution to particle size it affects both dry and wet removal processes as well as the particles' interaction with radiation. Absorption and/or scattering of radiation can be modified by aqueous coatings on insoluble particles. On the one hand, for instance, BC absorbs more radiation per unit volume if it is coated by non-absorbing material than if no coating is present due to a focusing effect (Bohren, 1986). On the other hand, absorption by BC-containing particles may be overestimated if a uniform mixture with the coating material is assumed (Jacobson, 2000). Absorption enhancement w.r.t. BC in uncoated particles also occurs, but is much weaker, if the BC is attached to particles consisting of non-absorbing species rather than coated by those species (Moteki et al., 2014). Furthermore, aerosol water also regulates gas–particle partitioning of semi-volatile species by controlling the concentrations of ions in solution.

Particles, or their chemical components, can be very broadly classified into two categories with respect to their ability to take up water: hydrophobic ones, which repel it, and hydrophilic ones, which take it up. Another particle (component) property that is related to water uptake is hygroscopicity, the ability to take up and bind H_2O, e.g., by dissolution. It can be measured in terms of the hygroscopic growth factor GF, which is defined as the ratio of a particle's diameter at a high RH ($\sim$90 %) and that at a low RH ($\lesssim$20 %). Alternatively, or complementarily, the hygroscopicity parameter κ (Petters & Kreidenweis, 2007) can be used. It is related to the decrease in water vapor saturation ratio over a particle's surface at constant aerosol water content with respect to a wettable, insoluble particle. If the particle is at equilibrium with its surroundings that saturation ratio is equal to RH. While GF is a purely diagnostic quantity that can only be related to a particle as a whole, a particle's κ value can also be derived from the individual chemical component hygroscopicity parameters.

In general, inorganic salts are the most hygroscopic components of the atmospheric aerosol, with κ values between $\sim$0.5 and $\sim$1.4 (Petters & Kreidenweis, 2007). Hence, these components are expected to lead to quickest particle growth, and thus to contribute most strongly to CCN concentrations, for instance. Organic substances are typically less hygroscopic (Petters & Kreidenweis, 2007), or even hydrophobic, which would correspond to $\kappa = 0$. As Aitken mode particles often contain more organic material and accumulation mode particles more inorganic components, hygroscopicity of fine mode particles often increases with particle size (e.g., Wu et al., 2013; Liu et al., 2014).

Insoluble particle components, e.g., DU and BC, are often hydrophobic upon emission. They can be transferred into a hydrophilic state once they become internally mixed with hygroscopic components (e.g., Shi et al., 2008; Sullivan et al., 2009; Popovicheva et al., 2010, 2011). The time scale for such transformations strongly depends on environmental conditions and, using computer models, has been estimated to range from minutes to several days or even weeks (Tsigaridis & Kanakidou, 2003; Riemer et al., 2009; Liu et al., 2011; Lund & Berntsen, 2012; Oshima & Koike, 2013; Shen et al., 2014; Fierce et al., 2015). CCN properties of insoluble particles are controlled by the degree to which these particles are coated with soluble components (e.g., Petzold et al., 2005; Dalirian et al., 2015).

2.2 The influence of ship emissions

Ocean-going ships were responsible for about 15 % of global NO_x emissions and for 4 to 9 % of global SO_2 emissions in the early 2000s (Eyring et al., 2010). Oxidation products of these gases, mainly HNO_3 and H_2SO_4, can lead to growth of pre-existing particles in the MBL, e.g., SS particles, through gas-to-particle conversion. Although less abundant, co-emitted particles, which mainly consist of POM and BC, also play a role in NO_3 and SO_4 formation from ship emissions. SO_4 produced from the emitted SO_2 is the main contributor to ship-induced aerosol mass, at least in areas where no fuel sulfur content limits are in place (Lack et al., 2009). Further emitted gaseous species include carbon dioxide (CO_2), carbon monoxide (CO), and volatile organic compounds (VOCs).

Ship emissions are special in that they can perturb the aerosol and thus affect clouds in an environment where clouds play an especially important role. Over the dark ocean surface the increase in albedo due to the presence of clouds is especially high. Öström et al. (2000) and Chen et al. (2011), in the introductions of their articles, summarized why and how pollution, or more specifically, aerosol particles affect these clouds. Their main points are that (1) marine stratus clouds, covering about a quarter to a third of the earth's oceans (Warren et al., 1988; Hartmann et al., 1992), are highly susceptible to pollution in the form of additional CCN; and that (2) through various processes inside these clouds and interactions with their surroundings such additional CCN can lead to changes in the clouds' albedo. For a summary of the processes and feedbacks responsible for these changes see the introduction of the article by Chen et al. (2015b). The magnitude of the changes depends on the type and altitude of the clouds (Christensen et al., 2014; Chen et al., 2015b). In some cases ship emissions can even lead to an increase in cloud cover and thus further increase their indirect RE (Goren & Rosenfeld, 2012, 2014).

Typical diameters of CCN that nucleate MBL cloud droplets fall between a few tens and a few hundreds of nanometers (Öström et al., 2000; Twohy et al., 2013). The effect of additional particles on such clouds therefore depends on their size. In the case of ship emissions, particle size is determined by the type of engine and fuel used (Hobbs et al., 2000). For example, within the same air mass, a ship that uses a diesel engine can induce a "ship track", i.e., a line-shaped cloud, while another one that employs a steam turbine fed with distilled fuel may not (Noone et al., 2000). As particles can grow while a ship plume ages (Petzold et al., 2008), both the size of the primary emitted particles and the amount of co-emitted, e.g. sulfur-containing, aerosol precursor gases play an important role. Cappa et al. (2014), for instance, found only very low CCN activity of the aerosol in a ship plume that was characterized by small primary particles ($\lesssim$70 nm) and low fuel sulfur content, while the ship track studies by Lu et al. (2007, 2009) demonstrated significant effects of ship emissions on MBL clouds. Furthermore, Sorooshian et al. (2015) pointed out that ocean-going ships may also be responsible for additional emissions of (coarse mode) SS particles.

As almost 70 % of all ship emissions occur within 400 km of the coasts (Eyring et al., 2010), ship traffic also contributes to air quality degradation in coastal areas and harbor cities. Up to, or even more than, 10 % of the aerosol concentrations in the vicinity of major ports can be attributed to ship emissions (Yau et al., 2013; Zhao et al., 2013c; Kivekäs et al., 2014; Contini et al., 2015). Fuel sulfur content is therefore regulated in some so-called emission control areas. Such regulations can lead to reductions in ship-induced particulate matter concentrations in coastal areas of up to 50 % (Kotchenruther, 2015) and they will become more stringent in the future (IMO, 2011).

2.3 Aerosol modeling

Computer models of the atmospheric aerosol are tools that are used for two main purposes. One is to interpret measured data, e.g., in terms of contributions of individual processes to total effects. Thus, cause–consequence relationships can be established and investigated. The other major use case of these models is to predict (up to days) or project (up to centuries) changes in the composition and concentration of the atmospheric aerosol. Climatic and health effects associated with aerosol particles can thus be investigated, and the contributions of different sources and types of aerosol to global chemistry and climate perturbations can be quantified. The models can be very detailed, e.g., for box model studies focusing on individual pollution plumes (e.g., Tian et al., 2014) or individual processes (e.g., Kaiser et al., 2011), or they can be more simplified for application within regional or global atmospheric chemistry general circulation models (AC-GCMs), i.e., "climate models" (without interactive ocean models) that include atmospheric chemistry treatments. The emphasis will be on the latter in this section, in line with the topic of the present work.

Ghan & Schwartz (2007) and Ghan et al. (2012, in their introduction) provided a comprehensive overview over the motivation for, approaches to, and capabilities of aerosol submodels for regional and global AC-GCMs. An explicit treatment of aerosol microphysics in AC-GCMs is essential for feedback analyses between the aerosol and atmospheric chemistry and climate. High spatial and temporal variability of particle concentrations and composition leads to unavoidable inaccuracies when using global climatologies. Aerosol microphysics and chemistry representations are required to accurately reproduce past trends, e.g., the surface warming during the last centuries (Ghan & Schwartz, 2007) and decades (Ekman, 2014). They are also essential in the description of important processes such as the cloud–aerosol interaction (Wang et al., 2013a) and its consequence, the indirect aerosol radiative forcing (RF) (Bellouin et al., 2013a).

This section is organized as follows. First, it contains some examples of what aerosol (sub)models have been used for and a summary of relevant results. This includes recent studies on the climatic effects of ship emissions. Next, the motivation for the development of the new submodel, MADE3, that forms the basis of the present work is laid out. Subsequently, the employed numerical approach is described and put into context. The last-but-one subsection is dedicated to a discussion of potential alternatives to the new submodel, before this section ends with a brief history of the predecessors to MADE3.

2.3.1 Selected results

The major natural contributions to the aerosol radiative effect (RE) were quantified in a modeling study by Rap et al. (2013). The largest globally averaged contribution to the direct RE was found to stem from sea spray (SS) particles ($-0.44\,\mathrm{W\,m^{-2}}$), and to the indirect RE from sulfate (SO_4) derived from oceanic precursor emissions ($-0.76\,\mathrm{W\,m^{-2}}$). Estimates of the current anthropogenic aerosol forcings are similar in magnitude (Boucher et al., 2013) and may mask up to one half of the concurrent forcing of long-lived greenhouse gases (GHGs) (Naik et al., 2013). Although negative in total, the direct aerosol RE can also be positive for individual components due to absorption of radiation (e.g., Myhre et al., 2013a; Zelinka et al., 2014), as is the case for black carbon (BC), for instance.

Due to reductions in anthropogenic emissions of both particulate and gaseous precursor emissions, aerosol loading and, thus, aerosol RF may decrease in the future (e.g., Pietikäinen et al., 2015), possibly even to the natural, pre-industrial levels by the end of the 21$^{\mathrm{st}}$ century (Takemura, 2012; Smith & Bond, 2014). This may lead to an accelerated global mean temperature rise if GHG concentrations continue to increase. Levy et al. (2013), for instance, calculated

1 K of global average surface warming due to a reduced atmospheric aerosol burden during the 21st century. Temperature and precipitation extremes are also projected to increase in case of strong aerosol emission reductions during the 21st century (Sillmann et al., 2013).

One of the unique features of aerosol models as compared to observations is that individual processes can be tracked and analyzed separately, or even "switched on and off". As cloud–aerosol interactions are among the processes that are associated with the largest uncertainties w.r.t. aerosol effects on climate they often receive special attention. Using a cloud-resolving model, for instance, i.e., considering a horizontal domain of the order of 10^4 square kilometers with a resolution of $\sim$1 km, Khairoutdinov & Yang (2013) found that negative aerosol RF becomes stronger with increased cloud condensation nuclei (CCN) concentrations over the tropical oceans. Xiao et al. (2014), who employed a similar-scale model, found a reduction of precipitation, reduced diameters of the smaller cloud droplets ($\lesssim 20\,\mu$m), and increased number concentrations of these droplets in response to higher aerosol loading. With the help of even finer scale models, Feingold et al. (2013) showed that the precipitation susceptibility of clouds can additionally depend on the cloud contact time of the aerosol-laden air parcel.

Emissions are also among the processes that can be switched on and off in models, or which can be parameterized in different ways. Thus, the study by Fierce et al. (2013) provided further insight as to whether size or composition is the main driver of CCN activity: at supersaturations $< 0.2\,\%$ the modeled diesel soot particles had hardly any influence on CCN concentrations, while at higher supersaturations activation depended more strongly on emission size than on composition.

On a different note, the ability to include arbitrary emissions in aerosol models also enables the assessment of aerosol-related methods of geoengineering (e.g., Jones & Haywood, 2012). In this context, it is interesting to note that while injection of additional accumulation mode SS particles into the marine boundary layer (MBL) likely entails a negative RF, adding coarse mode SS particles could actually lead to the opposite result (Alterskjær & Kristjánsson, 2013). The positive RF induced by additional coarse mode aerosol is due to competition for water vapor: although the particles do act as CCN, this effect is overcompensated by the concurrent reduction in supersaturation.

Non-local effects are yet another use case for aerosol models, specifically for regional and global models. For example, Sand et al. (2013) found that elevated concentrations of carbonaceous aerosol particles in the midlatitudes can lead to a significant increase in Arctic surface temperatures. Aerosol particles could also be among the primary drivers of sea surface temperature variability in the North Atlantic, which in turn affects the Sahel droughts and other climatic phenomena (Booth et al., 2012). Furthermore, atmospheric dynamics can be altered by the presence of aerosol particles both in the troposphere and in the stratosphere, or between the two (e.g., Hsieh et al., 2013; Randles et al., 2013; Tosca et al., 2013; Salzmann et al., 2014). Mineral dust (DU) aerosol could even have an impact on oceanic circulation (Serra et al., 2014), where the response is non-local not only geographically, but also in time.

As the present work deals with ship emissions, effects of aerosol particles over the oceans are of particular interest here. An increase in cloud droplet number concentration (CDNC) over oceans can exert a strong RF, as, for instance, Jones et al. (2009) showed. Such an increase can be caused by additional aerosol particles, but the magnitude of the effect strongly depends on both the CDNC prior to the perturbation and the particle sizes (Andrejczuk et al., 2014). The study by Wood et al. (2012) indicated that the increase in CDNC, which usually leads to a suppression of precipitation, may be amplified by a feedback loop, as less precipitation also leads to higher CDNC. Since existing particles are modified by ship exhaust and ships also emit additional particles, one can also expect a ship emissions-induced effect on clouds and thus on climate.

Prior work concerning ship emissions effects on aerosol and climate

Year 2000 global average contributions of ship-induced aerosol to the atmospheric burdens of SO_4, nitrate (NO_3), and BC are estimated to be in the range of 1 to 3 % (Eyring et al., 2010). They are smaller over land, but in the MBL these contributions can reach values of several 10 % (Righi et al., 2013). Due to the special role of clouds above oceans and their sensitivity to aerosol perturbations, the associated effects on the earth's radiation budget can be large. Simulations of the RE and RF caused by ship-induced aerosol perturbations (Capaldo et al., 1999; Lauer et al., 2007, 2009; Righi et al., 2011; Bauer & Menon, 2012; Olivié et al., 2012; Peters et al., 2012, 2013; Righi et al., 2013) showed that the total anthropogenic RF may be offset by up to a few hundred $\mathrm{mW\,m^{-2}}$ through the indirect aerosol RE of ship emissions. This could amount to a 10 % or more reduction of the overall anthropogenic effective RF, which is mainly caused by GHGs and estimated to be 1 to $3\,\mathrm{W\,m^{-2}}$ (Myhre et al., 2013b). However, as Fuglestvedt et al. (2009) pointed out, the time scales on which these forcings act are very different: while aerosol particles have an atmospheric lifetime of a few weeks at most, carbon dioxide (CO_2), for instance, stays in the atmosphere for centuries.

A possible range of ship emission RFs of -668 to $26\,\mathrm{mW\,m^{-2}}$ is reported in the recent review by Eyring et al. (2010) for the year 2000 when including all effects, i.e., aerosol and GHG forcings. The large spread of these values is mainly caused by the uncertainties in the indirect aerosol RE. The main drivers of diversity among simulation results are the geographical distribution of the emissions (Lauer et al., 2007) and the assumptions on the size distributions of emitted particles (Righi et al., 2011; Peters et al., 2012, 2013; Righi et al., 2013). The latter are of specific importance because emitted particle numbers are diagnosed from the emitted mass and the size distributions, and they differ greatly when different particle diameters are used for the conversion. The sensitivity of clouds over the oceans to additional aerosol particles thus entails a high sensitivity of the ship emissions-induced aerosol indirect RE to the size distribution assumptions. Possibly, the timing of emissions also plays a role for their climatic effect (Jenkins et al., 2013).

Several authors studied possible future effects of ship emissions on atmospheric composition and climate. For an annual emissions growth rate of 2.2 % Eyring et al. (2007) found that the SO_4 aerosol direct RE would double from $-13\,\mathrm{mW\,m^{-2}}$ to $-26\,\mathrm{mW\,m^{-2}}$ by the year 2030. Although it is not clear whether the indirect aerosol RE would increase by the same factor it is very likely that it would also become much more negative. The consideration of new regulations, which require more and more stringent reductions of the ship fuel sulfur content (IMO, 2011), however, might change such projections. Lauer et al. (2009), Righi et al. (2011), and Partanen et al. (2013) performed simulations for possible reduction scenarios and found that the magnitude of the associated indirect aerosol RE would always decrease with reduced fuel sulfur content. Depending on the actually implemented regulations, the effect could even become almost negligible (Partanen et al., 2013). Future regulations might also lead to reduced ship emissions of carbonaceous species, i.e., BC and particulate organic matter (POM), but the effect of such reductions on the earth's radiation budget may be insignificant (Peters et al., 2012, 2013).

Transient effects on radiation induced by the shipping sector were also assessed. According to the projections by Olivié et al. (2012) the strongest, i.e., most negative, non-CO_2 RF will be reached around 2050, with about $-100\,\mathrm{mW\,m^{-2}}$. During the second half of the 21$^{\mathrm{st}}$ century the effect will diminish and will be close to zero in 2100. A simpler model and a different emissions inventory were used by Tronstad Lund et al. (2012). Their study did include the CO_2 effect and showed the most negative ship-induced forcing (between 1900 and 2050) around the year 2015. Their 2050 estimates ranged from $\sim\!-40\,\mathrm{mW\,m^{-2}}$ to $\sim\!-10\,\mathrm{mW\,m^{-2}}$, depending on the parameterization of the aerosol indirect effect. Fuglestvedt et al. (2009) studied the transient response of the global mean surface air temperature to sustained ship emissions, including

CO_2, for several hundred years into the future. Thus, they also took into account the different lifetimes of the ship emission components. According to their simulations, the current net cooling effect will eventually turn into a warming effect, but the time until this switch-over occurs is highly sensitive to a number of uncertain parameters. Hence, the values reported in Fuglestvedt et al. (2009) span a range from 30 years to >1000 years.

2.3.2 Motivation to expand on previous work

Consideration of the role of coarse mode particles

Coarse mode aerosol particles and their interactions with condensable gases have so far received little attention in global AC-GCMs, although they may play an important role in many of the processes discussed in the previous sections. For instance, a modeling study by Lee et al. (2009) showed that competition of coarse DU particles and fine mode aerosol for sulfuric acid (H_2SO_4) condensation may lead to fewer CCN due to reduced growth of fine mode particles. A similar conclusion, namely activation of fewer CCN due to reduced nitric acid (HNO_3) condensation on these particles in the presence of more numerous coarse mode particles, was reached by Romakkaniemi et al. (2005). Furthermore, Lee et al. (2009) suggested that the number of Aitken mode particles will be reduced by coagulation with the coarse mode particles, a process whose importance is also underlined by a study by Tian et al. (2014). In addition, Luo et al. (2007) and other authors found that SS and DU have significant effects on SO_4 and NO_3 formation. This is in large part due to interactions of the coarse mode aerosol with the precursor gases (McInnes et al., 1994; Kerminen et al., 1997; Lee et al., 2008, 2014; Fitzgerald et al., 2015).

In the context of the present work it is especially interesting to note on the one hand that Lauer et al. (2009) and Righi et al. (2011) found that NO_3 replaced substantial fractions of the SO_4 that was "lost" from the aerosol in the simulations with reduced ship fuel sulfur content. On the other hand, numerous field measurements have shown that large, and in many cases the major, fractions of aerosol NO_3 reside in the coarse mode, especially under polluted conditions and when SS is present (Hara et al., 1999; Zhuang et al., 1999; Yeatman et al., 2001; Cavalli et al., 2004; Nolte et al., 2008; Bian et al., 2014). NO_3 was also found to partition to a high degree to coarse mode particles in continental and urban locations (Makkonen et al., 2012; Li et al., 2013; Xu et al., 2014), rendering the phenomenon rather ubiquitous. Aerosol NO_3 may even repartition from smaller to larger particles via the gas phase (e.g., Landi et al., 2013). Furthermore, consideration of the NO_3 partitioning between coarse and fine mode particles may lead to improved agreement of the fine mode NO_3 concentrations with observations (Trump et al., 2015).

Neither Lauer et al. (2009) nor Righi et al. (2011) considered coarse mode interactions with condensable gases (other than water vapor) or with fine mode particles. Thus, it becomes obvious that in order to reduce the uncertainties in the quantification of ship emissions-induced aerosol radiative effects such interactions, especially with HNO_3, have to be included in the aerosol submodel. This is where MADE3 (Chap. 3) comes in and improves upon MADE, which was used by Lauer et al. (2009) and Righi et al. (2011).

Inclusion of HCl and Cl in gas–particle partitioning

When considering coarse mode aerosol interactions with condensable gases one of the most important processes is the so-called "chloride depletion" of SS by formation of NO_3 (and SO_4, and organic) salts, which releases hydrochloric acid (HCl) to the gas phase (e.g., Raes et al., 2000; Laskin et al., 2012). Many authors of measurement studies cited in the previous paragraphs mentioned such effects. Specifically, strong chloride depletion was observed when SS particles

interacted with acidic gases (Teinilä et al., 2014) and with pollution (Niemi et al., 2005). The fraction of replaced chloride can reach values up to 95 % (Kerminen et al., 1997).

The benefit of including such interactions in aerosol submodels was shown by Im (2013) who achieved considerable improvements in the simulation of aerosol NO_3 when adding SS and its interaction with HNO_3 to their model. Furthermore, consideration of chloride (Cl) formation on aerosol particles may be required in the future to accurately reproduce or interpret measurements. Tobo et al. (2010), for instance, showed that the reaction of Cl with calcium (Ca) in DU particles may transform them from a hydrophobic to a hydrophilic state. Another case in point is the study by Crisp et al. (2014), which indicated that aerosol Cl production from the gas phase could be an important process when considering chlorine chemistry in the polluted MBL.

Many aerosol submodels currently in use with AC-GCMs or earth system models (ESMs), however, treat SS as one single species (see Table 2.1), so that chloride depletion cannot be simulated. This limitation also affects MADE and was removed during the development of MADE3 (see Sect. 3.1.2).

2.3.3 The computational approach[1]

A typical idealization assumption in aerosol modeling is to treat all particles as spheres. While this may lead to errors up to ∼10 % in the calculation of the aerosol direct RE (Räisänen et al., 2013), it greatly simplifies the formulation of the aerosol dynamics equation. Note that it is also possible to take non-sphericity into account (e.g., as suggested by Kajino, 2011), but most current aerosol (sub)models do not share this feature.

Assuming spherical particles, one can describe the aerosol population by a size distribution function $n(D,t)$, where D is the particle diameter and $n(D,t)\,\mathrm{d}D$ is the number concentration of particles with diameters in the range $[D, D+\mathrm{d}D]$ at time t. The aerosol dynamics equation then reads (formulation adapted from Whitby & McMurry, 1997, reduced to the processes treated in the submodel that was developed for the present work; see Sect. 3.2):

$$\begin{aligned}\frac{\partial M_j(t)}{\partial t} = &\underbrace{\int_0^\infty \frac{\mathrm{d}D^j}{\mathrm{d}V_\mathrm{p}(D)} \cdot \frac{\partial V_\mathrm{p}(D)}{\partial t} \cdot n(D,t)\,\mathrm{d}D}_{\text{condensation/evaporation}} \\ &+ \underbrace{\int_0^\infty D^j \cdot \dot{n}_\mathrm{nuc}(D,t)\,\mathrm{d}D}_{\text{nucleation}} \\ &+ \underbrace{\frac{1}{2}\int_0^\infty \int_0^\infty \left((D_1)^3 + (D_2)^3\right)^{\frac{j}{3}} \cdot \beta(D_1,D_2) \cdot n(D_1,t) \cdot n(D_2,t)\,\mathrm{d}D_1\,\mathrm{d}D_2}_{\text{coagulation gain}} \\ &- \underbrace{\frac{1}{2}\int_0^\infty \int_0^\infty \left((D_1)^j + (D_2)^j\right) \cdot \beta(D_1,D_2) \cdot n(D_1,t) \cdot n(D_2,t)\,\mathrm{d}D_1\,\mathrm{d}D_2}_{\text{coagulation loss}}.\end{aligned} \tag{2.1}$$

Here, $V_\mathrm{p}(D)$ is the volume of a particle of diameter D, $\dot{n}_\mathrm{nuc}(D,t)\,\mathrm{d}D$ is the rate of particle production at diameter D per unit volume, and $M_j(t)$ is the j^th moment of the size distribution:

$$M_j(t) = \int_0^\infty D^j \cdot n(D,t)\,\mathrm{d}D. \tag{2.2}$$

[1]Parts of this subsection appeared in similar form in a recent publication (Kaiser et al., The MESSy aerosol submodel MADE3 (v2.0b): description and a box model test, Geosci. Model Dev., 7(3), 1137–1157).

The zeroth moment, $M_0(t)$, directly yields the total particle number concentration, the second moment is related to particle surface area concentration, and the aerosol mass concentration can be computed from the average aerosol density, ρ, and the third moment as:

$$m(t) = \frac{\pi}{6} \cdot \rho \cdot M_3(t). \tag{2.3}$$

For brevity, time dependencies are not written out explicitly in the remainder of this thesis, except where it seems necessary to avoid confusion.

Different numerical representations are used in aerosol (sub)models for the particle number size distribution function. The choice mainly depends on the target application and the available computational resources. In the method of moments (MOM) the aerosol dynamics equation is solved for multiple moments of the size distribution, from which measurable quantities can be extracted. The sectional approach (BIN), as an alternative, relies on a discretization of particle sizes into so-called bins. While MOM and BIN, in principle, allow for arbitrary shapes of the size distribution, they suffer from a relatively high demand on computational resources and from numerical problems at long time steps. A very efficient and numerically stable size distribution representation is used in the modal approach. It relies on the central (simplifying) assumption that the "[atmospheric] aerosol may be viewed as an assemblage of distinct populations [or modes] of particles, distinguished by size or chemical composition" (Whitby & McMurry, 1997). Due to the necessary a priori assumptions on the shape of the size distribution, this approach is arguably less accurate than the other two. Studies that compared models employing the sectional and the modal scheme led to contradictory results in terms of accuracy in the reproduction of observations, as summarized by Easter et al. (2004) and Mann et al. (2012). Comparing the sectional and the modal approach within the same 3-D AC-GCM Mann et al. (2012) found the differences between the two to be generally smaller than the model–observations differences. Hence, for long-term global climate simulations, and if large numbers of sensitivity studies are desired, a modal aerosol (sub)model is a suitable choice.

In the modal approach the aerosol number size distribution is approximated by a superposition of lognormal functions $n_k(\ln \tilde{D}, t)$, the so-called modes (cf. Fig. 3.1):

$$n(\ln \tilde{D}) = \frac{\mathrm{d}N(\ln \tilde{D})}{\mathrm{d} \ln \tilde{D}} = \sum_{k=1}^{K} n_k(\ln \tilde{D}) = \sum_{k=1}^{K} \frac{N_k}{\sqrt{2\pi} \ln \sigma_k} e^{-\frac{[\ln \tilde{D} - \ln \tilde{D}_{\mathrm{g},k}]^2}{2(\ln \sigma_k)^2}}. \tag{2.4}$$

Here, $\tilde{D}$ is the particle diameter, made dimensionless by division by 1 µm, and $N(\ln \tilde{D})$ is the cumulative number concentration of particles with diameters smaller than $\tilde{D}$. Each mode k ($k = 1, \ldots, K$) is described by three parameters, namely the number concentration of particles N_k in that mode, its median particle diameter (geometric mean diameter) $\tilde{D}_{\mathrm{g},k}$, and its width (geometric standard deviation) σ_k. A lognormal mode is therefore fully defined if three of its moments are known.

The choice of this functional form is motivated by its mathematical convenience (Whitby & McMurry, 1997): it enables and facilitates the analytical solution of the integrals that appear in the aerosol dynamics equation (Eq. 2.1). Furthermore, superpositions of log-normal functions have proven to be reasonable approximations of measured aerosol size distributions. This is evident from their frequent use in the literature as a fit function to measured data.

Many aerosol (sub)models for global application use fixed mode widths. This means that only two moments of the lognormal function have to be predicted per mode, which leads to a further reduction of a submodel's computational burden. Note that it is also possible to treat more than two moments of the size distribution prognostically. However, to the author's knowledge, this has so far only been done in models for regional application (e.g., Binkowski & Roselle, 2003; Yu et al., 2003; Kajino et al., 2012).

2.3.4 Existing aerosol microphysics submodels

Submodels that explicitly simulate aerosol microphysics were first implemented into regional models, and later, i.e., in the early 2000s when enough computational power became available, also into AC-GCMs. Since then many different models have been developed for application on different spatial and temporal scales, and to examine different aspects of the aerosol life cycle at varying degrees of complexity. For lists of the relevant references see the articles by Textor et al. (2006) and Mann et al. (2014). In this subsection the discussion will be limited to submodels that have been used within AC-GCMs or ESMs. Most of them fall into one of two classes (Table 2.1): they typically employ either the modal or the sectional approach. There are (at least) two other submodels, one using a mixture of the two schemes (PAM) and one that tags aerosol mass concentrations by their origin and mode (CAM4-Oslo).

As the submodel developed for this work is intended to be usable for large sets of sensitivity studies and multi-annual simulations computational efficiency is paramount. Furthermore, the ability to represent different particle mixing states is vital for the application of the new submodel in future projects. Together, these requirements prohibit the use of a sectional aerosol submodel. As there is no clear evidence that any of the other approaches would outperform a modal model the decision here is to stay with the modal approach. The discussion in this subsection will therefore be further limited to the available modal aerosol submodels. For a brief summary of the most relevant features of these submodels please refer to Table 2.1.

As detailed in Sect. 2.3.2 coarse mode NO_3 is a required ingredient for the present work. Since the submodels HAM2, GLOMAP-mode, IMPACT, MIRAGE, and TM5 do not include this component, they will not be considered in the following. Although MADE and MADE-in allow for the simulation of fine mode NO_3 their coarse modes consist exclusively of SS, DU, and water (H_2O). They do not allow for any interactions of the coarse mode particles with the gas phase, except for water uptake.

While MAM7 and MATRIX do allow for secondary components in their coarse modes, both have severe limitations when it comes to gas–particle partitioning. In MAM7 re-evaporation of volatile species is neglected entirely. While MATRIX does include an equilibrium partitioning scheme the total aerosol mass concentration is used in this calculation. Subsequently, the condensed material is distributed among the modes according to their SO_4 content. This may significantly bias the partitioning of NO_3 between the fine and coarse modes, as SO_4 is typically found predominantly in fine mode particles, whereas coarse mode fractions of NO_3 can reach values greater than 50 % (see previous subsection). Furthermore, the approach used in MATRIX neglects the likely non-equilibrium state of the coarse mode particles. Gas diffusion is the rate-limiting "step" in the equilibration of NH_3/NH_4, HNO_3/NO_3, and HCl/Cl between the gas and aerosol phases. This process is much slower for coarse mode particles than for the smaller ones, as will be explained in Sect. 3.2.1. Finally, MATRIX does not include a separate Cl tracer, so that chloride depletion cannot be represented.

GMXe is the aerosol submodel that comes closest to MADE3, the submodel developed in the present work. Although it is a modal model, too, it employs a different numerical approach to solving the terms of the aerosol dynamics equation (Eq. 2.1). Furthermore, it includes a dedicated nucleation mode (cf. Sect. 2.1.3), which MADE3 does not, and it does not feature modes for fully soluble particles, which MADE3 does (Sect. 3.1.1). Hence, it might be interesting to compare the results reported in Chapter 7 with simulations using GMXe in the future.

Table 2.1: Available aerosol microphysics submodels for global atmospheric models. The host model is given in parentheses, except in the case of CAM4-Oslo, in which the aerosol submodel does not have a separate name. In the third column, "gas" refers to ammonia (NH_3), HNO_3, and HCl (as far as applicable). Note that "POM" stands for "particulate organic matter" here. MAM7 includes two separate tracers, for primary organic material and for secondary organic aerosol (SOA), in the version described by He & Zhang (2014) but can also be run in a mode with several organic aerosol tracers (He et al., 2015); HAM2 subdivides the SOA into five different types. Note also that MIRAGE has a separate tracer for methane sulfonic acid, which is not part of the SO_4 tracer.

Name	Simulated "species" (tracers)	gas–coarse mode partitioning	Recent reference(s)
Modal models			
GMXe (EMAC)	SO_4, ammonium (NH_4), NO_3, sodium (Na), Cl, SS, POM, BC, DU	per-mode equilibrium, with flux limit	Pringle et al. (2010a,b); Vignati et al. (2004)
MAM7 (CESM/CAM5.1)	SO_4, NH_4, NO_3, Na, Cl, POM, BC, DU	irreversible per-mode condensation	He & Zhang (2014)
MATRIX (GISS-ModelE)	SO_4, NH_4, NO_3, SS, POM, BC, DU	bulk equilibrium	Bauer et al. (2008)
MADE-in (EMAC)	SO_4, NH_4, NO_3, SS, POM, BC, DU	none	Aquila et al. (2011)
MADE (EMAC)	SO_4, NH_4, NO_3, SS, POM, BC, DU	none	Lauer et al. (2007)
HAM2 (ECHAM5)	SO_4, SS, POM, BC, DU	—	Zhang et al. (2012)
GLOMAP-mode (HadGEM3)	SO_4, SS, POM, BC, DU	—	Mann et al. (2010)
IMPACT (CAM3)	SO_4, SS, POM, BC, DU	—	Wang et al. (2009)
MIRAGE (CCM2)	SO_4, SS, POM, BC, DU	—	Easter et al. (2004)
TM5 (EC-Earth)	SO_4, SS, POM, BC, DU	—	van Noije et al. (2014)
Sectional models			
CUACE/Aero (BCC_AGCM2.0.1)	SO_4, NH_4, NO_3, SS, POM, BC, DU	equilibrium	Wang et al. (2015); Zhou et al. (2012)
TOMAS (ModelE2)	SO_4, NH_4, SS, POM, BC, DU	SO_4 neutralization	Lee et al. (2015)
TOMAS (GISS II-prime)	SO_4, NH_4, SS, POM, BC, DU	not specified	Lee et al. (2013c)
CAM (GEM)	SO_4, SS, POM, BC, DU	—	Gong et al. (2012)
GEMS/MACC (CNRM-CM)	SO_4, SS, POM, BC, DU	—	Michou et al. (2015)
Other approaches			
PAM (CanAM4)	SO_4, SS, POM, BC, DU	—	Peng et al. (2012)
CAM4-Oslo	SO_4, SS, POM, BC, DU	—	Kirkevåg et al. (2013)

2.3.5 MADE3 as a successor of MADE and MADE-in[2]

The primary motivation of this work is to enable a re-quantification of the effects of ship emissions on the global aerosol under consideration of coarse mode interactions with the gas phase and the fine modes. This can be best accomplished by extending one of the submodels that were previously used to quantify such effects, namely MADE (Lauer et al., 2007, 2009; Righi et al., 2011, 2013).

The first generation of the aerosol submodel MADE (Modal Aerosol Dynamics model for Europe) was developed for application in a regional model (Ackermann et al., 1998) and shares its roots with the aerosol submodel of CMAQ (the Community Multiscale Air Quality model; Binkowski & Roselle, 2003). Both were derived from work by Whitby et al. (1991) and Binkowski & Shankar (1995). At present, in the context of regional modeling, MADE is employed as the aerosol submodel in many studies using WRF-Chem (e.g., Ochoa et al., 2012; Zhao et al., 2013b; Archer-Nicholls et al., 2014; Wyant et al., 2015).

Lauer et al. (2005) adapted MADE for global applications and implemented it into the general circulation model ECHAM4 (the fourth development cycle of the HAMburg version of the ECMWF (European Center for Medium-Range Weather Forecasts) model; Roeckner et al., 1999). MADE was then transformed into a submodel (Lauer et al., 2007) for the MESSy framework (Modular Earth Submodel System, Jöckel et al., 2005). It has since been used for numerous studies as part of EMAC, the ECHAM/MESSy Atmospheric Chemistry model (Corbett et al., 2007; Lauer et al., 2009; Winebrake et al., 2009; Righi et al., 2011; Tronstad Lund et al., 2012; Righi et al., 2013, 2015).

The second generation submodel MADE-in was developed by Aquila et al. (2011) as an extension to the MADE version used by Lauer et al. (2007). It was created to enable the simulation of number concentrations and mixing states of particles containing the insoluble components black carbon and mineral dust.

MADE-in was now used as the basis for the development of MADE3. The abbreviation stands for the "Modal Aerosol Dynamics model for Europe, adapted for global applications, 3rd generation". For the first version of the third generation submodel the microphysical calculations were extended to also take into account coarse mode particles, which were formerly regarded as passive (see previous subsection). For version 2.0, the gas–particle partitioning scheme was also extended, namely by inclusion of the HCl/Cl system, in order to enable simulation of the chloride depletion described in Sect. 2.3.2.

During the MADE3 development major parts of the MADE-in microphysics code were restructured and rewritten. Despite its extended capabilities, the microphysics routines of MADE3 thus consist of little more than half the number of code lines that were used for MADE-in. Nevertheless, the third generation submodel still shares with its predecessors most of its features and the concepts underlying the computer code.

[2]Parts of this subsection appeared in similar form in a recent publication (Kaiser et al., The MESSy aerosol submodel MADE3 (v2.0b): description and a box model test, Geosci. Model Dev., 7(3), 1137–1157).

Chapter 3

The aerosol submodel MADE3[1]

The term "aerosol (sub)model" is used here to refer to the computer code used to solve the aerosol dynamics equation (Eq. 2.1). This chapter provides a reference for the physical concepts and mathematics on which the new submodel MADE3 (Modal Aerosol Dynamics model for Europe, adapted for global applications, 3rd generation) is based. The first section deals with the representation of aerosol properties, the second one is dedicated to a description of the microphysics treatment.

3.1 Aerosol characteristics

3.1.1 Modes

In MADE3 the aerosol size distribution is represented by nine modes (cf. Sect. 2.3.3; $K = 9$), so that the mode index k runs from $k = 1$ to $k = 9$. These modes (Fig. 3.1) are representative of three size ranges, namely those of the Aitken, accumulation, and coarse modes. In each size range MADE3 includes one mode of fully soluble particles, one mode of insoluble particles, and one mixed mode. For internally mixed particles that consist of both insoluble and soluble material a core–shell structure is assumed, with the insoluble part coated by the soluble species. The choice of this set of aerosol modes follows the ideas presented by Aquila et al. (2011), now extended to cover also the coarse mode size range, so that consistent transfer of particles between all size classes is ensured.

The explicit representation of particle mixing state (cf. Sect. 2.1.3) that is possible with this set of modes has several advantages. On the one hand, for example, pure mineral dust (DU) particles can serve as efficient ice nuclei (IN) (e.g., DeMott et al., 2003; Pratt et al., 2009), but coatings can reduce their ice nucleating ability significantly (e.g., Chernoff & Bertram, 2010; Sullivan et al., 2010; Tan et al., 2014; Augustin-Bauditz et al., 2014). Such effects may, for instance, alter the conclusions on the effect of IN on cirrus clouds (Hendricks et al., 2011). On the other hand, externally mixed black carbon (BC) particles are typically hydrophobic and can be transformed to a hydrophilic state by condensation of soluble material such as sulfuric acid (H_2SO_4) (e.g., Popovicheva et al., 2011). Transformation of particles from an externally mixed population into internal mixtures can thus strongly influence the climatic effect of aerosol particles, as has been shown by numerous studies, especially on BC mixing state (e.g., Ching et al., 2012; Matsui et al., 2013; Yun et al., 2013; Zhang et al., 2014b).

3.1.2 Species

Particles in MADE3 consist of up to nine different components (Fig. 3.1, Table 3.1), often also called tracers, as they may represent more than one chemical species: sulfate (SO_4), ammonium (NH_4), nitrate (NO_3), Na (a tracer that contains sea spray components other than chloride), chloride (Cl), particulate organic matter (POM), BC, DU, and water (H_2O). Note

[1]Parts of this chapter appeared in similar form in a recent publication (Kaiser et al., The MESSy aerosol submodel MADE3 (v2.0b): description and a box model test, Geosci. Model Dev., 7(3), 1137–1157).

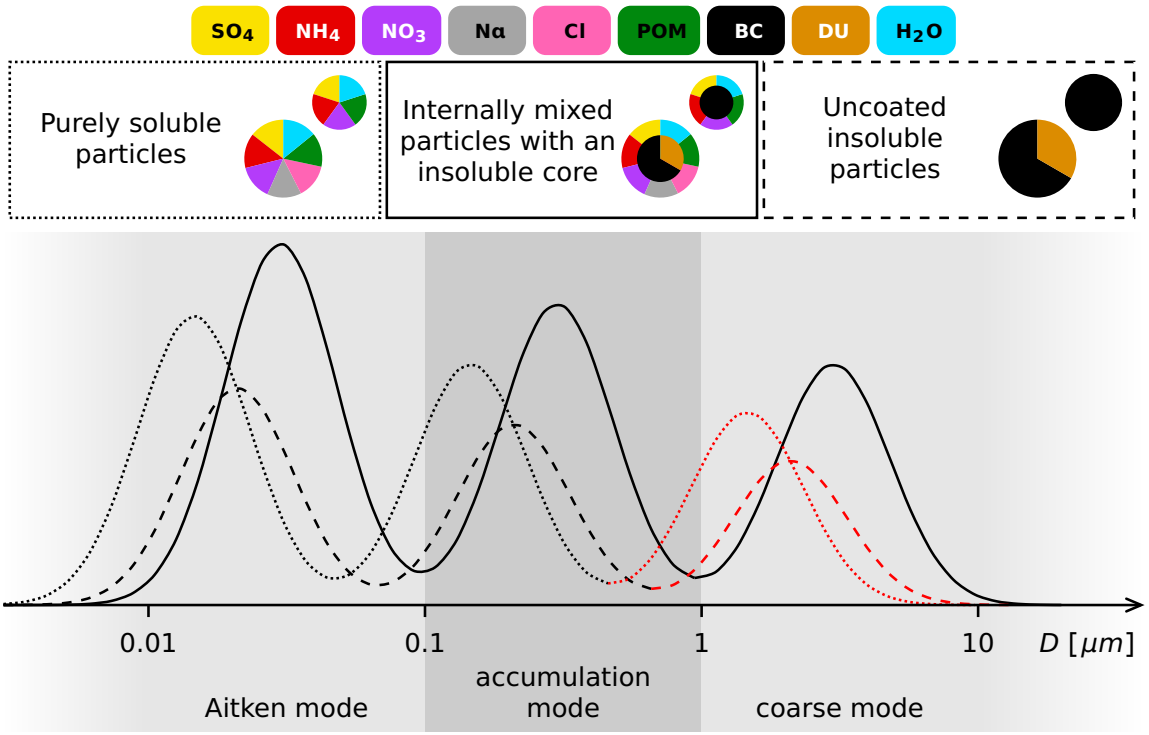

Figure 3.1: Schematic illustration of the MADE3 modes and aerosol composition. Each size range (Aitken, accumulation, and coarse mode size range) is represented by three model modes: soluble (dotted lines), insoluble (dashed lines), and mixed particles (solid lines). Red lines indicate the new modes in MADE3 with respect to its predecessor MADE-in. Small "pie charts" show possible Aitken mode particle compositions, larger "pie charts" stand for accumulation and coarse mode particles. Note that the MADE3 code in principle allows all components to be present in each of the modes, but some components do not appear in significant amounts in certain types of particles in the real atmosphere (e.g., DU in Aitken mode particles).

that charges are not added to the tracer names here because different oxidation states of the aerosol components are not distinguished. For instance, the SO_4 tracer includes SO_4^{2-}, HSO_4^-, and liquid H_2SO_4, as well as the sulfate in $(NH_4)_2SO_4$ and other crystalline salts. Densities for the tracers are given in Table 3.1.

The inclusion of NO_3 used to be a feature of MADE (and now MADE3) that was not shared by many other aerosol (sub)models (Table 2.1 and Kirkevåg et al., 2013). As detailed in Sect. 2.3.2, NO_3 may play an important role in the ship emissions-induced aerosol effect on climate in the future, and ammonium nitrate (NH_4NO_3) is projected to globally surpass SO_4 as the major inorganic anthropogenic contribution to the aerosol in the coming decades (Adams et al., 2001; Hauglustaine et al., 2014).

In order to represent the chemical interactions of sea spray with condensable trace gases more accurately, the sodium (Na) tracer is further speciated into different components within the thermodynamic equilibrium solver EQSAM (Sect. 3.2.1). The assumed constituent fractions for sodium, SO_4, magnesium (Mg), calcium (Ca), and potassium (K) are similar to those of the synthetic sea salt Sigma Aldrich S9883 (Sigma Aldrich, 2014).

Representing all particulate organic matter as only one tracer may seem inappropriate in light of the plethora of organic species found in atmospheric particles. Due to their vast range of different properties (see, e.g., Murphy et al., 2014a), however, a straightforward method of their classification into a set of tracers that is manageable in a global AC-GCM has remained elusive until recently (Napier et al., 2014). The simplification of using only one tracer was therefore justified at the time when MADE was developed, and inclusion of a more sophisticated approach is outside the scope of the present work (but could be an interesting project for the future, see

Table 3.1: Parameters used in MADE3: mode widths, bulk aerosol component densities, accommodation coefficients for gas adsorption on aerosol particles, and diffusivities of trace gases in air. Abbreviations are defined in the text.

	Symbol	Value	Unit
Mode widths			
soluble Aitken	σ_1	1.7	
mixed Aitken	σ_2	1.7	
insoluble Aitken	σ_3	1.7	
soluble accumulation	σ_4	2.0	
mixed accumulation	σ_5	2.0	
insoluble accumulation	σ_6	2.0	
soluble coarse	σ_7	2.2	
mixed coarse	σ_8	2.2	
insoluble coarse	σ_9	2.2	
Component densities			
SO_4	ρ_{SO_4}	$1.8 \cdot 10^3$	$kg\,m^{-3}$
NH_4	ρ_{NH_4}	$1.8 \cdot 10^3$	$kg\,m^{-3}$
NO_3	ρ_{NO_3}	$1.8 \cdot 10^3$	$kg\,m^{-3}$
Na	ρ_{Na}	$2.2 \cdot 10^3$	$kg\,m^{-3}$
Cl	ρ_{Cl}	$2.2 \cdot 10^3$	$kg\,m^{-3}$
POM	ρ_{POM}	$1.0 \cdot 10^3$	$kg\,m^{-3}$
BC	ρ_{BC}	$2.2 \cdot 10^3$	$kg\,m^{-3}$
DU	ρ_{DU}	$2.5 \cdot 10^3$	$kg\,m^{-3}$
H_2O	ρ_{H_2O}	$1.0 \cdot 10^3$	$kg\,m^{-3}$
Accommodation coefficients			
H_2SO_4	$\alpha_{H_2SO_4}$	1.0	
NH_3	α_{NH_3}	0.1	
HNO_3	α_{HNO_3}	0.1	
HCl	α_{HCl}	0.1	
SOA	α_{SOA}	1.0	
Gas diffusivities			
H_2SO_4	$\Delta_{H_2SO_4}$	0.09	$cm^2\,s^{-1}$
NH_3	Δ_{NH_3}	0.1	$cm^2\,s^{-1}$
HNO_3	Δ_{HNO_3}	0.1	$cm^2\,s^{-1}$
HCl	Δ_{HCl}	0.1	$cm^2\,s^{-1}$
SOA	Δ_{SOA}	0.05	$cm^2\,s^{-1}$

Chap. 8). Some further justification is supplied by Tost & Pringle (2012), who did not achieve much improvement with respect to observations when switching from one organic aerosol tracer to a more detailed scheme with six of them.

Similar to sea spray aerosol, mineral dust can consist of many different chemical species, some of which can also be chemically active (Kelly & Wexler, 2005). However, the EQSAM version used in MADE3 was not designed to simulate such processes, so that the DU tracer is still treated as chemically inactive here. This simplification is also justified by the large uncertainties in the exact mineralogy of dust from different sources. They are so high that even the sign of the direct RF of mineral dust is uncertain (Scanza et al., 2015).

3.1.3 Mathematical representation of aerosol characteristics

Information about particle composition is not included in the size distribution representation that is given by Eq. (2.4) and used in MADE3. Hence, the mass concentrations per unit volume of air, $c_{a,k}$, have to be tracked individually for each of the A considered species ($a = 1, \ldots, A$; $A = 9$ in MADE3) in each of the K modes ($k = 1, \ldots, K$; $K = 9$ in MADE3). The number of equations to be solved is thus $K \times (1 + A)$, i.e., one equation for the number concentration (N_k) in each of the K modes and A equations for the different aerosol component species in each of the K modes. For MADE3 this means that 90 equations are required.

All particles in one mode k are assumed to have the same composition, i.e., the mass fractions $c_{a,k}/\sum_{s=1}^{A} c_{s,k}$ are the same for these particles. In each mode the particles are thus considered to be internally mixed (cf. Sect. 2.1.3). In order to also include external mixtures in a modal (sub)model one has to define additional model modes, as is done in MADE3 (Fig. 3.1) or track the degree of external mixing for each mode and each species.

The median diameter $\tilde{D}_{\mathrm{g},k}$ (Sect. 2.3.3) of mode k can be derived from the component mass concentrations $c_{a,k}$ in that mode under the assumption of spherical particles:

$$\tilde{D}_{\mathrm{g},k} = \frac{1}{1\,\mu\mathrm{m}} \left(\frac{6V_k}{\pi N_k} e^{-\frac{9}{2}(\ln \sigma_k)^2} \right)^{\frac{1}{3}}, \tag{3.1}$$

with

$$V_k = \sum_{a=1}^{A} \frac{c_{a,k}}{\rho_a} \tag{3.2}$$

being the particle volume concentration of mode k, and ρ_a the density of species a (Table 3.1).

The moments (cf. Sect. 2.3.3) of the lognormal distribution of mode k are computed as:

$$\begin{aligned} M_{j,k} &= \int_{-\infty}^{\infty} \tilde{D}^j \cdot 1\,\mu\mathrm{m}^j \cdot n_k(\ln \tilde{D})\, \mathrm{d} \ln \tilde{D} \\ &= N_k \cdot (D_{\mathrm{g},k})^j \cdot e^{\frac{j^2}{2}(\ln \sigma_k)^2}. \end{aligned} \tag{3.3}$$

These moments are useful, for instance, in the calculations of particle coagulation and vapor condensation rates (Whitby et al., 1991; Lauer et al., 2005; Aquila et al., 2011). The corresponding equations are presented in Sect. 3.2. Mode widths are fixed in MADE3, which was also the case for its predecessor submodels (Lauer et al., 2005; Aquila et al., 2011). The values of σ_k are listed in Table 3.1.

3.2 Aerosol processes

Generally speaking, aerosol dynamics includes emissions, gas–particle partitioning, transport, physical and chemical processing, and deposition of particles. In this section, the focus is on internal processes, i.e., those that are actually calculated by the aerosol submodel MADE3. The remaining processes are the subject of Chap. 5. Aerosol particle composition, concentration, and size distribution undergo changes during the atmospheric processing of the aerosol. MADE3 calculates the evolution of the particle population due to three main processes: (1) gas–particle partitioning of semi-volatile species and water, which adds or removes particulate mass depending on environmental parameters (such as temperature or relative humidity); (2) gas-to-particle conversion of low-volatility species by condensation on pre-existing particles or in-situ formation of new particles; (3) mass transfer between particles by coagulation, which concurrently reduces particle number concentration. Employing an operator splitting approach, MADE3 first calculates compositional changes due to gas–particle partitioning alone. Subsequently, condensation/new particle formation and coagulation are treated simultaneously.

3.2.1 Gas–particle partitioning

Gas–particle partitioning of water and semi-volatile atmospheric trace constituents (ammonia (NH_3)/NH_4, nitric acid (HNO_3)/NO_3, hydrochloric acid (HCl)/Cl) is calculated in MADE3 by a thermodynamic equilibrium model. This model, called EQSAM (EQuilibrium Simplified Aerosol Model; Metzger et al., 2002, 2006), was designed for high efficiency in global atmospheric chemistry general circulation model (AC-GCM) applications. In the version used here (v03d, with additional inclusion of HCl/Cl) it calculates the equilibrium concentrations of NH_3(g), NH_4(p), HNO_3(g), NO_3(p), HCl(g), Cl(p), and H_2O(p) under consideration of the SO_4(p) concentration and those of the minerals sodium(p), Ca(p), K(p), and Mg(p) as part of the Na tracer (keys in parentheses denote *g*aseous and *p*articulate species, respectively). Chemical reactions inside aqueous aerosol droplets are thus considered implicitly. Furthermore, EQSAM takes into account deliquescence and efflorescence of particles that contain soluble material. Note that it does not include effects of organics, e.g., the possible increase in equilibration time due to organic coatings (Cruz et al., 2000), or the influence of organic acids on deliquescence of sea spray particles as indicated by Miñambres et al. (2014).

EQSAM is applied separately to the three size ranges, with the total species concentrations across all three modes per size range as input parameters. This is analogous to the procedure adopted by Aquila et al. (2011). The assumption of equilibrium between the gas and condensed phases is well justified for fine particles because they equilibrate on timescales of the order of seconds up to a few minutes (e.g., Meng & Seinfeld, 1996; Dassios & Pandis, 1999), i.e., well within the typical time step used for aerosol studies with EMAC (∼30 min in T42 resolution, namely approximately $2.8° \times 2.8°$). The sequence of EQSAM equilibrium calculations on the three aerosol size ranges is (1) Aitken modes, (2) accumulation modes, and (3) coarse modes, as smaller particles equilibrate faster and have a lower impact on gas phase concentrations due to their smaller mass concentration.

For large particles (in the size range of micrometers and greater), however, gas diffusion may be too slow to enable equilibration within this time frame (e.g., Wexler & Seinfeld, 1990, 1992; Meng & Seinfeld, 1996). Hence, the equilibrium assumption may introduce substantial errors (Moya et al., 2002; Koo et al., 2003; Feng & Penner, 2007; Athanasopoulou et al., 2008), but fully dynamical calculations of the involved fluxes are infeasible in long-term simulations with AC-GCMs. Several solutions to this problem have been proposed (Capaldo et al., 2000; Pilinis et al., 2000; Jacobson, 2005; Zaveri et al., 2008). However, most of them are still computationally too expensive for application in MADE3 within EMAC, and the solution by Zaveri et al. (2008) would require a complete revision of the aerosol chemistry scheme that was used in previous simulations with MADE (e.g., Lauer et al., 2007; Aquila et al., 2011; Righi et al., 2011, 2013). Consequently, possible non-equilibrium effects are accounted for in MADE3 by limiting the gas–particle fluxes involving coarse mode particles in a similar manner as described by Pringle et al. (2010a,b). The maximum possible diffusion fluxes of the semi-volatile trace gases are calculated (using equations equivalent to Eqs. (3.5) and (3.6) below, with $g_{X,\mathrm{s}} = 0$), and an equilibrium calculation is performed with EQSAM. If the fluxes required to reach this equilibrium surpass the maximum fluxes the amount of material that condenses during one time step is capped accordingly.

3.2.2 Condensation of H_2SO_4 and organic vapors

Due to its very low equilibrium vapor pressure, all H_2SO_4 that is transferred from the gas phase to the aerosol phase is assumed to remain in the aerosol particles. Depending on the magnitude of the condensation flux, the transfer can occur via condensation alone or via condensation and new particle formation (Sect. 3.2.3). To determine the amount of H_2SO_4 that can condense during one time step, the condensation flux is calculated explicitly. This is also necessary to

obtain the proper distribution of the condensate among the differently sized particles. An equilibrium assumption does not yield this distribution. While potential errors in the distribution of condensing material among differently sized particles will be corrected by re-evaporation in the case of the semi-volatile species, this is not possible for H_2SO_4, since the assumption that all H_2SO_4 that was transferred to the aerosol phase remains there means that it cannot re-evaporate in MADE3. The total condensation flux of H_2SO_4 is the sum of the rates of change of mass concentrations $c_{H_2SO_4,k}$ for all modes ($k = 1, \ldots, 9$):

$$\left(\frac{\mathrm{d}c_{H_2SO_4,k}}{\mathrm{d}t}\right)_{\mathrm{cond}} = \int_0^\infty \frac{\mathrm{d}m_\mathrm{p}(D)}{\mathrm{d}t}\, n_k(D)\, \mathrm{d}D, \tag{3.4}$$

where $\mathrm{d}m_\mathrm{p}(D)/\mathrm{d}t$ is the rate of change of mass for an individual particle of diameter D and $n_k(D)\,\mathrm{d}D = n_k(\ln \tilde{D})\,\mathrm{d}\ln \tilde{D}$. Note that with $\mathrm{d}\ln \tilde{D}/\mathrm{d}D = 1/D$ one obtains $n_k(\ln \tilde{D})/D$ as the functional form for $n_k(D)$, where $n_k(\ln \tilde{D})$ has to be inserted as given in Eq. (2.4). The rate of change of particle mass depends on the ratio of the particle diameter D and the mean free path $\lambda_{H_2SO_4}$ of H_2SO_4 molecules in the gas phase. As atmospheric aerosol particles span a large range of sizes, two limiting cases have to be considered. In the continuum regime, i.e., for $D \gg \lambda_{H_2SO_4}$, one obtains (see Seinfeld & Pandis, 2006):

$$\left(\frac{\mathrm{d}m_\mathrm{p}(D)}{\mathrm{d}t}\right)^{\mathrm{cont}} = 2\pi D \Delta_{H_2SO_4} (g_{H_2SO_4,\infty} - g_{H_2SO_4,\mathrm{s}}) \tag{3.5}$$

with the gas phase diffusivity, $\Delta_{H_2SO_4}$ (Table 3.1), and the gas phase concentration of H_2SO_4, $g_{H_2SO_4}$. The additional indices "∞" and "s" specify concentrations far away from the particle surface and directly above it, respectively. The corresponding expression for the kinetic, or free molecular, regime where $D \ll \lambda_{H_2SO_4}$ is (see Seinfeld & Pandis, 2006):

$$\left(\frac{\mathrm{d}m_\mathrm{p}(D)}{\mathrm{d}t}\right)^{\mathrm{free}} = \frac{\pi D^2}{4} \alpha_{H_2SO_4}\, \omega_{H_2SO_4} (g_{H_2SO_4,\infty} - g_{H_2SO_4,\mathrm{s}}). \tag{3.6}$$

Here, $\alpha_{H_2SO_4}$ is the accommodation coefficient (Table 3.1), or sticking probability, and $\omega_{H_2SO_4}$ the thermal speed of the H_2SO_4 molecules:

$$\omega_{H_2SO_4} = \sqrt{\frac{8RT}{\pi M_{H_2SO_4}}}, \tag{3.7}$$

where R is the universal gas constant, T the absolute temperature, and $M_{H_2SO_4}$ the molar mass of H_2SO_4. Note that a wide range of values for $\alpha_{H_2SO_4}$ has been derived from measurements (0.02 to 0.79; e.g., Van Dingenen & Raes, 1991; Kerminen & Wexler, 1995; Jefferson et al., 1997; Bardouki et al., 2003) and used in models (0.1 to 1; e.g., Capaldo et al., 2000; Vignati et al., 2004; Zaveri et al., 2008; Mann et al., 2010; Kajino et al., 2012). Here, as in former generations of the submodel, $\alpha_{H_2SO_4} = 1$ is used, which was also found to be in agreement with field measurements by Eisele & Tanner (1993). The value is the same for all modes, i.e., condensation is treated in the same way, regardless of whether particles contain soluble material or not. The near-surface concentration is set to $g_{H_2SO_4,\mathrm{s}} = 0$ due to the very low equilibrium vapor pressure of H_2SO_4. The far-away concentration $g_{H_2SO_4,\infty}$ is determined as the solution to the ordinary differential equation that describes the temporal evolution of the gas phase H_2SO_4 concentration:

$$\frac{\mathrm{d}g_{H_2SO_4}}{\mathrm{d}t} = P_{H_2SO_4} - L_{H_2SO_4} \cdot g_{H_2SO_4}. \tag{3.8}$$

Here, $P_{H_2SO_4}$ is the production rate of gaseous H_2SO_4, and $L_{H_2SO_4}$ is the sum of the integrals as given in Eq. (3.4) for all nine modes with the factor $g_{H_2SO_4,\infty}$ removed, i.e., the overall loss

rate coefficient due to condensation:

$$L_{\mathrm{H_2SO_4}} = \frac{\sum_{k=1}^{9} \left(\frac{\mathrm{d}c_{\mathrm{H_2SO_4},k}}{\mathrm{d}t}\right)_{\mathrm{cond}}}{g_{\mathrm{H_2SO_4},\infty}}. \tag{3.9}$$

Production of gaseous H_2SO_4 and condensation on the particles are thus considered in parallel.

The integral in Eq. (3.4) can be evaluated analytically with both the continuum regime and the free molecular regime expressions for $\mathrm{d}m_{\mathrm{p}}(D)/\mathrm{d}t$ (Whitby et al., 1991). However, there is also a transition regime, where D and $\lambda_{\mathrm{H_2SO_4}}$ are of the same order of magnitude. Therefore, the method of Binkowski & Shankar (1995) is applied in MADE3, using half the harmonic mean of the two integrals as the condensation rate of H_2SO_4 on mode k. According to Chen et al. (2013) this might lead to an overestimation of the particle volume growth rate. They do not provide exact numbers, however, except for an upper limit estimation of 83 %. Hence, particle sizes may be overestimated, and the new particle formation rate (see next subsection) potentially underestimated. The associated error is expected to be small, however, except in cases where condensation on aerosol particles dominates either particle growth, or the H_2SO_4 removal from the gas phase, or both. For more details on the condensation calculations see the description in Appendix A of the article by Aquila et al. (2011) or the original work by Whitby et al. (1991).

Secondary organic aerosol (SOA) formation from condensing organic vapors is treated in the same simplified manner in MADE3 as in MADE-in (Aquila et al., 2011). Using an externally supplied total mass formation rate of SOA,

$$P_{\mathrm{SOA}} = \sum_{k=1}^{9} \left(\frac{\mathrm{d}c_{\mathrm{SOA},k}}{\mathrm{d}t}\right)_{\mathrm{cond}}, \tag{3.10}$$

a similar procedure as outlined above for H_2SO_4 condensation is also applied for SOA formation. The near-surface gas phase concentration is again set to zero ($g_{\mathrm{SOA,s}} = 0$, neglecting semi-volatile organic species because organic gas phase chemistry is not considered). Analogous expressions to Eqs. (3.5) and (3.6) for SOA are then used together with Eq. (3.10) to obtain $g_{\mathrm{SOA},\infty}$, so that the integral in Eq. (3.4) can be evaluated for SOA just as for H_2SO_4 for the individual modes.

3.2.3 New particle formation

New particle formation (NPF) by nucleation of molecular H_2SO_4/H_2O clusters is calculated in MADE3 after solving the production–condensation equation (Eq. 3.8). This approach corresponds to method 2C as discussed by Wan et al. (2013). In terms of the nucleation sink for gaseous H_2SO_4, they showed this method to be the best-performing among sequential methods for solving the full H_2SO_4 equation, i.e., Eq. (3.8) plus a nucleation loss term.

To calculate the nucleation rate, $(\mathrm{d}N_1/\mathrm{d}t)_{\mathrm{nuc}}$, the parameterization by Vehkamäki et al. (2002, 2013) is applied. It represents binary homogeneous nucleation of H_2SO_4–H_2O droplets and is based on temperature, relative humidity (RH), and H_2SO_4 concentration. Following Binkowski & Roselle (2003), the rapid growth of the freshly nucleated particles to detectable sizes is accounted for by assuming a monodisperse size distribution with $D = 3.5\,\mathrm{nm}$ upon formation. The H_2SO_4 fraction of these particles is calculated from the ambient RH as described in Binkowski & Roselle (2003), based on measurements by Nair & Vohra (1975). Subsequently, number and mass concentrations of the newly formed particles are added to the soluble Aitken mode ($k = 1$). NPF from organic precursor gases is not considered in MADE3.

While this scheme captures the behavior of the free troposphere well (Liu et al., 2005), a number of studies have shown that it cannot accurately reproduce observed NPF in the

planetary boundary layer (e.g., Stier et al., 2005). An additional power law term of the type $(\mathrm{d}N_1/\mathrm{d}t)_{\mathrm{nuc}}^{\mathrm{BL}} = J \cdot (g_{\mathrm{H_2SO_4}})^q$ with $q \in [1, 2]$ has therefore been included in a few aerosol (sub)models recently (e.g., Makkonen et al., 2009; Karl et al., 2012; Makkonen et al., 2014). The rate constant J in this expression likely depends on the concentrations of other species that can stabilize the initial H_2SO_4 molecule clusters, e.g., organic vapors (Riccobono et al., 2014). Despite some improvements in the model–observation agreement that could be achieved with such an additional boundary layer term, the nucleation parameterization in MADE3 was not changed in the present work. Given the prevailing uncertainties associated with J and q, and since the focus of this work is on the other end of the size spectrum of atmospheric aerosol particles, a significant impact of this simplification on the results presented here is not expected. The studies by Carslaw et al. (2013), Lee et al. (2013a,b), and Westervelt et al. (2014) also suggest a small impact of nucleation mode microphysics on cloud condensation nuclei (CCN) concentrations, for example.

3.2.4 Coagulation

Similar to the condensation treatment, coagulation calculations in MADE3 are also performed by mode. Number and mass concentration changes are calculated separately:

$$\left(\frac{\mathrm{d}N_k}{\mathrm{d}t}\right)_{\mathrm{coag}} = \sum_{l=1}^{9}\sum_{m=l}^{9}\left(a_{lm}^k \cdot \int_0^\infty \int_0^\infty \beta(D_1, D_2) n_l(D_1) n_m(D_2)\,\mathrm{d}D_1\,\mathrm{d}D_2\right), \tag{3.11}$$

$$\begin{aligned}\left(\frac{\mathrm{d}c_{a,k}}{\mathrm{d}t}\right)_{\mathrm{coag}} = \frac{\pi}{6} \cdot \sum_{l=1}^{9}\sum_{m=l}^{9}\Bigg[& \\ & (\delta_{k,\tau_{lm}} - \delta_{k,l}) \cdot \frac{c_{a,l}}{\sum_{s=1}^{A} c_{s,l}} \cdot \rho_l \cdot \int_0^\infty \int_0^\infty (D_1)^3 \beta(D_1, D_2) n_l(D_1) n_m(D_2)\,\mathrm{d}D_1\,\mathrm{d}D_2 \\ & + (\delta_{k,\tau_{lm}} - \delta_{k,m}) \cdot \frac{c_{a,m}}{\sum_{s=1}^{A} c_{s,m}} \cdot \rho_m \cdot \int_0^\infty \int_0^\infty (D_2)^3 \beta(D_1, D_2) n_l(D_1) n_m(D_2)\,\mathrm{d}D_1\,\mathrm{d}D_2\Bigg].\end{aligned} \tag{3.12}$$

The parameters ρ_l and ρ_m in Eq. (3.12) stand for the densities of particles in modes l and m, respectively. The coefficients a_{lm}^k are calculated as follows:

$$a_{lm}^k = \delta_{k,\tau_{lm}} \cdot \left(1 + \frac{\delta_{l,m}}{2}\right) - \delta_{k,l} - \delta_{k,m}. \tag{3.13}$$

Here, as in Eq. (3.12), the Kronecker symbol $\delta_{x,y}$ has been used. Its value is $\delta_{x,y} = 1$ if $x = y$, and $\delta_{x,y} = 0$ otherwise. The matrix elements τ_{lm} are used for the assignment of number and mass concentrations of coagulated particles to a target mode, depending on the modes of origin, l and m. The rules for this assignment, i.e., the values of the matrix elements τ_{lm}, follow Aquila et al. (2011):

- intramodal coagulation produces particles in the same mode ($\tau_{ll} = l$);
- intermodal coagulation produces particles in the size range of the larger mode;
- the exact target mode for intermodal coagulation depends on the mass fraction x of soluble material and water in the final particles:

  $x = 1$: soluble mode,

  $0.1 \leq x < 1$: mixed mode,

  $x < 0.1$: insoluble mode.

Table 3.2: Matrix elements τ_{lm} (table cells) for assignment of particles that result from coagulation of particles from mode l (row) with particles from mode m (column). The mode naming convention is "k", "a", "c" as a first letter to specify the Aitken, accumulation, or coarse mode, respectively, and "s", "m", "i" as a second letter for the soluble, mixed, or insoluble mode, respectively. Thus, the soluble coarse mode, for instance, is named "cs". Corresponding numbers are as follows: ks = 1, km = 2, ki = 3, as = 4, am = 5, ai = 6, cs = 7, cm = 8, and ci = 9.

	ks	km	ki	as	am	ai	cs	cm	ci
ks	ks	km	km/ki	as	am	am/ai	cs	cm	ci
km	km	km	km/ki	am	am	am/ai	cm	cm	ci
ki	km/ki	km/ki	ki	am/ki	am/ki	ai	cm	cm	ci
as	as	am	am/ki	as	am	am/ai	cs	cm	cm/ci
am	am	am	am/ki	am	am	am/ai	cm	cm	cm/ci
ai	am/ai	am/ai	ai	am/ai	am/ai	ai	cm/ai	cm/ai	ci
cs	cs	cm	cm	cs	cm	cm/ai	cs	cm	cm/ci
cm	cm	cm	cm	cm	cm	cm/ai	cm	cm	cm/ci
ci	ci	ci	ci	cm/ci	cm/ci	ci	cm/ci	cm/ci	ci

For instance, particles that result from intermodal coagulation of particles from modes $l = 1$ (soluble Aitken mode, or "ks" in Table 3.2) and $m = 4$ (soluble accumulation mode, or "as") are assigned to mode $\tau_{14} = 4$ ("as"). Hence, $a^4_{14} = 0$, which means that this process does not add to the particle number concentration in mode $k = 4$ ("as"). It does, however, add mass from mode $l = 1$ ("ks") to mode $k = 4$ ("as"). This is reflected in the parentheses with the Kronecker symbols in Eq. (3.12): the first pair of parentheses evaluates to one, the second pair to zero. In case of intramodal coagulation, i.e., if $l = k$ and $m = k$, the value of the coefficient in Eq. (3.11) is $a^k_{kk} = -0.5$. It is negative because one particle per such event is lost, but the factor is only -0.5 because of the double integration over the same mode. For intramodal coagulation all the Kronecker symbols in Eq. (3.12) evaluate to one, so that all summands are zero, and no mass is added to, or removed from, mode k.

In total, Eq. (3.11) and Eq. (3.12) include 45 and 90 summands for each mode k, respectively, but many of them are zeros. For example, coagulation losses and gains in the soluble coarse mode ("cs" in Table 3.2) are described by seven non-zero terms in the number equation (Eq. 3.11), and eight non-zero terms in the mass equation (Eq. 3.12).

For the Brownian coagulation kernel, $\beta(D_1, D_2)$, the approximate formulations developed by Whitby et al. (1991) that can be integrated analytically are used. As in the case of condensation, two different expressions are required again, depending on the size of the particles. For the continuum regime the function is given as (Whitby et al., 1991):

$$\beta^{\text{cont}}(D_1, D_2) = \frac{2k_\text{B}T}{3\nu} \cdot \left[2 + 2\lambda_{\text{air}} G \left(\frac{1}{D_1} + \frac{D_2}{(D_1)^2}\right) + 2\lambda_{\text{air}} G \left(\frac{1}{D_2} + \frac{D_1}{(D_2)^2}\right) + \frac{D_2}{D_1} + \frac{D_1}{D_2}\right], \tag{3.14}$$

with Boltzmann's constant k_B, atmospheric dynamic viscosity ν, and the constant $G = 1.246$ that accounts for the reduced drag on small particles. Atmospheric dynamic viscosity is calculated from temperature (T):

$$\nu = B \cdot \frac{T^{\frac{3}{2}}}{T + S}, \tag{3.15}$$

with $B = 1.458 \cdot 10^{-6}\,\mathrm{Pa\,s\,K^{-0.5}}$ and $S = 110.4\,\mathrm{K}$. The mean free path of air depends on both temperature, T, and pressure, p:

$$\lambda_{\mathrm{air}} = \Lambda \cdot \frac{p_0 T}{T_0 p}, \tag{3.16}$$

where $\Lambda = 6.6328 \cdot 10^{-8}\,\mathrm{m}$, $p_0 = 101325\,\mathrm{Pa}$, and $T_0 = 288.15\,\mathrm{K}$. For the free molecular regime, the coagulation kernel becomes (Whitby et al., 1991):

$$\beta^{\mathrm{free}}(D_1, D_2) = \sqrt{\frac{6 k_{\mathrm{B}} T}{\rho_1 + \rho_2}} \cdot \left(\sqrt{D_1} + 2\frac{D_2}{\sqrt{D_1}} + \frac{(D_2)^2}{(D_1)^{\frac{3}{2}}} + \frac{(D_1)^2}{(D_2)^{\frac{3}{2}}} + 2\frac{D_1}{\sqrt{D_2}} + \sqrt{D_2} \right), \tag{3.17}$$

where ρ_1 (ρ_2) is the density of the particle with diameter D_1 (D_2). Note that a correction factor is required for the integrals in Eqs. (3.11) and (3.12) if this kernel approximation for the free molecular regime is used. It is set constant at 0.8 for unimodal and 0.9 for bimodal coagulation in MADE3. After evaluation of the coagulation integrals for both regimes (i.e., with $\beta^{\mathrm{cont}}(D_1, D_2)$ and $\beta^{\mathrm{free}}(D_1, D_2)$, respectively) the halved harmonic means of the resulting rates are used to redistribute mass and numbers among the modes, as was done by Aquila et al. (2011, see their Appendix B). According to the evaluation by Chen et al. (2013), this scheme performs well at small and intermediate coagulation rates, with slightly degrading accuracy at high rates.

3.2.5 Renaming

As particles grow by condensation and coagulation, the Aitken modes may grow into the size range of the accumulation modes. In order to avoid mode merging, i.e., to keep the modes approximately within their assigned size ranges, a procedure called renaming is applied (Binkowski & Roselle, 2003). One of two criteria must be met in MADE3 to trigger renaming within a time step. Either the volume growth rate of the Aitken mode must be larger than that of the corresponding accumulation mode, or the median diameter of the Aitken mode must exceed 30 nm and its number concentration must be greater than that of the corresponding accumulation mode. In such a case the number concentration of particles greater than the intersection diameter of the two number size distributions is shifted from the Aitken to the corresponding accumulation mode. The associated mass concentration is also transferred. Renaming is performed only between modes of the same particle type, i.e., either between the two soluble modes, or between the two insoluble modes, or between the two mixed modes. Note that particles are not renamed from the accumulation to the coarse modes because their diameters are changed much less by condensation and coagulation than those of the Aitken mode particles.

3.2.6 Aging of insoluble particles

The aerosol processing in the atmosphere is also termed aging. For insoluble particles this term often refers to the acquisition of a coating of soluble components that transforms them from an initially hydrophobic state to a hydrophilic one. This transformation has a strong influence on the wet deposition of BC, for instance (Ching et al., 2012; Shen et al., 2014; Taylor et al., 2014). As it depends on the local atmospheric conditions (such as vapor concentrations and RH), its effects can vary by region and time of day (e.g., Sullivan et al., 2007; Healy et al., 2014). An explicit representation of BC aging can improve agreement between modeled and observed BC concentrations in the Arctic, for example (Vignati et al., 2010; Lund & Berntsen, 2012).

Therefore, this process is simulated explicitly in MADE3 by transfer of number and mass concentrations from the insoluble modes to the mixed modes in analogy to the procedure described by Aquila et al. (2011). Following their approach, a threshold mass concentration

fraction of 10 % of soluble material and water in an insoluble mode is used to trigger this transfer. In addition to the references cited by Aquila et al. (2011), this threshold value is also supported by recent measurements at the U.K.'s North Sea coast (Liu et al., 2013). For comparison, Kirkevåg et al. (2013) assume a threshold thickness of the coating on insoluble particles of 2 nm in their model for using the hygroscopicity of the coating material instead of that of a homogeneously mixed particle. At a typical BC particle core diameter of 80 nm this corresponds to a mass threshold of about 8 %, which is comparable to the value used here. Measurements of cloud residual coating thicknesses on BC particles by Schroder et al. (2015b,a) suggest that coatings required for activation at 0.5 % water vapor supersaturation might have to be substantially thicker than that. However, it is unclear to what degree the material that they counted as a coating was actually produced inside the sampled cloud droplets.

Note that the photochemical oxidation of particle surfaces can also lead to transformations from hydrophobic to hydrophilic states. Such processes, however, are not represented in MADE3.

Chapter 4

Box model tests[1]

Some essential processes, e.g., particle transport and deposition, are not included in MADE3 because they are treated by other submodels within the MESSy framework (Chap. 5). It is therefore not feasible to evaluate a box model setup of MADE3 by comparison with measured data. Instead, a test of the algorithms used in MADE3 for solving the aerosol microphysics equations given in Sect. 3.2 is presented in this chapter. In order to assess improvements, strengths, and weaknesses of the new submodel it is compared in a box model application to its predecessor MADE and to the particle-resolved stand-alone aerosol model PartMC-MOSAIC (Riemer et al., 2009; Zaveri et al., 2008). For that purpose a marine background setup is defined with added emissions representative of heavy ship traffic. MADE is used for this comparison because previous studies on the ship emissions-induced effect on the atmospheric aerosol were carried out with this submodel (Lauer et al., 2007, 2009; Righi et al., 2011, 2013). PartMC-MOSAIC is regarded as a reference to test how well MADE3 performs as a solver for the aerosol dynamics equation.

This chapter briefly summarizes the most important improvements of MADE3 over its predecessor MADE (Sect. 4.1) and the main features of PartMC-MOSAIC (Sect. 4.2) with a focus on the differences to MADE3. Furthermore, it contains the definition of the marine boundary layer (MBL) test case scenario (Sect. 4.3). The main part of this chapter is dedicated to the presentation and discussion of the simulations of this scenario with the three different (sub)models (Sect. 4.4).

4.1 Model description: MADE vs. MADE3

MADE is used here in the version described by Lauer et al. (2005). Although the code underwent major restructuring and was expanded for the development of MADE3 via MADE-in, the new submodel still shares with MADE the computational approaches to aerosol size distribution representation, gas–particle partitioning, sulfuric acid (H_2SO_4) and secondary organic aerosol (SOA) condensation, new particle formation (NPF), and coagulation. Therefore, only the major physically motivated changes in MADE3 w.r.t. MADE are pointed out here.

The most obvious difference is in the number of modes, which increased from three (MADE) to nine (MADE3). The representation of aerosol particles by three modes per size range allows for the modeling of both internally mixed particles and externally mixed particle populations (Aquila et al., 2011).

Furthermore, while particles in the MADE coarse mode are considered passive (only water uptake by coarse mode particles is included), they interact with both other particles and condensable trace gases in MADE3. Coarse mode particle composition as well as effects of coarse mode particles on fine mode particles and the gas phase can therefore be resolved in much more detail with MADE3 than what is feasible with MADE. Note also that coarse mode particles in MADE are composed of sea spray, mineral dust, and water only, while MADE3 allows all aerosol components to be present in the coarse modes.

[1]The contents of this chapter appeared in similar form in a recent publication (Kaiser et al., The MESSy aerosol submodel MADE3 (v2.0b): description and a box model test, Geosci. Model Dev., 7(3), 1137–1157).

In combination with the larger number of modes, the newly introduced interactions of coarse mode particles also entail a larger number of different possible coagulation pathways: 45 in MADE3 vs. 3 in MADE. The calculations to determine target modes based on the soluble mass fraction of the coagulated particles (Sect. 3.2.4) are not necessary in MADE, while they are required for 14 of the coagulation pathways in MADE3.

In addition, chloride (Cl) is considered as a separate species in MADE3, whereas all sea spray components are lumped into one tracer in MADE. The explicit Cl representation enables the calculation of gas–aerosol partitioning for hydrochloric acid (HCl) by EQSAM, which is not considered in MADE, but is required for accurate modeling of processes in the marine boundary layer and in coastal areas.

With the larger number of modes, the inclusion of the coarse mode particle interactions, and the inclusion of the Cl tracer, the number of aerosol species tracers increased from 18 in MADE to 81 in MADE3.

4.2 Model description: PartMC-MOSAIC

PartMC-MOSAIC is a stochastic particle-resolved aerosol model that consists of the microphysics code PartMC (Particle-resolved Monte Carlo model, Riemer et al., 2009) and the gas and condensed phase chemical solver MOSAIC (MOdel for Simulating Aerosol Interactions and Chemistry, Zaveri et al., 2008). The PartMC-MOSAIC version used for the present work (v. 2.2.1) corresponds to the detailed description in Tian et al. (2014), so that only a brief summary of the relevant features is given here.

The model solves the aerosol dynamics equation (Eq. 2.1) on a per-particle basis. While the size distribution is constrained in MADE3 by the assumption of lognormal modes, it can freely evolve in PartMC-MOSAIC, where $n(D, t)$ (Sect. 2.3.3) is represented by a finite number N_p of computational particles with discrete sizes. For the present work a value of $N_\mathrm{p} \approx 10^5$ was chosen, as was done in previous applications of PartMC-MOSAIC (e.g., Riemer et al., 2009; Tian et al., 2014). In order to capture the large range of possible sizes and concentrations, one computational particle can represent a larger number of real particles (DeVille et al., 2011). The number and mass weighting of these computational particles for the microphysics and chemistry calculations is performed automatically. As particles are constantly emitted, but loss processes (except for coagulation) are not considered in the box model scenario used here, half of the particles are randomly picked out and discarded whenever the number of computational particles exceeds twice its initial value.

Aerosol composition can be resolved into more separate species in PartMC-MOSAIC than in MADE3. Eleven tracers are used here: sulfate (SO_4), ammonium (NH_4), nitrate (NO_3), sodium (Na), Cl, organic carbon (OC), black carbon (BC), calcium (Ca), carbonate (CO_3), other inorganic material (OIN), and water (H_2O).

Particle emissions and coagulation are treated stochastically in PartMC. Random samples are added at each time step such that the number of emitted particles per unit time is Poisson-distributed around a prescribed continuous mean emission rate. The composition and mean size distribution of these particles are also prescribed. For coagulation the maximum number of collision events during the time step is estimated, and a corresponding number of candidate particle pairs is randomly selected. Subsequently, an accept–reject procedure is applied to determine whether these pairs actually coagulate. The probability for acceptance is based on the Brownian coagulation kernel.

Condensation of H_2SO_4 and gas–particle partitioning of semi-volatile gases is dynamically calculated by the deterministic model MOSAIC. This is in contrast to the equilibrium assumption in MADE3, so that no special treatment of large particles is required here. Note

that, besides the different approaches to aerosol microphysics, the use of different codes for the thermodynamic calculations (EQSAM in MADE3 vs. MOSAIC in PartMC-MOSAIC) can be a major driver of differences in simulation results. The validity of the PartMC microphysics routines was demonstrated by Riemer et al. (2009) and MOSAIC was shown to perform well in comparison to other aerosol chemistry codes (Zaveri et al., 2008) that included more details than the treatment in MADE3. The combined model (PartMC-MOSAIC) was successfully applied in a recent study of a ship plume (Tian et al., 2014). In summary, PartMC-MOSAIC is able to capture many more details of the aerosol evolution than MADE3 and can therefore serve as a reference here.

4.3 Test case scenario

The initial conditions for the test simulations with MADE3, MADE, and PartMC-MOSAIC are representative of the marine background boundary layer. The setup was designed to mimic the goal of this work to apply MADE3 within the atmospheric chemistry general circulation model (AC-GCM) EMAC for a reassessment of the ship emissions-induced effect on the global atmospheric aerosol. Coarse mode particle interactions with condensable gases and with small particles may play an important role in this context. Therefore, the scenario contains BC emissions and prescribed gaseous H_2SO_4 and nitric acid (HNO_3) production rates representative of an episode of heavy ship traffic.

Aerosol processing was simulated for 24 h (without transport and deposition) under constant environmental conditions, with a constant BC emission rate as well as constant H_2SO_4 and HNO_3 formation rates. This scenario can be regarded as an idealized representation of a stagnant air mass in a shipping corridor. Typical, model-specific values were chosen for the time steps: 1800 s, i.e., 30 min, in MADE3 and MADE, and 1 s in PartMC-MOSAIC. Gas phase chemistry is not considered because the focus is placed on the particulate phase here.

Environmental parameters as well as initial gas and aerosol concentrations were extracted from a previous multi-year EMAC simulation using the MADE3 predecessor MADE-in (evaluated by Aquila et al., 2011). A grid box in the Indian Ocean with $T = 286\,\mathrm{K}$, $p = 1.02 \cdot 10^5\,\mathrm{Pa}$, and $RH = 0.771$ was selected for the test case scenario. The initial aerosol state (as represented in MADE3) is shown in Fig. 4.1, and the initial number and species mass concentrations per size range, i.e., summed over the respective soluble, mixed, and insoluble modes, are given in Table 4.1. Initial gas concentrations are as follows: $g_{H_2SO_4} = 3.75 \cdot 10^{-7}\,\mu\mathrm{g\,m^{-3}}$, $g_{NH_3} = 0.240\,\mu\mathrm{g\,m^{-3}}$, $g_{HNO_3} = 0$, and $g_{HCl} = 0$.

As MADE-in represents coarse mode particles by only one mode, the species mass concentrations were redistributed among the MADE3 coarse modes as follows:

- sea spray (SS): 50 % to the soluble mode, 50 % to the mixed mode;
- mineral dust (DU): 50 % to the mixed mode, 50 % to the insoluble mode;
- H_2O: approximately 50 % each to the soluble mode and the mixed mode, and $1.6 \cdot 10^{-4}$ % to the insoluble mode (in order to keep the H_2O mass fraction of the latter below the 10 % threshold upon initialization).

Other species are not included in the initial coarse mode particle composition because MADE-in cannot simulate other components in the coarse mode. Splitting up the MADE-in SS tracer, 45 % of the mass concentration was assigned to the MADE3 Na tracer and 55 % to the MADE3 Cl tracer. This speciation is in accordance with the assumptions in EQSAM on sea spray composition. The redistribution of number concentration was derived from the mass concentrations in the coarse modes under the assumption that all three modes should initially have the same median diameter.

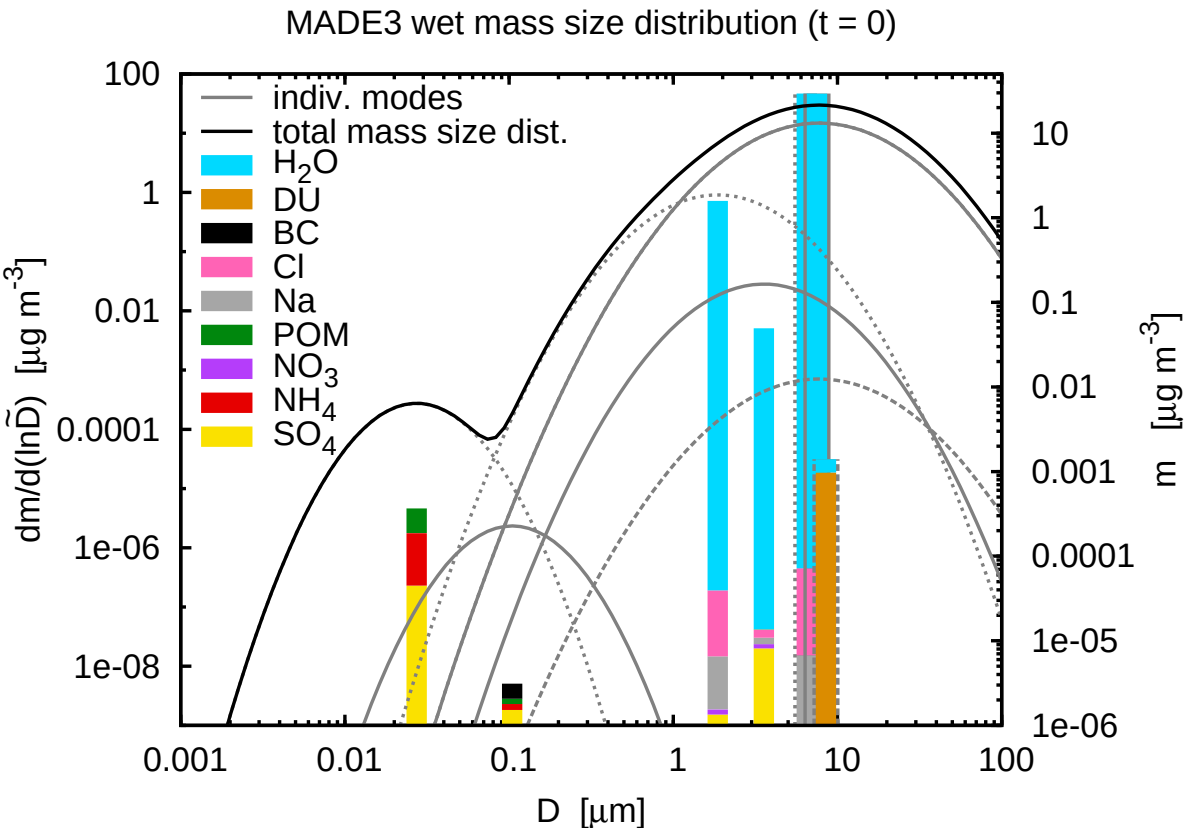

Figure 4.1: Initial aerosol mass size distribution and composition as represented in MADE3. The thick black line represents the mass size distribution calculated as the sum of the modes shown in gray (left vertical axis; dotted lines for soluble modes, solid lines for mixed modes, dashed lines for insoluble modes). Insoluble Aitken and accumulation mode mass concentrations are initially so small that these modes do not appear in the figure, and the curves for the soluble and mixed coarse modes lie on top of each other. The colored bars show the contributions of the individual species to the mass concentration (right vertical axis) of the respective mode (from left to right: soluble Aitken, mixed Aitken, soluble accumulation, mixed accumulation, soluble coarse, mixed coarse, insoluble coarse). Note that while the right vertical axis is logarithmic, the species fractions in the bars add up linearly to the total mass concentrations, i.e., the axis only applies to the total mass concentration in each mode but not to the individual contributions. Note further that the three coarse mode bars were artificially spread out along the diameter axis, and gray borders corresponding to the line styles of the respective modes were added for clarity.

Transformation of the initial aerosol state to the MADE representation is straightforward: mass and number concentrations from the MADE-in Aitken modes were summed up and assigned to the MADE Aitken mode, and the same procedure was applied to the accumulation modes. For the coarse mode, the MADE-in output could be used without modifications.

In terms of median diameters, number concentrations, and mode widths, PartMC-MOSAIC was initialized with the same modes as MADE3, translated to a population of individual particles. However, the MADE3 Na and DU tracers had to be further speciated for use with PartMC-MOSAIC. Following again the sea spray composition assumptions in EQSAM, 69 % of the MADE3 Na tracer mass concentration was assigned to the PartMC-MOSAIC Na tracer, 17 % were added to the PartMC-MOSAIC SO_4 tracer, 3 % to the Ca tracer, and 11 % to the other inorganic material (OIN) tracer. For the speciation of the MADE3 DU tracer into PartMC-MOSAIC tracers the following mass fractions were assumed: 2 % of Ca, 3 % of CO_3, and 95 % of OIN (corresponding to 5 % calcium carbonate ($CaCO_3$), based on data in Glaccum & Prospero, 1980; Kandler et al., 2009; Scheuvens et al., 2013; Formenti et al., 2014).

Table 4.1: Initial number and species mass concentrations in the Aitken, accumulation, and coarse mode size ranges (summed over the respective soluble, mixed, and insoluble modes). Abbreviations are as follows: POM for particulate organic matter and DU for mineral dust.

	Aitken mode	Accumulation mode	Coarse mode
Number concentrations $\left[\mathrm{m}^{-3}\right]$			
	$7.34 \cdot 10^7$	$3.51 \cdot 10^6$	$3.44 \cdot 10^6$
Species mass concentrations $\left[\mu\mathrm{g\,m}^{-3}\right]$			
SO_4	$2.37 \cdot 10^{-4}$	0.0425	0
NH_4	$8.89 \cdot 10^{-5}$	$2.86 \cdot 10^{-8}$	0
NO_3	0	0.0161	0
Na	0	0.161	6.51
Cl	0	0.200	8.10
POM	$4.17 \cdot 10^{-5}$	$9.31 \cdot 10^{-5}$	0
BC	$1.12 \cdot 10^{-6}$	$7.24 \cdot 10^{-6}$	0
DU	0	$2.42 \cdot 10^{-6}$	0.00266
H_2O	0	1.21	44.1

BC emissions are added to the (insoluble) Aitken and accumulation modes in MADE (MADE3), and as separate particles in PartMC-MOSAIC. The BC emission flux (Table 4.2) is based on values for ship emissions reported in the Lamarque et al. (2010) dataset for the year 2000, under the assumption of a typical marine boundary layer height of 500 m. The data was taken from a grid box off the coast of Normandy, France, and a bimodal size distribution was assumed as given in Table 4.2 and further described in Sect. 5.2. For the formation rates of gaseous H_2SO_4 and HNO_3 (Table 4.2) relatively high values were assumed in order to fully explore the effects of the condensation process on the microphysical calculations. The rates correspond to a direct conversion of the sulfur dioxide (SO_2) and the reactive nitrogen oxides (NO_x) emitted by ships (again drawn from the Lamarque et al., 2010, dataset), i.e., their choice implicitly contains the assumption of equilibrium SO_2 and NO_x concentrations with respect to ship emissions and formation of gaseous H_2SO_4 and HNO_3.

New particle formation (NPF) is treated in the same way in MADE and MADE3, but differently in PartMC-MOSAIC. Due to the large uncertainties associated with the choice of parameterizations (cf. Sect. 3.2.3), consideration of NPF would make the interpretation of the simulation results rather difficult. The process is therefore neglected in the present test case

Table 4.2: Emission and formation rates used in the test case scenario.

Species	Mass conc. rate of change $\left[\mu\mathrm{g\,m}^{-3}\,\mathrm{s}^{-1}\right]$	Number conc. rate of change $\left[\mathrm{m}^{-3}\,\mathrm{s}^{-1}\right]$
Aitken mode BC ($D_\mathrm{g} = 70\,\mathrm{nm}$, $\sigma = 1.45$)	$1.9 \cdot 10^{-7}$	$2.6 \cdot 10^2$
Accumulation mode BC ($D_\mathrm{g} = 260\,\mathrm{nm}$, $\sigma = 1.25$)	$5.0 \cdot 10^{-8}$	2.0
H_2SO_4	$1.5 \cdot 10^{-5}$	–
HNO_3	$1.7 \cdot 10^{-5}$	–

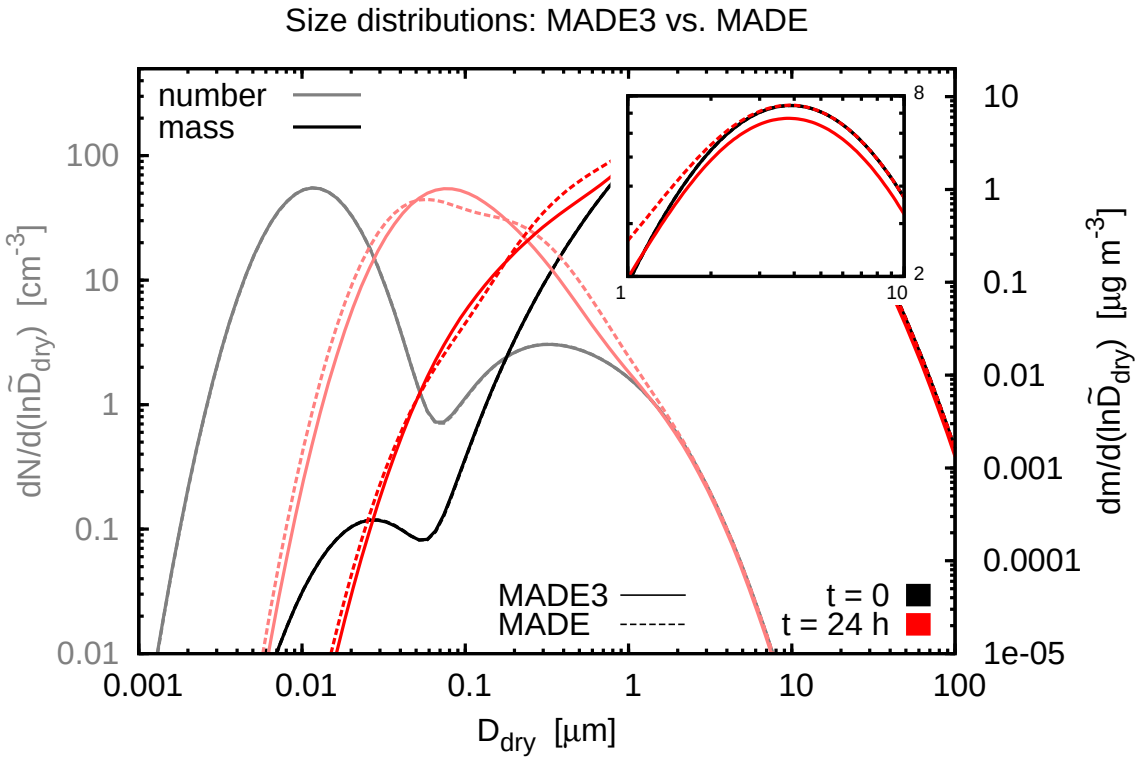

Figure 4.2: Initial (gray, black) and final (light red, red) size distributions in MADE3 and MADE vs. dry diameter (i.e., neglecting aerosol water). Light colors (gray, light red) are used for number distributions (left vertical axis), full colors (black, red) for dry mass distributions (right vertical axis). MADE3 output is shown as solid lines, MADE output as dashed lines. The inset magnifies the coarse mode dry mass size distributions. Note that the initial ($t = 0$) size distributions are identical.

scenario. It was switched on in a sensitivity experiment in MADE, where a NPF event was detected after ∼3 h of simulated time. The number and mass size distributions of these nucleated particles as simulated by MADE were added to the initial aerosol state for all three (sub)models. Subsequently, NPF was switched off again and the simulations were rerun. Differences in the 24 h number and mass size distributions between these and the original simulations were negligible for all (sub)models. Hence, it can be assumed that the atmospheric processing of nucleated particles is adequately treated by MADE3, i.e., growth by condensation and removal by coagulation with larger particles are properly represented.

Since some processes are treated by stochastic approaches in PartMC-MOSAIC the model was run ten times and the averages of aerosol mass and number concentrations across the ensemble of simulations were calculated. This procedure ensures that the discussion does not focus on an "outlier" and allows for the quantification of uncertainties.

4.4 Results: MADE3 vs. MADE

4.4.1 Size distributions

Number and dry mass size distributions in MADE3 and MADE at the beginning and at the end of the 24 h simulation are plotted vs. dry diameter in Fig. 4.2. Dry quantities are calculated from all aerosol components except water. Although water constitutes the largest fraction of the aerosol mass (see Fig. 4.3), the dry representation was chosen here because the large H_2O mass masks finer features in the size distribution. As aerosol water content is diagnosed

from the composition of the dry aerosol anyway, no essential information is lost from the size distributions when neglecting H_2O here. Deviations in the size distributions after 24 h in Fig. 4.2 are small and can be explained by the new features of MADE3 as follows.

In the fine particle size range the 24 h MADE number size distribution displays a bimodal shape, which is not visible in the corresponding MADE3 distribution. This difference is due to different overlaps of the initial Aitken and accumulation modes in the two submodels, which leads to a stronger convergence of median mode diameters in MADE3 than in MADE. For the initial MADE Aitken (accumulation) mode the species mass and number concentrations of the initial MADE3 Aitken (accumulation) modes were summed up. The associated mixing of particles in MADE leads to greater median diameters for both modes with respect to the median diameters of the soluble Aitken and accumulation modes in MADE3. These soluble modes overlap more strongly during the first hours of the simulation than the Aitken and the accumulation mode in MADE. Hence, more particles are renamed (Sect. 3.2.5) from the Aitken mode to the accumulation mode in MADE3 during that time and the accumulation mode is thus shifted towards smaller diameters. The renaming stops when the number concentration of accumulation mode particles surpasses that of the Aitken mode (Sect. 3.2.5). This happens after about 14 h and after about 18 h of simulated time in MADE3 and MADE, respectively. Subsequently, the Aitken mode particles grow towards the accumulation modes by condensation. As this growth begins earlier in the MADE3 simulation than in the MADE simulation the associated convergence of median diameters is more pronounced there.

In the coarse mode size range the difference in the 24 h mass size distributions is due to the inclusion of the HCl/Cl equilibrium in MADE3. As the gas phase is initialized without HCl (Sect. 4.3), equilibration requires that some of the Cl initially evaporates from the particles (Fig. 4.3). This reduction in Cl is responsible for the coarse mode particles' mass loss in MADE3 with respect to MADE.

4.4.2 Composition

The temporal evolution of total aerosol species mass concentrations in MADE3 and MADE is plotted in Fig. 4.3. In both MADE3 and MADE the aerosol components DU, BC, particulate organic matter (POM) (below 0.001 $\mu g\,m^{-3}$ in this simulation), and Na (as part of the sea spray tracer in MADE) always remain in the condensed phase. Since particle mass sinks other than evaporation are neglected in the test case scenario, the results for these tracers are therefore identical. SO_4 formation is faster in MADE3 than in MADE due to the inclusion of H_2SO_4 condensation on the coarse mode particles. The most significant differences are seen in the Cl, H_2O, NH_4, and NO_3 evolutions, where the Cl deviation was already described at the end of the previous subsection and the loss of H_2O in MADE3 is due to the loss of Cl.

The NH_4 uptake in MADE3 in the beginning of the simulation is coupled to SO_4 uptake into the soluble Aitken mode particles. This process also occurs in the soluble accumulation mode, but only after sodium nitrate ($NaNO_3$) has been completely displaced by sodium sulfate (Na_2SO_4) ($\sim$600 min; note that no Na is present in the Aitken modes in the test case discussed here). In EQSAM (Sect. 3.2.1) sodium ions and sulfate are neutralized first. NO_3 therefore evaporates from the soluble accumulation mode particles because of the condensation of H_2SO_4 and subsequent replacement of $NaNO_3$ by Na_2SO_4. When sulfate can no longer be neutralized by Na_2SO_4 formation alone it becomes available for neutralization by ammonium, leading to uptake of the latter into the particles. This transition is visible as the kink in the MADE3 NH_4 curve ($\sim$600 min). The same applies to the MADE Aitken and accumulation modes (see kink at $\sim$300 min) but proceeds faster because coarse mode particles are not a sink for the semi-volatile gases in MADE. This missing sink is also the reason for the second kink in the MADE NH_4 evolution. As all the H_2SO_4 condenses on the fine mode particles in MADE they eventually enter the sulfate rich regime ($\sim$1050 min). From this point on sulfate ions can

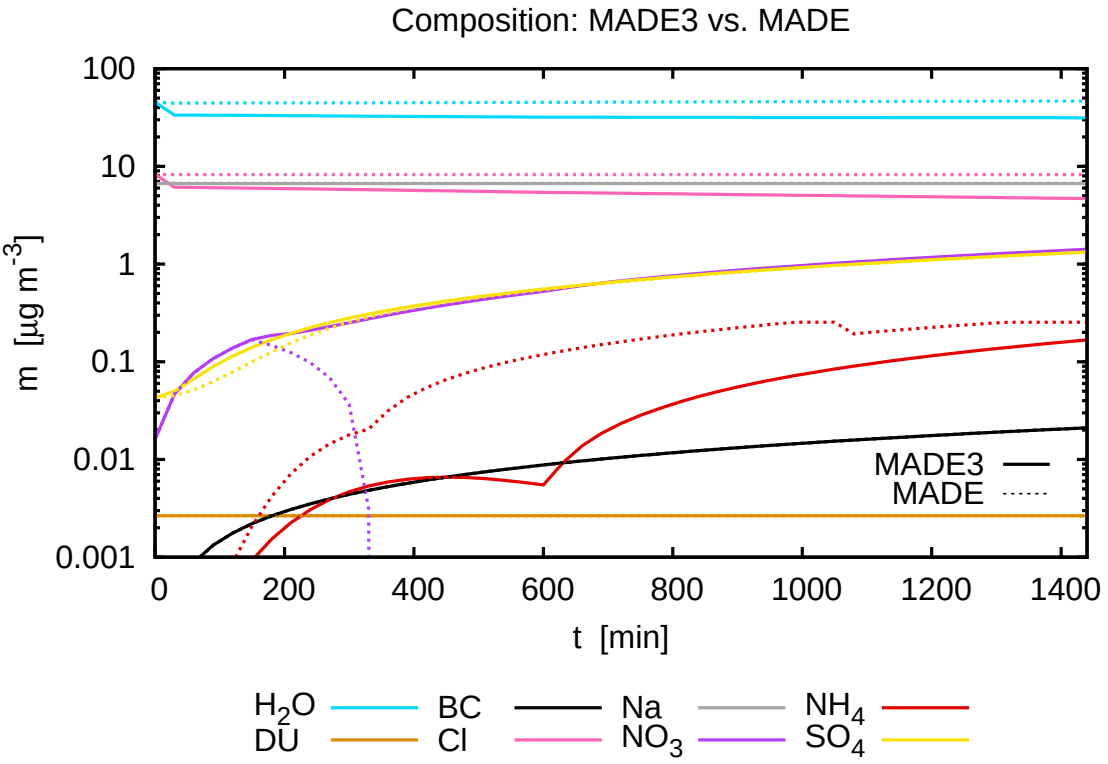

Figure 4.3: Temporal evolution of total aerosol species mass concentrations in MADE3 (solid lines) and MADE (dotted lines). Note that the particulate organic matter (POM) concentration is below $0.001\,\mu g\,m^{-3}$ and therefore does not appear in the plot.

bind less ammonium ions because EQSAM then assumes that sulfate exists in the forms of ammonium sulfate ($(NH_4)_2SO_4$), letovicite ($(NH_4)_3H(SO_4)_2$), and ammonium hydrogen sulfate (NH_4HSO_4) in the aerosol, whereas only $(NH_4)_2SO_4$ is considered in the sulfate neutral and sulfate poor regimes.

NO_3 is taken up by the coarse mode sea spray particles in MADE3 via $NaNO_3$ formation despite the loss from the soluble accumulation mode. MADE, however, cannot represent this process because it considers coarse mode particles as passive and only a small amount of sea spray is present in the accumulation mode size range in this test case scenario. Hence, aerosol NO_3 content increases continuously in MADE3, whereas this component is completely removed from the MADE aerosol. The initial NO_3 uptake is due to condensation of HNO_3, which is available more quickly than H_2SO_4.

4.5 Results: MADE3 vs. PartMC-MOSAIC

4.5.1 Size distributions

In analogy to Sect. 4.4.1, the size distributions calculated by MADE3 and PartMC-MOSAIC are compared first (Fig. 4.4). Note that the PartMC-MOSAIC results are averaged over ten model runs, but the variability is less than the size of the crosses in the figure. Only at the large-diameter and small-diameter limits of the size distributions as shown here is the variability higher because of the very few available computational particles.

In the coarse mode size range ($\gtrsim 1\,\mu m$ here) the 24 h distributions of the two models agree very well. The disagreement between MADE3 and PartMC-MOSAIC in the Aitken mode size range exposes a weakness of the modal approach with fixed mode widths. The Aitken mode

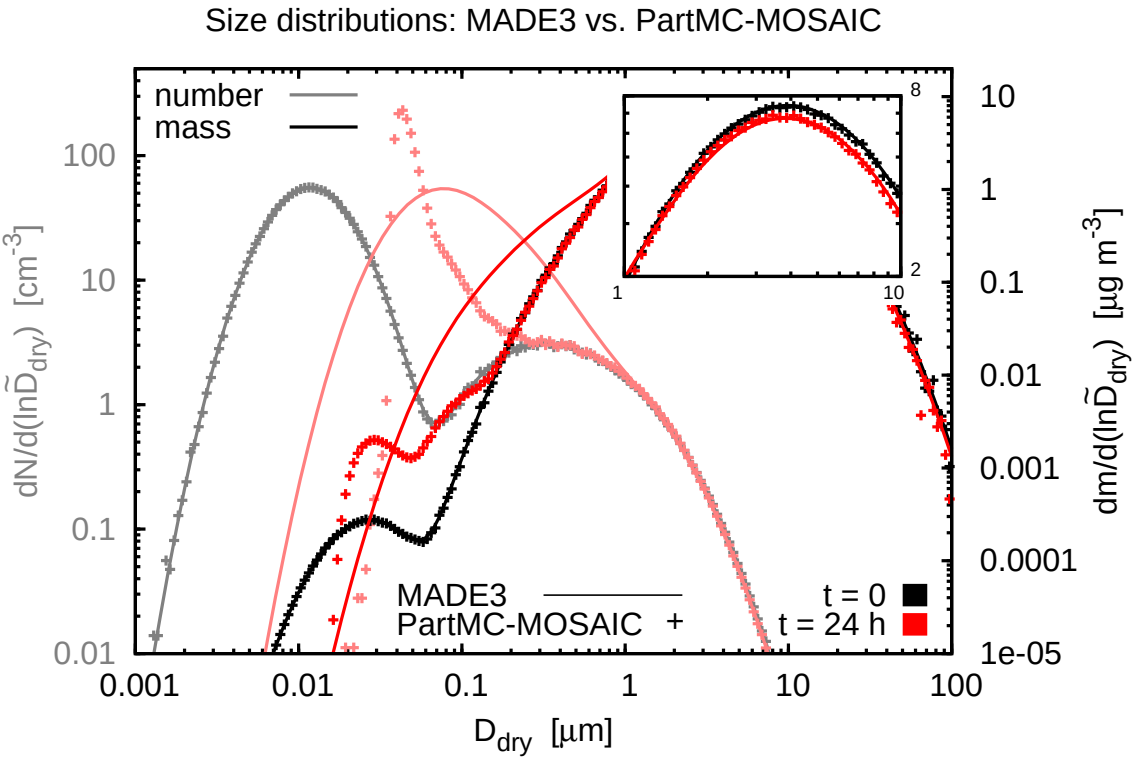

Figure 4.4: Same as Fig. 4.2, but for MADE3 (solid lines) vs. PartMC-MOSAIC (crosses) instead of vs. MADE.

becomes very narrow over the course of the PartMC-MOSAIC simulation. However, such narrowing cannot be simulated by MADE3, as the widths of its modes remain constant. The fast growth of the smallest particles (and slower growth of the larger Aitken mode particles) by condensation, for instance, can thus not be captured as accurately in MADE3. The 24 h MADE3 size distribution therefore contains more particles of very small diameters than the corresponding PartMC-MOSAIC distribution.

Furthermore, although total number and mass concentrations of freshly emitted BC particles are the same in both models, the size distributions upon emission are different. PartMC-MOSAIC can use the original distributions from the emissions dataset as given in Table 4.2 (see the "shoulder" to the right of the sharp peak in the 24 h number size distribution in Fig. 4.4). In MADE3 the particles are added to the wider modes, so that their contribution to the number size distribution cannot be distinguished in Fig. 4.4. In addition, particle aging (Sect. 3.2.6) contributes to the less pronounced Aitken mode peak in MADE3. When the emitted Aitken mode BC particles acquire a coating that surpasses the mass threshold of 10 % they are transferred to the mixed Aitken and accumulation modes. This leads to an increase of the median diameter of the mixed Aitken mode and to a reduction of the median diameter of the mixed accumulation mode. Hence, the two modes are no longer separately visible in the total number size distribution.

Quicker growth of soluble Aitken mode particles in terms of both mass and diameter further adds to the shift of the peak in the MADE3 number size distribution with respect to the PartMC-MOSAIC distribution. That growth is due to water uptake on these particles that is predicted by EQSAM (Sect. 3.2.1), but not by MOSAIC. Hence, some of the particles are renamed (Sect. 3.2.5) from the soluble Aitken to the soluble accumulation mode, so that the median (dry) diameter of the soluble accumulation mode is reduced. The latter mode thus also contributes to the wide peak in the MADE3 number size distribution.

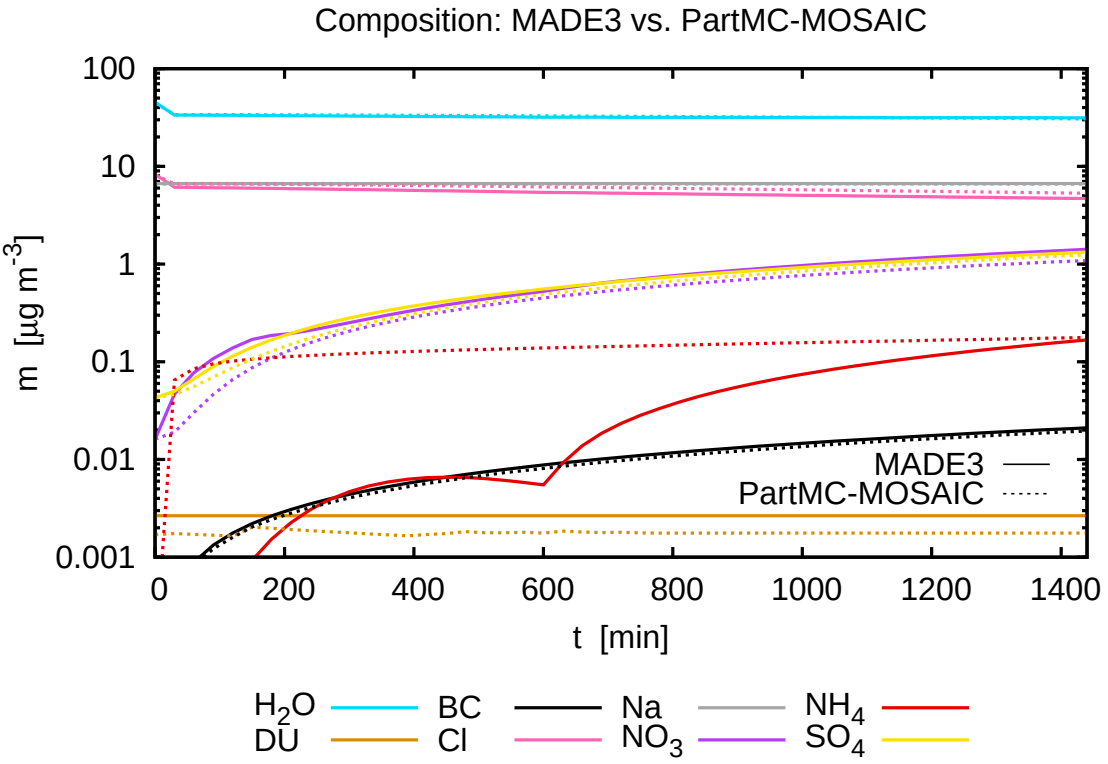

Figure 4.5: Same as Fig. 4.3, but for MADE3 (solid lines) vs. PartMC-MOSAIC (dotted lines) instead of vs. MADE.

In conclusion, there are potentially significant differences between MADE3 and PartMC-MOSAIC in the size ranges of the fine particles. Such deviations had to be expected due to the simplifications and restrictions that come with the modal approach to represent particle size distributions. Despite these differences, simulation results with both models agree well in the coarse mode size range (see also next subsection and the size-resolved composition plots in Appendix A.1). This indicates that the coarse mode particle interactions that were newly introduced in MADE3 are properly represented. Furthermore, the comparison of the 3-D simulation results with MADE3 to observations (Chap. 6) does not indicate that the MADE3–PartMC-MOSAIC deviation in the fine modes that is seen in the present test setup can be generalized.

4.5.2 Composition

The evolution of total species mass concentrations generally agrees well between MADE3 and PartMC-MOSAIC (Fig. 4.5). It should be noted that this agreement was achieved only after inclusion of the HCl/Cl equilibrium in EQSAM, which leads to the decrease in Cl concentration and to the associated reduction of aerosol water content as described in Sects. 4.4.1 and 4.4.2. The difference in the DU concentration is due to the very low number concentration of dust-containing particles. The stochastic nature of PartMC-MOSAIC thus leads to a relatively large spread of the DU concentrations in the ten simulations (not shown). Since the MADE3 result falls within the range of simulated values this deviation does not impair the overall agreement.

NO_3 is taken up more quickly in MADE3 than in PartMC-MOSAIC due to the assumption that equilibrium is attained during each time step. Note, however, that the flux limit described in Sect. 3.2.1 is never reached in the present test case scenario. In addition, there is more NO_3 partitioning to the condensed phase in MADE3 as it displaces Cl from the particles, leading to a slightly lower Cl content of the MADE3 aerosol. These differences can be explained by

the different chemistry codes. While MOSAIC allows for the coexistence of sodium chloride (NaCl) and $NaNO_3$ at arbitrary Na concentrations, NaCl can exist in EQSAM only when all the available nitrate has been bound to the sodium ions.

SO_4 uptake is slightly slower in PartMC-MOSAIC than in MADE3. As H_2SO_4 condensation is limited by gas phase diffusion, the difference is due to the different assumptions for the accommodation coefficient: $\alpha_{H_2SO_4} = 1$ in MADE3 and $\alpha_{H_2SO_4} = 0.1$ in PartMC-MOSAIC. Hence, the H_2SO_4 flux to the particles is greater in MADE3 than in PartMC-MOSAIC (see Eq. 3.6). This explanation was confirmed by a sensitivity simulation, in which $\alpha_{H_2SO_4}$ was set to 0.1 in MADE3.

The only qualitative difference between the two models in terms of composition evolution is in the NH_4 concentration. It is due to the different treatments of activity coefficients by EQSAM and MOSAIC (for details see Metzger et al., 2002; Zaveri et al., 2005b). While the activity coefficient in MOSAIC allows some condensed phase ammonium chloride (NH_4Cl) to be produced in the accumulation mode size range, EQSAM predicts that this compound will not form in the present test case scenario.

In MADE3 NH_4 partitions only to the fine mode particles because there are not enough anions available in the coarse modes to neutralize it. In the beginning of the simulation NH_4 is formed only in the smallest particles as $(NH_4)_2SO_4$. These particles eventually grow into the accumulation mode, where NO_3 is taken up as $NaNO_3$ because HNO_3 is available more quickly than H_2SO_4. However, Na_2SO_4 formed by H_2SO_4 condensation eventually displaces the $NaNO_3$ in the MADE3 accumulation mode particles. When all NO_3 has left these particles ($\sim$600 min) the additionally condensing SO_4 is available for $(NH_4)_2SO_4$ formation. Thus, the NH_4 concentration rises more quickly thereafter.

4.6 Summary and conclusions

Similar results were obtained in a box model setup with MADE3 and MADE for a MBL test case scenario, but there were differences especially in the coarse mode size range. When switching from MADE to MADE3 in EMAC less Cl and more NO_3 are expected in the aerosol particles on global average. The evaporation of some of the Cl to the gas phase (as HCl) may entail differences in aerosol water content if the lost particulate Cl is not fully replaced by NO_3. This, in turn, may affect the prediction of cloud condensation nuclei (CCN) concentrations and aerosol optical depth calculations. Total aerosol mass concentrations may also differ whenever sea spray particles dominate the aerosol mass concentration.

Good agreement between MADE3 and PartMC-MOSAIC was found in terms of total aerosol composition evolution and coarse mode particle size distribution predictions ($\gtrsim 1\,\mu m$), despite some potentially significant differences in the size distributions of fine particles. It is important to note that the particle size distribution is one of the main factors that govern the conversion of aerosol particles to cloud droplets. In the test case scenario presented here MADE3 results showed a particularly large deviation from the PartMC-MOSAIC results in the size range where this activation primarily takes place. However, as will be shown in Chap. 6, the 3-D model application of MADE3, i.e., the inclusion of the processes omitted here and the consideration of many different combinations of environmental parameters and aerosol population states, did not show a general deviation in this size range in comparison to observations. Thus, the conclusion here is that the comparison of MADE3 with PartMC-MOSAIC shows improvements in the representation of coarse mode aerosol particles and total aerosol composition w.r.t. MADE. As simulation results for the fine modes were very similar with MADE3 and MADE, the new submodel is expected to improve on MADE once implemented into a 3-D atmospheric model. This implementation is the subject of the next chapter.

Chapter 5

MADE3 in the atmospheric chemistry general circulation model EMAC

Besides the microphysics described in Chap. 3, a number of other processes are important for a comprehensive treatment of aerosol dynamics. In mathematical form these are expressed by the following equation:

$$\frac{\partial Y_k}{\partial t} = \underbrace{\dot{Y}_{\mathrm{emi},k}}_{\text{emissions}} \underbrace{+\frac{\partial}{\partial z}\left(\zeta \cdot \frac{\partial Y_k}{\partial z}\right)}_{\text{(vertical) diffusion}} \underbrace{-\nabla\left(\vec{v} \cdot Y_k\right)}_{\text{ad-/convection}} \underbrace{+Cld(Y_k)}_{\text{cloud processing}} \underbrace{-v_{\mathrm{d},k} \cdot \frac{\partial Y_k}{\partial z}}_{\text{dry deposition}} \underbrace{-v_{\mathrm{s},k}\frac{\partial Y_k}{\partial z}}_{\text{sedimentation}}, \tag{5.1}$$

where Y_k stands for either number concentration, N_k, or mass concentration of species a, $c_{a,k}$, in mode k. The symbols are as follows: $\dot{Y}_{\mathrm{emi},k}$ for the rate of particle or species mass emissions per unit volume (Sect. 5.2), z for the vertical spatial coordinate, ζ for a diffusion coefficient (Sect. 5.3), $\vec{v}$ for the 3-D wind field, Cld for the rate of change of aerosol concentrations due to in-cloud and precipitation processes (Sects. 5.6 and 5.7), $v_{\mathrm{d},k}$ for the dry deposition velocity (Sect. 5.8), and $v_{\mathrm{s},k}$ for the sedimentation velocity (Sect. 5.9). Note that almost all terms actually describe aerosol particle size-dependent processes and should therefore contain integrals over the size distribution. However, in (model) practice, they are all treated on a per-mode basis and are therefore also written in that way here.

To solve Eq. (5.1) the atmospheric chemistry general circulation model (AC-GCM) EMAC is applied in the present work. According to its website (`www.messy-interface.org`),

> "the ECHAM/MESSy Atmospheric Chemistry (EMAC) model is a numerical chemistry and climate simulation system that includes sub-models describing tropospheric and middle atmosphere processes and their interaction with oceans, land and human influences (Jöckel et al., 2010). It uses the second version of the Modular Earth Submodel System (MESSy2) to link multi-institutional computer codes. The core atmospheric model is the 5th generation European Centre Hamburg general circulation model (ECHAM5, Roeckner et al., 2006)."

ECHAM5 is used to calculate meteorological variables such as temperature, pressure, relative humidity (RH), and wind speed, as well as variables related to clouds and precipitation. In addition, a number of further submodels (Fig. 5.1 and Table 5.1) are used for the individual terms in the integration of Eq. (5.1). The equation is thus solved in an operator-splitting fashion. The numerics of this approach as well as the theory of discretization in space and time can be found elsewhere (Roeckner et al., 2003; Jöckel et al., 2005). Here, only the relevant individual operators are described, and an implementation-side view is adopted.

Although they are regarded as one particulate organic matter (POM) tracer in the MADE3-internal microphysical calculations, hydrophobic and hydrophilic POM are actually tracked separately when MADE3 is used within EMAC. As will be described in Sect. 5.2, some of the emitted POM is assumed to be hydrophobic. Its atmospheric aging is considered via a transformation into hydrophilic POM with an e-folding lifetime of 1 day (Lohmann et al., 1999) as in previous versions of the submodel.

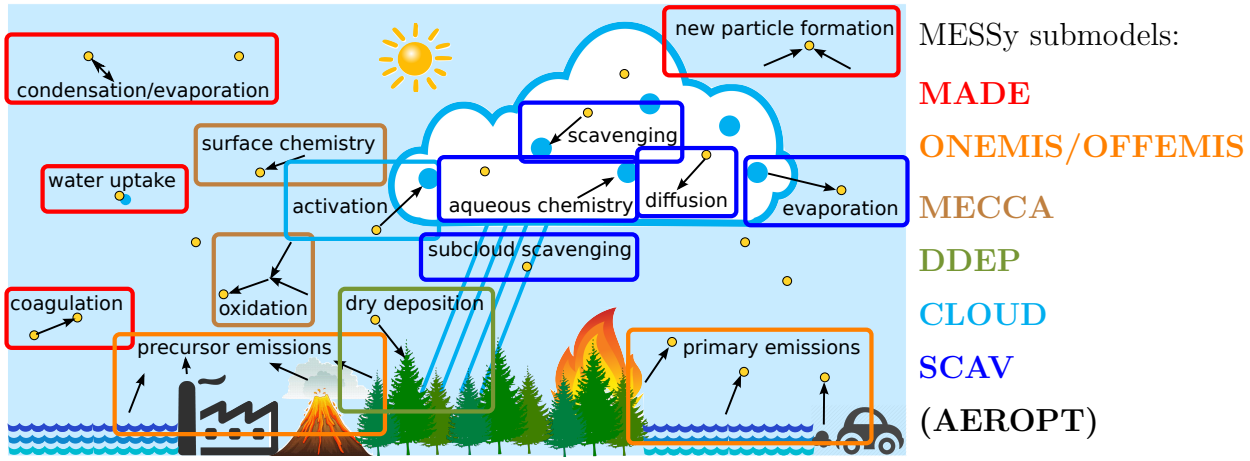

Figure 5.1: Processes relevant for aerosol dynamics in the atmosphere and MESSy submodels used for their description within EMAC. The submodel AEROPT is used to calculate aerosol optical properties. Note that the background image is the same as Fig. 2.2, i.e., it is adapted from Ghan & Schwartz (2007), their Fig. 1.

The basic settings of EMAC as used here, the emissions setup, the treatment of aerosol transport by the base model, and the main features of the relevant submodels that influence the aerosol distribution and composition are briefly described in the following sections. The last section of this chapter explains how optical properties of the atmospheric aerosol are calculated.

5.1 Basic settings

For the reference simulation discussed in Chaps. 6 and 7 a model setup is used that was designed by Righi et al. (2013). The setup was "translated" from the MESSy1 to the MESSy2 environment (version 1.4 to version 2.50) and updated where appropriate. The following quote is the second part of what the MESSy consortium requests to be included in each publication for which the MESSy framework is used (`www.messy-interface.org`).

> "For the present study EMAC (ECHAM5 version 5.3.02, MESSy version 2.50) was applied in the T42L19-resolution, i.e. with a spherical truncation of T42 (corresponding to a quadratic Gaussian grid of approx. 2.8 by 2.8 degrees in latitude and longitude) with 19 vertical hybrid pressure levels up to 10 hPa. The applied model setup comprised the submodels given in Tab. 5.1."

A model time step Δt of 30 min is used.

The simulations discussed here are so-called time slice experiments. Several years are simulated with different meteorology, but with identical values for the prescribed emissions, which are representative of a certain period. Thus, it is possible to simulate the variability of the atmospheric aerosol even without a dataset of transient emissions. Here, eleven years are simulated with emissions representative of the year 2000. The first year is regarded as the spin-up phase and the ten years that follow are actually evaluated. In all experiments, the model's meteorology is nudged towards ECMWF analyses for the years 1995 to 2005. Nudging means that an artificial "force" is applied that drives the model's meteorological variables towards observed values (Jeuken et al., 1996). For the simulations in the present work, wind divergence and vorticity, sea surface and land temperature, and surface pressure are nudged. This is done in order to reduce the amount of simulated time that is required to detect significant differences between the experiments. If the model was applied in free-running mode, i.e., without nudging,

Table 5.1: MESSy submodels used for the present work. Submodels of the type "prognostic" influence model dynamics, the "diagnostic" ones are only used for online calculation of output parameters.

Name	Function	Type	Reference(s)
AEROPT	aerosol optical properties	diagnostic	Lauer et al. (2007); Pozzer et al. (2012)
CLOUD	cloud and precipitation formation and evaporation	prognostic	Roeckner et al. (2006) and references therein
CONVECT	convective air movement	prognostic	Tost et al. (2006b)
CVTRANS	convective transport of trace gases and aerosols	prognostic	Tost (2006)
DDEP	dry deposition of trace gases and aerosols	prognostic	Kerkweg et al. (2006a, 2009)
H2O	consistency between water vapor as chemical species and humidity	prognostic	Jöckel et al. (2006)
JVAL	photolysis rate coefficients for trace gases	prognostic	Sander et al. (2014)
LNOX	lightning NO_x emissions	prognostic	Tost et al. (2007)
MADE3	aerosol microphysics	prognostic	Kaiser et al. (2014)
MECCA	gas phase chemistry	prognostic	Sander et al. (2011)
OFFEMIS	prescribed emissions	prognostic	Kerkweg et al. (2006b)
ONEMIS	online emissions	prognostic	Kerkweg et al. (2006b)
RAD	radiative processes	prognostic	Roeckner et al. (2006); Jöckel et al. (2006)
SCAV	cloud and precipitation processing of trace gases and aerosols	prognostic	Tost et al. (2006a)
SEDI	aerosol sedimentation	prognostic	Kerkweg et al. (2006a, 2009)
SURFACE	surface properties (e.g., temperature, snow depth, etc.)	prognostic	Jöckel et al. (2015)
TNUDGE	nudging of trace gas concentrations	prognostic	Kerkweg et al. (2006b)
TROPOP	tropopause height and planetary boundary layer height	diagnostic	Jöckel et al. (2006)

internal weather variability would generate much more noise that would obscure the signal in such comparisons, so that much longer computation times would be required.

Conditions at the lower atmospheric boundary are provided by data from the ECMWF. These include orography, the land-sea, glacier, and lake masks, as well as soil and vegetation data. Further data for the lower boundary are provided for the online emissions of dimethyl sulfide (DMS) from the sea surface (Sect. 5.2) and for the dry deposition calculations (Sect. 5.8). The production of reactive nitrogen oxides (NO_x) from lightning is calculated by the submodel LNOX (Tost et al., 2007), using a parameterization by Grewe et al. (2001), which is based on convective mass flux and the thickness of convective clouds.

For the upper boundary of the model domain a climatology of fluxes of nitrogen-containing species is applied in order to account for unresolved stratospheric chemistry (A. Lauer, pers. comm.). Furthermore, a climatology of HALOE data (Russell et al., 1993) is used to account for extinction of solar radiation by ozone (O_3) above the model domain when calculating photolysis rates for the troposphere.

Note that the only feedback of the aerosol on the atmosphere in the simulations discussed here is due to gas–aerosol partitioning in connection with cloud and gas phase chemistry. The mechanism for the latter is briefly described in Sect. 5.4. Clouds are predicted on the basis of meteorological and thermodynamic parameters only (Roeckner et al., 2003), i.e., without consideration of the aerosol simulated with MADE3. The radiative forcing of the atmosphere due to direct aerosol–radiation interactions is taken into account through a climatology of aerosol optical properties (Tanré et al., 1984). For the calculation of radiation-induced (thermo)dynamics, volume mixing ratios of radiatively active trace gases are specified either as constant throughout the atmosphere ([carbon dioxide (CO_2)] = 367 ppm, [methane (CH_4)] = 1750 ppm, and [nitrous oxide (N_2O)] = 316 ppb), as following constant vertical profiles (chlorofluorocarbons, values representative of the year 2000), or, in the case of O_3, from a climatology (Fortuin & Kelder, 1998).

5.2 Emissions

Emissions are differentiated into so-called "online" emissions that depend on model variables such as wind speed, and "offline" (or prescribed) emissions. The two types are handled in EMAC by the submodels ONEMIS and OFFEMIS.

In the present work ONEMIS is used for size-resolved, wind speed-dependent emissions of sea spray (SS) particle mass and numbers, and for wind speed- and sea surface temperature (SST)-dependent oceanic DMS emissions. These are added to the lowermost model layer. Wind speeds and SSTs are provided by the base model ECHAM5. The SS emissions parameterization is a combination of those by Monahan et al. (1986) and Smith & Harrison (1998), and was compiled and successfully evaluated by Guelle et al. (2001). Spada et al. (2013), in a comparative study on SS emissions parameterizations, also found reasonable agreement between observed SS concentrations and those modeled with a parameterization very similar to that by Guelle et al. (2001). Forty-five percent of the SS mass is assigned to the Na tracers, 55 % to the Cl tracers (Sect. 3.1.2). Oceanic DMS emissions are calculated according to a formulation by Liss & Merlivat (1986). Climatological near-surface sea water DMS concentrations (Lana et al., 2011) are used as an input to this parameterization.

Although online mineral dust (DU) emission schemes are also provided by ONEMIS, none of them could be applied for the present work because they are all resolution-dependent. The coarse representation of orography in a T42 grid leads to an intolerable overestimation of DU emissions in Asia as shown by Gläser et al. (2012). Furthermore, the resolution dependence can be exacerbated by the lack of consideration of sub-grid wind speed distributions (Ridley

et al., 2013) in the emission schemes provided by ONEMIS. Note that Ridley et al. (2013) do not find this to be problematic for SS emissions because wind speeds are less variable over the oceans than over land, and the source regions of SS are much more spread out than the very localized ones of DU. Hence, for DU, an offline emissions dataset of monthly mean values is used that was originally created for the AeroCom project (Textor et al., 2006). It was produced as described by Ginoux et al. (2001, 2004), using a model that was driven by year 2000 meteorology. DU emissions are added to the lowermost layer of the model atmosphere by the submodel OFFEMIS.

The AeroCom compilation (Dentener et al., 2006) is also used for annual mean volcanic sulfur emissions (based on the GEIA (Global Emissions IntitiAtive) database; Andres & Kasgnoc, 1998), and for P_{SOA} (Sect. 3.2.2), the monthly mean secondary organic aerosol (SOA) formation rate from natural emissions (also based on the GEIA database; Guenther et al., 1995). Volcanic emissions are assigned to multiple layers of the model atmosphere between 25 m and 4500 m. Thus, injection heights and the initial dispersion of the emitted sulfur dioxide (SO_2) and sulfate (SO_4) during the model time step are taken into account. The direct emission of SO_4 is a consequence of the relatively long time step compared to the time scale of new particle formation in volcanic plumes. Following Dentener et al. (2006), 2.5 % of the emitted SO_2 mass is assumed to be converted to particulate SO_4 "at emission", and the SO_2 emissions are split accordingly between the SO_2 and the SO_4 tracers. The SOA is distributed online among the aerosol modes in the lowermost model layer by MADE3, depending on the relative surface area concentrations of the modes (Sect. 3.2.2). Modeled and measured particle size distributions and number concentrations were shown to agree better when using this approach than when using a particle mass-proportional scheme (D'Andrea et al., 2013).

Further natural emissions considered here include monthly mean climatological terrestrial DMS emissions (Spiro et al., 1992) and the monthly mean biogenic production of carbon monoxide, methanol, and formic acid representative of the year 2000. The geographical distribution of the latter is based on the GEIA database (Guenther et al., 1995), while the values were scaled to match more recent estimates of the global totals (Bates et al., 1995; Kesselmeier et al., 1998; Jacob et al., 2005). All these natural emissions are added to the lowermost layer of the model atmosphere.

The basis for the anthropogenic emissions dataset used in the present work is the compilation by Lamarque et al. (2010) that was created in preparation of the 5$^{\mathrm{th}}$ IPCC assessment report. Year 2000 emissions of nitrogen oxide (NO), carbon monoxide (CO), SO_2, non-methane hydrocarbons, black carbon (BC), POM, and SO_4 are used (they are based on data from Andreae & Merlet, 2001; Christian et al., 2003; Endresen et al., 2003; Eyring et al., 2005; Kasischke et al., 2005; van der Werf et al., 2006; Heil, 2007; Wang et al., 2008; Eyring et al., 2010; Lee et al., 2010). Monthly mean values are provided for the aircraft (AIR), biomass burning (BB), and shipping (SHIP) sectors; for anthropogenic non-traffic (ANT), agricultural waste burning (AWB), and land transport (LAND) emissions only annual mean values are available. Except for AIR and ANT emissions, 2.5 % of the emitted SO_2 mass is again assumed to be converted to particulate SO_4 (Dentener et al., 2006) at emission, and the SO_2 emissions are scaled accordingly. In the case of AIR, a fraction of 2.2 % is applied instead of 2.5 %, because explicit measurements are now available from which this value can be derived (Jurkat et al., 2011). Note that AIR SO_2 emissions are not provided in the Lamarque et al. (2010) dataset. Instead, they were calculated as described by Righi et al. (2013), based on BC and SO_2 emission factors from Lee et al. (2010). For ANT "direct" SO_4 emissions are not considered at all.

The anthropogenic emissions from the surface are distributed among different model levels according to the profiles compiled by Pozzer et al. (2009), except for BB, where the vertical distribution is based on the recommendations in Dentener et al. (2006). The vertical distribution accounts for plume rise and dispersion effects that cannot be resolved with a time step of 30 min. Hence, LAND emissions are added to the model layer that contains the 45 m level,

AWB emissions to the one that contains the 140 m level, SHIP emissions are distributed between 45 m and 140 m, ANT emissions between 45 m and 800 m, and BB emissions between 50 m and 4500 m. AIR emissions are added between ∼300 m and ∼15000 m as prescribed in the Lamarque et al. (2010) dataset.

Emissions of the long-lived greenhouse gases CO_2 and CH_4 are implicitly considered by relaxing their near-surface mixing ratios to observed values for the year 2000 (based on data from the Advanced Global Atmospheric Gases Experiment (AGAGE) and the National Oceanic and Atmospheric Administration/Earth System Research Laboratory (NOAA/ESRL), as compiled by P. Graf). This task is fulfilled by the submodel TNUDGE.

Particle numbers, size distributions, and mixing states are usually not included in emissions datasets. Hence, typical mixing states and size distributions are assumed here in order to obtain number emissions from the mass data. Following Cooke et al. (1999) and Lohmann et al. (1999), 80 % of the emitted BC and 50 % of the emitted POM are assumed to be hydrophobic. The hydrophobic fraction of BC is assigned to the insoluble modes of MADE3, the hydrophilic fraction to the mixed modes. Hydrophobic POM goes into the soluble modes, but can only be activated into cloud droplets once it has been transformed to a hydrophilic state (see above and Sect. 5.6). Hydrophilic POM and SO_4 are distributed between the soluble and mixed modes. As for the study by Aquila et al. (2011), the fractions that are assigned to the mixed modes are determined by the mass required for a 5 % contribution of hydrophilic POM and SO_4 as a coating of the BC particles that are emitted into the mixed modes. Volcanic SO_4 is assigned exclusively to the soluble modes, as no insoluble particles from volcanic emissions are considered that would require a coating. The entire DU emissions are assigned to the insoluble modes, in which particles are assumed to be hydrophobic. SS emissions are assigned exclusively to the soluble modes.

Unless explicitly specified in the datasets, i.e., for all emissions except those of SS and DU, number emissions are derived from the mass emissions in analogy to the procedure employed by Righi et al. (2013). Inserting Eq. (3.3) into Eq. (2.3) individually for each mode k, i.e., $m(t) = c_k$ and $\rho = \rho_k$, and rearranging for the number concentration, N_k, one obtains:

$$N_k = \frac{6}{\pi} \cdot \frac{c_k}{\rho_k (D_{\mathrm{g},k})^3} \cdot e^{-\frac{9}{2}(\ln \sigma_k)^2}, \tag{5.2}$$

with the modal mass concentration $c_k = \sum_{e=1}^{E} c_{e,k}$ that is made up of the emitted species $e = 1, \ldots, E$; the modal geometric mean diameter, $D_{\mathrm{g},k}$; the modal geometric standard deviation, σ_k; and the average particle density in the mode,

$$\rho_k = \frac{c_k}{V_k} = \frac{\sum_{e=1}^{E} c_{e,k}}{\sum_{e=1}^{E} \frac{c_{e,k}}{\rho_e}}, \tag{5.3}$$

where V_k is the particle volume concentration in mode k (Eq. 3.2). Under the assumptions for the size distribution parameters given in Table 5.2 the number emissions can thus be computed from the species mass emissions. These number emission fluxes are then added to the corresponding MADE3 modes along with the mass emission fluxes from which they were derived.

5.3 Transport

Aerosol particle transport is computed by the tracer advection and vertical diffusion schemes of the base model ECHAM5 and by the convective transport submodel CVTRANS. Horizontal diffusion of particles is not considered in ECHAM5, but it is anyway not expected to contribute significantly to transport on the scales of the model grid boxes as used here. For advection the approach by Lin & Rood (1996) is applied, which is guaranteed to conserve mass and to be

Table 5.2: Size distributions assumed for emitted particles. $\frac{m}{m_{\text{tot}}}$ specifies the mass fraction provided by the respective mode. The "MADE3" columns contain the species and modes to which the emissions are assigned. For mode abbreviations see Table 3.2. The value "variable" in the mass fraction and median diameter columns indicates that both number and mass emissions are specified, so that number emissions do not have to be derived from the mass emissions. For anthropogenic emission sector abbreviations see text.

Sector	Mode 1				Mode 2				Reference(s)
	$\frac{m}{m_{\text{tot}}}$	D_{g} [nm]	σ	MADE3	$\frac{m}{m_{\text{tot}}}$	D_{g} [nm]	σ	MADE3	
Natural emissions									
Sea spray (online)	variable	variable	2.0	Na, Cl: as	variable	variable	2.2	Na, Cl: cs	(Guelle et al., 2001) + MADE3 σ_k
Mineral dust	variable	variable	1.59	DU: ai	variable	variable	2.0	DU: ci	Dentener et al. (2006)
Volcanic	0.5	30	1.8	SO_4: ks	0.5	80	1.8	SO_4: as	Dentener et al. (2006)
Anthropogenic emissions									
AIR	0.91	25	1.55	BC: ki, km SO_4: km, ks	0.09	150	1.65	BC: ai, am SO_4: am, as	Petzold et al. (1999), Righi et al. (2013)
ANT	1.0	30	1.8	BC: ki, km POM, SO_4: km, ks	—	—	—	—	Dentener et al. (2006)
AWB	1.0	80	1.8	BC: ai, am POM, SO_4: am, as	—	—	—	—	Dentener et al. (2006)
BB	1.0	80	1.8	BC: ai, am POM, SO_4: am, as	—	—	—	—	Dentener et al. (2006)
LAND	1.0	30	1.8	BC: ki, km POM, SO_4: km, ks	—	—	—	—	Dentener et al. (2006)
SHIP	0.8	70	1.45	BC: ki, km POM, SO_4: km, ks	0.2	260	1.25	BC: ai, am POM, SO_4: am, as	Righi et al. (2011)

numerically unconditionally stable. The code solves a time- and space-discretized version of the advection term in Eq. (5.1) using a first-order finite difference approach. CVTRANS couples the tracer fluxes to the convective air mass fluxes supplied by the submodel CONVECT for solving the convection term of Eq. (5.1). It is assumed that tracers travel with the air masses during convection events, i.e., tracer fluxes are directly proportional to air mass fluxes (Tost, 2006). Turbulent vertical transport outside convective plumes is parameterized as a diffusion process. The diffusion coefficient (ζ in Eq. 5.1) is derived from meteorological parameters such as the turbulent kinetic energy and atmospheric stability (Roeckner et al., 2003), where the latter is mainly influenced by the vertical profiles of temperature and humidity.

5.4 Gas phase chemistry

Reactions of the emitted trace gases are treated by the submodel MECCA here. For computational efficiency the simplified tropospheric chemistry scheme that was created by Lauer et al. (2007) is used. It includes 33 gases, 45 chemical reactions, and 13 photolysis reactions to describe NO_x-HO_x-CH_4-CO-O_3 chemistry and the tropospheric sulfur cycle. Reactive hydrogen oxides (HO_x), i.e., the hydroxyl (OH) and hydroperoxy (HO_2) radicals, as well as O_3, hydrogen peroxide (H_2O_2), and other oxidants are responsible for the conversion of the emitted NO_x and SO_2 into the condensable species nitric acid (HNO_3) and sulfuric acid (H_2SO_4). For details of the applied gas phase chemical mechanism see Appendix A.2. Reaction rates often depend on temperature, pressure, and RH, which are all provided by the base model ECHAM5. The photolysis rates are calculated by the submodel JVAL. Heterogeneous reactions, i.e., reactions of trace gases on or with aerosol particle surfaces, are not included. Note, however, that reactions on cloud droplet surfaces are included via the cloud phase chemistry (Sect. 5.6).

Volatile organic compounds (VOCs) can play an important role for the oxidative capacity of the atmosphere. Hence, neglecting their chemistry almost completely here by taking into account only species with one carbon atom might lead to systematic biases. For instance, reactions of the ozonolysis products of organic vapors, so-called Criegee intermediates, with SO_2 have been suggested as a source of additional H_2SO_4 in the atmosphere (e.g., Berndt et al., 2014, and references therein). Prior studies with MADE and MADE-in as part of EMAC, however, also relied on the simplified scheme used here and were able to reasonably reproduce observations. It is therefore not expected that the simplifications will strongly affect the results of the present work in that respect. This assumption is further corroborated by the findings presented by Pierce et al. (2013), who could not detect a significant contribution of Criegee intermediate–SO_2 reactions to the uncertainties in simulated cloud condensation nuclei (CCN) concentrations and the associated aerosol indirect effect.

5.5 Cloud formation

5.5.1 Stratiform clouds

The submodel CLOUD allows for the selection of different schemes to calculate the properties of stratiform, or large-scale, clouds. These schemes are of varying complexity, the main distinction being that between single-moment and two-moment schemes. The term “moment” here refers to the size distribution of cloud droplets and ice crystals. In single-moment schemes, only total cloud water or cloud ice content is predicted, while two-moment schemes also treat cloud droplet and/or ice crystal number concentrations prognostically. With the latter type of schemes the simulated aerosol particle number concentrations and sizes can be directly used as an input

to cloud formation calculations and to predict aerosol effects on cloud droplet or ice crystal number concentrations.

Although previous studies with the MADE3 predecessors were carried out with two-moment schemes, the standard ECHAM5 single-moment scheme was chosen for the present work. This is sufficient here, as no attempt is made to quantify the climatic impact of aerosol particles. Hence, an explicit representation of the influence of aerosol particles on cloud formation is not necessary. Furthermore, there is actually even an advantage to this method: it facilitates the detection of the aerosol response to perturbations in sensitivity experiments, as the feedback between such perturbations and cloud formation is eliminated.

The scheme used here predicts in-cloud water vapor, cloud liquid water content, cloud ice content, and fractional cloud cover per grid cell. Furthermore, many microphysical in-cloud processes are included, such as precipitation formation through autoconversion of cloud droplets or aggregation of ice crystals, evaporation or sublimation of cloud droplets or ice crystals and precipitation, accretion of cloud droplets or ice crystals by precipitation, etc. However, the scheme relies on meteorological and thermodynamic variables only; aerosol particles as simulated by MADE3 are not considered as CCN or ice nuclei (IN). A detailed description of this scheme was provided by Roeckner et al. (2003). One important difference w.r.t. this reference is the method how fractional cloud cover is determined. The simple parameterization developed by Sundqvist et al. (1989) is used here instead of the ECHAM5 default that is based on work by Tompkins (2002). Note that aerosol microphysical calculations with MADE3 are performed only for the cloud-free part of each grid box.

In the near future, but beyond the present work, the MADE3 aerosol will be coupled to a two-moment cloud scheme. This will allow for climate response calculations with the new submodel (Sect. 8).

5.5.2 Convective clouds

Convective clouds are parameterized in terms of their liquid and ice water content, precipitation, fractional cloud cover, and vertical transport of air and moisture. Such parameterizations are necessary because convection occurs on scales much smaller than the size of the grid boxes in T42 resolution (a few tens of kilometers vs. a few hundred kilometers), but it has important effects on the grid scale meteorology. The parameterizations are included and can be selected in EMAC via the submodel CONVECT. For the present work the choice fell on the original ECHAM5 scheme, which is based on work by Tiedtke (1989) and Nordeng (1994), with modifications by Brinkop & Sausen (1997). Details of the original implementation were described by Roeckner et al. (2003). The tracer transport associated with convection is calculated by the submodel CVTRANS (Sect. 5.3). As CONVECT does not provide any two-moment schemes for convection, aerosol effects on convective clouds cannot currently be considered in EMAC, except for radiative heating effects. These are not included in the setup used here, however (see Sects. 5.1 and 5.10).

5.6 Cloud and precipitation processing of the aerosol

Although the modeled aerosol is not considered to influence cloud formation in the present work, cloud and precipitation processing of the aerosol particles cannot be neglected. Chemical reactions in the aqueous phase can strongly affect aerosol composition when cloud droplets or hydrometeors evaporate. For instance, a major fraction of aerosol SO_4 can be produced via this pathway, and the chloride depletion described in Sect. 2.3.2 can also proceed via the aqueous phase. In the model setup for the present work, cloud and precipitation processing of the aerosol is treated by the submodel SCAV.

The uptake of aerosol particles by suspended cloud droplets or ice crystals or by precipitation is called scavenging. For both cloud droplets and ice crystals SCAV distinguishes between nucleation and impaction scavenging. In SCAV terminology, which is adopted for this and the following section, "nucleation scavenging" refers to both the actual nucleation of cloud droplets or ice crystals, and scavenging due to their Brownian motion. Nucleation is the most efficient uptake process for the largest aerosol particles, while Brownian motion dominates at the smallest sizes. The latter is currently not included in many global aerosol models, although it may have a substantial impact on particle number concentration of about 10 % and a large aerosol indirect radiative effect (RE) of about $1\,\mathrm{W\,m^{-2}}$ (Pierce et al., 2015). Impaction scavenging as defined by SCAV summarizes the processes through which aerosol particles are taken up by precipitation. These processes include Brownian motion of aerosol particles towards hydrometeors, impaction of hydrometeors upon aerosol particles, and interception of aerosol particles by hydrometeors. Impaction, in this context, describes the collection of aerosol particles by falling hydrometeors in the case that the inertia of the particles is so large that they cannot follow the air flow around the hydrometeors. If aerosol particles do follow that flow, but are large enough to still be captured by the hydrometeors, the process is called interception. Again, Brownian motion is most efficient for the smallest aerosol particles, while interception and impaction are dominant for the largest ones. Both nucleation scavenging and impaction scavenging therefore have minimum efficiencies at intermediate aerosol particle sizes, i.e., for large Aitken and small accumulation mode particles.

In contrast to the procedure in SCAV as described by Tost et al. (2006a), the sequence of operations in the SCAV version distributed with MESSy version 2.50 is:

1. ice nucleation scavenging,
2. liquid nucleation scavenging,
3. snow impaction scavenging,
4. rain impaction scavenging.

The applied algorithms are briefly described in the following paragraphs. For details the reader is referred to the original article by Tost et al. (2006a). Both the liquid nucleation and the rain impaction scavenging operators include an explicit treatment of liquid phase chemistry. The mechanism selected for the present work consists of 35 chemical species and 45 reactions. Heterogeneous processes like the formation of aqueous HNO_3 from gaseous dinitrogen pentoxide (N_2O_5) on droplet surfaces are also considered here. Further details can be found in Appendix A.3.

For ice nucleation scavenging a very simple approach is used in SCAV. If the ambient temperature, which is calculated by the base model ECHAM5, exceeds 238.15 K, a uniform scavenging rate of $\eta_{\mathrm{inu},k} = 0.1/\Delta t$ is applied to mass and number concentrations for all modes k ($k = 1, \ldots, 9$; Δt is the model time step). Below this temperature $\eta_{\mathrm{inu},k}$ is reduced to $0.05/\Delta t$ for aerosol particles in the soluble modes ($k \in \{1, 4, 7\}$, corresponding to "ks", "as", and "cs"; Table 3.2), while for the others it remains at $0.1/\Delta t$ ($k \in \{2, 3, 5, 6, 8, 9\}$, corresponding to "km", "ki", "am", "ai", "cm", and "ci"). Note that hydrophobic POM, which is contained in the soluble modes, is treated differently, and is also assigned $\eta_{\mathrm{inu}} = 0.1/\Delta t$ below $T = 238.15\,\mathrm{K}$. Summing up, one obtains:

$$\eta_{\mathrm{inu},k} = \begin{cases} \frac{0.1}{\Delta t} & \text{for } T > 238.15\,\mathrm{K}, \quad \forall\, k, \\ \frac{0.1}{\Delta t} & \text{for } T < 238.15\,\mathrm{K}, \quad k \in \{2, 3, 5, 6, 8, 9\}, \quad \text{and POM in } k \in \{1, 4, 7\}, \\ \frac{0.05}{\Delta t} & \text{otherwise,} \end{cases} \tag{5.4}$$

which is analogous to the treatment described by Aquila et al. (2011). The distinction of different particle types below 238.15 K is a MADE(-in)-specific feature and was kept for MADE3.

Note that even particles of the same type from different environments can display different ice nucleation behavior (Wex et al., 2014). However, such a level of detail is beyond the limits of the present work.

As stated above, liquid nucleation scavenging as defined by SCAV includes both the actual nucleation of cloud droplets, and the Brownian motion scavenging of aerosol particles by suspended cloud droplets. Actual nucleation is taken into account via an empirical function that is applied to the hydrophilic fraction of the soluble and mixed modes, i.e., to the fraction of particles that allows for hygroscopic growth. The fraction of these hydrophilic particles scavenged by nucleation per unit time, $\eta_{\mathrm{lnu},k}^{\mathrm{nuc}}$ (with $k \in \{1,2,4,5,7,8\}$, corresponding to "ks", "km", "as", "am", "cs", and "cm"; Table 3.2), is assumed to have a sigmoidal shape as a function of aerosol particle diameter (Tost et al., 2006a):

$$\eta_{\mathrm{lnu},k}^{\mathrm{nuc}} = \frac{2}{\pi \cdot \Delta t} \cdot \arctan\left(\left[2.5 \cdot \tilde{D}_{\mathrm{g},k}\right]^6\right), \tag{5.5}$$

with the dimensionless diameter $\tilde{D}_{\mathrm{g},k}$ (measured in µm as described in Sect. 2.3.3). For Brownian motion a semi-empirical formulation of the scavenging coefficient by Pruppacher & Klett (1997) is used, which leads to a scavenging rate of

$$\eta_{\mathrm{lnu},k}^{\mathrm{Br}} = \frac{1 - e^{-\frac{1.35 \cdot LWC \cdot \Delta_{\mathrm{p},k}}{r_{\mathrm{cld}}^2} \cdot \Delta t}}{\Delta t}. \tag{5.6}$$

Here, LWC is the cloud liquid water content (mass per unit volume) as computed by CLOUD and CONVECT (Sect. 5.5), and r_{cld} is the effective cloud droplet radius, which is set constant at $r_{\mathrm{cld}} = 17.5\,\mu\mathrm{m}$. The aerosol particle diffusivity $\Delta_{\mathrm{p},k}$ is computed as

$$\Delta_{\mathrm{p},k} = \frac{k_{\mathrm{B}} \cdot T \cdot s_k}{3 \cdot \pi \cdot \nu \cdot D_{\mathrm{g},k}}. \tag{5.7}$$

The factor

$$s_k = 1 + \left(2.514 + 0.8 \cdot e^{-0.55 \cdot \frac{D_{\mathrm{g},k}}{\lambda_{\mathrm{air}}}}\right) \cdot \frac{\lambda_{\mathrm{air}}}{D_{\mathrm{g},k}} \tag{5.8}$$

is known as the "slip correction". Note that SCAV uses its own functions to calculate the mean free path of air, λ_{air}, and the atmospheric dynamic viscosity, ν. While the λ_{air} formulation differs only slightly from that used in MADE3 (Eq. 3.16), ν is computed from another function: $\nu = 1.8274 \cdot 10^{-5}\,\mathrm{Pa\,s} \cdot (T/293.15\,\mathrm{K})^{0.74}$. Combining the two scavenging rates (Eqs. 5.5 and 5.6) one arrives at the total liquid nucleation scavenged fraction for mode k per unit time:

$$\eta_{\mathrm{lnu},k} = \eta_{\mathrm{lnu},k}^{\mathrm{nuc}} + \eta_{\mathrm{lnu},k}^{\mathrm{Br}} - \eta_{\mathrm{lnu},k}^{\mathrm{nuc}} \cdot \eta_{\mathrm{lnu},k}^{\mathrm{Br}}. \tag{5.9}$$

The negative term accounts for the fact that aerosol particles cannot be scavenged at the same time by both nucleation and Brownian motion.

Snow impaction scavenging is again parameterized in a very simple way in SCAV: the scavenging rate is given as

$$\eta_{\mathrm{sim},k} = \frac{1 - e^{-360\,\mathrm{m^2\,s\,kg^{-1}} \cdot F_{\mathrm{s}}}}{\Delta t}, \tag{5.10}$$

with the snow mass flux F_{s} per unit area and time, which is provided by CLOUD and CONVECT (Sect. 5.5) for large-scale and convective precipitation, respectively. The rate coefficient $\eta_{\mathrm{sim},k}$ is applied to all modes ($k = 1, \ldots, 9$).

Finally, the rain impaction scavenging rate is assumed to be

$$\eta_{\mathrm{rim},k} = \frac{1 - e^{-0.75 \cdot F_{\mathrm{r}} \cdot \Delta t \cdot \sum_{i=1}^{6} \frac{W_i \cdot E_{k,i}}{r_{\mathrm{r},i}}}}{\Delta t}, \tag{5.11}$$

where F_r is the rain mass flux per unit area and time, also provided by CLOUD and CONVECT. The terms $W_i \cdot E_{k,i}/r_{r,i}$ are computed for six different values of the rain droplet radius $r_{r,i}$ ($i = 1, \ldots, 6$), namely for 0.1 mm, 0.2 mm, 0.5 mm, 1 mm, 2 mm and 5 mm. $E_{k,i}$ is the collision efficiency of aerosol particles of size $D_{g,k}$ and rain droplets of size $r_{r,i}$ as parameterized by Slinn (1984), with weights W_i based on the rain droplet radii $r_{r,i}$. Compared to measurements, $E_{k,i}$ is likely underestimated for fine mode aerosol particles, which is a problem of any theoretically derived formulation for this parameter (Wang et al., 2010). As for snow impaction scavenging, the rain impaction scavenging rate is also applied to all MADE3 modes ($k = 1, \ldots, 9$).

The SCAV code had to be modified for use with MADE3, especially the redistribution routines for aerosol mass and numbers among the different modes upon evaporation or sublimation of cloud droplets or ice crystals and precipitation. The submodel had been designed to work with MADE and another aerosol submodel called GMXe (cf. Sect. 2.3.4). Both these submodels include fewer modes than MADE3, and the assumptions on their water uptake properties are different. Hence, as part of the present work, a completely new scheme was designed and implemented to redistribute the residuals among the aerosol modes when precipitation or suspended cloud droplets or ice crystals evaporate or sublimate. This process plays a key role in the simulation of the 3-D aerosol concentrations field, as it is also triggered at the end of each time step if a cloud persists. Since in-cloud droplet and in-ice crystal aerosol concentrations are not tracked separately from the interstitial ones in EMAC, this "pseudo-evaporation" cannot be avoided. For the assumptions, logic, and mathematics underlying the implemented residual assignment scheme see Appendix A.4. Briefly summarized, it takes into account scavenging of multiple aerosol particles per cloud droplet, ice crystal, or hydrometeor; formation or loss of aerosol mass within or from the cloud droplets or ice crystals; and coagulation of cloud droplets or ice crystals.

5.7 Wet deposition

Wet deposition, i.e., the removal of aerosol particles (and trace gases) from the atmosphere with precipitation, is also computed by the submodel SCAV. Any aerosol (and trace gas) that is not released from the hydrometeors either via equilibration with the gas phase or via evaporation of the hydrometeors, is deposited, i.e., it is subtracted from the atmospheric concentrations. The fractions of aerosol particles thus removed per unit time derive directly from the scavenging rates given in the previous section (Eqs. 5.4, 5.9, 5.10, and 5.11) under consideration of the precipitation formation rates supplied by the submodels CLOUD and CONVECT (Sect. 5.5).

5.8 Dry deposition

In addition to scavenging by precipitation, aerosol particles (and trace gases) can also be removed from the atmosphere when they are transported close to the earth's surface. The main processes that contribute to this so-called dry deposition are turbulence, diffusion, and uptake by the surface or canopy (Hicks et al., 1987). In the model configuration used here dry deposition is handled by the submodel DDEP, which uses the so-called "big leaf" approach. Details of the surface structure are neglected in this approach, and only a few different surface types are distinguished. DDEP takes into account six types, namely water, ice, snow, bare soil, vegetation, and wet skin, i.e., the wetted parts of bare soil and vegetation (Kerkweg et al., 2006b). In the present setup vegetation parameters required for the calculations (leaf area index, canopy height, drag coefficient, and soil pH value) are drawn from a climatology compiled by L. Ganzeveld (pers. comm.).

The basic concept of the big leaf approach is to define a proportionality factor $v_{\mathrm{d},k}$, called the deposition velocity (for mode k; see also Eq. 5.1), such that

$$F_{\mathrm{d},a,k} = v_{\mathrm{d},k} \cdot c_{\mathrm{s},a,k}. \tag{5.12}$$

Here, $F_{\mathrm{d},a,k}$ is the dry deposition flux of species a in mode k (in units of $\mathrm{kg\,m^{-2}\,s^{-1}}$), and $c_{\mathrm{s},a,k}$ the corresponding concentration in the atmosphere near the surface. The dry deposition flux for aerosol particle numbers is defined in the same way. In analogy to electrical circuits, a resistance model is used to describe the contributions by the individual processes to dry deposition:

$$v_{\mathrm{d},k} = \frac{1}{R_{\mathrm{ady}} + R_{\mathrm{qlb},k} + R_{\mathrm{srf},k}}. \tag{5.13}$$

If the dry deposition flux is taken as analogous to the electric current and the concentration as analogous to the electric potential, the "conductance" $v_{\mathrm{d},k}$ can be derived from the series of "resistances" R_{ady}, $R_{\mathrm{qlb},k}$, and $R_{\mathrm{srf},k}$. These are called the aerodynamic, quasi-laminar boundary layer, and surface resistance, respectively, and they describe the contributions to dry deposition by turbulence, diffusion, and surface uptake.

The formulation in Eq. (5.13) was originally developed for trace gases. For aerosol particles the terms that depend on particle size, i.e., $R_{\mathrm{qlb},k}$ and $R_{\mathrm{srf},k}$, are usually combined into one resistance, as they cannot be easily separated. The aerodynamic resistance, R_{ady}, only depends on atmospheric conditions such as wind speed and boundary layer height, which are provided by the base model ECHAM5, and on the surface type (climatological values, see above). For the particle property-dependent resistances, DDEP uses modal aerosol densities and size distributions as computed by MADE3. A detailed description of how the various terms that make up the dry deposition velocity are calculated in DDEP was provided by Kerkweg et al. (2006a, 2009).

5.9 Sedimentation

Sedimentation, or gravitational settling, of aerosol particles can also lead to their removal from the atmosphere, especially in case of coarse mode particles. In the present work the associated aerosol concentration tendencies are calculated by the submodel SEDI. At the core of this calculation is the sedimentation velocity $v_{\mathrm{s},k}$ (for mode k, see also Eq. 5.1), which is deduced from Stokes' law of friction (Kerkweg et al., 2006a):

$$v_{\mathrm{s},k} = \frac{g}{18 \cdot \nu} \cdot (\rho_k - \rho_{\mathrm{air}}) \cdot s_k \cdot (D_{\mathrm{g},k})^2 \cdot \begin{cases} e^{2(\ln \sigma_k)^2} & \text{for number concentrations,} \\ e^{8(\ln \sigma_k)^2} & \text{for mass concentrations.} \end{cases} \tag{5.14}$$

Here, $g = 9.80665\,\mathrm{m\,s^{-2}}$ is the earth's gravitational acceleration; ν the atmospheric dynamic viscosity, calculated using yet another parameterization than those of MADE3 and SCAV, namely

$$\nu = \begin{cases} (1.718 + 0.0049 \cdot (T - 273.15\,\mathrm{K})) \cdot 10^{-5}\,\mathrm{Pa\,s} \text{ for } T \geq 273.15\,\mathrm{K} \\ (1.718 + 0.0049 \cdot (T - 273.15\,\mathrm{K}) - 1.2 \cdot 10^{-5} \cdot (T - 273.15\,\mathrm{K})^2) \cdot 10^{-5}\,\mathrm{Pa\,s} \text{ otherwise;} \end{cases} \tag{5.15}$$

ρ_{air} the density of air; and s_k the slip correction factor defined in Eq. (5.8). The exponentials stem from the averaging of the sedimentation velocity over each mode w.r.t. number and mass, respectively. SEDI uses the same input parameters from MADE3 as DDEP, namely the average density, ρ_k, and the size distribution parameters $D_{\mathrm{g},k}$ and σ_k for each mode.

The fraction of particles within a grid box that reaches the box below, or the ground in case of surface layer boxes, is determined from the distance that the particles can fall at the

sedimentation velocity within one time step. The ratio of this distance to the vertical extent of the grid box directly yields the fraction of the aerosol that is transferred to the next-lower model level, or removed from the atmospheric concentration when it reaches the surface.

5.10 Optical properties

The submodel AEROPT (Pozzer et al., 2012), which is based on the concept and code developed within MADE by Lauer et al. (2007), is used to calculate aerosol optical properties. Its output includes the following three parameters that are typically encountered in the description of aerosol particle interactions with radiation.

1. The **extinction cross section**, C_{ext}, measures which fraction of the incoming radiation intensity a particle intercepts at a given wavelength. It can be integrated over all particles and the whole atmospheric column to obtain the aerosol optical depth (AOD), which is evaluated against observations in Sect. 6.2.4.

2. The **single scattering albedo**, ω, is the fraction of the extinction cross section that is due to scattering rather than absorption.

3. The **asymmetry parameter**, γ_{asy}, describes how much intensity is scattered into which direction. It ranges from -1 to 1, where $\gamma_{\text{asy}} = -1$ means pure backward scattering and $\gamma_{\text{asy}} = 1$ means pure forward scattering. For aerosol particles that are small w.r.t. the dominant wavelengths of solar radiation, forward and backward scattering are of similar magnitude ($\gamma_{\text{asy}} \approx 0$), while less intensity is scattered into the transversal directions. For larger particles ($\gtrsim 1\,\mu\text{m}$), γ_{asy} will be close to -1.

All these quantities depend on particle size, wavelength, and particle complex refractive index, ε. Particle size, D_{p}, and wavelength, λ can be combined into one parameter, namely the Mie size parameter $y = \pi D_{\text{p}}/\lambda$. AEROPT uses pre-calculated lookup tables that contain C_{ext}, ω, and γ_{asy} as a function of y_k, $Re(\varepsilon_k)$, and $Im(\varepsilon_k)$, i.e., the Mie size parameter for the median diameter of mode k and the real and imaginary parts of the complex refractive index of particles in mode k. The pre-calculations were originally performed by A. Lauer and T. Zinner with the software libRadtran (Mayer & Kylling, 2005). They are based on Mie theory, i.e., the theory of scattering for spherical particles of sizes that are in the range of the wavelength of the radiation ($y \sim 1$). Lognormal aerosol particle size distributions of the widths σ_k (Table 3.1) were assumed for the lookup table calculations. Note that Scarnato et al. (2015) and Sorribas et al. (2015) found that optical properties cannot always be accurately estimated under the assumption of sphericity, and morphology also plays a role, especially in case of DU particles. However, there is currently no possibility to include such effects in the AEROPT calculations.

The real and imaginary parts of the complex refractive index and their wavelength dependence are tabulated for a number of different species classes. Following Ouimette & Flagan (1982), it is assumed that the refractive index of particles in each mode can be computed as the volume average over the chemical components of that mode. The six components considered for this purpose in AEROPT as used here are (together with references for their refractive indices):

- water soluble inorganic aerosol (Hess et al., 1998), i.e., the SO_4, ammonium (NH_4), and nitrate (NO_3) tracers in this work,
- black carbon (Hess et al., 1998), i.e., the BC tracer in this work,
- particulate organic matter (Sutherland & Khanna, 1991; Hess et al., 1998; Kirchstetter et al., 2004), i.e., the POM tracer in this work,

- mineral dust (Hess et al., 1998), i.e., the DU tracer in this work,
- sea spray (Shettle & Fenn, 1979, I. Sokolik), i.e., the sodium (Na) and chloride (Cl) tracers in this work, and
- aerosol water (Hale & Querry, 1973), i.e., the water (H_2O) tracer in this work.

Input parameters to AEROPT, i.e., particle size and composition, are provided by MADE3.

Absorption and scattering of radiation by BC-containing aerosol particles depend on particle mixing state (Sect. 2.1.3). The volume averaging in the calculation of the particles' complex refractive indices as done in AEROPT includes the implicit assumption of homogeneous mixtures of the particles' chemical components. Thus, the contribution of BC to AOD might be overestimated in the present work, but it appears that this effect is not significant (Klingmüller et al., 2014).

In the future, the output of AEROPT will be used as input to the radiation submodel RAD in order to simulate also the aerosol feedback on radiation. The above-mentioned effects of BC mixing state might also be included then. However, in the present work, aerosol optical properties are a purely diagnostic quantity, and they are derived as in previous studies with MADE and MADE-in.

Chapter 6

Evaluation of simulated tropospheric aerosol properties

MADE3 is evaluated as the aerosol microphysics submodel of EMAC by comparison of model output to observational data. The setup described in Chap. 5 is used for this purpose. After a brief summary of important considerations on the issue of data comparability in the first section, the second section of this chapter contains the standard evaluation that is usually performed for new or updated global aerosol (sub)models (e.g., for MADE and MADE-in: Lauer et al., 2005; Aquila et al., 2011; Righi et al., 2013). This evaluation was done with the help of the ESMValTool (Eyring et al., 2015), which was also used to create the corresponding figures. A third section is dedicated to the comparison of the MADE3 simulation with a corresponding MADE simulation. Besides that, a new type of evaluation that also addresses the new representation of coarse mode microphysics and chemistry in MADE3 was developed as part of the present work. It is presented together with a first application in the fourth section.

Note that much more simulation data and other data representations are available than what is shown in this chapter. The choice of the subset discussed here is motivated by the availability and format of observational data that can be used for evaluation. Further figures that complement the ones in this chapter towards a full description of the year 2000 aerosol in the present MADE3 reference simulation are given in Appendix A.5.

6.1 Data comparability

A number of issues have to be considered when comparing model output to observational data. This section gives a general overview of the most important points in the context of the present work. Limitations specific to the individual comparisons are stated within the corresponding subsections.

Due to the coarse spatial resolution model data necessarily reflects an average over large areas and volumes. Hence, urban–rural concentration differences as presented by Putaud et al. (2010) and Hand et al. (2014), for instance, cannot be resolved here. Emissions in the model are also far more spread-out than in the real atmosphere, so that measurements near emission sources cannot be straightforwardly used for model evaluation. As far as possible, the following evaluation therefore relies on measurements that can be regarded as representative of areas or volumes that are comparable to the resolved scales of the model.

The temporal resolution of the simulation output is 12 h. This could lead to biases w.r.t. observations in case of strong diurnal cycles of aerosol concentrations or properties. Typical tropospheric residence times of most aerosol species, however, are of the order of days. Hence, potential biases should be small.

Regular measurements within station networks provide both spatial and temporal data coverage that is well-suited for evaluation of atmospheric chemistry general circulation models (AC-GCMs). Currently, however, these measurements are limited to near-surface concentrations or column-integral properties such as the aerosol optical depth (AOD). A 3-D evaluation therefore requires the use of additional datasets, which can be obtained from aircraft measurement campaigns. Of course, such campaigns cannot provide the same spatial and temporal

coverage as the station networks. Rather, they typically cover only limited time spans or regions. The value of aircraft measurement data for the model evaluation as performed here therefore increases with the number of available datasets.

Another important consideration is that of the correspondence between observed and modeled microphysical and chemical aerosol properties. Most measurement methods are only sensitive to a certain part of the atmospherically relevant particle size spectrum. Specifically, the focus of measurements has been on fine mode particles until now, i.e., on particles up to diameters of $\sim$2.5 µm. This has to be taken into account when comparing "total" aerosol (species) mass and number concentrations.

In addition, there is often not a one-to-one correspondence between modeled and measured aerosol species. The MADE3 particulate organic matter (POM) tracer mass, for instance, includes the total organic aerosol mass, whereas measurement data often only contains the organic carbon (OC) mass, i.e., only the contribution of carbon atoms to the total organic aerosol mass. Another prominent issue in this context is related to measurements of '*"black carbon", "soot", "elemental carbon", "equivalent black carbon" and "refractory black carbon"* [which] *synonymously refer to the most refractory and light-absorbing component of carbonaceous combustion particles*' (Petzold et al., 2013). Different and partially inconsistent terminology has been, and is, used in the corresponding literature, so that a proper comparison of modeled black carbon (BC) with measurement data is difficult. The confusion that this inconsistent terminology has created is evident in the online discussion on the manuscript submitted by Buseck et al. (2012), and it was also documented by Bond & Bergstrom (2006) and by Petzold et al. (2013).

Finally, some measurements may be inherently biased due to the method of particle sampling. According to Ames & Malm (2001), for instance, fine mode nitrate (NO_3) may be underestimated in one station network (CASTNET), while it could be overestimated in another (IMPROVE). The author is not aware of other species for which known measurement biases are as large as for NO_3, however.

6.2 The MADE3 aerosol within EMAC

This section is organized as follows. First, simulated aerosol particle mass concentrations are evaluated as completely as possible, i.e., they are compared to near-surface measurements from four different station networks (Sect. 6.2.1) and to vertical profiles from aircraft measurements (Sect. 6.2.2). Particle number concentrations are also evaluated against measured vertical profiles (Sect. 6.2.2) and against airborne as well as ground-based size distribution measurements (Sect. 6.2.3). Subsequently, as an aerosol measure derived from the 3-D particle concentrations, composition, and size distributions, AOD is compared to satellite measurements and station network data (Sect. 6.2.4). In the fifth subsection global burdens of the simulated aerosol particle species are presented along with the species' tropospheric residence times. Although this is not part of the evaluation in a strict sense because these quantities cannot be observed, it is interesting to compare the results to those obtained with other models.

Note that the current section is mostly descriptive and only gives some possible reasons for discrepancies between simulations and observations. A thorough investigation of these discrepancies would require a large number of sensitivity simulations. Although beyond the scope of the present work it should be conducted as part of future studies, also for quantification of simulation uncertainties.

6.2.1 Near-surface mass concentrations

Ten-year average simulated near-surface mass concentrations are compared here to the averages of available observational data in the period 1996 to 2005 from the following station networks:

the Interagency Monitoring of Protected Visual Environments network (IMPROVE, Hand et al., 2011)[1] and the Clean Air Status and Trends Network (CASTNET, AMEC Environment & Infrastructure, Inc., 2015)[2] in the USA, the European Monitoring and Evaluation Programme network (EMEP, Hjellbrekke, 2014)[3], and the acid deposition monitoring network in East Asia (EANET, Network Center for EANET, 2014)[4]. The simulation data discussed here is always the sum of the contributions from all modes in the lowermost model layer, i.e., up to ∼100 m. The comparison provides an indication of the model's ability to reproduce the climatological state of the northern hemisphere continental aerosol, where emissions are highest. As the emissions dataset is assumed to represent year 2000 conditions (Sect. 5.2), the period for the observational data was chosen symmetric to the year 2000. Note, however, that most of the stations (across networks) do not provide complete temporal coverage of the years 1996 to 2005, which may lead to biases. Specifically, all EANET data that went into the comparison stems from the years after 2000. EMEP and EANET have fewer stations and can thus provide less data than IMPROVE and CASTNET (see Table 6.1).

Some further general aspects have to be considered when comparing the simulated near-surface mass concentrations to the measured ones. There will inevitably be discrepancies, partly also caused outside the aerosol microphysics submodel. For instance, the simplified gas phase chemistry may lead to inaccuracies in the aerosol precursor species. Furthermore, the simulated boundary layer height does not necessarily match the conditions during the measurements. It can strongly influence near-surface concentrations, as it controls the volume that is available for dispersion of the emitted species. Orography is another factor that may lead to mismatches. As orography is also averaged over the entire grid boxes, stations at high altitudes may not be well represented. They may be located in the free troposphere, while the model would simulate them as belonging to the boundary layer.

Concentrations of the secondary inorganic aerosol species SO_4, NH_4, and nitrate (NO_3) are the most widely measured and typically have the longest records. For other species data coverage is less comprehensive (see Table 6.1). This subsection is ordered accordingly: the secondary species are discussed first, the (mostly) primary aerosol components thereafter.

The geographical distribution of near-surface SO_4 concentrations (Fig. 6.1) is well reproduced over Europe and East Asia, albeit with a general high bias. Over the USA, agreement between modeled and measured concentrations is better in the east than in the northwest. Hence, the model does not fully capture the west–east gradient seen in the observations. Apart from this discrepancy and the general high bias, however, the spatial SO_4 distribution over the USA is also reproduced well. The relative overestimation of near-surface SO_4 concentrations is notably higher w.r.t. IMPROVE than compared to the other networks (Table 6.1). As Ames & Malm (2001) do not find systematic differences in SO_4 concentrations between co-located IMPROVE and CASTNET measurements, a possible reason for this difference lies in the locations of the IMPROVE stations. SO_4 concentrations are most severely overestimated (in relative terms) in the northwestern part of the USA (Fig. 6.1), where most of the stations used in the comparison are IMPROVE stations. Note that these stations are mostly located in national parks and wilderness areas, i.e., in rather clean environments.

Observed values of NH_4 concentrations are spatially more heterogeneous than those of SO_4 concentrations, down to scales that cannot be captured by the coarse resolution of the model. Furthermore, emissions of NH_4 precursors are much more uncertain and variable than those of SO_4 precursors. That said, model performance is generally similar for NH_4 as for SO_4 (Fig. 6.1). This also means that the west–east gradient over the USA is again underestimated. Note that in case of NH_4 most IMPROVE stations from which data is available for the comparison are

[1] `http://views.cira.colostate.edu/web/DataWizard/`
[2] `http://epa.gov/castnet/javaweb/index.html`
[3] `http://ebas.nilu.no`
[4] `http://ebas.nilu.no`

Table 6.1: Statistical summary of the simulation–observations comparison of monthly mean near-surface concentrations from the reference simulation with MADE3 in EMAC by station network and species. $\langle OBS \rangle$ ($\langle MOD \rangle$) stands for the arithmetic mean over all data points of the observations (simulation), σ_{obs} (σ_{mod}) for the standard deviation, $fac2$ for the percentage of simulated values that are within a factor of two of the corresponding observational values, and N_{pts} for the number of data points, i.e., monthly averages, that went into the comparison. Scatter plots of modeled vs. observed data can be found in Appendix A.6.

Species	$\langle OBS \rangle$ [µg m^{-3}]	σ_{obs} [µg m^{-3}]	$\langle MOD \rangle$ [µg m^{-3}]	σ_{mod} [µg m^{-3}]	$\langle OBS \rangle / \langle MOD \rangle$	$fac2$ [%]	N_{pts}
IMPROVE							
sulfate (SO_4)	1.61	1.72	3.27	2.23	2.04	36.6	13162
ammonium (NH_4)	1.16	0.56	1.69	0.57	1.45	75.2	609
NO_3	0.50	0.75	0.95	0.84	1.92	38.3	13162
sodium (Na)	0.09	0.16	0.87	1.53	9.65	11.7	12658
chloride (Cl)	0.10	0.20	0.44	1.11	4.63	17.3	11471
POM	1.72	2.01	2.18	1.88	1.27	65.2	13106
BC	0.27	0.27	0.30	0.32	1.12	68.3	13106
CASTNET							
SO_4	3.15	2.38	4.42	2.70	1.40	71.6	8215
NH_4	1.10	0.77	1.60	0.77	1.45	64.7	8215
NO_3	0.87	1.07	1.22	0.94	1.40	45.9	8215
Na	0.18	0.35	0.61	1.02	3.45	29.7	5391
Cl	0.18	0.70	0.29	0.72	1.59	23.7	2256
EMEP							
SO_4	2.25	1.70	3.45	2.24	1.54	68.5	9039
NH_4	0.96	0.91	1.62	1.06	1.70	52.9	3466
NO_3	1.63	1.82	1.60	1.39	0.99	53.4	3654
Na	0.55	0.65	2.59	2.08	4.67	11.1	1563
Cl	1.34	4.32	1.78	1.74	1.33	22.7	1044
EANET							
SO_4	3.42	4.88	4.22	2.74	1.24	56.6	1276
NH_4	0.94	1.50	1.68	1.10	1.79	34.6	1256
NO_3	0.99	2.08	1.53	1.33	1.55	33.0	1247
Na	0.88	1.42	2.24	2.13	2.54	26.1	1164
Cl	1.15	2.26	1.55	1.80	1.35	24.6	1154

located in the eastern part of the USA, where agreement of the simulated concentrations with the observations is slightly better than in the west (see also Table 6.1). The north–south gradient over Europe is generally well captured, with the exception of Spain and the western Mediterranean.

The simulated near-surface NO_3 concentrations agree remarkably well with the observations across Europe (Fig. 6.1). With respect to the IMPROVE data for the USA it must be noted that several ten percent of the simulated NO_3 mass belong to the coarse modes. In contrast to CASTNET, however, IMPROVE stations analyze only particles up to a size of ∼2.6 µm (IMPROVE, 1995), so that substantial deviations have to be expected. The comparison of NO_3 concentrations to data from CASTNET and EANET yields similar results as for NH_4.

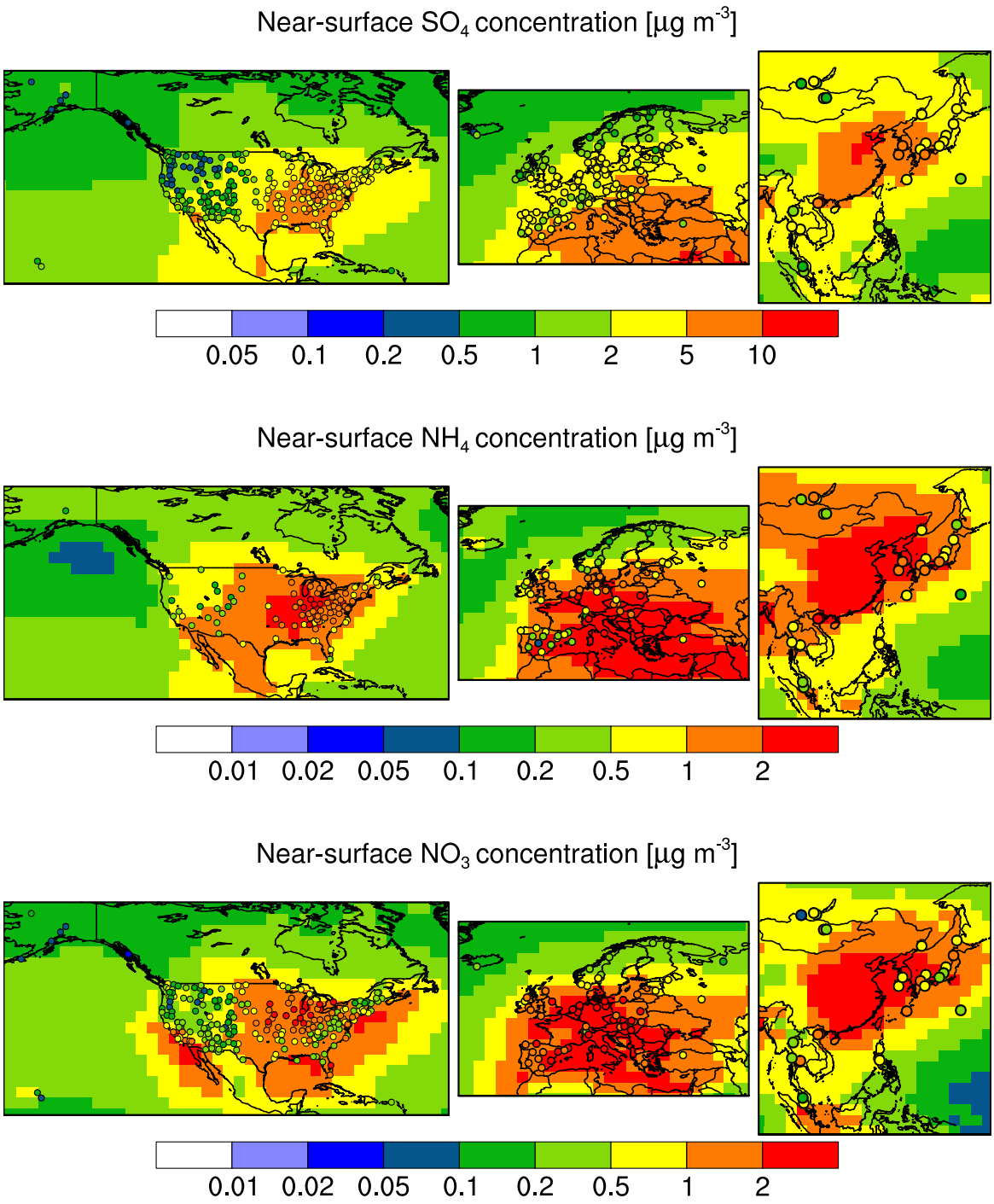

Figure 6.1: Reference simulation with MADE3 (background color; "pixels" correspond to the model grid) vs. observations from station networks (filled circles): near-surface secondary inorganic aerosol species mass concentrations, i.e., sulfate (SO_4, top), ammonium (NH_4, middle), and nitrate (NO_3, bottom). The observational data in the three panels of each row is drawn from CASTNET and IMPROVE (left), EMEP (middle), and EANET (right).

Variability in the simulation–observations agreement is higher for the sea spray (SS) components, i.e., for Na and Cl, than for the other aerosol species (Fig. 6.2; see also Table 6.1 and the scatter plots in Appendix A.6). The discrepancies between simulated and observed values are generally highest for these two components (Table 6.1). On average, Na and Cl concentrations are overestimated by the model w.r.t. the station network data. Partly, this may be due to the sharp land–sea gradients that cannot be accurately resolved by the model (Fig. 6.2), especially in the vicinity of islands with sizes similar to or smaller than those of the model grid boxes. It is also possible that the sea spray emissions parameterization leads to too high Na

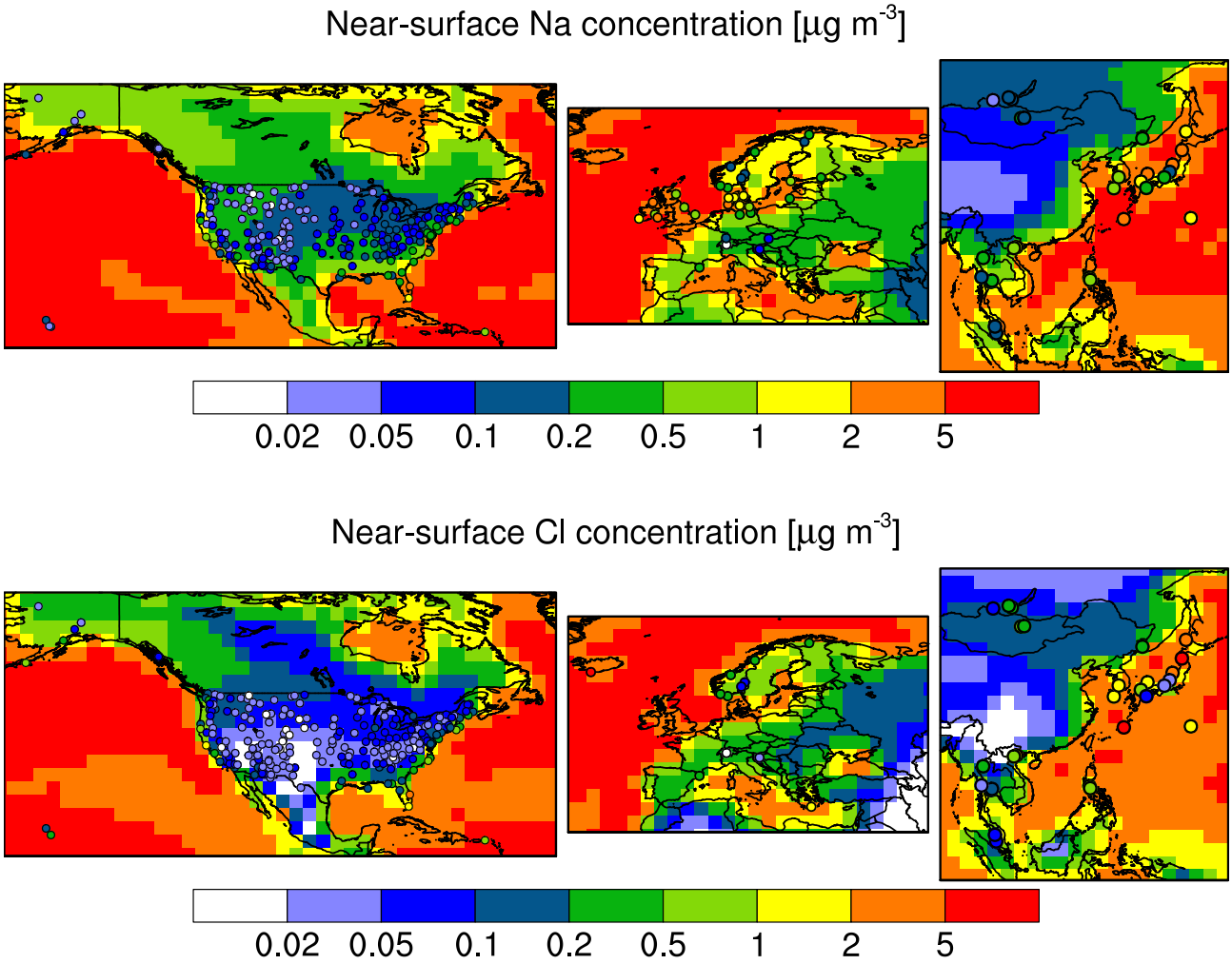

Figure 6.2: Same as Fig. 6.1, but for the sea spray aerosol components sodium (Na, top) and chloride (Cl, bottom).

and Cl concentrations in our model setup, possibly because it does not take into account the dependence of these emissions on sea surface temperatures (Jaeglé et al., 2011). However, as will be discussed in Sect. 6.2.5, the reason is probably more intricate and could have to do with underestimated deposition of fine mode particles in combination with overestimated deposition of coarse mode particles. The overestimation in near-surface concentration is less for Cl than for Na. This is likely due to the formation of gaseous hydrochloric acid (HCl) from aerosol Cl.

Mineral dust (DU) is not reported by any of the station networks discussed in the previous paragraphs. Nevertheless, near-surface DU concentration measurement data covering several months up to years is available from a number of independent stations and experiments. For the comparison here (Fig. 6.3) the dataset compiled by Huneeus et al. (2011) is used. Where the model simulates low concentrations it generally agrees well with the measurements, but it seems that the decrease in concentration with increasing distance from the sources is underestimated in some cases. However, it should be stressed again here that the DU emissions used in the simulation most likely do not represent the conditions during the measurements. Furthermore, large uncertainties are associated with the magnitude of the global DU cycle in general, due to differences in observational datasets, uncertainties in size distributions, and a strong dependence on meteorology (Albani et al., 2014). Especially the latter cannot be accurately represented with the prescribed monthly mean year 2000 DU emissions used here (Sect. 5.2).

Only IMPROVE stations routinely monitor carbonaceous aerosol components. Hence, the POM and BC simulation–observations comparison (Fig. 6.4) includes only data in the USA. Both the magnitude and the spatial distribution of simulated near-surface concentrations gen-

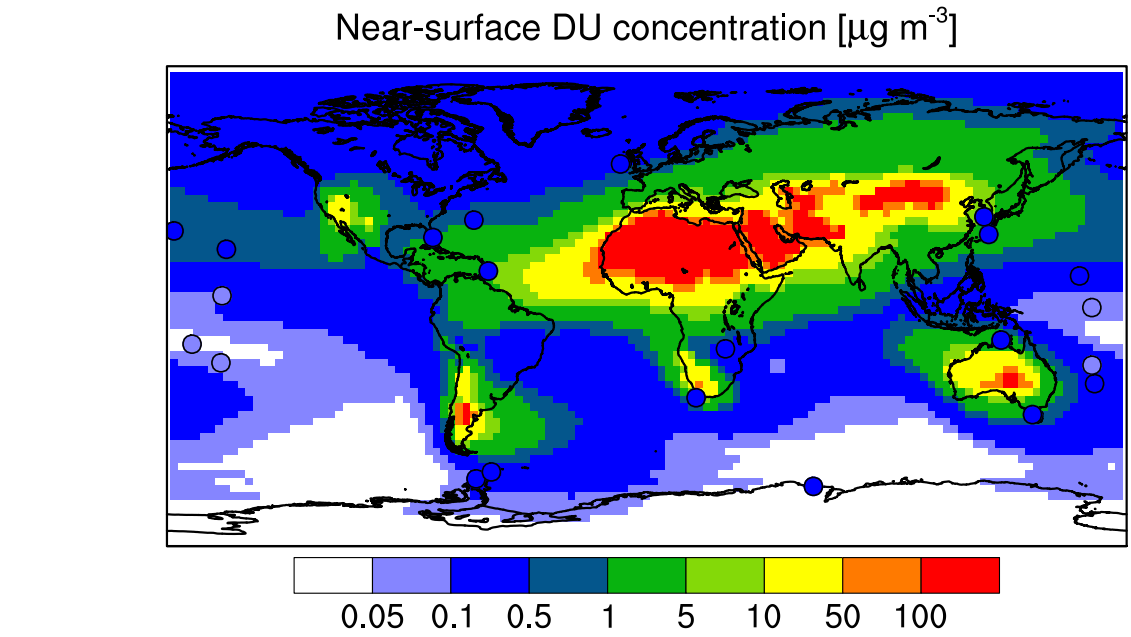

Figure 6.3: Reference simulation with MADE3 (background color; "pixels" correspond to the model grid) vs. observations from various long-term measurement campaigns (filled circles): near-surface mineral dust (DU) mass concentrations.

erally agree well with the observations. This was expected as the uncertainties associated with gas phase precursor chemistry and gas–particle partitioning do not affect these components in our simulations. On average, however, POM and BC concentrations are also overestimated by the model, albeit less than in the case of the species discussed above.

A comparison of simulated near-surface concentrations of various aerosol species to observations at high latitudes yields the same picture (not shown). Observational data for those regions is scarce, so that only a plausibility check could be performed. Simulated BC concentrations are similar to those measured over two years in North Greenland (as reported by Massling et al., 2015), while simulated SO_4 concentrations are roughly a factor of two higher than the measured ones. Total aerosol mass concentrations over Antarctica may be overestimated compared to measurements taken by Hara et al. (2014) during the austral summer 2007/2008.

In conclusion, a general high bias is seen in the simulation w.r.t. the observations (Table 6.1). This may indicate a too low efficiency of the deposition processes, which might also explain

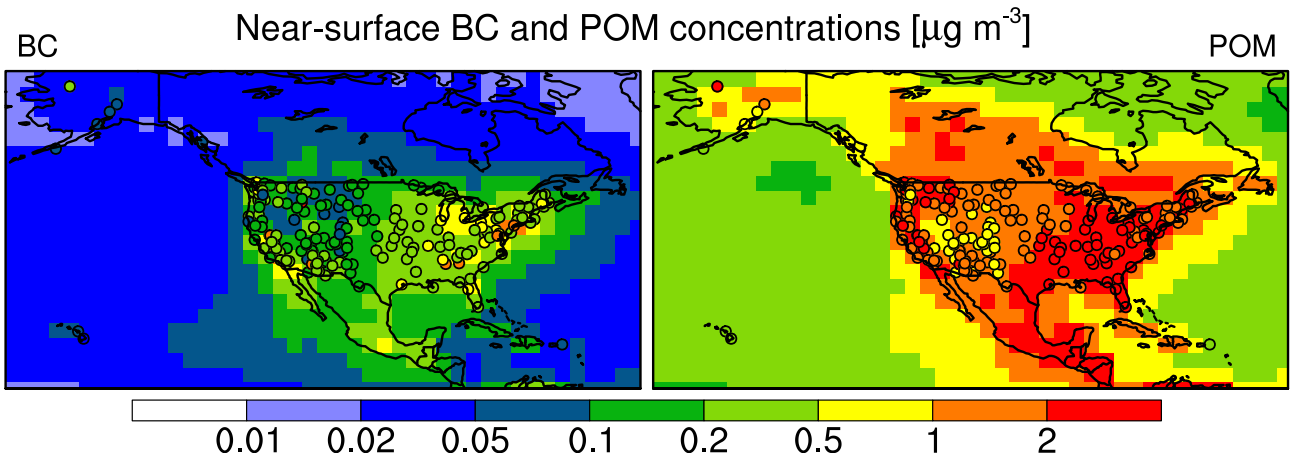

Figure 6.4: Reference simulation with MADE3 (background color; "pixels" correspond to the model grid) vs. observations from the station network IMPROVE (filled circles): near-surface black carbon (BC, left) and particulate organic matter (POM, right) mass concentrations.

some of the discrepancies discussed in the next subsection that deals with vertical profiles of BC and particle number concentrations. That the overestimation is generally larger for soluble components indicates that cloud processing may also play a role in the deviations. Note, however, that model performance is notably better when using MADE3 than when using MADE as the aerosol microphysics submodel (Sect. 6.3). Furthermore, the statistics of the comparison with IMPROVE data are very similar to those obtained with a previous EMAC version using MADE-in (Aquila et al., 2011). The only exception here is NO_3, which could not form on coarse mode particles in MADE-in, and therefore could not reach as high concentrations as in the present work. However, as mentioned above, the IMPROVE stations do not provide any insight into NO_3 concentrations associated with particles $\gtrsim$2.6 µm.

The general overestimation of near-surface mass concentrations found here is not typically seen in studies with other global aerosol models. Although (relative) discrepancies are often of similar magnitude, the deviations are typically more variable in their directions for different species (e.g., Bauer et al., 2008; Mann et al., 2010; Pozzer et al., 2012; Lee et al., 2015). Nevertheless, to simulate several ten percent of monthly mean values within a factor of two of observations indicates a quality of EMAC with MADE3 that is similar to that of other models (e.g., Pozzer et al., 2012; Kirkevåg et al., 2013). To the author's knowledge, percentages greater than 90 %, as achieved by Pozzer et al. (2012) for SO_4, have so far not been reached for multiple species in the same simulation. Furthermore, even the large discrepancies for the SS components that were found here are not unprecedented: similar deviations were reported by Lee et al. (2015).

6.2.2 Vertical distributions

It is even more delicate to evaluate the global 3-D aerosol distribution than to evaluate the 2-D near-surface distribution. In contrast to the multi-year time series of measurements provided by the (surface-bound) station networks, aircraft measurements can only sample the aerosol along a specific flight trajectory. Hence, the spatio-temporal data coverage is limited. Although arguably representative for the season and weather pattern during which the flight(s) took place, there is much more uncertainty associated with the comparison of climatological model output to aircraft measurements than with that to station network data. Nevertheless, aircraft campaigns provide a unique way to measure vertical aerosol concentration profiles. Hence, they are routinely used to evaluate the performance of global aerosol models in simulating the vertical aerosol distribution.

Here, the observational data is taken from campaigns between 1990 and 2011 over the Pacific Ocean, over North and South America, and over Europe, as summarized in Table 6.2. The datasets include BC and total aerosol mass mixing ratios (aerosol mass per unit mass of air; Fig. 6.5) as well as aerosol particle number concentrations (Fig. 6.6). Depending on what the individual dataset provides, either mean values and standard deviations, or medians and percentiles, or both are compared between simulation and observations. The variability of the measured data includes spatial and temporal concentration variations during and between the flights. The variability of the model output rather describes the concentration variations around a climatological state. Simulation output data was selected from the grid boxes that include the flight trajectories and from the time steps corresponding to the days or months of the year during which the flights took place. Model meteorology-induced variability turned out to be captured well even if only data for single days is extracted from each year of the simulation.

The general picture that emerges from the comparison of the mass mixing ratio profiles is similar to that from the near-surface concentrations comparison: in most cases the model is biased high. There is an interesting difference, however, between the profiles from individual campaigns and the more "climatological" data over the Pacific Ocean from the HIPPO project (including more than 700 profiles; Schwarz et al., 2013). Compared to other, spatially

Table 6.2: Summary of relevant details and references for the aircraft measurement datasets used in the evaluation of vertical profiles simulated with MADE3 in EMAC. The values in parentheses in the column "Time" are the numbers of measurement flights.

Name	Location	Time (#)	Reference
UCN-Pacific	Pacific Ocean	1990-05 (15), 1995-11 (33), 1996-09 (21), 1999-03 (19)	Clarke & Kapustin (2002)
INCA (Punta Arenas)	Chile	2000-03/04*	Minikin et al. (2003)
INCA (Prestwick)	Ireland	2000-09/10*	
Texas	Texas	2004-11-10 (1), 2004-11-12 (1)	Schwarz et al. (2006)
CR-AVE	Costa Rica	2006-02 (3)	Schwarz et al. (2008)
CIRRUS	Northern Europe	2006-11 (6)	Baumgardner et al. (2008)
TC4	Costa Rica/Panama	2007-08 (5)	Spackman et al. (2011)
HIPPO	Pacific Ocean	2009-01+, 2009-11+, 2010-03/04+, 2011-06+, 2011-08+	Schwarz et al. (2013)

* 9 to 10 flights per campaign, numbers not given separately

+ more than 700 profiles in total, numbers not given separately, number of flights not given

and temporally more localized campaigns the model simulates a more continuous decline in both total aerosol and BC mass mixing ratio with altitude than found in the observations, especially between ∼700 hPa and ∼300 hPa. Compared to the HIPPO data the model qualitatively captures the profiles well besides its high bias, with the exception of the latitude band between 80°S and 60°S. The high bias of the simulation w.r.t. the measured profiles could indicate an underestimation of aerosol scavenging as also hypothesized in the previous subsection. Likewise, overestimated upward transport, possibly in convective plumes, could explain such discrepancies. It remains for future studies to investigate these hypotheses in detail.

Several other model evaluation or sensitivity studies included comparisons to the observational datasets used here. For instance, Lohmann et al. (2007, ECHAM5-HAM) achieved close agreement of the BC and total aerosol mass mixing ratio profiles with the Texas data, but, using the same model with some modifications to aerosol-related mixed-phase cloud processes, Lohmann & Hoose (2009) found a similar overestimation of the CR-AVE data as that in Fig. 6.5. While Bauer et al. (2008, MATRIX) could better reproduce the decline of the BC mixing ratios with altitude close to the surface in the CR-AVE and TC4 data, EMAC with MADE3 performs better towards the top of the model domain.

Generally, BC concentrations are overestimated by many models in the upper troposphere (e.g., Koch et al., 2009, 2010; Schwarz et al., 2013; Allen & Landuyt, 2014). Several authors, among them Kipling et al. (2013, HadGEM3-UKCA), Wang et al. (2013a, CAM5), and Allen & Landuyt (2014, CAM5), found improved agreement with measured vertical profiles when improving the representation of aerosol–convection interactions. This includes aerosol activation, vertical transport, and wet removal in convective clouds. Note, however, that EMAC with MADE3 performs better in the BC comparison to HIPPO data than the multi-model average of the models that took part in the AeroCom project (Schwarz et al., 2013).

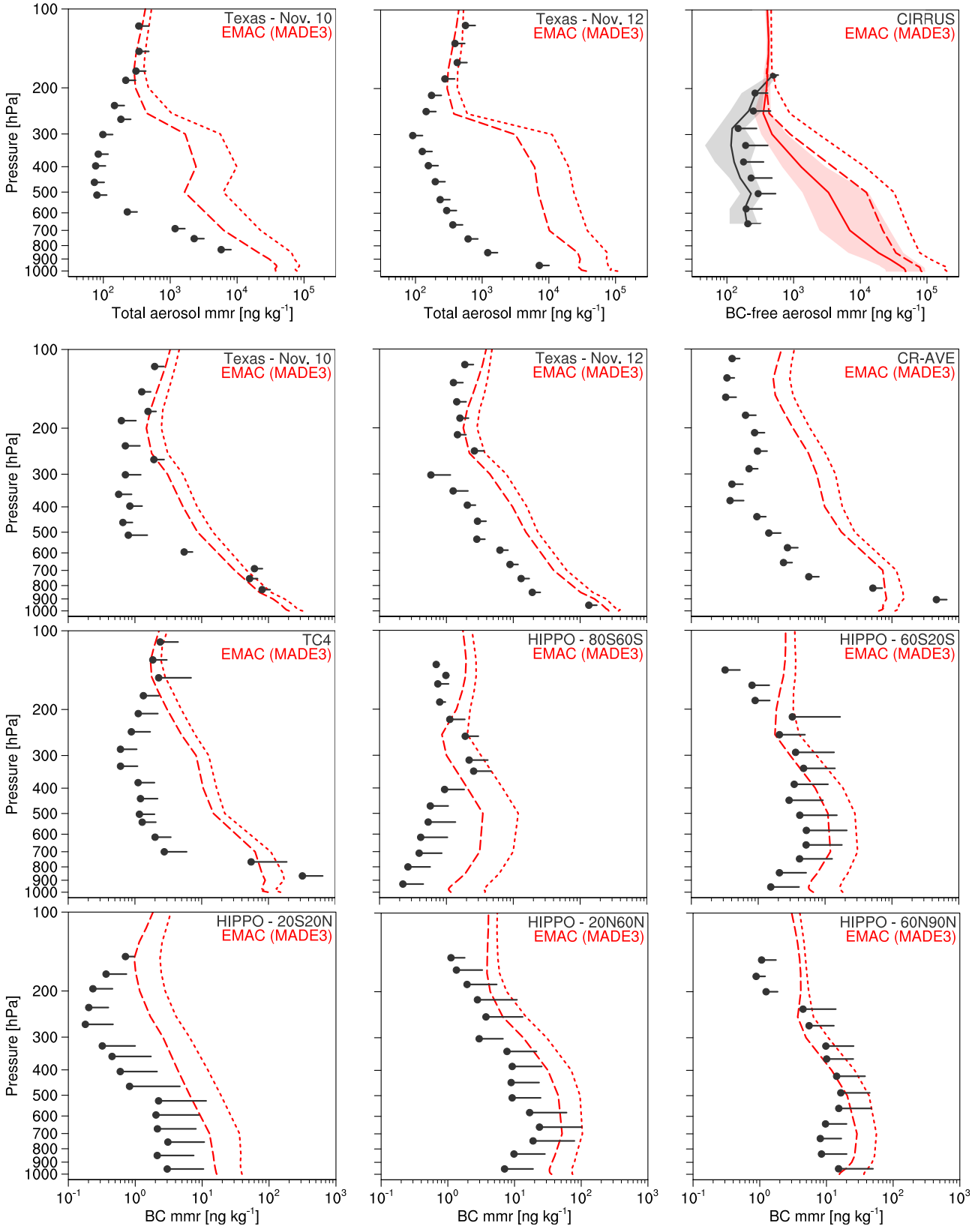

Figure 6.5: Aerosol mass mixing ratios (mmr) in the reference simulation with MADE3 (red) vs. measurements during various field campaigns (black). Long-dashed lines and dots represent mean values, short-dashed lines and whiskers represent standard deviations, which are only shown in the direction of larger values for clarity. Solid lines stand for median values. Shadings indicate the 25$^{\text{th}}$ to 75$^{\text{th}}$ percentiles. Descriptions of the campaigns are provided in Table 6.2 and in the text. Note that the vertical axis of the left plot in each row applies to the other plots of that row as well, and the horizontal axes of the plots in the lowermost row also apply to the plots in the two middle rows.

When comparing simulated aerosol particle number concentration profiles to measurements (Fig. 6.6) the best agreement is again detected over the Pacific Ocean, where, again, both spatial and temporal coverage by the observations are most extensive (more than 200 UCN-Pacific profiles; Clarke & Kapustin, 2002). The conclusion to draw from the comparison to the other datasets, which are based on more localized campaigns, is less clear. Discrepancies may in part be due to the sensitivity of the simulated concentrations to the cut-off diameter, i.e., the diameter down to which an instrument can actually sample aerosol particles. This is especially evident in the left and middle panel of the third row in Fig. 6.6. While the observed concentrations, measured with two instruments with different cut-off diameters at the same time, are very similar in both plots, the simulated number concentrations of particles greater than 14 nm are much lower than those of particles greater than 5 nm between 400 hPa and 200 hPa. The simulation values are the result of an integration of the number size distribution from the cut-off diameter upwards. This sensitivity may also explain some of the deviations seen in the other plots. It is worth noting that the agreement in the concentration of particles greater than 120 nm, i.e., the cloud condensation nuclei-sized particles, is better than for the smaller particles.

Deviations in the upper free troposphere, i.e., between ∼400 hPa and ∼200 hPa, might be related to the new particle formation (NPF) treatment in MADE3 (Sect. 3.2.3). Due to the fixed width of the Aitken mode, to which newly formed particles are assigned, it is unavoidable that at least a fraction of these particles enters the integral over the size distribution from the instrumental cut-off diameter to larger sizes. However, a large fraction of these particles may escape detection by the instruments due to their very small initial sizes. Of course, it is also possible that NPF is underrepresented in the observational data due to the intermittent nature of such events. The high bias of the simulated number concentrations could also be a result of an overestimated nucleation rate. Kazil et al. (2010, ECHAM5-HAM), who found a general high bias w.r.t. the UCN-Pacific data in the reference configuration of their model, achieved much improved agreement when lowering the rate of binary sulfuric acid–water nucleation by a factor of 10. Furthermore, Zhang et al. (2012, ECHAM-HAM2) obtained a strong reduction in nucleation mode number concentrations between ∼400 hPa and ∼150 hPa when switching from the Vehkamäki et al. (2002, 2013) scheme used here to a more recent parameterization.

Ouwersloot et al. (2015) found increased mixing ratios of an artificial tracer in the free troposphere when using an improved convective transport scheme that was recently developed for future versions of MESSy. This may mean that the general tendency of the model as used here to overestimate both observed aerosol mass and number concentrations could actually be even greater. Combined with the fact that discrepancies tend to increase with altitude this provides further evidence that aerosol scavenging may be under- or upward transport overestimated. In addition, previous studies with MADE (MADE-in) rather showed a negative (slightly negative) bias of simulated vs. measured concentrations (Lauer, 2004; Aquila, 2009), so that the overestimation in the present work is likely to be caused outside the aerosol microphysics submodel.

6.2.3 Size distributions

Size distributions provide more detailed information on the aerosol population than integral particle number concentrations. Here, simulated size distributions are compared against the following three sets of observational data.

Melpitz: The data taken at the ground-based station Melpitz, Germany, represents a 17-month period from March 1996 to August 1997, during which up to five lognormal modes were fit to the measurements (Birmili et al., 2001). Individual measurements (except for the two smallest-sized modes) were assigned to one of five groups based on the concurrent synoptic situation, and size distributions were subsequently averaged within the groups. According to the classification

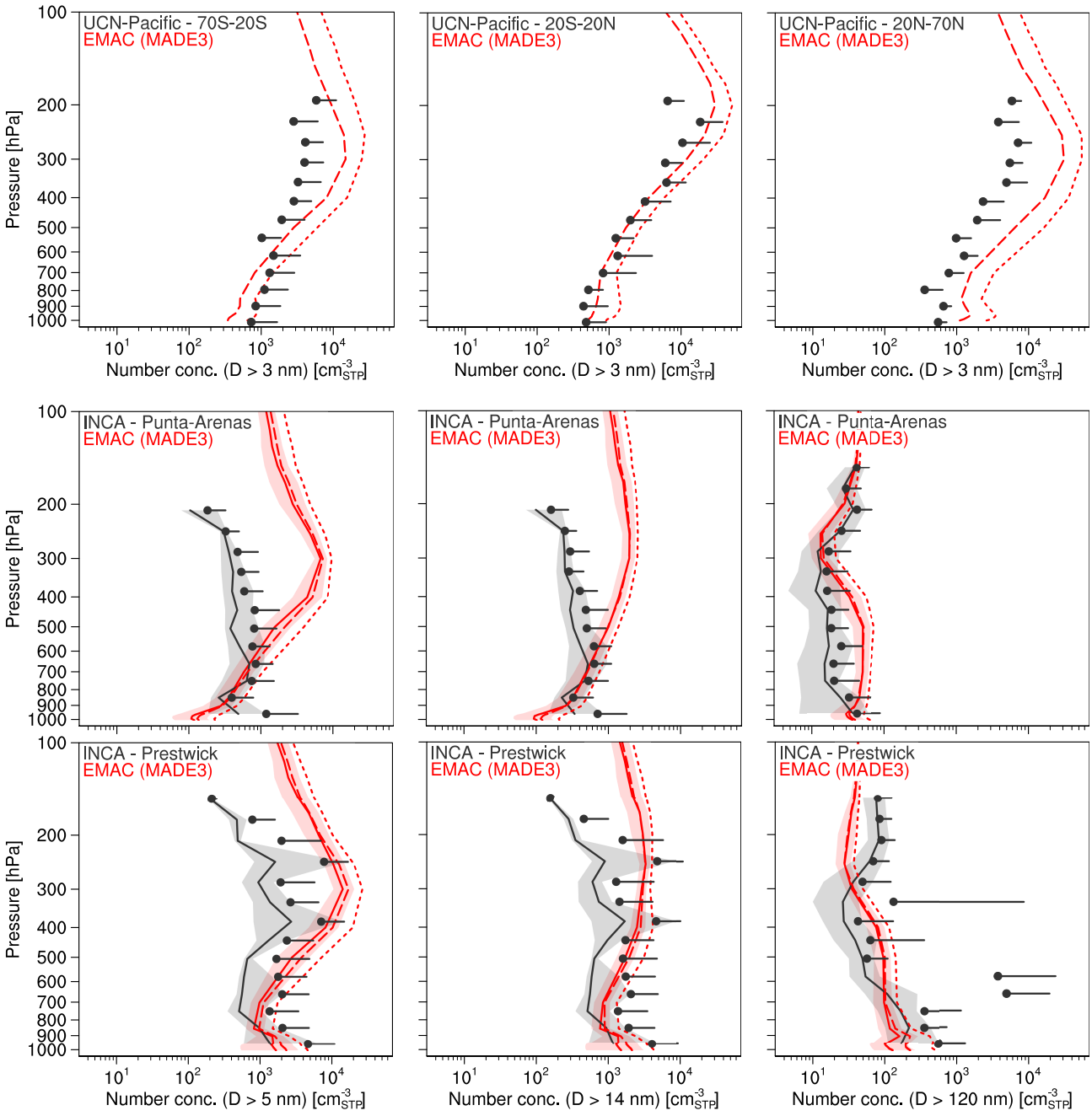

Figure 6.6: Same as Fig. 6.5, but for aerosol particle number concentrations (converted to standard temperature and pressure, STP), with various cut-off diameters. The horizontal axes of the plots in the lowermost row also apply to the plots in the middle row.

by Putaud et al. (2003), the station represents near-city conditions, as it is located ∼40 km to the northeast of Leipzig.

LACE: During the LACE aircraft campaign in July and August 1998 aerosol particle size distributions were measured at different altitudes over northeastern Germany (Petzold et al., 2002). Data from these measurements is used here in the form of three-mode fits to the measured size distributions for four to five individual flights, depending on the flight altitude.

Putaud: The data compiled by Putaud et al. (2003) is drawn from ten ground-based stations that monitored aerosol particle size distribution during at least one full season, i.e., either winter (December, January, February) or summer (June, July, August) in the 1990s or early 2000s. The authors fitted up to three modes to the measured distributions for three times of the day,namely the morning, the afternoon, and the night.

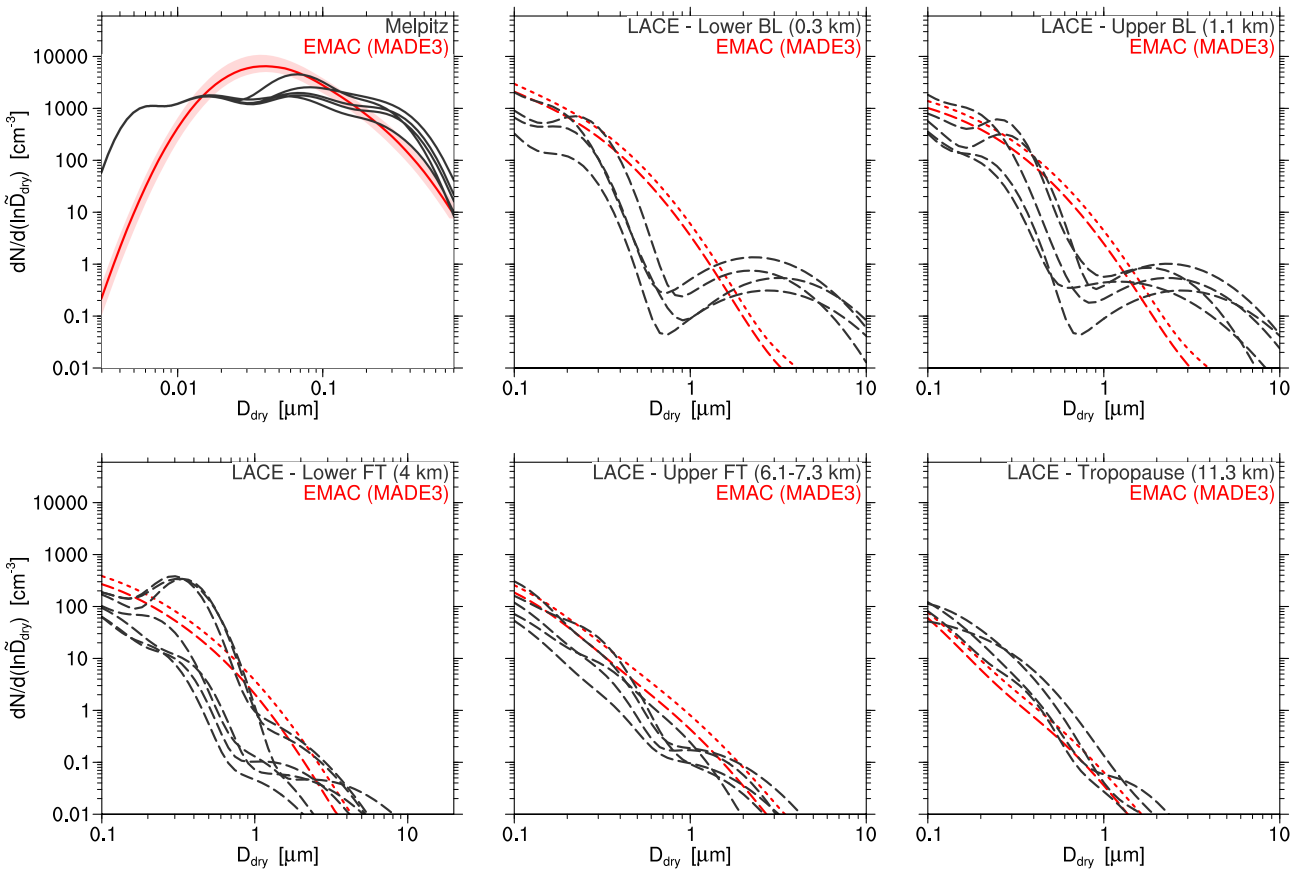

Figure 6.7: Aerosol particle size distributions in the reference simulation with MADE3 (red) vs. measurements (black) for five different synoptic situations at the near-city site Melpitz, Germany, and for four to five individual flights (depending on altitude) during the LACE campaign over northeastern Germany. Solid lines stand for median values, the shading indicates the 25$^{\text{th}}$ to 75$^{\text{th}}$ percentiles. Long-dashed lines represent mean values, short-dashed lines represent standard deviations, which are only shown in the direction of larger values for clarity. Abbreviations are as follows: BL for the planetary boundary layer, FT for the free troposphere. Note that the vertical axis of the left plot in each row always applies to the other plots of that row as well.

For each comparison plot (Figs. 6.7 and 6.8) simulated size distributions are taken from the grid boxes corresponding to the geographical coordinates or regions of the measurements, and only from those time steps (in each simulated year) that correspond to the days or months of the observations. As in the case of the vertical profiles, variability due to model meteorology is captured well with this approach.

The dataset from the LACE campaign is especially useful for the evaluation presented here as it includes measurements at different altitudes. Within the model's capabilities, the simulated size distributions agree well with the LACE observations (Fig. 6.7). Some notable differences exist, however. First, the coarse mode, which declines with altitude in the measurements, does not appear at all in the simulation. This may have to do with local, anthropogenically-induced dust emissions that are not included in the emissions dataset used here. Second, the widths of the accumulation modes that were fitted to the measured data are much narrower than those assumed in MADE3 ($\sigma \leq 1.6$ vs. $\sigma = 2.0$). However, agreement improves with altitude, i.e., with increasing particle age. The peak at ~300 nm in the upper boundary layer/lower free troposphere measurements was caused by a forest fire aerosol layer that cannot be reproduced in the simulation because this specific fire is not contained in the emissions dataset.

Figure 6.7 also contains the comparison of the simulated aerosol particle size distribution with the medians of the long-term observations at Melpitz. The model underestimates the concentration of particles smaller than about 10 nm, which could have to do with NPF in the

boundary layer. MADE3 does not include a dedicated nucleation mode (cf. Sect. 3.1.1), nor does it include a dedicated boundary layer nucleation parameterization (Sect. 3.2.3). Several modeling studies suggest that the latter may be required for a more accurate reproduction of observed aerosol particle number concentrations (e.g., Spracklen et al., 2006; Matsui et al., 2013; Makkonen et al., 2014; Pietikäinen et al., 2014). Furthermore, Lee et al. (2013a,b) found that boundary layer nucleation could also contribute up to several 10 % to the uncertainty in number concentrations of particles larger than 50 nm. In addition, the fixed mode widths in MADE3 again limit its capability to reproduce the observed size distributions, as the MADE3 modes are too wide to allow for the steep flanks seen in the measurements. It is interesting to compare the Melpitz plot (Fig. 6.7, top left) to the LACE lower boundary layer plot (Fig. 6.7, top middle) in terms of the particle number concentration density at diameters $\gtrsim 200$ nm. While slightly underestimated w.r.t. the Melpitz data, it is overestimated w.r.t. the LACE data, which was taken less than 300 km north of Melpitz (but at a different time).

The comparison of the simulation output to the Melpitz station data further reveals a deficit in finer structure of the MADE3 aerosol particle size distributions, which is persistent across other sites that went into the evaluation presented here (Fig. 6.8): the MADE3 distributions appear almost unimodal in many cases, whereas the observations often show two or more distinct modes. This finding is consistent with the result of the box model test (Sect. 4.4.1). Here, it is seen to be independent of season and location. The discrepancy is likely caused by the size distributions assumed for the emissions in connection with the wide MADE3 modes. Furthermore, the modeled aerosol particle size distributions generally exhibit less seasonal variation than the observed ones (Fig. 6.8).

The small variability of the simulated size distributions reflects the coarse geographical resolution of the model and the coarse time resolution of the emissions. For each station or experiment considered in the comparison simulation results for only one grid box are plotted, and emissions change only once per month. Hence, the simulation data for stations in grid cells that contain major emission sources is strongly influenced by the particle size distributions at emission, with little influence from other factors such as meteorological conditions. The coarse model resolution and associated mixing of different conditions that occur in the real atmosphere is especially evident when comparing data from the two London stations and the Harwell station to the simulation: all three stations fall into the same grid box, for which only one size distribution can be realized at any given time in the model. Higher concentrations than measured at remote locations (top row in Fig. 6.8) and lower concentrations than measured at kerb-side (bottom row in Fig. 6.8) are thus expected from the simulation.

Compared to the published results of other global model–observation comparisons of aerosol particle size distributions EMAC performs reasonably well with MADE3. While Zhang et al. (2012, ECHAM5-HAM2) achieved better agreement with some of the distributions presented here, Lee et al. (2015, ModelE2-TOMAS) found similar deviations with their sectional model. Wang et al. (2009, CAM3-IMPACT) also saw large discrepancies when comparing their simulations to some of the observations shown in Fig. 6.8.

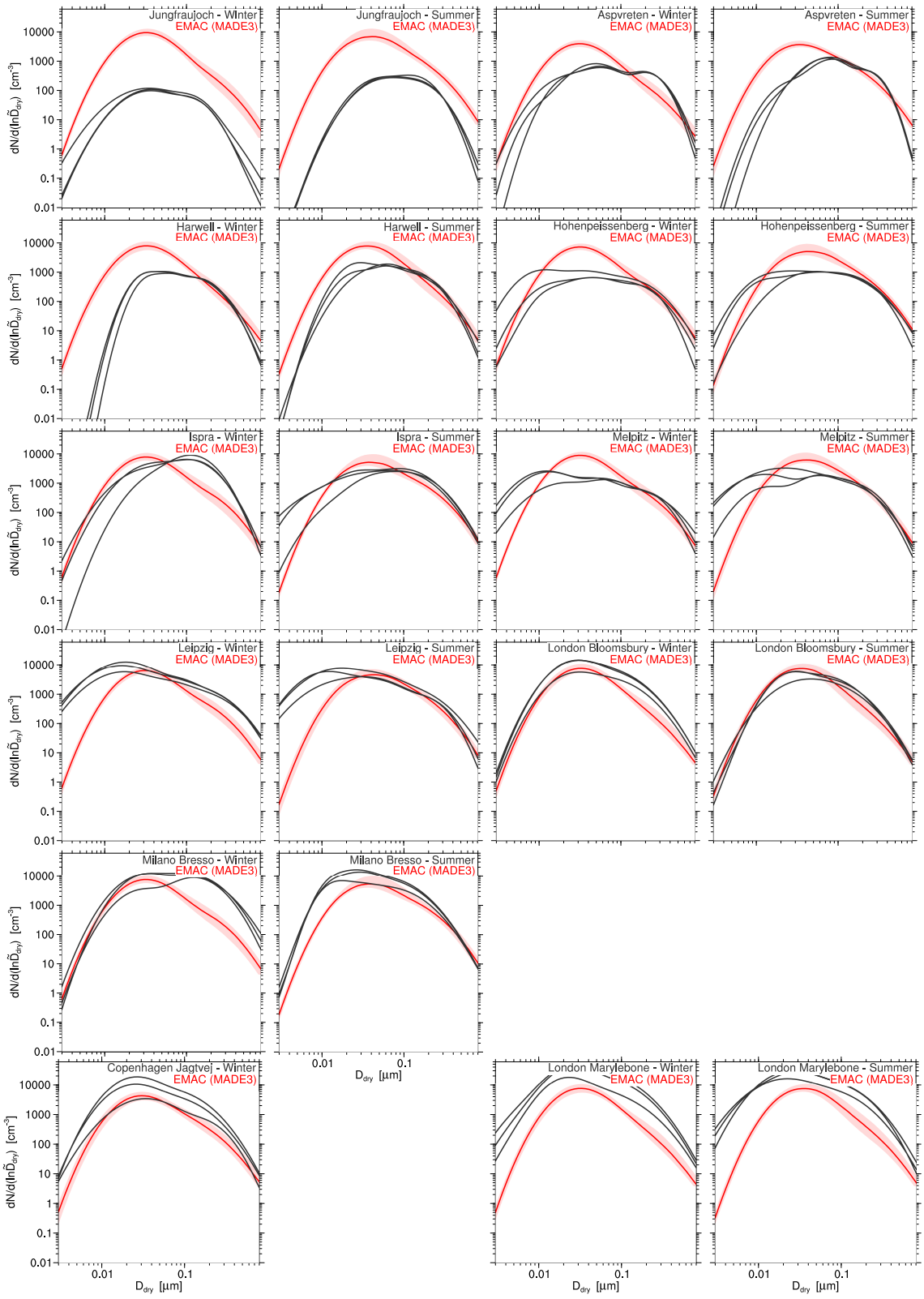

Figure 6.8: Aerosol particle size distributions in the reference simulation with MADE3 (red) vs. measurements compiled by Putaud et al. (2003, black) during winter (columns 1 and 3) and summer (columns 2 and 4) at the same locations (columns 1 and 2, 3 and 4). Each plot contains three measured size distributions: one for the morning, one for the afternoon, and one for the night hours. Row 1: remote, row 2: rural, row 3: near-city, rows 4 and 5: urban, row 6: kerb-side conditions (terminology adapted from Putaud et al., 2003). Solid lines stand for median values, shadings indicate the 25^{th} to 75^{th} percentiles. Note that the vertical axis of the left plot in each row applies to the other plots of that row as well, and the horizontal axes of the plots in the lowermost row also apply to the other plots in the respective columns.

6.2.4 Aerosol optical depth

Aerosol optical depth (AOD) provides an integral measure of the atmospheric aerosol. On the one hand, it can be computed from the simulated aerosol properties discussed in the previous subsections, i.e., particle composition, particle sizes, and their vertical distributions, under the assumptions mentioned in Sect. 5.10. On the other hand, AOD can also be derived from measurements with ground-based and satellite-borne radiometers. Here (Fig. 6.9), the simulated AOD is compared to data from the ground-based AErosol RObotic NETwork (AERONET, Holben et al., 1998, 2001)[5] and against satellite data from the Along Track Scanning Radiometers (ATSR; ERS2 and ENVISAT satellites; North et al., 1999; Bevan et al., 2012; Holzer-Popp et al., 2013; de Leeuw et al., 2015)[6], from the Multi-angle Imaging SpectroRadiometer (MISR; over land; Terra satellite)[7], and from the MODerate resolution Imaging Spetroradiometer (MODIS; over oceans; Terra satellite)[8]. The MISR and MODIS satellite datasets used in this work were obtained from the obs4MIPs project (`https://www.earthsystemcog.org/projects/obs4mips/`) hosted on the Earth System Grid Federation (`http://esgf.org`). Since AOD regionally changed by up to 10 % during the last decade (2000 to 2010, e.g., Yoon et al., 2014; Pozzer et al., 2015), only year 2000 data is used in the comparisons of annual mean AODs here. Note that the MISR/MODIS data covers only the period March to December 2000. Hence, model output was also averaged over this period instead of the whole year for the comparison to data from these instruments.

The picture that emerges from the plots in Fig. 6.9 is relatively clear. The model reproduces AOD better at larger distances from the major pollution plumes that originate in the eastern USA, Europe, and East Asia. The large overestimations in these plumes were not present in a previous simulation with MADE as part of EMAC (MESSy version 1.4, not shown). The main differences between that simulation and the current one are larger particles simulated with MADE3 (MESSy version 2.50) and a higher aerosol water content. Li et al. (2014) also found that AOD was strongly affected by differences in hygroscopic growth, i.e., water uptake due to aerosol particle hygroscopicity. The overestimation of AOD is consistent with the general tendency of the model to overestimate aerosol mass concentrations as seen in Sects. 6.2.1 and 6.2.2. Furthermore, changes in the scavenging scheme for aerosol particles entrained into convective clouds can also lead to several 10 % different annual mean AOD values (Croft et al., 2012). As the corresponding submodel, SCAV, was substantially modified between MESSy versions 1.4 and 2.50, it is likely that these changes contribute to the overestimation that is now detected.

Despite the large regions of overestimation, the model tends to underestimate AOD where DU is abundant, especially over the Sahara and the Arabian peninsula. Potential reasons for this underestimation include the use of prescribed monthly mean year 2000 DU emissions, the DU size distribution upon emission, and the DU representation in AEROPT, the submodel that computes aerosol optical properties (Sect. 5.10). As AEROPT evolved from the scheme developed by Lauer et al. (2007), it is interesting to note that these authors also found underestimated AOD values in the regions dominated by DU aerosol. Johnson et al. (2012) and Nabat et al. (2012) found improved agreement of simulated AOD with observations when using a parameterization with more of the emitted DU mass in the coarse mode. Furthermore, the studies by Zhao et al. (2013a) and Mahowald et al. (2014) indicated that a modal representation of DU particles with fixed mode widths may have unavoidable shortcomings.

[5] `http://aeronet.gsfc.nasa.gov/cgi-bin/combined_data_access_new`

[6] `http://www.icare.univ-lille1.fr/archive/dir=CCI-Aerosols`

[7] references in `http://earthsystemcog.org/site_media/projects/obs4mips/TechNote_MODIS_L3_C5_Aerosols.pdf`, accessed on 2015-05-28

[8] references in `http://earthsystemcog.org/site_media/projects/obs4mips/TechNote_MISR_L3_F12_0022_Aerosols.pdf`, accessed on 2015-05-28

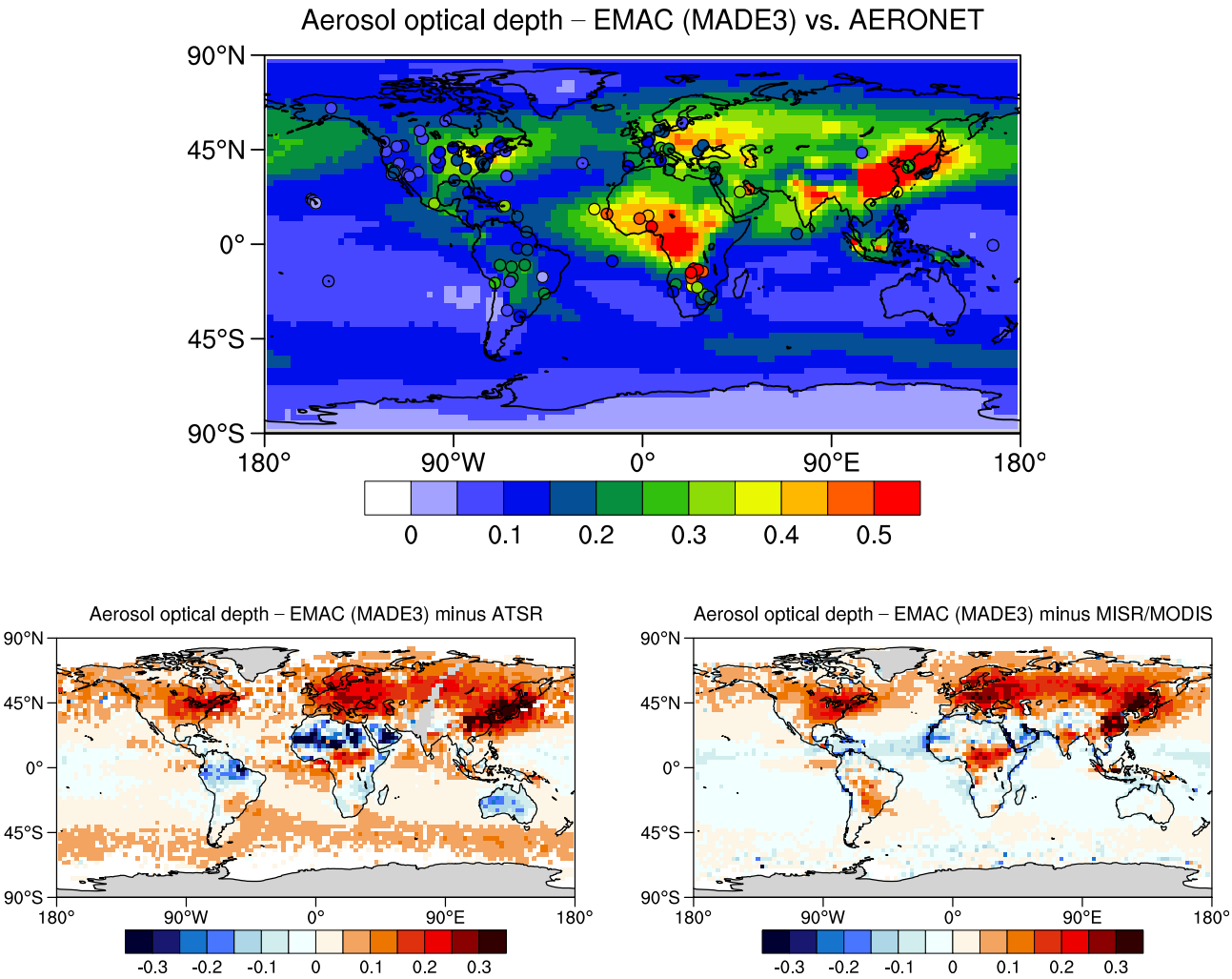

Figure 6.9: Year 2000 annual mean aerosol optical depth (AOD) in the reference simulation with MADE3 (top, background color) vs. observations from the AERONET network (top, filled circles) and vs. satellite data from the ATSR instrument (bottom left) and from the MISR and MODIS instruments (over land and ocean, respectively; bottom right). "Pixels" in the panels correspond to the model grid.

Simulated oceanic AOD agrees well with the MODIS data, except where the continental pollution plumes are located, but is higher than that derived from ATSR measurements, especially over the southern oceans. A comparison with a large dataset of ship-borne measurements showed that ATSR data may be more reliable in this region than the MODIS data (Kinne et al., 2015). Hence, the model's overestimation may indicate too high sea spray emissions, as also mentioned in Sect. 6.2.1, but could as well be due to overestimated concentrations of other aerosol components.

AOD data from different satellite instruments does not agree perfectly. This even holds for data from the same instruments if it is obtained with different retrieval algorithms. Hence, one cannot expect perfect agreement of simulated AOD with these observations either. Furthermore, uncertainties involved in the calculation of particle optical properties can of course also contribute to deviations. While different models have different strengths and weaknesses, it is interesting to note that many models underestimate AOD on a global annual average basis rather than overestimate it as seen here (e.g., Pozzer et al., 2012; Kirkevåg et al., 2013; van Noije et al., 2014; Lee et al., 2015; Michou et al., 2015). The global average overestimation by EMAC version 2.50 with MADE3 for the year 2000 is 23 % (2.8 %) with respect to the ATSR (MISR/MODIS) data. Relative underestimations in some of the mentioned studies are actually greater than these values.

Table 6.3: Annual average values for global tropospheric aerosol burdens and residence times simulated with MADE3 in EMAC. The ranges of values for the ten evaluated years are given in brackets. Furthermore, the ranges of values from a compilation of other studies (Lauer & Hendricks, 2006; Textor et al., 2006; Bauer et al., 2008; Wang et al., 2009; Mann et al., 2010; Pozzer et al., 2012; Kirkevåg et al., 2013; He & Zhang, 2014; van Noije et al., 2014; Lee et al., 2015; Michou et al., 2015) are shown in the table. Note that this is not meant to be a comprehensive literature review, but should yield a representative picture. Extreme values may stem from specific sensitivity studies.

	Burden [Tg]		Residence time [d]	
Species	This work Mean [Range]	Other studies Range	This work Mean [Range]	Other studies Range
SO_4	3.44 [3.19;3.55]	[0.90;3.35]	10.4 [10.2;10.6]	[1.28;5.60]
NH_4	0.95 [0.88;0.98]	[0.13;0.46]	9.25 [8.99;9.35]	[1.49;4.50]
NO_3	0.52 [0.50;0.55]	[0.02;1.64]	2.09 [2.04;2.15]	[1.37;6.40]
Na	2.32 [2.26;2.39]	[1.95;3.04]	0.16 [0.15;0.17]	[0.19;1.20]*
Cl	1.77 [1.72;1.85]	[4.47;4.52]	0.14 [0.14;0.15]	—
POM	2.64 [2.54;2.73]	[0.99;4.79]	4.57 [4.41;4.77]	[2.56;9.52]
BC	0.18 [0.17;0.19]	[0.08;0.34]	3.69 [3.54;3.84]	[2.44;9.60]
DU	9.58 [8.84;10.3]	[8.63;41.6]	1.12 [1.04;1.21]	[1.56;5.92]

*Values for sea spray

6.2.5 Global tropospheric burdens and residence times

Although it is not an evaluation in the sense of a check against observational data, a comparison of global tropospheric aerosol burdens and residence times to estimates from other modeling studies is also interesting. The burden $m_{\mathrm{tot},a}$ of aerosol species a is computed here as the sum over the volume integrals of the mass concentrations c_a in all grid boxes. The species' residence times, $t_{\mathrm{res},a}$, are derived from the burdens and the sums of the deposition fluxes (Sects. 5.7–5.9), $F_{\mathrm{dep},a}$, as

$$t_{\mathrm{res},a} = \frac{m_{\mathrm{tot},a}}{F_{\mathrm{dep},a}}. \tag{6.1}$$

Simulated burdens and residence times are presented in Table 6.3.

Several discrepancies stand out when comparing the burdens and residence times simulated with MADE3 in EMAC to previous estimates with other (sub)models. Some of them may have to do with different emissions datasets used in the other studies. A detailed analysis of such discrepancies is beyond the scope of the present work, but some possible reasons shall be mentioned in the following paragraphs. Three groups of species can be distinguished in this discussion: secondary inorganics, components with a dominant coarse mode at emission, and carbonaceous material.

For the secondary inorganic species, i.e., SO_4, NH_4, and NO_3, the partitioning between the coarse and fine modes appears to play an important role. While SO_4 and NH_4 are found predominantly in the fine modes (>95 % on average), NO_3 partitions roughly equally between the fine and the coarse modes on average. The large burdens of SO_4 and NH_4 are consistent with the model's general tendency to overestimate observed near-surface concentrations (Sect. 6.2.1). A likely reason for these large values are the long residence times, which could be due to an underestimation of one or more of the sink processes for these species or for the fine modes in general. In case of NO_3, both the burden and the residence time fall within the range of previous estimates.

Large fractions of the emissions of DU and the SS components Na and Cl belong to the coarse aerosol modes. The residence times of these species are small in the present simulation

compared to the estimates from other studies. Although other models may not provide an accurate reference, this could imply that one or more loss processes that mainly affect the coarse modes are overestimated here. Thus, the difference between SO_4 and NH_4 on the one hand and NO_3 on the other hand could also be explained. Overestimated coarse mode NO_3 deposition might be balanced by underestimated fine mode NO_3 deposition so that the simulated values fall within the range of other estimates. Note that the (lower) Cl burden was reported in only one of the cited studies. On average, continental near-surface Cl concentrations are overestimated rather than underestimated here w.r.t. observations. Similar to the NO_3 issue, it is possible that fine and coarse mode Cl behave differently, and that continental measurements are biased towards the fine mode particles.

For the carbonaceous species, i.e., for POM and BC, it is even more difficult to draw any conclusions than for the two groups discussed above. The ranges of previous estimates for these species are among the widest, which suggests that large uncertainties are associated with these components across models anyway. In any case, it is encouraging that the burdens and residence times simulated here fall within the ranges of results from other studies.

6.2.6 Summary and conclusions

Simulated aerosol (species) mass and number concentrations, size distributions, and AOD were compared to surface-based, airborne, and satellite measurement data.

The main conclusion from the near-surface mass concentration comparisons is that EMAC with MADE3 mostly captures the observed annual average spatial patterns of all aerosol species included in the model. Best agreement was obtained for BC and POM, but they could only be compared over the USA. Among the other species, quantitative agreement is typically best for SO_4, with up to $\sim$70 % of the simulated monthly mean values within a factor of two of the observations. Concentrations of the nitrogen-containing components, NH_4 and NO_3, are spatially less heterogeneous in the simulations than in the observations. This is likely caused by the coarse model resolution and by higher temporal variability of the precursor emissions compared to those of SO_4, which leads to larger uncertainties in the emissions datasets. Poorest agreement was found for Na and Cl, which might be caused in part by the SS emissions parameterization, but could also be due to too inefficient removal of fine mode particles from the atmosphere. The latter could also help to explain the general high bias of the average of the simulated values vs. the observations for all species. Note, however, that near-surface mass concentrations could only be evaluated over the northern hemisphere continents, with very few exceptions.

The comparison of vertical mass mixing ratio and number concentration profiles revealed that simulated values are often larger than the observed ones. Underestimated fine mode particle deposition could as well be part of the reason for these deviations. In the case of number concentrations this finding could also indicate an overestimation of the NPF rate. Nevertheless, compared to results from studies with other models, EMAC with MADE3 yielded good agreement with the vertical profile observations.

Simulated near-surface size distributions, or rather their level of agreement with observations, was strongly affected by the coarse spatial and temporal model resolution. The simulated distributions often showed a rather unimodal shape, whereas observed ones were flatter than a single lognormal mode in the Aitken to accumulation mode size range in many cases. This may have to do with the procedure of renaming particles from the Aitken to the accumulation modes in MADE3, but could also be a consequence of the relatively wide accumulation modes in comparison to those fitted to the observational data. Furthermore, weaker seasonal variability was found in the simulation than in observations across Europe.

The comparison of simulated AOD to ground-based and satellite observations provided further evidence for some of the conclusions drawn above. AOD is overestimated where secondary

species, i.e., SO_4, NH_4, and NO_3, are most abundant, and possibly over parts of the oceans, where SS particles dominate. However, with a global annual average bias of 2.8 to 23 % the model performs well in comparison to others.

Besides uncertainties in many of the parameters that are part of the aerosol microphysics calculations there are numerous issues that have to be taken into account when comparing simulations to observations. Among those are the location, time, and meteorological and emissions situation of the observations; the correspondence of measured and simulated species; and as well the uncertainties inherent in the observations, which are rarely reported. A detailed analysis of all these factors is beyond the scope of the present work. In comparison to other models long tropospheric residence times of species that mainly partition to the fine modes and rather short ones of species with a dominant coarse mode were found here. These deviations will be addressed in more detail in a follow-up study. Here, the main conclusion is that, in all "disciplines", the simulation with MADE3 achieved a level of agreement with observations that falls within the range of results reported by other authors from simulations with their models. The new submodel can therefore be considered ready for application.

6.3 Comparison to MADE

The simulation discussed above was repeated with an identical setup, except that the aerosol submodel MADE was used instead of MADE3 in order to compare the performance of the two submodels. To this end, and in support of an answer to scientific question 1 of this work (Sect. 1.2), the evaluation presented in the previous section was repeated for the MADE simulation. It was found that the MADE3 results for mass concentrations generally agree better with the observations, but that observed number concentrations are in some cases better represented by MADE. This section gives a brief summary of the comparison of the two submodels.

Near-surface mass concentrations. The fraction of simulation data points within a factor of two of the observations is lower when using MADE than when using MADE3 in all cases, i.e., for all species and with respect to all networks. Furthermore, the model bias is larger in almost all cases. Both these findings can be explained by the higher simulated near-surface concentrations in almost all cases when using MADE. The largest relative difference is found for the Cl concentration, which was expected, as evaporation of Cl from the SS aerosol is not considered in MADE.

Vertical distributions. Mass mixing ratios are slightly higher throughout the depth of the atmosphere when using MADE than when using MADE3. Qualitatively, the MADE and MADE3 profiles look similar except for the highest latitudes in the comparison to the HIPPO observations. Here, concentrations near the surface are notably higher when using MADE than when using MADE3. The relative difference between the concentrations in the two simulations decreases with altitude from a factor of ∼4 (∼8) at surface level to a factor of ∼2 (∼3) at 700 hPa in the latitude band between 60°N and 90°N (60°S and 80°S), so that agreement with the observations is worse when using MADE.

The number concentration profiles simulated with MADE are very similar to those simulated with MADE3 if particles down to diameters of 3 nm or 5 nm are taken into account. At larger cut-off diameters the MADE profiles agree better with the observational data, at least in the altitude range between ∼700 hPa and ∼200 hPa. In most cases this is due to lower number concentrations of larger particles aloft simulated with MADE, as particle sizes tend to be smaller in the MADE simulations.

Size distributions. MADE and MADE3 generally yield size distributions of very similar shapes and magnitudes. Hence, agreement with the observational data is also very similar. In a few cases MADE distributions show a slightly clearer separation of the Aitken and the accumulation mode than the MADE3 distributions, which may be due to the smaller number of individual modes in MADE.

Aerosol optical depth. As one might expect from the high bias in near-surface concentrations, AOD is also overestimated w.r.t. the observations when using MADE. The high bias is larger than when using MADE3, the ratio of the multi-annual and multi-site average of simulated and AERONET observational data being 1.51 for MADE vs. 1.36 for MADE3. The two submodels yield almost identical results in terms of the geographical distribution of both simulated AOD itself and the overestimation.

Global tropospheric burdens and residence times. The burdens of DU and SS simulated with MADE fall into the range of values estimated in other studies. However, for some of the species that MADE allows only in the fine modes, especially SO_4 and NH_4, residence times are simulated to be far greater than previously estimated. Correspondingly, the burdens are also larger, albeit less drastically. As such large values were not found in a former study with MADE and the GCM ECHAM4 (Lauer & Hendricks, 2006), this again indicates an underestimation of fine mode particle deposition in the EMAC version used for the present work, which will be investigated in more detail as part of a follow-up study.

Conclusion. Concentrations of secondary species appear to be larger in the MADE simulation than in the MADE3 simulation. A fraction of these species is taken up into coarse mode particles in the MADE3 case. As coarse mode particles are deposited more quickly, the main conclusion drawn from the MADE3–MADE comparison is that the inclusion of coarse mode particle interactions leads to faster removal of secondary species from the atmosphere.

6.4 New features of MADE3

In order to enable a specific evaluation of the new coarse mode particle representation in MADE3 it is useful to compare model output to size-resolved particle composition measurements. However, such data rarely includes coarse mode particles and the correspondence between modeled and measured quantities is not always straightforward. A strategy how to evaluate modeled size-resolved aerosol composition with the help of electron microscopy data of in-situ sampled aerosol particles is therefore presented here. For an initial application of this strategy a dataset was chosen from the SAMUM-2 campaign that took place in Cape Verde in January and February 2008 (Kandler et al., 2011). The data is compared to output from EMAC in the configuration described in Chap. 5.

Particle sizes as determined in the electron microscopy measurements are given as equivalent diameters of the particles' projected areas. It is assumed that these can be directly compared to the diameters derived from the modeled aerosol particle number and component mass concentrations, the mode widths, and the assumed component densities (Eqs. 3.1 and 3.2).

The experimental analysis is performed on individual particles, i.e., 48599 particles in the dataset used here. Thirteen different elements can be detected. Based on the relative contributions of the elements the total volume of each particle is assigned to one of 43 different groups. Finally, each group of particles is mapped to one of 12 different particle classes, e.g., sulfates, chlorides, oxides, silicates, etc.

For the comparison to model output this procedure has a severe drawback. It would require classification of the MADE3 particles according to the same, or analogous, rules as the measured particles. However, since all particles within each mode have the same fractional composition, only particles of a maximum of nine different compositions can coexist at the same time in each grid box of the model. Classification of model particles, or rather modes, is therefore not reliable from a statistical point of view. For instance, consider a mode that contains both SO_4 and Cl. Its total volume can always be assigned to only one class, either to the sulfates or to the chlorides. However, if a similar mode was present in the measurements as well, it would likely contain both particles with a major contribution from SO_4 (assigned to the sulfates class) and particles with a major contribution from Cl (assigned to the chlorides class). Hence, classification of the model modes would create unacceptable sampling biases.

Furthermore, some elements only produce weak signals in the measurements, and material from the sampling substrates can also affect the analysis. Of the species simulated by MADE3, only SO_4, Na, Cl, and DU can therefore be determined reliably in the measurements of contributions to particle composition.

For these reasons a different view on the electron microscopy data was adopted. In the approach employed here the component masses of each analyzed particle are assigned to one of five diameter "bins" according to the particle's size. Only those components that can be compared to model output are considered (i.e., SO_4, Na, Cl, and DU). The Cl fraction is measured directly, and considered to derive exclusively from sea spray. The sodium fraction is also measured directly, but for correspondence to the MADE3 Na tracer, the sea spray SO_4 fraction has to be added (see Sect. 3.1.2). The latter can be derived from the Cl fraction under the assumption of a typical sea spray composition, i.e., 54.6 % of chlorine atoms, and 2.82 % of sulfur atoms (K. Kandler, pers. comm.), and under the assumption that all this sulfur is present in the form of SO_4. The rest of the detected sulfur is also assumed to stem from SO_4 and can be compared to the MADE3 SO_4 tracer. The DU contribution is derived from multiple elements that are typical of mineral dust, i.e., mainly silicon and metals.

The model output is binned into the same diameter intervals as the measurement data by integrating the mass size distribution of each mode from the lower to the upper bin boundary and then summing up the contributions of the individual modes. Thus, measurement data and model output are brought to the same format and can be compared.

An example comparison is shown in Fig. 6.10. The measurement panel (left) displays the average particle composition over the whole SAMUM-2 campaign, i.e., over measurements from 26 individual days, or 48205 particles. The rest of the analyzed particles fell outside the size range presented here. With 3729 particles, the rightmost bin has the smallest data base. For the model plot 12-hourly output from the grid box that contains the measurement station was averaged over the measurement period in all of the ten evaluated simulation years.

The preliminary result shown in Fig. 6.10 must be interpreted with caution. It is not possible to reproduce the conditions during the SAMUM-2 campaign with the model setup used here (Chap. 5), except by chance. Especially, the monthly mean year 2000 DU and SO_4 emissions in the simulation may not be representative of the actual situation in the beginning of the year 2008. Local pollution sources cannot be resolved either. That said, the comparison reveals similarities between the simulated and measured data in the decrease of the SO_4 fraction and the increases of the sea spray (Na plus Cl) and DU fractions with increasing size. Major discrepancies, however, exist in the composition of the smallest compared particles. The range of simulated campaign period average values in the ten evaluated years is shown in Fig. 6.11. Judging by this variability, meteorology alone cannot explain the discrepancies.

For the future, simulations of specific episodes with the appropriate meteorology and emissions are planned. The size distribution of the measured aerosol particles should also be taken into account for a thorough comparison, especially that of the surface area available for SO_4

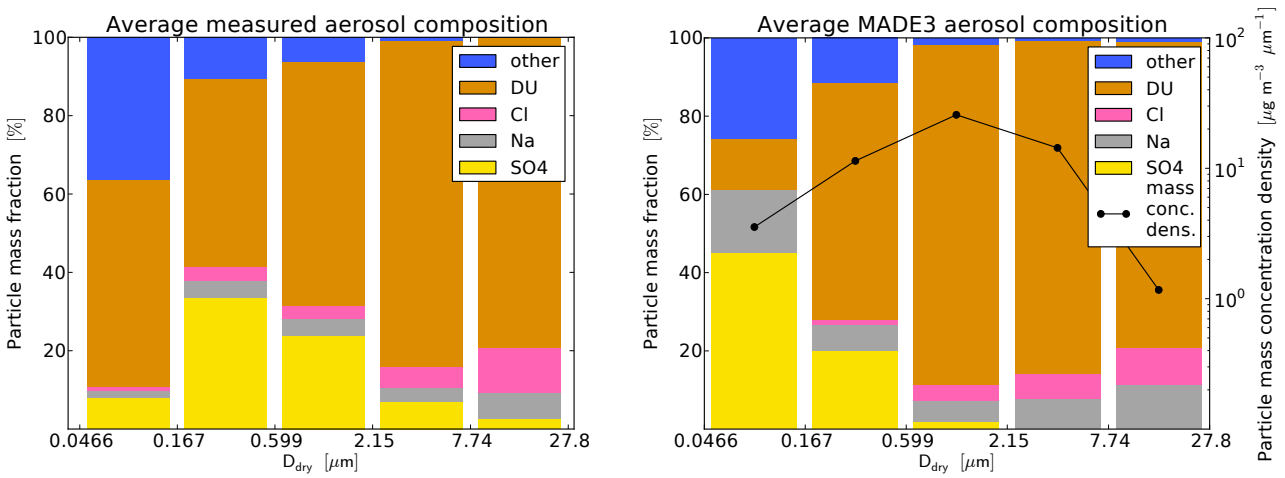

Figure 6.10: Average size-resolved aerosol composition as measured during the SAMUM-2 campaign (left) and as simulated for the corresponding grid box and time period in the ten evaluated simulation years (right). Only the mass fractions of species that can be compared between measurement data and model output are depicted (left vertical axes). The mass size distribution of the simulated aerosol is shown in black for reference (right vertical axis). Measurement data on the size distribution was not available to the author at the time of writing.

condensation. Such data, however, has to be measured with different instruments. For some campaigns both size-resolved composition and size distribution measurements are available. MADE3 will be checked against these in the future with the method presented here.

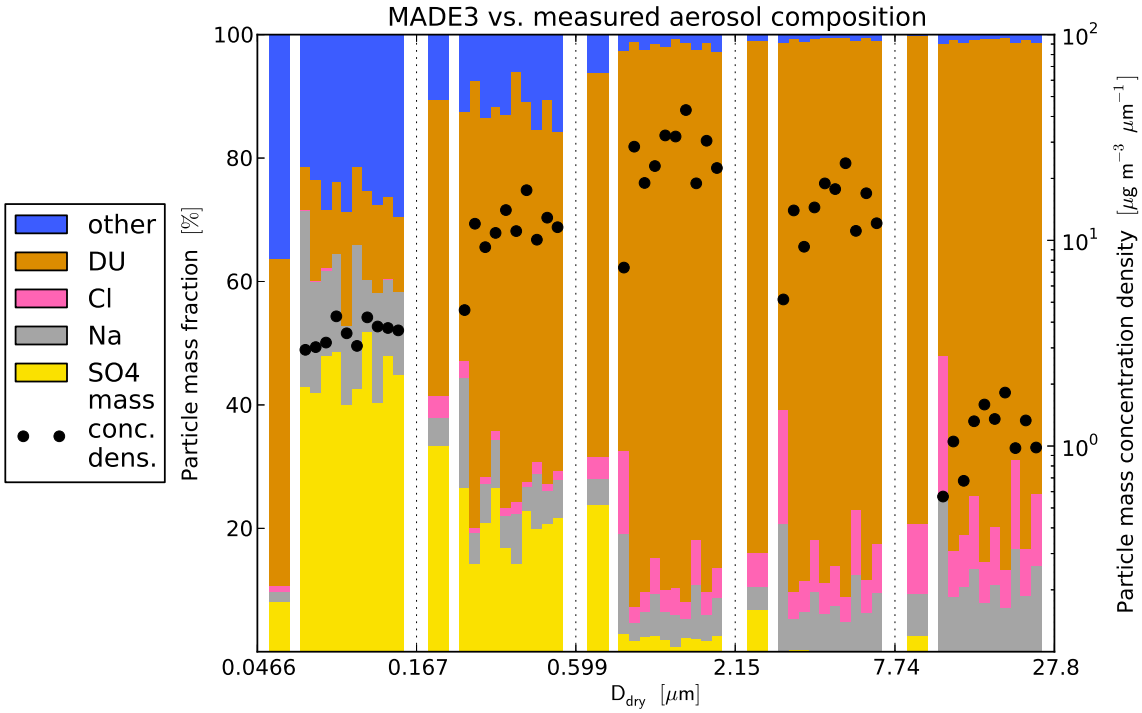

Figure 6.11: Average size-resolved aerosol composition as measured during the SAMUM-2 campaign (wide bar at the left of each diameter bin; same data as in Fig. 6.10) vs. average simulated data for the corresponding grid box and time period in the individual evaluated years (rest of the bars in each bin). Only the mass fractions of species that can be compared between measurement data and model output are depicted (left vertical axis). The black dots represent the variability in the simulated mass size distribution (right vertical axis). For clarity they were not connected with lines as in Fig. 6.10.

Chapter 7

Effects of oceanic ship emissions on atmospheric aerosol particles

In order to provide data to answer scientific questions 2 and 3 of this work (Sect. 1.2), further simulations besides the ones discussed in the previous chapter were performed with MADE3 and MADE. The additional simulations include one each with MADE3 and MADE where ship emissions were switched off completely, and one each with reduced emissions of sulfur dioxide (SO_2) and sulfate (SO_4) from the shipping sector. All other settings are identical to the simulations evaluated in Chap. 6.

The effect of year 2000 ship emissions on the near-surface aerosol is quantified by comparing the reference simulations, i.e., those with full ship emissions, to those without ship emissions (Sect. 7.1). All simulations were run with both MADE3 and MADE in order to determine the role of coarse mode particle interactions with both fine mode particles and the gas phase in the ship emission effects on the atmospheric aerosol. To this end, not only differences between the simulations with and without ship emissions are discussed in the following sections. Rather, the changes in these differences when switching from MADE to MADE3 are also presented. Furthermore, where possible, the results are compared to estimates from previous studies with MADE in an earlier version of EMAC (MESSy version 1.4): L07 (Lauer et al., 2007), L09 (Lauer et al., 2009), and R13 (Righi et al., 2013). Changes in the ship emission effects due to anticipated reductions in the average ship fuel sulfur content are assessed using the two remaining simulations (Sect. 7.2).

The following discussion is based on differences, e.g., in aerosol species mass concentrations, between simulations with different amounts of emissions. Nonlinearities in the response of the aerosol to changes in emissions cannot be quantified with this so-called perturbation method. Such nonlinearities were shown by R13 to exist for ship emissions-induced SO_4 and nitrate (NO_3). Hence, concentration differences between simulations are not necessarily equal to the contributions of the respective emissions to the total concentrations. Nevertheless, for the ease of reading and for the lack of a more appropriate term, they will be referred to as contributions in this chapter. Except where stated otherwise, the reference for "relative contributions" are the values in the simulations that include ship emissions.

7.1 Effects of year 2000 emissions

In this section the results from the reference simulations with MADE3 and MADE are compared to the corresponding ones with ship emissions switched off. The ship emission effects on the atmospheric aerosol are quantified in terms of near-surface concentrations (SO_4, NO_3, particulate organic matter (POM), black carbon (BC), and particle number; Sect. 7.1.1), size distributions (Sect. 7.1.2), and tropospheric burdens (Sect. 7.1.3). As in Chap. 6, the term "near-surface" is used here as an abbreviation for "in the lowermost model layer".

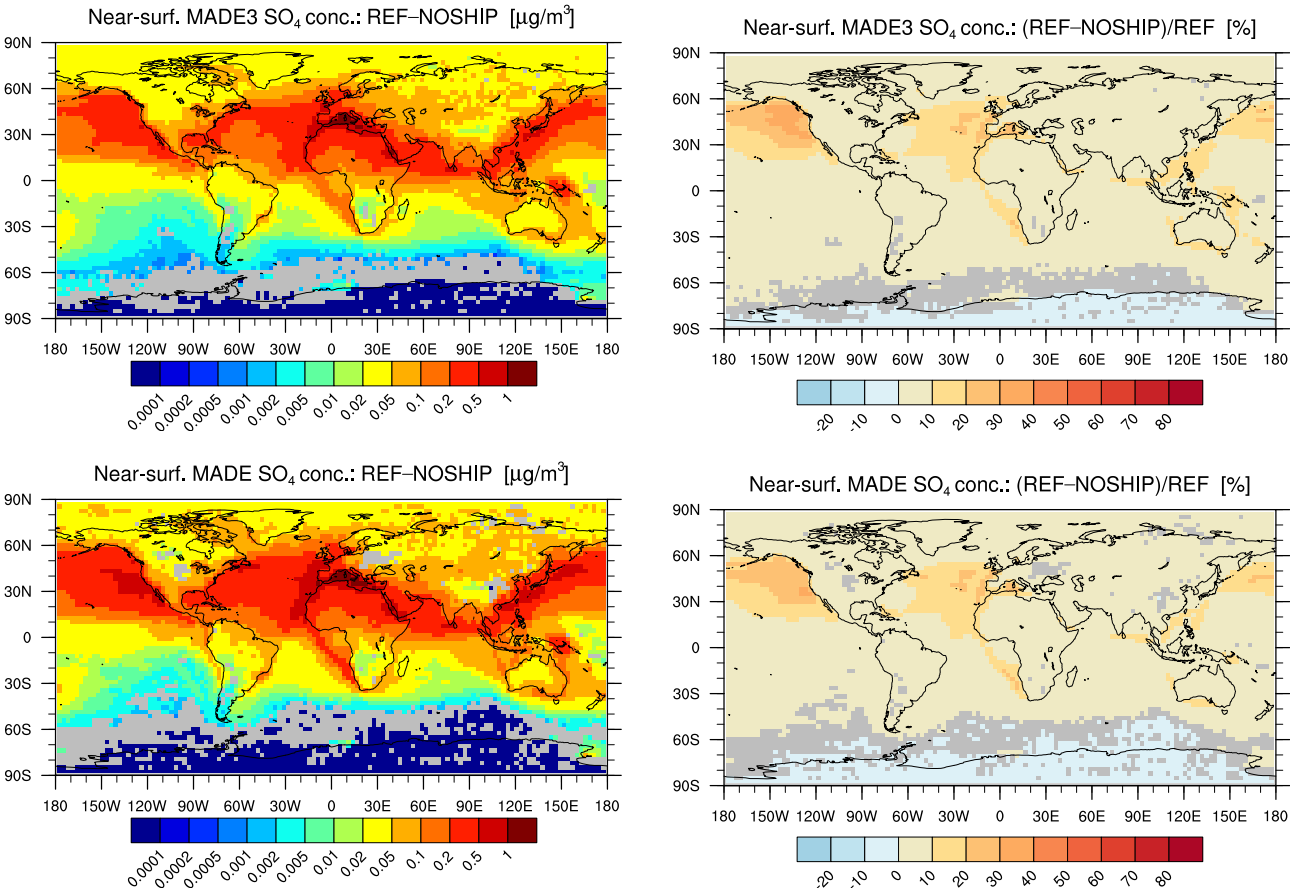

Figure 7.1: Ten-year average absolute (left) and relative (right) differences in near-surface SO_4 concentrations (sum over all modes) between simulations with ship emissions (REF, standard fuel) and without (NOSHIP). Simulations were performed with MADE3 (top) and MADE (bottom). Reference for the relative values is the respective simulation with ship emissions (REF). Differences in the gray areas could not be distinguished from interannual variability at the 95 % confidence level according to a uni-variate t test.

7.1.1 Near-surface concentrations

The discussion in this subsection is based on ten-year average values of near-surface concentrations. Figure 7.1 shows the absolute and relative contributions of ship emissions to total near-surface SO_4. The relative contribution (right panels) reaches values greater than 10 % mainly in those regions where heavy ship traffic occurs in an otherwise rather pristine atmosphere, namely over the northern hemisphere oceans. Maximum absolute contributions (left panels) are in the range of 0.2 to 1 µg m^{-3} where ship traffic is densest. Although the (negative) contribution over the Antarctic continent is statistically significant its relevance is questionable due to its very small magnitude. The MADE3 and MADE simulations yield similar values for the ship emissions-induced contributions to SO_4 concentrations, as only a very small amount of SO_4 partitions to the coarse modes in MADE3.

Absolute contributions to near-surface NO_3 concentrations are much larger over most of the northern hemisphere oceans and major ship routes in the southern hemisphere when simulated with MADE3 than when simulated with MADE (Fig. 7.2, top vs. bottom left). This is due to uptake of NO_3 into coarse mode sea spray (SS) particles by substitution for chloride (Cl) in the MADE3 simulation. Thus, the absolute contribution by ship emissions to the aerosol NO_3 content is of the same order of magnitude as the contribution to SO_4 when simulated with MADE3. It is much lower when using MADE because NO_3 can only be taken up by fine mode particles in MADE. Both submodels yield similar results when comparing the contributions to

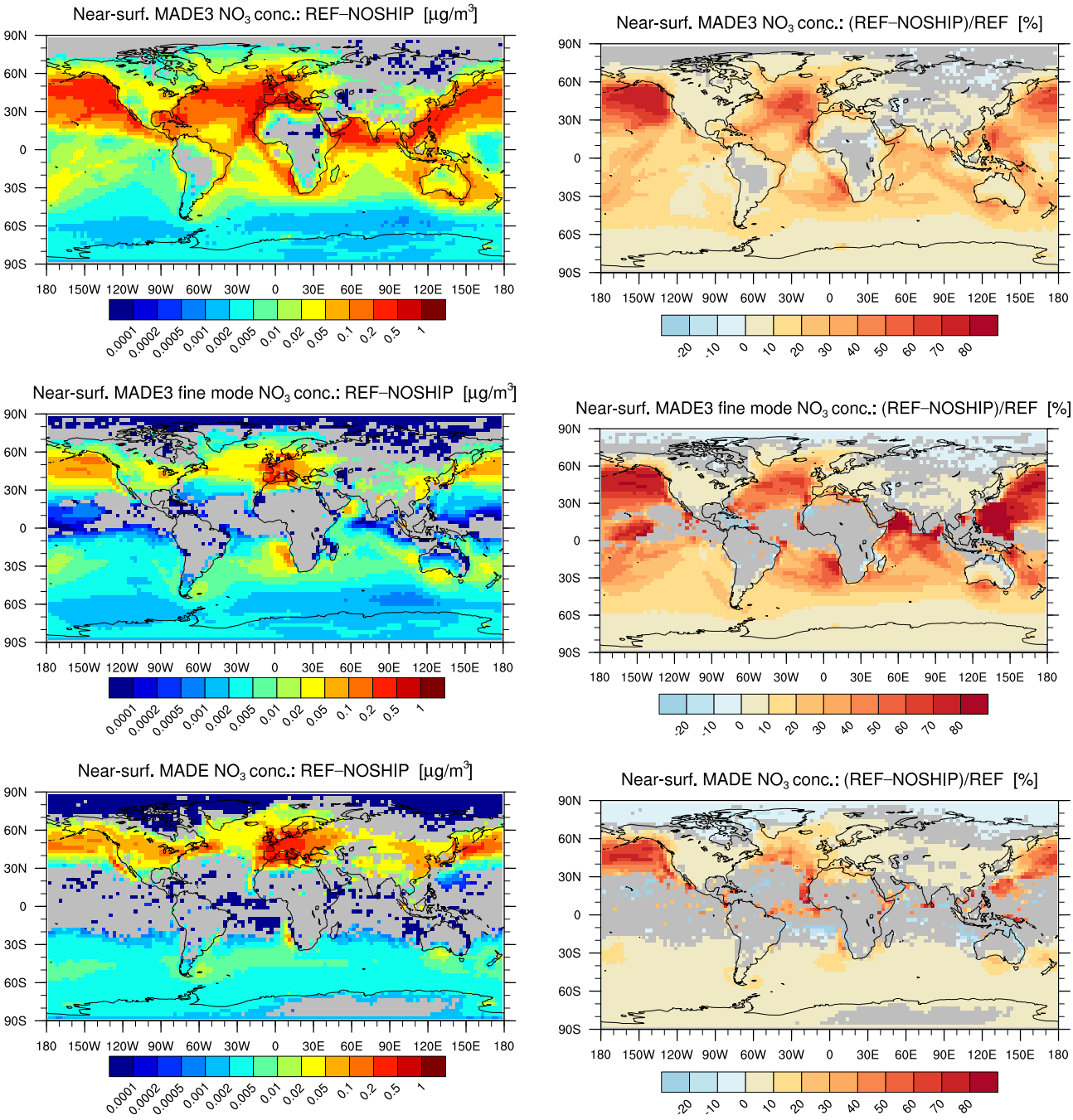

Figure 7.2: Top and bottom rows: same as Fig. 7.1, but for NO_3. Middle: same as top, but for the Aitken and accumulation mode NO_3 only.

the fine modes only (Fig. 7.2, middle and bottom left). With maximum values greater than 70 % the relative contribution by ship emissions to NO_3 is considerably larger than that to SO_4. It is even larger in the MADE3 simulations than in those with MADE, especially when considering only the fine modes (Fig. 7.2, middle right panel), where NO_3 replaces the Cl in accumulation mode SS particles. Since the MADE SS tracer is considered to be chemically inert, this pathway for NO_3 formation is not available in MADE. Furthermore, the background fine mode NO_3 concentration is larger in the simulation with MADE due to the longer residence time (Sect. 6.3). This also explains the larger absolute contributions to NO_3 concentrations over parts of the northern hemisphere continents seen in the MADE simulations, as the particles can be transported further inland.

As in the case of SO_4, the annual average fractions of POM and BC in the MADE3 coarse modes are of the order of a few percent or less. Hence, there is virtually no difference between

the comparisons of total and fine mode-only contributions by ship emissions-induced aerosol to these components. Both relative and absolute POM contributions are much smaller than those to SO_4 and NO_3. The relative BC contribution, however, is substantial over the northern mid-latitude Atlantic and Pacific oceans although its absolute contribution is also much smaller than those discussed above. Atlantic relative near-surface BC contributions reach up to ∼30 % with both submodels, while the maximum over the Pacific is about 20 percentage points larger with MADE3 (∼50 %) than with MADE.

Conclusions on aerosol particle number concentrations are independent of whether the coarse modes are included or not, as the number fraction in the coarse modes is negligible. This applies to both MADE3 and MADE. Both submodels yield similar absolute and relative contributions to the near-surface number concentrations. Again, the maximum relative contributions of 30 to 40 % are simulated over the North Pacific.

The absolute contributions by ship emissions-induced aerosol to near-surface fine mode SO_4, NO_3, and particle number concentrations simulated here are very similar to those obtained by R13 ("REF" simulation). This is not surprising, as the same emissions inventory and the same assumptions on the size distributions of the emitted particles were used. Nevertheless, L09 (scenario "ICOADS 2012 No control", see supplement) also obtained similar values for SO_4 using a different emissions inventory and a different size distribution.

In terms of relative SO_4 contributions the geographical pattern simulated here also resembles that obtained by R13, as well as those reported by L07 (Inventory C), L09, and Capaldo et al. (1999). However, while the magnitude of the values in the present study is similar to that found by Capaldo et al. (1999), it strongly differs from the results of the previous studies with MADE (L07, L09, R13). Those studies yielded relative contributions to SO_4 that were larger by a factor of up to ∼2, or more than 20 percentage points. This discrepancy may be caused by the longer residence times and associated higher background concentrations in the present work compared to other studies (Sects. 6.2.5 and 6.3). Another possible reason for different relative SO_4 contributions is the use of a new sea water dimethyl sulfide (DMS) climatology (Lana et al., 2011, Sect. 5.2) that may yield substantially different background SO_4 concentrations compared to the Kettle et al. (1999) climatology (Mahajan et al., 2015), which was used, for instance, in the R13 simulations.

Contributions by ship emissions to near-surface NO_3 concentrations were only reported by R13. Their results for the absolute contributions are remarkably similar to those obtained for the fine modes in the MADE3 simulation. Both the spatial distribution and the magnitude agree very well. Relative contributions also show a similar pattern, but are higher in the MADE3 simulation. This could be due to the different formation pathways of NO_3, as SS was not chemically active in the R13 study. Hence, NO_3 was added to the pre-existing aerosol in the R13 simulation, while it entered the MADE3 aerosol mainly by displacement of Cl from the SS particles.

Together, the similarities and differences in terms of ship emissions-induced SO_4 and NO_3 contributions between the present simulations and previous studies may also entail differences in the ship-induced radiative forcing (RF). Such effects will be the focus of a follow-up study with MADE3.

7.1.2 Near-surface size distributions

Annual and geographical median number and volume size distributions of particles in the lowermost atmospheric layer over the oceans are shown in the top panels of Fig. 7.3. The values are taken from the reference simulations with both MADE3 and MADE. While the number distributions look similar with the two submodels, it is evident from the volume distributions that coarse mode particles are larger in MADE3 than in MADE. With both submodels the

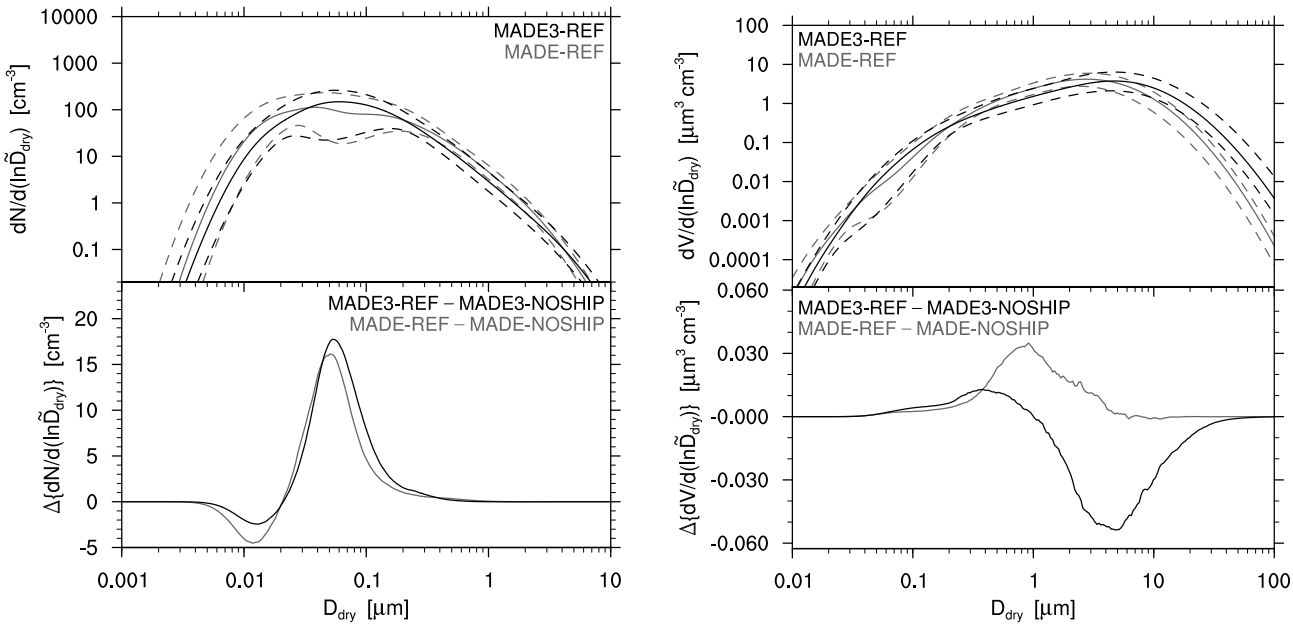

Figure 7.3: Top panels: annual and geographical median near-surface aerosol particle number (left) and volume (right) size distributions over the oceans in the reference simulations with MADE3 (black) and MADE (gray). The dashed lines show the 25$^{\text{th}}$ and 75$^{\text{th}}$ percentiles of the distributions. Lower panels: differences in size distributions between the reference simulations (REF) and those without ship emissions (NOSHIP).

peak number concentration densities are a few 10 % larger than those obtained by R13. A likely reason for such a difference lies again in the long residence times of the fine mode particles in the present simulations compared with previous studies (Sects. 6.2.5 and 6.3). As also mentioned in the size distribution evaluation (Sect. 6.3), the Aitken and accumulation modes can be more easily distinguished in the MADE size distribution than in the one derived from the MADE3 simulation.

Particle size can play an important role in the activation of aerosol particles into cloud droplets (Sect. 2.1.2). Changes in particle size can therefore lead to cloud perturbations, which in turn affect the earth's radiation budget. In order to judge the potential of the ship emissions-induced aerosol modifications to influence climate it is therefore useful to look at changes in the size distribution of the near-surface aerosol. To this end, the bottom panels of Fig. 7.3 show the differences in the size distributions between the reference simulations and those without ship emissions. Particle volume concentration density mainly changes in the accumulation mode size range when ship emissions are switched on in the MADE simulation (bottom right panel). In contrast, the MADE3 volume size distribution mainly changes in the coarse mode size range, which is not possible with MADE. The negative sign of this change is likely due to particle growth and subsequently more efficient deposition. Both the volume increase in MADE and the decrease in MADE3, however, are very small effects of the order of 1 %.

In terms of particle number concentration densities an increase is simulated with both submodels in the accumulation mode. This is likely due to growth of Aitken mode particles by condensation of ship-induced gas phase components and may provide additional cloud condensation nuclei (CCN) to the marine boundary layer (MBL). The relative increase in accumulation mode number concentration density due to ship emissions as simulated with both submodels is of the order of 10 %. Both this increase and the accompanying decrease in Aitken mode particle number concentration density seen in the bottom left panel of Fig. 7.3 were also simulated by R13 ("REF" simulation). One can thus expect that the change in activated CCN associated with ship emissions would also be similar in the present simulations as in the R13 simulations. Thus, the ship-induced RF of approximately $-150\,\mathrm{mW\,m^{-2}}$ (R13) can also be expected from

Table 7.1: Changes in multi-annual average global tropospheric and MBL aerosol burdens: values from simulations with ship emissions (standard fuel) minus values from simulations without. MBL values are calculated from the two lowest model layers, i.e., up to ∼230 m. The reference (denominator) for the relative difference given in parentheses is the value from the respective simulation that includes ship emissions. Cl is not simulated by MADE. MBL burdens were only calculated for the species also reported by R13.

Species	Δ(Burden global) [Tg]		Δ(Burden MBL) [Gg]	
	MADE3	MADE	MADE3	MADE
SO_4	0.11 (3.2 %)	0.14 (3.1 %)	7.84 (8.2 %)	10.64 (7.5 %)
NH_4	0.02 (2.1 %)	0.00 (0 %)	1.32 (6.1 %)	0.85 (2.9 %)
NO_3	0.02 (3.8 %)	0.00 (0 %)	5.54 (23.1 %)	1.17 (12.7 %)
Na*	0.00 (0 %)	0.00 (0 %)	—	—
Cl	−0.02 (−1.1 %)	—	—	—
POM	0.00 (0 %)	0.00 (0 %)	0.39 (0.9 %)	0.29 (0.8 %)
BC	0.00 (0 %)	0.00 (0 %)	0.22 (4.1 %)	0.23 (3.6 %)
DU^+	0.00 (0 %)	0.00 (0 %)	—	—

* for MADE: SS values

+ mineral dust

simulations with MADE3. As mentioned above, the quantification of this forcing will be the subject of a follow-up study with MADE3.

7.1.3 Tropospheric burdens

Switching on ship emissions leads to an increase in the tropospheric SO_4 burden (calculated as in Sect. 6.2.5). With both submodels, i.e., with MADE3 and MADE, approximately 3 % of the SO_4 in the reference simulations can be attributed to ship emissions (columns "Δ(Burden global)" of Table 7.1). This value is in line with previous estimates obtained using MADE (L07, L09), although the absolute contributions calculated here are 2 to 3 times as large as those found by L07 (Inventory C), Fuglestvedt et al. (2008), and L09 (scenarios "2002" and "2012 No control"). As the burdens simulated here are also much larger than those found in the referenced studies this is not surprising. A similar relative contribution as for SO_4 is also simulated for the NO_3 burden with MADE3. The value of 3.8 % falls between the results reported by L07 and L09. Absolute contributions are again higher than in these studies.

In MADE3 the major fraction of the additional NO_3 is formed by displacement of Cl from the SS particles, which is not possible in MADE. Hence, the Cl burden decreases in the MADE3 simulations when switching on ship emissions, while the MADE SS burden remains constant. The additional ammonium (NH_4) formation simulated with MADE3 but not with MADE (Table 7.1) indicates that in the MADE3 simulation a substantial fraction of the anions is bound to sodium (Na) rather than NH_4 in the simulation without ship emissions. Hence, there is still some ammonia (NH_3) available to neutralize additional SO_4 and NO_3 when switching on these emissions, which is apparently not the case in the MADE simulation. Effects of ship emissions on tropospheric POM and BC burdens could not be detected in the present simulations.

In order to also compare the results obtained here to those reported by R13, oceanic burdens in the two lowermost model levels (up to ∼230 m, Table 7.1) were computed in addition to the global full-column burdens. The results are strikingly different. In this comparison the results

of the present MADE simulations are very similar to those obtained by R13 in terms of absolute contributions, but the relative contributions are about a factor of two lower here. Absolute contributions to NO_3 and NH_4 are larger with MADE3 than with MADE due to the reasons described above, and relative contributions to these two species are close to the R13 values in the MADE3 simulation. The rest of the contributions are similar in the MADE3 and MADE simulations performed here. The differences to the study by R13 can be explained as follows. Concentrations in the lowermost model layers are controlled mainly by emissions or their absence. Hence, absolute contributions by ship emissions are similar in the two studies, as the same emissions inventories were used. However, due to the higher background concentrations in the present simulations, the corresponding relative contributions are lower. Furthermore, for NO_3 and NH_4 in the MADE3 simulations, there are differences in the absolute contributions due to the uptake of NO_3 into coarse mode particles and due to the NH_4 formation from excess NH_3 as described above.

7.2 Effects of an idealized fuel sulfur content reduction

This section is dedicated to changes in the ship emission effects on the aerosol when switching from standard fuel to low-sulfur fuel. It is based on the results of simulations with MADE3 and MADE in which ship emissions were set at year 2000 levels, except for the sulfur-containing species, for which the year 2000 values were reduced by a factor of 10. This is the global average factor that corresponds to the reductions in fuel sulfur content by the year 2020 due to new regulations as described by L09.

Since other aerosol components are affected less by ship emissions (see previous section) the focus here is on SO_4 and NO_3 concentrations. Only "contributions" of ship emissions (defined as in the beginning of this chapter) to the fine mode concentrations are considered, because they are the potential drivers of changes in aerosol–cloud interactions. Furthermore, the effect of ship emissions on the size distribution is re-quantified for the low-sulfur fuel scenario and compared to the results presented in the previous section.

The top left panel of Fig. 7.4 shows the absolute contribution of emissions from ships to the near-surface fine mode SO_4 concentrations ("near-surface" meaning "in the lowermost model layer" as above) under the low-sulfur fuel scenario. Although the geographical pattern is similar to that when using standard fuel (Fig. 7.1, top left), the magnitude of the SO_4 contribution is much smaller when using the idealized low-sulfur fuel and is now comparable to that of the NO_3 contribution (Fig. 7.4, top right). The middle panels of Fig. 7.4 show the differences, i.e., the SO_4 reduction and NO_3 increase, when switching from standard to low-sulfur fuel. It is immediately evident that the additional NO_3 uptake cannot balance the "loss" of SO_4. The same conclusion holds for the simulations with MADE, as shown in the bottom panels of Fig. 7.4. Both the SO_4 reduction and the NO_3 increase are slightly higher than when using MADE3, but the differences are generally small. In the present simulations coarse mode particle interactions apparently do not strongly affect the changes in fine mode SO_4 and NO_3 concentrations when switching to low-sulfur ship fuel.

The corresponding changes in fine mode number size distributions are also very similar in the MADE3 and MADE simulations (Fig. 7.5, bottom left panel vs. Fig. 7.3, bottom left panel): Aitken mode particles grow less if low-sulfur fuel is used, due to reduced SO_4 availability. Accumulation mode particles also grow less, which is mainly visible in the reduced volume growth simulated by MADE in that size range compared to the reference simulation (bottom right panel of Fig. 7.5 vs. bottom right panel of Fig. 7.3). Since the shipping effect on coarse mode particle volume concentration density—as simulated with MADE3—is mainly due to NO_3 uptake, it does not change substantially when switching to low-sulfur ship fuel.

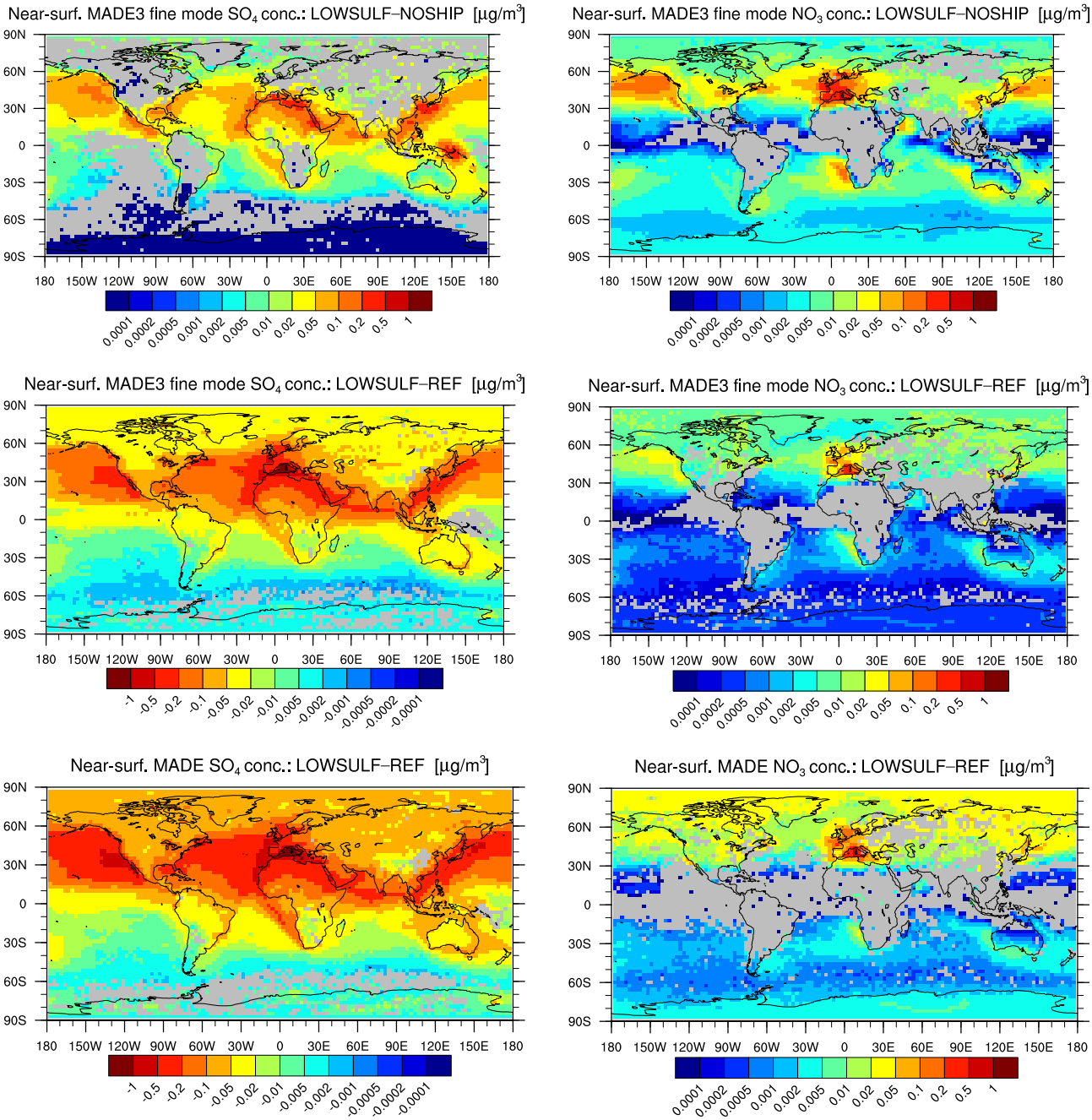

Figure 7.4: Ten-year average absolute differences in near-surface SO_4 (left) and NO_3 (right) concentrations between different simulations. Top: simulation with emissions from ships using low-sulfur fuel (LOWSULF) vs. simulation without ship emissions (NOSHIP), i.e., the effect of low-sulfur fuel ship emissions on aerosol concentrations (MADE3); middle: simulation with low-sulfur fuel ship emissions vs. reference simulation (REF, standard fuel), i.e., the change in effect of ship emissions when switching from standard to low-sulfur fuel (MADE3); bottom: same as middle, but for MADE simulations. Note the negative numbers in the middle and bottom left panels, which are used to ease the visual comparison to the right-hand side panels of this figure and to the left-hand side panels of Fig. 7.1. Differences in the gray areas could not be distinguished from interannual variability at the 95 % confidence level according to a uni-variate t test.

Both the relative reduction in SO_4 and the relative increase in NO_3 concentrations when switching to low-sulfur ship fuel appear to be substantially smaller here than in previous studies (L09; Righi et al., 2011). It will be tested as part of a future study with MADE3 whether this difference is caused by the long residence times of fine mode particles in the present simulations.

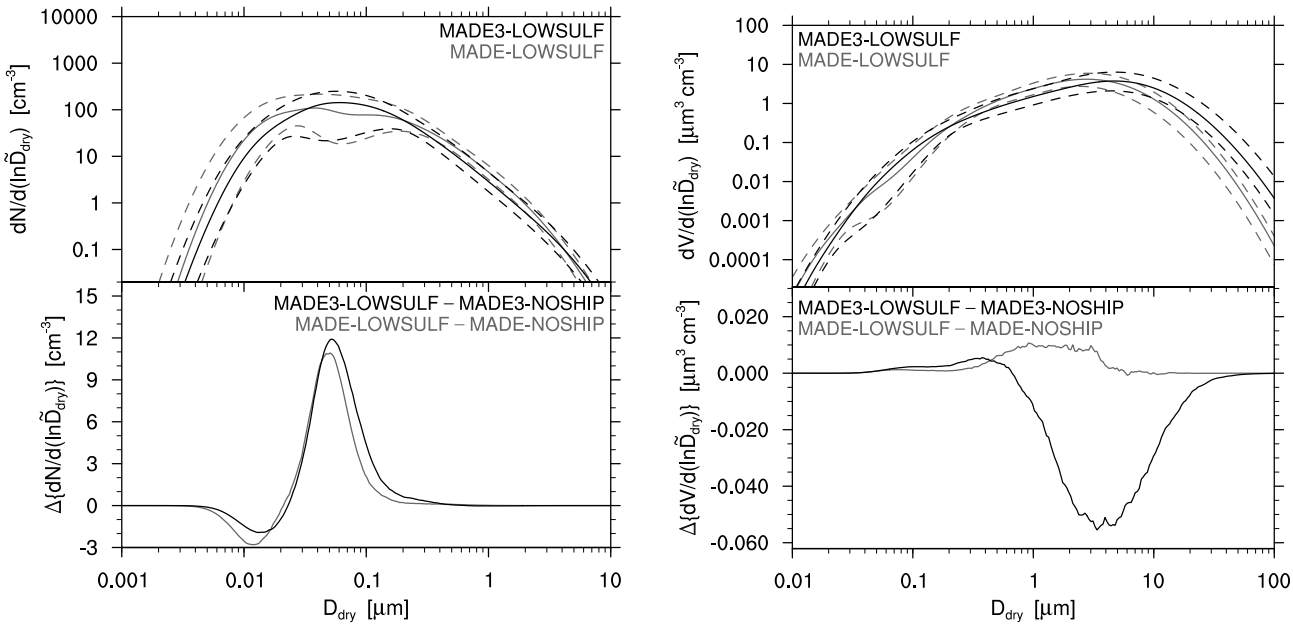

Figure 7.5: Same as Fig. 7.3, but for low-sulfur fuel simulations (LOWSULF) instead of the reference simulations.

7.3 Summary and conclusions

The effects of ship emissions on atmospheric aerosol composition and size distribution were simulated with the new submodel MADE3 and its predecessor MADE in EMAC (MESSy version 2.50). Comparing the results obtained with the two submodels allowed for an assessment of the role of coarse mode particles in these effects. The reference simulations were conducted with an emissions dataset representative of the year 2000. In order to also estimate the effect of current and future regulations on ship fuel sulfur content, additional sensitivity simulations were performed, with sulfur emissions reduced by 90 %.

Ship emissions at year 2000 levels provided an absolute contribution to near-surface SO_4 concentrations of up to $\sim$1 µg m^{-3} where ship traffic is densest, and a relative contribution of up to $\sim$40 % over the northern hemisphere oceans. As SO_4 was found to partition mainly to the fine modes, coarse mode particle interactions did not affect this result. For NO_3, however, the difference between the MADE3 and MADE simulations was large when the absolute increase in near-surface concentration was considered. This was due to additional uptake of NO_3 into coarse mode SS particles by substitution for Cl in MADE3, which is not possible in MADE. Thus, in the MADE3 simulations, the NO_3 increase was similar to that of SO_4, whereas it was much smaller in the MADE simulations. When the analysis was reduced to the fine modes, similar results were again obtained with both submodels. Maximum relative increases of near-surface fine mode NO_3 were about twice as large as those of SO_4. Ship emissions also include BC and POM but these were found to be minor contributors to aerosol mass concentration changes. Particle number concentrations increased due to ship emissions, with maximum relative contributions of 30 to 40 %. Mostly, these additional particles were found in the accumulation modes, as growth of Aitken mode particles was enhanced by the oxidation products of the ship emissions. The maxima of the ship effects on near-surface concentrations of both particle mass and number were located over the North Pacific and, with slightly lower values, over the North Atlantic. Global tropospheric burdens were affected much less by ship emissions than near-surface concentrations. For SO_4 a relative contribution of $\sim$3 % was simulated with both submodels. For NO_3 the relative contribution was of a similar magnitude when

using MADE3 due to the uptake into coarse mode SS particles, but much smaller in the MADE simulation. Ship emission effects on other species were minor compared to those on SO_4 and NO_3.

When switching to low-sulfur fuels the absolute contributions of fine mode SO_4 and NO_3 to near-surface concentrations were of a similar magnitude, as SO_4 formation was strongly reduced and NO_3 formation slightly increased. This led to a smaller enhancement of accumulation mode particle number concentrations than in the standard fuel simulations. Both submodels yielded similar results here.

Two main findings emerged from the comparison of the present simulations with MADE3 and MADE in EMAC (MESSy version 2.50), and from the comparison of these simulations to previous studies that employed MADE as part of EMAC (MESSy version 1.4). Firstly, in the comparisons to the studies with the older EMAC version, the long residence times and associated large background concentrations of the fine mode species in the present simulations were a recurrent theme. For instance, the absolute contributions to near-surface SO_4 simulated here agreed well with those found in a recent study by Righi et al. (2013), while the relative contributions were smaller here by a factor of up to $\sim$2. The long residence times will therefore be investigated in detail in a follow-up study. Secondly, the NO_3 formation by displacement of Cl from SS particles, which only MADE3 can simulate, played a role for ship emission effects on coarse mode particles. Much more NO_3 was taken up in the MADE3 simulations than in the MADE simulations, the additional uptake being almost exclusively due to the interaction of coarse mode SS particles with the ship exhaust. It remains for a follow-up study to assess in how far these differences will alter the conclusions from previous studies on the ship emissions-induced aerosol effects on climate.

Chapter 8

Summary, conclusions, and outlook

Summary

Motivated by deficiencies in the aerosol microphysics (sub)models that have been used to quantify the climatic impact of ship emissions-induced aerosol perturbations, the MESSy submodel MADE for the atmospheric chemistry general circulation model EMAC was substantially extended as part of the present work. Both the first and the second generation (MADE-in) of the submodel were not capable of simulating the microphysics of coarse mode particles. Furthermore, they lacked a description of the so-called chloride depletion of sea spray particles. However, these processes potentially play an important role in the ship emissions-induced aerosol perturbations. Both processes were therefore implemented into MADE-in to create the third generation submodel, MADE3. For this purpose the microphysics code was completely revised and extended by several important features. The formerly passive coarse mode is now considered in both the particle coagulation and the gas–particle partitioning calculations. It was split up into one mode each for fully soluble particles, for insoluble particles, and for mixed particles in analogy to the MADE-in fine modes. Thus, aging of insoluble particles can now also be simulated for the coarse modes, e.g., for mineral dust (DU) particles. The number of possible coagulation processes more than doubled between MADE-in and MADE3. Furthermore, the gas–particle equilibrium solver was also extended, namely by the partitioning of chlorine between hydrochloric acid in the gas phase and chloride in the aerosol phase. The inclusion of interactions of condensable gases with coarse mode particles in this solver required additional considerations because—in contrast to fine mode particles—coarse mode particles may take longer than a typical model time step of 30 min to attain equilibrium with the gas phase. A flux-limiting approach was chosen and implemented to tackle this problem.

The new generation of the submodel was first applied in an idealized box model test case scenario. It could thus be compared to its predecessor MADE, which was used in previous assessments of ship emissions-induced aerosol perturbations, and to the much more detailed, particle-resolved aerosol model PartMC-MOSAIC. The latter was used as a benchmark for the description of the aerosol microphysical processes in MADE3. The intercomparison showed similar performance of MADE3 and MADE in reproducing the PartMC-MOSAIC solution in the fine mode size range. For the coarse mode size distribution and for total aerosol composition it clearly revealed an improved performance of MADE3 w.r.t. MADE.

Having achieved this intermediate goal, the new submodel was implemented into EMAC. Extensive adaptations of the model system were necessary for this purpose. The new mode structure of MADE3 had to be implemented into the submodel that computes aerosol optical properties and into the submodel that treats the effects of clouds and precipitation on the aerosol. Especially the routines that are involved in the redistribution of aerosol among the modes after cloud or precipitation processing required careful revision. Furthermore, the emissions dataset had to be reprocessed for appropriate allocation of aerosol emissions to the MADE3 modes.

Once the implementation into EMAC was accomplished, the coupled model was evaluated with respect to observed properties of the atmospheric aerosol. The evaluation included comparisons to station network measurements of near-surface aerosol component mass concentrations,

to airborne measurements of vertical aerosol mass mixing ratio and number concentration profiles, to ground-based and airborne measurements of particle size distributions, and to station network and satellite measurements of aerosol optical depth (AOD). It was thus shown that the new model successfully reproduces observed properties of the atmospheric aerosol such as the spatial patterns of component mass concentrations, for instance. Deviations were within the range of discrepancies occurring also in simulations with other, comparable models. Such discrepancies were expected, as, for instance, the localization of measurements in space and time vs. the coarse model resolution, measurement limitations, and other comparability issues inevitably lead to differences between simulations and observations. Average aerosol concentrations were found to be biased high in a number of cases. Together with a comparison of speciated tropospheric burdens and residence times to estimates from other models, this finding led to the conclusion that deposition of fine mode particles may be underestimated in the current version of EMAC, and deposition of coarse mode particles potentially overestimated. A thorough investigation of these issues was beyond the scope of the present work, but will be performed as part of a follow-up study. That said, the fraction of simulated monthly mean near-surface concentrations within a factor of two of the observations was often greater than 50 %, even in the cases with average overestimation. Thus, EMAC with MADE3 performs well in comparison to the results from similar studies with other models. The same applies to deviations from observed vertical profiles, size distributions, and AOD. In conclusion, the extensive model evaluation showed that MADE3 with its detailed representation of mixing state and coarse mode particle interactions is ready for application as part of EMAC.

In order to assess the effect of the newly introduced features of MADE3, an identically designed evaluation simulation was performed with the predecessor submodel MADE. A comparison of the results showed that a fraction of the secondary species is taken up into coarse mode particles in MADE3, which leads to more efficient removal of these components from the atmosphere.

Subsequently, EMAC was applied with MADE3 to (re)quantify the ship emissions-induced effects on the atmospheric aerosol. The findings for year 2000 conditions were broadly similar to those reported in other publications. The dominant species in this context was found to be sulfate (SO_4), with an absolute contribution to near-surface concentrations of up to $1\,\mu g\,m^{-3}$ where ship traffic is densest. The largest relative contributions were found over the northern hemisphere oceans. With up to ∼40 % they were lower than in previous studies with MADE in an older EMAC version. Fine mode particle growth, which is important for the climatic effect of aerosol particles, was similar in the present simulations as in a recent simulation with the older model version. As ship fuel sulfur content is expected to decrease in the future due to increasingly stringent regulations, an idealized simulation of such reductions was also performed here. It showed large reductions in the contribution of ship traffic to the near-surface SO_4 concentrations. Consequently, fine mode particle growth was also reduced, as additional nitrate (NO_3) uptake w.r.t. to the standard fuel scenario only compensated for a fraction of the reduction in fine mode SO_4 formation.

The ship traffic-related simulations were also performed with MADE. Important differences between the MADE3 simulations and the MADE simulations, i.e., effects due to the inclusion of coarse mode microphysics and the gas–particle partitioning of chlorine, were mainly seen in the coarse mode chloride (Cl) and NO_3 concentrations over the oceans. While NO_3 could only be formed in the fine mode particles in MADE, the major fraction of this component was found in the coarse modes in the MADE3 simulations. However, this did not mean that the fine modes were depleted in NO_3 w.r.t. the MADE simulations. Rather, coarse mode NO_3 formed in addition to the fine mode NO_3. Furthermore, NO_3 was formed via different pathways in the MADE3 and MADE simulations. While it was added to the pre-existing aerosol in the MADE simulations, it rather formed by substitution for Cl in sea spray particles in the MADE3 simulations. Ship emissions-induced growth of small aerosol particles to sizes

relevant for activation as cloud condensation nuclei was similar to that found in a previous study with MADE in the older EMAC version.

Conclusions

Briefly summarized, the conclusions from the present work and the answers to the scientific questions (Sect. 1.2) are as follows.

- The representation of coarse mode particle size distribution and total aerosol composition were improved in MADE3 w.r.t. MADE.
- The new model, i.e., EMAC with MADE3, is able to reproduce the climatology of globally observed aerosol properties.
- The inclusion of coarse mode particle interactions with fine particles and with the gas phase leads to quicker removal of secondary aerosol species from the atmosphere, and thus to lower concentrations of these species (Question 1). Other species and number concentrations are affected less.
- The present work supports the main conclusions from previous studies on the effects of ship emissions on the global fine mode aerosol, and specifically on SO_4 concentrations.
- The inclusion of coarse mode particle interactions allows the formation of much larger amounts of NO_3 from ship emissions, mainly by substitution for Cl in sea spray particles. This conclusion holds for both year 2000 conditions and a scenario representative of anticipated future ship fuel sulfur content reductions (Questions 2 and 3).

Outlook

The influence of the inclusion of coarse mode microphysics and chloride depletion on the calculated radiative effect (RE) of ship emissions-induced perturbations to the atmospheric aerosol will be re-quantified in a follow-up study. For the calculation of the RE the MADE3 aerosol will be coupled to a two-moment cloud scheme that will be driven by the MADE3 aerosol properties as an input. Furthermore, the explicit representation of mixing state that is possible with the three modes per size range in MADE3 allows for many new applications beyond the investigation of shipping effects. In particular, the model will be applied to assess aerosol effects on ice clouds, with a specific focus on emissions of the transport sector as a whole, i.e., including also land transport and aviation. Additionally, it is planned to perform simulations specific to the episodes during which measurement campaigns took place. Thus, deviations between simulations and observations due to different meteorology and emissions can be minimized. On the one hand, such simulations will allow for an in-depth, process-oriented model evaluation with the potential to identify areas of further model improvement. On the other hand, they are expected to provide valuable input for the interpretation of measurement results.

Further model developments are conceivable and could be explored in the future. A short, non-exhaustive summary of what the author regards as the most promising or interesting options shall conclude this thesis. For instance, new parameterizations of DU and sea spray (SS) emissions were recently developed and could be tested in EMAC with MADE3. They could possibly help to improve simulated AOD in regions where DU and SS are dominant, and to obtain better agreement with sodium and Cl concentration measurements. In addition, as previous studies showed a strong dependence of climatic effects on the size distributions of emitted particles, the assumptions on those may be varied, for example in order to estimate an uncertainty range of the calculated RE. Besides emissions size distributions, the effects of changes in a number of further uncertain parameters may be investigated. A very interesting

example in this context could be the mode widths, as measurements often find narrower accumulation modes than what is currently assumed in MADE3. Furthermore, knowledge of the mixing state of insoluble particles is crucial for future studies on ice cloud effects. It would therefore be worthwhile to compare simulation results with different aging criteria for these particles, e.g., a scheme that shifts mass and number concentrations more continuously from the insoluble to the mixed modes than the current treatment. Finally, various sensitivity studies on the interactions between the gas and the aerosol phase are conceivable. These include an investigation of the effects of the simplifications in the gas phase chemical mechanism; a test of different, more advanced gas–particle partitioning schemes; inclusion of the chemical activity of DU particles; and inclusion of organic gas phase chemistry and gas–particle partitioning. Many of the above-mentioned changes to the model system could also have an effect on the ship emissions-induced aerosol perturbation investigated as part of the present work. All of them would help identify areas that warrant more detailed studies in the future.

Appendix

A.1 Particle evolution in the box model study

Figure A.1 shows the initial and final states of the aerosol population as simulated by MADE3 and PartMC-MOSAIC. The figure illustrates the evolution of the aerosol composition under additional consideration of the size distribution. Composition is shown in a size-binned representation to facilitate the comparison of the individual panels. The top left panel contains the same data as Fig. 4.1 (note that the mass fractions of mineral dust are so small that they are not visible in Fig. A.1).

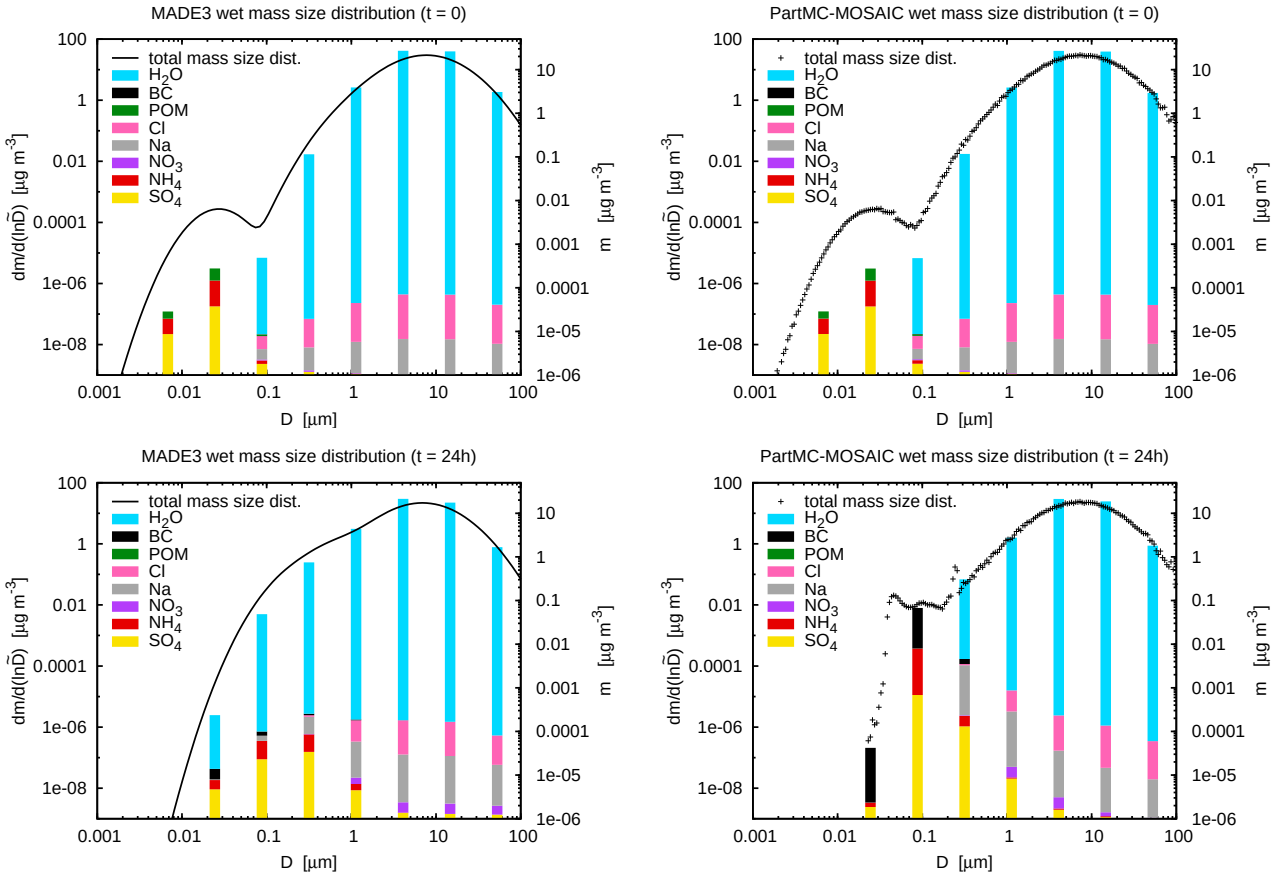

Figure A.1: Aerosol mass size distributions and size-resolved composition at $t = 0$ (top panels) and $t = 24\,\mathrm{h}$ (bottom panels) for MADE3 (left panels) and PartMC-MOSAIC (right panels) in the test case scenario described in Sect. 4.3. Total mass size distributions are shown in the MADE3 panels as black lines (calculated as the sums over the modes), in the PartMC-MOSAIC panels as black crosses (left vertical axes). The colored bars show the contributions of the individual species (POM = particulate organic matter, BC = black carbon) to the respective mass concentrations (right vertical axes). In the PartMC-MOSAIC plots particles were binned into size sections, and the bars show the average compositions in these sections. For the MADE3 plots the binned mass concentrations were computed as the sums (across all modes) over the fractions of particles that fell within the same size sections. Note that while the right vertical axes are logarithmic, the species fractions in the bars add up linearly to the total mass concentrations (i.e., the axes only apply to the total mass concentration in each bin, but not to the individual contributions).

The two lower row plots in Fig. A.1, representing the aerosol state after 24 h of simulated time, show the same general features: higher SO_4 fractions in the fine particles, predominant NO_3 partitioning to large rather than small particles, and notable black carbon (BC) concentrations only in fine particles. Despite this agreement, one can also see that the modal approach leads to distribution of the components over wider size ranges. Since, due to their width, the modes contain particles of a broad range of sizes, this is inevitable in modal models.

The smallest particles do not take up water in PartMC-MOSAIC because they are assumed to be dry initially (Zaveri et al., 2005a) and the deliquescence relative humidity of ammonium sulfate ($(NH_4)_2SO_4$) is higher than the environmental relative humidity specified in our experiment (0.771). Conversely, in EQSAM, these particles do take up water due to the presence of small quantities of other components that reduce the particles' deliquescence relative humidity.

A.2 Gas phase chemical mechanism

The following pages were output automatically when creating the chemistry mechanism for MECCA.

The Chemical Mechanism of MECCA

KPP version: `2.2.1_rs5`

MECCA version: `3.6`

Date: March 9, 2015.

Selected reactions:
"`Tr && G && !C && !Cl && !Br && !I && !Hg`"

Number of aerosol phases: 0

Number of species in selected mechanism:

Gas phase:	33
Aqueous phase:	0
All species:	33

Number of reactions in selected mechanism:

Gas phase (Gnnn):	45
Aqueous phase (Annn):	0
Henry (Hnnn):	0
Photolysis (Jnnn):	13
Aqueous phase photolysis (PHnnn):	0
Heterogeneous (HETnnn):	0
Equilibria (EQnn):	0
Isotope exchange (DGnnn):	0
Dummy (Dnn):	0
All equations:	58

This document is part of the electronic supplement to our article
"The atmospheric chemistry box model CAABA/MECCA-3.0"
in Geosci. Model Dev. (2011), available at:
`http://www.geosci-model-dev.net`

Table 1: Gas phase reactions

#	labels	reaction	rate coefficient	reference
G1000	UpStTrG	$O_2 + O(^1D) \rightarrow O(^3P) + O_2$	3.3E-11*EXP(55./temp)	Sander et al. (2011)
G1001	UpStTrG	$O_2 + O(^3P) \rightarrow O_3$	6.E-34*((temp/300.)**(-2.4))*cair	Sander et al. (2011)
G2100	UpStTrG	$H + O_2 \rightarrow HO_2$	k_3rd(temp,cair,4.4E-32,1.3,7.5E-11, -0.2,0.6)	Sander et al. (2011)
G2104	UpStTrG	$OH + O_3 \rightarrow HO_2 + O_2$	1.7E-12*EXP(-940./temp)	Sander et al. (2011)
G2105	UpStTrG	$OH + H_2 \rightarrow H_2O + H$	2.8E-12*EXP(-1800./temp)	Sander et al. (2011)
G2107	UpStTrG	$HO_2 + O_3 \rightarrow OH + 2\ O_2$	1.E-14*EXP(-490./temp)	Sander et al. (2011)
G2109	UpStTrG	$HO_2 + OH \rightarrow H_2O + O_2$	4.8E-11*EXP(250./temp)	Sander et al. (2011)
G2110	UpStTrG	$HO_2 + HO_2 \rightarrow H_2O_2 + O_2$	k_HO2_HO2	Christensen et al. (2002), Kircher and Sander (1984)*
G2111	UpStTrG	$H_2O + O(^1D) \rightarrow 2\ OH$	1.63E-10*EXP(60./temp)	Sander et al. (2011)
G2112	UpStTrG	$H_2O_2 + OH \rightarrow H_2O + HO_2$	1.8E-12	Sander et al. (2011)
G3101	UpStTrGN	$N_2 + O(^1D) \rightarrow O(^3P) + N_2$	2.15E-11*EXP(110./temp)	Sander et al. (2011)
G3103	UpStTrGN	$NO + O_3 \rightarrow NO_2 + O_2$	3.E-12*EXP(-1500./temp)	Sander et al. (2011)
G3106	StTrGN	$NO_2 + O_3 \rightarrow NO_3 + O_2$	1.2E-13*EXP(-2450./temp)	Sander et al. (2011)
G3108	StTrGN	$NO_3 + NO \rightarrow 2\ NO_2$	1.5E-11*EXP(170./temp)	Sander et al. (2011)
G3109	UpStTrGN	$NO_3 + NO_2 \rightarrow N_2O_5$	k_NO3_NO2	Sander et al. (2011)*
G3110	StTrGN	$N_2O_5 \rightarrow NO_2 + NO_3$	k_NO3_NO2/(2.7E-27*EXP(11000./temp))	Sander et al. (2011)*
G3200	TrGN	$NO + OH \rightarrow HONO$	k_3rd(temp,cair,7.0E-31,2.6,3.6E-11, 0.1,0.6)	Sander et al. (2011)
G3201	UpStTrGN	$NO + HO_2 \rightarrow NO_2 + OH$	3.3E-12*EXP(270./temp)	Sander et al. (2011)
G3202	UpStTrGN	$NO_2 + OH \rightarrow HNO_3$	k_3rd(temp,cair,1.8E-30,3.0,2.8E-11,0., 0.6)	Sander et al. (2011)
G3203	StTrGN	$NO_2 + HO_2 \rightarrow HNO_4$	k_NO2_HO2	Sander et al. (2011)*
G3204	TrGN	$NO_3 + HO_2 \rightarrow NO_2 + OH + O_2$	3.5E-12	Sander et al. (2011)
G3205	TrGN	$HONO + OH \rightarrow NO_2 + H_2O$	1.8E-11*EXP(-390./temp)	Sander et al. (2011)
G3206	StTrGN	$HNO_3 + OH \rightarrow H_2O + NO_3$	k_HNO3_OH	Sander et al. (2011)*
G3207	StTrGN	$HNO_4 \rightarrow NO_2 + HO_2$	k_NO2_HO2/(2.1E-27*EXP(10900./temp))	Sander et al. (2011)*
G3208	StTrGN	$HNO_4 + OH \rightarrow NO_2 + H_2O$	1.3E-12*EXP(380./temp)	Sander et al. (2011)
G4101	StTrG	$CH_4 + OH \rightarrow CH_3O_2 + H_2O$	1.85E-20*EXP(2.82*log(temp)-987./temp)	Atkinson (2003)
G4102	TrG	$CH_3OH + OH \rightarrow HCHO + HO_2$	2.9E-12*EXP(-345./temp)	Sander et al. (2011)
G4103	StTrG	$CH_3O_2 + HO_2 \rightarrow CH_3OOH + O_2$	4.1E-13*EXP(750./temp)	Sander et al. (2011)*
G4104	UpStTrGN	$CH_3O_2 + NO \rightarrow HCHO + NO_2 + HO_2$	2.8E-12*EXP(300./temp)	Sander et al. (2011)
G4105	TrGN	$CH_3O_2 + NO_3 \rightarrow HCHO + HO_2 + NO_2$	1.3E-12	Atkinson et al. (2006)

Table 1: Gas phase reactions (... continued)

#	labels	reaction	rate coefficient	reference
G4106a	StTrG	$CH_3O_2 + CH_3O_2 \rightarrow 2\ HCHO + 2\ HO_2$	9.5E-14*EXP(390./temp)/(1.+1./26.2*EXP(1130./temp))	Sander et al. (2011)
G4106b	StTrG	$CH_3O_2 + CH_3O_2 \rightarrow HCHO + CH_3OH + O_2$	9.5E-14*EXP(390./temp)/(1.+26.2*EXP(-1130./temp))	Sander et al. (2011)
G4107	StTrG	$CH_3OOH + OH \rightarrow .7\ CH_3O_2 + .3\ HCHO + .3\ OH + H_2O$	k_CH3OOH_OH	Sander et al. (2011)*
G4108	StTrG	$HCHO + OH \rightarrow CO + H_2O + HO_2$	9.52E-18*EXP(2.03*log(temp)+636./temp)	Sivakumaran et al. (2003)
G4109	TrGN	$HCHO + NO_3 \rightarrow HNO_3 + CO + HO_2$	3.4E-13*EXP(-1900./temp)	Sander et al. (2011)*
G4110	UpStTrG	$CO + OH \rightarrow H + CO_2$	(1.57E-13+cair*3.54E-33)	McCabe et al. (2001)
G4111	TrG	$HCOOH + OH \rightarrow CO_2 + HO_2 + H_2O$	4.0E-13	Sander et al. (2011)
G9200	StTrGS	$SO_2 + OH \rightarrow H_2SO_4 + HO_2$	k_3rd(temp,cair,3.3E-31,4.3,1.6E-12,0.,0.6)	Sander et al. (2011)
G9400a	TrGS	$DMS + OH \rightarrow CH_3SO_2 + HCHO$	1.13E-11*EXP(-253./temp)	Atkinson et al. (2004)*
G9400b	TrGS	$DMS + OH \rightarrow DMSO + HO_2$	k_DMS_OH	Atkinson et al. (2004)*
G9401	TrGNS	$DMS + NO_3 \rightarrow CH_3SO_2 + HNO_3 + HCHO$	1.9E-13*EXP(520./temp)	Atkinson et al. (2004)
G9402	TrGS	$DMSO + OH \rightarrow .6\ SO_2 + HCHO + .6\ CH_3O_2 + .4\ HO_2 + .4\ CH_3SO_3H$	1.E-10	Hynes and Wine (1996)
G9403	TrGS	$CH_3SO_2 \rightarrow SO_2 + CH_3O_2$	1.8E13*EXP(-8661./temp)	Barone et al. (1995)
G9404	TrGS	$CH_3SO_2 + O_3 \rightarrow CH_3SO_3$	3.E-13	Barone et al. (1995)
G9405	TrGS	$CH_3SO_3 + HO_2 \rightarrow CH_3SO_3H$	5.E-11	Barone et al. (1995)

*Notes:

Rate coefficients for three-body reactions are defined via the function `k_3rd`(T, M, k_0^{300}, n, $k_{\rm inf}^{300}$, m, $f_{\rm c}$). In the code, the temperature T is called `temp` and the concentration of "air molecules" M is called `cair`. Using the auxiliary variables $k_0(T)$, $k_{\rm inf}(T)$, and $k_{\rm ratio}$, `k_3rd` is defined as:

$$k_0(T) = k_0^{300} \times \left(\frac{300{\rm K}}{T}\right)^n \quad (1)$$

$$k_{\rm inf}(T) = k_{\rm inf}^{300} \times \left(\frac{300{\rm K}}{T}\right)^m \quad (2)$$

$$k_{\rm ratio} = \frac{k_0(T)M}{k_{\rm inf}(T)} \quad (3)$$

$$\texttt{k\_3rd} = \frac{k_0(T)M}{1+k_{\rm ratio}} \times f_{\rm c}^{\left(\frac{1}{1+(\log_{10}(k_{\rm ratio}))^2}\right)} \quad (4)$$

A similar function, called `k_3rd_iupac` here, is used by Atkinson et al. (2005) for three-body reactions. It has the same function parameters as `k_3rd` and it is defined as:

$$k_0(T) = k_0^{300} \times \left(\frac{300{\rm K}}{T}\right)^n \quad (5)$$

$$k_{\rm inf}(T) = k_{\rm inf}^{300} \times \left(\frac{300{\rm K}}{T}\right)^m \quad (6)$$

$$k_{\rm ratio} = \frac{k_0(T)M}{k_{\rm inf}(T)} \quad (7)$$

$$N = 0.75 - 1.27 \times \log_{10}(f_{\rm c}) \quad (8)$$

$$\texttt{k\_3rd\_iupac} = \frac{k_0(T)M}{1+k_{\rm ratio}} \times f_{\rm c}^{\left(\frac{1}{1+(\log_{10}(k_{\rm ratio})/N)^2}\right)} \quad (9)$$

G2110: The rate coefficient is: `k_HO2_HO2 = (1.5E-12*EXP(19./temp)+1.7E-33*EXP(1000./temp) *cair)* (1.+1.4E-21*EXP(2200./temp)*C(ind_ H2O))`. The value for the first (pressure-independent) part is from Christensen et al. (2002), the water term from Kircher and Sander (1984).

G3109: The rate coefficient is: `k_NO3_NO2 = k_ 3rd(temp,cair,2.E-30,4.4,1.4E-12,0.7,0.6)`.

G3110: The rate coefficient is defined as backward reaction divided by equilibrium constant.

G3203: The rate coefficient is: `k_NO2_HO2 = k_ 3rd(temp,cair,1.8E-31,3.2,4.7E-12,1.4,0.6)`.

G3206: The rate coefficient is: `k_HNO3_ OH = 2.4E-14 * EXP(460./temp) + 1./ ( 1./ (6.5E-34 * EXP(1335./temp)*cair) + 1./ (2.7E-17 * EXP(2199./temp)) )`

G3207: The rate coefficient is defined as backward reaction divided by equilibrium constant.

G4103: Sander et al. (2006) recommend a zero product yield for HCHO.

G4107: The rate coefficient is: `k_CH3OOH_OH = 3.8E-12*EXP(200./temp)`.

G4109: The same temperature dependence assumed as for $CH_3CHO+NO_3$. At 298 K, $k = 5.8 \times 10^{-16}$.

`k_PAN_M = k_CH3CO3_NO2/9.E-29*EXP(-14000./ temp)`, i.e. the rate coefficient is defined as backward reaction divided by equilibrium constant.

G9400: Addition path. The rate coefficient is: `k_DMS_OH = 1.0E-39*EXP(5820./temp)*C(ind_O2) / (1.+5.0E-30*EXP(6280./temp)*C(ind_O2))`.

Table 2: Photolysis reactions

#	labels	reaction	rate coefficient	reference
J1001a	UpStTrGJ	$O_3 + h\nu \rightarrow O(^1D) + O_2$	jx(ip_O1D)	see note
J1001b	UpStTrGJ	$O_3 + h\nu \rightarrow O(^3P) + O_2$	jx(ip_O3P)	see note
J2101	UpStTrGJ	$H_2O_2 + h\nu \rightarrow 2\ OH$	jx(ip_H2O2)	see note
J3101	UpStTrGNJ	$NO_2 + h\nu \rightarrow NO + O(^3P)$	jx(ip_NO2)	see note
J3103a	UpStTrGNJ	$NO_3 + h\nu \rightarrow NO_2 + O(^3P)$	jx(ip_NO2O)	see note
J3103b	UpStTrGNJ	$NO_3 + h\nu \rightarrow NO + O_2$	jx(ip_NOO2)	see note
J3104	StTrGNJ	$N_2O_5 + h\nu \rightarrow NO_2 + NO_3$	jx(ip_N2O5)	see note
J3200	TrGNJ	$HONO + h\nu \rightarrow NO + OH$	jx(ip_HONO)	see note
J3201	StTrGNJ	$HNO_3 + h\nu \rightarrow NO_2 + OH$	jx(ip_HNO3)	see note
J3202	StTrGNJ	$HNO_4 + h\nu \rightarrow .667\ NO_2 + .667\ HO_2 + .333\ NO_3 + .333\ OH$	jx(ip_HNO4)	see note
J4100	StTrGJ	$CH_3OOH + h\nu \rightarrow HCHO + OH + HO_2$	jx(ip_CH3OOH)	see note
J4101a	StTrGJ	$HCHO + h\nu \rightarrow H_2 + CO$	jx(ip_COH2)	see note
J4101b	StTrGJ	$HCHO + h\nu \rightarrow H + CO + HO_2$	jx(ip_CHOH)	see note

*Notes:

J-values are calculated with an external module and then supplied to the MECCA chemistry.

Values that originate from the Master Chemical Mechanism (MCM) by Rickard and Pascoe (2009) are translated according in the following way:

J(11) → jx(ip_COH2)
J(12) → jx(ip_CHOH)
J(15) → jx(ip_HOCH2CHO)
J(18) → jx(ip_MACR)
J(22) → jx(ip_ACETOL)
J(23)+J(24) → jx(ip_MVK)
J(31)+J(32)+J(33) → jx(ip_GLYOX)
J(34) → jx(ip_MGLYOX)
J(41) → jx(ip_CH3OOH)
J(53) → J($iC_3H_7ONO_2$)
J(54) → J($iC_3H_7ONO_2$)
J(55) → J($iC_3H_7ONO_2$)
J(56)+J(57) → jx(ip_NOA)

Table 3: Henry's law coefficients

substance	$\frac{k_{\mathrm{H}}^{\ominus}}{\mathrm{M/atm}}$	$\frac{-\Delta_{\mathrm{soln}}H/R}{\mathrm{K}}$	reference
O_2	1.3×10^{-3}	1500.	Wilhelm et al. (1977)
O_3	1.2×10^{-2}	2560.	Chameides (1984)
OH	3.0×10^{1}	4300.	Hanson et al. (1992)
HO_2	3.9×10^{3}	5900.	Hanson et al. (1992)
H_2O_2	$1.\times10^{5}$	6338.	Lind and Kok (1994)
H_2O	BIG	0.	see note
NO	1.9×10^{-3}	1480.	Schwartz and White (1981)
NO_2	7.0×10^{-3}	2500.	Lee and Schwartz (1981)*
NO_3	2.	2000.	Thomas et al. (1993)
N_2O_5	BIG	0.	see note
HONO	4.9×10^{1}	4780.	Schwartz and White (1981)
HNO_3	$2.45\times10^{6}/1.5\times10^{1}$	8694.	Brimblecombe and Clegg (1989)*
HNO_4	1.2×10^{4}	6900.	Régimbal and Mozurkewich (1997)
CH_3OH	2.20×10^{2}	5200.	Snider and Dawson (1985)
CH_3O_2	6.	5600.	Jacob (1986)*
CH_3OOH	3.0×10^{2}	5322.	Lind and Kok (1994)
CO_2	3.1×10^{-2}	2423.	Chameides (1984)
HCHO	7.0×10^{3}	6425.	Chameides (1984)
HCOOH	3.7×10^{3}	5700.	Chameides (1984)
SO_2	1.2	3120.	Chameides (1984)
H_2SO_4	$1.\times10^{11}$	0.	see note
CH_3SO_3H	BIG	0.	see note
DMS	5.4×10^{-1}	3500.	Staudinger and Roberts (2001)
DMSO	$5.\times10^{4}$	6425.	De Bruyn et al. (1994)*

*Notes:

The value "BIG" corresponds to virtually infinite solubility which is represented in the model using a very large but arbitrary number.

The temperature dependence of the Henry constants is:

$$K_{\mathrm{H}} = K_{\mathrm{H}}^{\ominus} \times \exp\left(\frac{-\Delta_{\mathrm{soln}}H}{R}\left(\frac{1}{T} - \frac{1}{T^{\ominus}}\right)\right)$$

where $\Delta_{\mathrm{soln}}H$ = molar enthalpy of dissolution [J/mol] and $R = 8.314$ J/(mol K).

NO_2: The temperature dependence is from Chameides (1984).

HNO_3: Calculated using the acidity constant from Davis and de Bruin (1964).

CH_3O_2: This value was estimated by Jacob (1986).

H_2SO_4: To account for the very high Henry's law coefficient of H_2SO_4, a very high value was chosen arbitrarily.

DMSO: Lower limit cited from another reference.

Table 4: Accommodation coefficients

substance	$\alpha^{\ominus}$	$\frac{-\Delta_{\mathrm{obs}}H/R}{\mathrm{K}}$	reference
O_2	0.01	2000.	see note
O_3	0.002	(default)	DeMore et al. (1997)*
OH	0.01	(default)	Takami et al. (1998)*
HO_2	0.5	(default)	Thornton and Abbatt (2005)
H_2O_2	0.077	3127.	Worsnop et al. (1989)
H_2O	0.0	(default)	see note
NO	5.0×10^{-5}	(default)	Saastad et al. (1993)*
NO_2	0.0015	(default)	Ponche et al. (1993)*
NO_3	0.04	(default)	Rudich et al. (1996)*
N_2O_5	(default)	(default)	DeMore et al. (1997)*
HONO	0.04	(default)	DeMore et al. (1997)*
HNO_3	0.5	(default)	Abbatt and Waschewsky (1998)*
HNO_4	(default)	(default)	DeMore et al. (1997)*
CH_3OH	(default)	(default)	see note
CH_3O_2	0.01	2000.	see note
CH_3OOH	0.0046	3273.	Magi et al. (1997)
CO_2	0.01	2000.	see note
HCHO	0.04	(default)	DeMore et al. (1997)*
HCOOH	0.014	3978.	DeMore et al. (1997)
SO_2	0.11	(default)	DeMore et al. (1997)
H_2SO_4	0.65	(default)	Pöschl et al. (1998)*
CH_3SO_3H	0.076	1762.	De Bruyn et al. (1994)
DMS	(default)	(default)	see note
DMSO	0.048	2578.	De Bruyn et al. (1994)

*Notes:

If no data are available, the following default values are used:
$\alpha^{\ominus} = 0.1$
$-\Delta_{\mathrm{obs}}H/R = 0$ K

The temperature dependence of the accommodation coefficients is given by (Jayne et al., 1991):

$$\frac{\alpha}{1-\alpha} = \exp\left(\frac{-\Delta_{\mathrm{obs}}G}{RT}\right) = \exp\left(\frac{-\Delta_{\mathrm{obs}}H}{RT} + \frac{\Delta_{\mathrm{obs}}S}{R}\right)$$

where $\Delta_{\mathrm{obs}}G$ is the Gibbs free energy barrier of the transition state toward solution (Jayne et al., 1991), and $\Delta_{\mathrm{obs}}H$ and $\Delta_{\mathrm{obs}}S$ are the corresponding enthalpy and entropy, respectively. The equation can be rearranged to:

$$\ln\left(\frac{\alpha}{1-\alpha}\right) = \frac{-\Delta_{\mathrm{obs}}H}{R} \times \frac{1}{T} + \frac{-\Delta_{\mathrm{obs}}S}{R}$$

and further:

$$\mathrm{d}\ln\left(\frac{\alpha}{1-\alpha}\right)\Big/\mathrm{d}\left(\frac{1}{T}\right) = \frac{-\Delta_{\mathrm{obs}}H}{R}$$

O_2: Estimate.

O_3: Value measured at 292 K.

OH: Value measured at 293 K.

NO: Value measured between 193 and 243 K.

NO_2: Value measured at 298 K.

NO_3: Value is a lower limit, measured at 273 K.

N_2O_5: Value for sulfuric acid, measured between 195 and 300 K.

HONO: Value measured between 247 and 297 K.

HNO_3: Value measured at room temperature. Abbatt and Waschewsky (1998) say $\gamma > 0.2$. Here $\alpha = 0.5$ is used.

HNO_4: Value measured at 200 K for water ice.

CH_3O_2: Estimate.

CO_2: Estimate.

HCHO: Value measured between 260 and 270 K.

H_2SO_4: Value measured at 303 K.

References (MECCA)

Abbatt, J. P. D. and Waschewsky, G. C. G.: Heterogeneous interactions of HOBr, HNO_3, O_3, and NO_2 with deliquescent NaCl aerosols at room temperature, J. Phys. Chem. A, 102, 3719–3725, 1998.

Atkinson, R.: Kinetics of the gas-phase reactions of OH radicals with alkanes and cycloalkanes, Atmos. Chem. Phys., 3, 2233–2307, 2003.

Atkinson, R., Baulch, D. L., Cox, R. A., Crowley, J. N., Hampson, R. F., Hynes, R. G., Jenkin, M. E., Rossi, M. J., and Troe, J.: Evaluated kinetic and photochemical data for atmospheric chemistry: Volume I – gas phase reactions of O_x, HO_x, NO_x and SO_x species, Atmos. Chem. Phys., 4, 1461–1738, 2004.

Atkinson, R., Baulch, D. L., Cox, R. A., Crowley, J. N., Hampson, Jr., R. F., Hynes, R. G., Jenkin, M. E., Kerr, J. A., Rossi, M. J., and Troe, J.: Summary of evaluated kinetic and photochemical data for atmospheric chemistry: Web version March 2005, `http://iupac.pole-ether.fr`, 2005.

Atkinson, R., Baulch, D. L., Cox, R. A., Crowley, J. N., Hampson, R. F., Hynes, R. G., Jenkin, M. E., Rossi, M. J., and Troe, J.: Evaluated kinetic and photochemical data for atmospheric chemistry: Volume II – gas phase reactions of organic species, Atmos. Chem. Phys., 6, 3625–4055, 2006.

Barone, S. B., Turnipseed, A. A., and Ravishankara, A. R.: Role of adducts in the atmospheric oxidation of dimethyl sulfide, Faraday Discuss., 100, 39–54, 1995.

Behnke, W., Scheer, V., and Zetzsch, C.: Production of $BrNO_2$, Br_2 and $ClNO_2$ from the reaction between sea spray aerosol and N_2O_5, J. Aerosol Sci., 25, S277–S278, 1994.

Behnke, W., George, C., Scheer, V., and Zetzsch, C.: Production and decay of $ClNO_2$ from the reaction of gaseous N_2O_5 with NaCl solution: Bulk and aerosol experiments, J. Geophys. Res., 102D, 3795–3804, 1997.

Brimblecombe, P. and Clegg, S. L.: Erratum, J. Atmos. Chem., 8, 95, 1989.

Chameides, W. L.: The photochemistry of a remote marine stratiform cloud, J. Geophys. Res., 89D, 4739–4755, 1984.

Christensen, L. E., Okumura, M., Sander, S. P., Salawitch, R. J., Toon, G. C., Sen, B., Blavier, J.-F., and Jucks, K. W.: Kinetics of $HO_2 + HO_2 \rightarrow H_2O_2 + O_2$: Implications for stratospheric H_2O_2, Geophys. Res. Lett., 29, doi:10.1029/2001GL014525, 2002.

Davis, Jr., W. and de Bruin, H. J.: New activity coefficients of 0-100 per cent aqueous nitric acid, J. Inorg. Nucl. Chem., 26, 1069–1083, 1964.

De Bruyn, W. J., Shorter, J. A., Davidovits, P., Worsnop, D. R., Zahniser, M. S., and Kolb, C. E.: Uptake of gas-phase sulfur species methanesulfonic acid, dimethylsulfoxide, and dimethyl sulfone by aqueous surfaces, J. Geophys. Res., 99D, 16 927–16 932, 1994.

DeMore, W. B., Sander, S. P., Golden, D. M., Hampson, R. F., Kurylo, M. J., Howard, C. J., Ravishankara, A. R., Kolb, C. E., and Molina, M. J.: Chemical kinetics and photochemical data for use in stratospheric modeling. Evaluation number 12, JPL Publication 97-4, Jet Propulsion Laboratory, Pasadena, CA, 1997.

Hanson, D. R., Burkholder, J. B., Howard, C. J., and Ravishankara, A. R.: Measurement of OH and HO_2 radical uptake coefficients on water and sulfuric acid surfaces, J. Phys. Chem., 96, 4979–4985, 1992.

Hynes, A. J. and Wine, P. H.: The atmospheric chemistry of dimethylsulfoxide (DMSO) kinetics and mechanism of the OH + DMSO reaction, J. Atmos. Chem., 24, 23–37, 1996.

Jacob, D. J.: Chemistry of OH in remote clouds and its role in the production of formic acid and peroxymonosulfate, J. Geophys. Res., 91D, 9807–9826, 1986.

Jayne, J. T., Duan, S. X., Davidovits, P., Worsnop, D. R., Zahniser, M. S., and Kolb, C. E.: Uptake of gas-phase alcohol and organic acid molecules by water surfaces, J. Phys. Chem., 95, 6329–6336, 1991.

Kircher, C. C. and Sander, S. P.: Kinetics and mechanism of HO_2 and DO_2 disproportionations, J. Phys. Chem., 88, 2082–2091, 1984.

Lee, Y.-N. and Schwartz, S. E.: Reaction kinetics of nitrogen dioxide with liquid water at low partial pressure, J. Phys. Chem., 85, 840–848, 1981.

Lind, J. A. and Kok, G. L.: Correction to "Henry's law determinations for aqueous solutions of hydrogen peroxide, methylhydroperoxide, and peroxyacetic acid" by John A. Lind and Gregory L. Kok, J. Geophys. Res., 99D, 21 119, 1994.

Magi, L., Schweitzer, F., Pallares, C., Cherif, S., Mirabel, P., and George, C.: Investigation of the uptake rate of ozone and methyl hydroperoxide by water surfaces, J. Phys. Chem. A, 101, 4943–4949, 1997.

McCabe, D. C., Gierczak, T., Talukdar, R. K., and Ravishankara, A. R.: Kinetics of the reaction OH + CO under atmospheric conditions, Geophys. Res. Lett., 28, 3135–3138, 2001.

Ponche, J. L., George, C., and Mirabel, P.: Mass transfer at the air/water interface: Mass accommodation coefficients of SO_2, HNO_3, NO_2 and NH_3, J. Atmos. Chem., 16, 1–21, 1993.

Pöschl, U., Canagaratna, M., Jayne, J. T., Molina, L. T., Worsnop, D. R., Kolb, C. E., and Molina, M. J.: Mass accommodation coefficient of H_2SO_4 vapor on aqueous sulfuric acid surfaces and gaseous diffusion coefficient of H_2SO_4 in N_2/H_2O, J. Phys. Chem. A, 102, 10 082–10 089, 1998.

Régimbal, J.-M. and Mozurkewich, M.: Peroxynitric acid decay mechanisms and kinetics at low pH, J. Phys. Chem. A, 101, 8822–8829, 1997.

Rickard, A. and Pascoe, S.: The Master Chemical Mechanism (MCM), `http://mcm.leeds.ac.uk`, 2009.

Rudich, Y., Talukdar, R. K., Imamura, T., Fox, R. W., and Ravishankara, A. R.: Uptake of NO_3 on KI solutions: Rate coefficient for the $NO_3 + I^-$ reaction and gas-phase diffusion coefficients for NO_3, Chem. Phys. Lett., 261, 467–473, 1996.

Saastad, O. W., Ellermann, T., and Nielsen, C. J.: On the adsorption of NO and NO_2 on cold H_2O/H_2SO_4 surfaces, Geophys. Res. Lett., 20, 1191–1193, 1993.

Sander, S. P., Friedl, R. R., Golden, D. M., Kurylo, M. J., Moortgat, G. K., Keller-Rudek, H., Wine, P. H., Ravishankara, A. R., Kolb, C. E., Molina, M. J., Finlayson-Pitts, B. J., Huie, R. E., and Orkin, V. L.: Chemical Kinetics and Photochemical Data for Use in Atmospheric Studies, Evaluation Number 15, JPL Publication 06-2, Jet Propulsion Laboratory, Pasadena, CA, `http://jpldataeval.jpl.nasa.gov`, 2006.

Sander, S. P., Abbatt, J., Barker, J. R., Burkholder, J. B., Friedl, R. R., Golden, D. M., Huie, R. E., Kolb, C. E., Kurylo, M. J., Moortgat, G. K., Orkin, V. L., and Wine, P. H.: Chemical Kinetics and Photochemical Data for Use in Atmospheric Studies, Evaluation No. 17, JPL Publication 10-6, Jet Propulsion Laboratory, Pasadena, `http://jpldataeval.jpl.nasa.gov`, 2011.

Schwartz, S. E. and White, W. H.: Solubility equilibria of the nitrogen oxides and oxyacids in dilute aqueous solution, in: Advances in Environmental Science and Engineering, edited by Pfafflin, J. R. and Ziegler, E. N., vol. 4, pp. 1–45, Gordon and Breach Science Publishers, NY, 1981.

Sivakumaran, V., Hölscher, D., Dillon, T. J., and Crowley, J. N.: Reaction between OH and HCHO: temperature dependent rate coefficients (202-399 K) and product pathways (298 K), Phys. Chem. Chem. Phys., 5, 4821–4827, 2003.

Snider, J. R. and Dawson, G. A.: Tropospheric light alcohols, carbonyls, and acetonitrile: Concentrations in the southwestern United States and Henry's law data, J. Geophys. Res., 90D, 3797–3805, 1985.

Staudinger, J. and Roberts, P. V.: A critical compilation of Henry's law constant temperature dependence relations for organic compounds in dilute aqueous solutions, Chemosphere, 44, 561–576, 2001.

Takami, A., Kato, S., Shimono, A., and Koda, S.: Uptake coefficient of OH radical on aqueous surface, Chem. Phys., 231, 215–227, 1998.

Thomas, K., Volz-Thomas, A., and Kley, D.: Zur Wechselwirkung von NO_3-Radikalen mit wässrigen Lösungen: Bestimmung des Henry- und des Massenakkomodationskoeffizienten, Ph.D. thesis, Institut für Chemie und Dynamik der Geosphäre 2, Forschungszentrum Jülich GmbH, Germany, 1993.

Thornton, J. and Abbatt, J. P. D.: Measurements of HO_2 uptake to aqueous aerosol: Mass accommodation coefficients and net reactive loss, J. Geophys. Res., 110D, doi:10.1029/2004JD005402, 2005.

Wilhelm, E., Battino, R., and Wilcock, R. J.: Low-pressure solubility of gases in liquid water, Chem. Rev., 77, 219–262, 1977.

Worsnop, D. R., Zahniser, M. S., Kolb, C. E., Gardner, J. A., Watson, L. R., van Doren, J. M., Jayne, J. T., and Davidovits, P.: The temperature dependence of mass accommodation of SO_2 and H_2O_2 on aqueous surfaces, J. Phys. Chem., 93, 1159–1172, 1989.

A.3 Liquid phase chemical mechanism

The following pages were output automatically when creating the liquid chemistry mechanism for SCAV.

The Chemical Mechanism of SCAV

Holger Tost & Rolf Sander & Astrid Kerkweg

tost@mpch-mainz.mpg.de, sander@mpch-mainz.mpg.de, akerkweg@mpch-mainz.mpg.de

Air Chemistry Department, Max-Planck Institute of Chemistry, PO Box 3060, 55020 Mainz, Germany

(mechanism generated on March 18, 2015)

Table 1: Heterogeneous reactions

#	labels	reaction	rate coefficient	reference
H1001f	TrAraMblScScm	$O_3 \rightarrow O_3(aq)$	k_exf(KPP_O3)	see note
H1001b	TrAraMblScScm	$O_3(aq) \rightarrow O_3$	k_exb(KPP_O3)	see note
H2102f	TrAraMblScScm	$H_2O_2 \rightarrow H_2O_2(aq)$	k_exf(KPP_H2O2)	see note
H2102b	TrAraMblScScm	$H_2O_2(aq) \rightarrow H_2O_2$	k_exb(KPP_H2O2)	see note
H3200f	TrAraNMblScScm	$NH_3 \rightarrow NH_3(aq)$	k_exf(KPP_NH3)	see note
H3200b	TrAraNMblScScm	$NH_3(aq) \rightarrow NH_3$	k_exb(KPP_NH3)	see note
H3201	TrAraMblNScScm	$N_2O_5 \rightarrow HNO_3(aq) + HNO_3(aq)$	k_exf_N2O5*C(KPP_H2O_1)	Behnke et al. (1994), Behnke et al. (1997)
H3203f	TrAraMblNScScm	$HNO_3 \rightarrow HNO_3(aq)$	k_exf(KPP_HNO3)	see note
H3203b	TrAraMblNScScm	$HNO_3(aq) \rightarrow HNO_3$	k_exb(KPP_HNO3)	see note
H4100f	TrAraMblScScm	$CO_2 \rightarrow CO_2(aq)$	k_exf(KPP_CO2)	see note
H4100b	TrAraMblScScm	$CO_2(aq) \rightarrow CO_2$	k_exb(KPP_CO2)	see note
H4101f	TrAraScScm	$HCHO \rightarrow HCHO(aq)$	k_exf(KPP_HCHO)	see note
H4101b	TrAraScScm	$HCHO(aq) \rightarrow HCHO$	k_exb(KPP_HCHO)	see note
H4103f	TrAraScScm	$HCOOH \rightarrow HCOOH(aq)$	k_exf(KPP_HCOOH)	see note
H4103b	TrAraScScm	$HCOOH(aq) \rightarrow HCOOH$	k_exb(KPP_HCOOH)	see note
H4104f	TrAraScScm	$CH_3OOH \rightarrow CH_3OOH(aq)$	k_exf(KPP_CH3OOH)	see note
H4104b	TrAraScScm	$CH_3OOH(aq) \rightarrow CH_3OOH$	k_exb(KPP_CH3OOH)	see note
H6200f	TrAraClMblScScm	$HCl \rightarrow HCl(aq)$	k_exf(KPP_HCl)	see note
H6200b	TrAraClMblScScm	$HCl(aq) \rightarrow HCl$	k_exb(KPP_HCl)	see note
H9100f	TrAraSMblScScm	$SO_2 \rightarrow SO_2(aq)$	k_exf(KPP_SO2)	see note
H9100b	TrAraSMblScScm	$SO_2(aq) \rightarrow SO_2$	k_exb(KPP_SO2)	see note
H9200	TrAraSMblScScm	$H_2SO_4 \rightarrow H_2SO_4(aq)$	k_exf(KPP_H2SO4)	see note

*Notes:

The forward (`k_exf`) and backward (`k_exb`) rate coefficients are calculated in the file `messy_scav_base.f90` using the accommodation coefficients in subroutine `scav_alpha` and Henry's law constants in subroutine `scav_henry`.

k_{mt} = mass transfer coefficient

lwc = liquid water content of aerosol mode

$fhet(X,Y) = k_{\mathrm{mt}}(X) \times lwc \times f(Y)[Y]/Het_T$, with f($H_2O$) = 1, f($Cl^-$) = 5.0E2, and $f(Br^-)$ = 3.0E5, [Y] = concentration of Y; $\mathrm{Het_T}$ = [H_2O] + f(Cl^-)[Cl^-] + f(Br^-)[Br^-]

H6301, H6302, H7601: The total uptake is determined by $k_{\mathrm{mt}}(ClNO_3)$. The relative rates are assumed to be the same as for N_2O_5 (H3201, H6300, H7300).

H7301, H7302, H7602: The total uptake is determined by $k_{\mathrm{mt}}(BrNO_3)$. The relative rates are assumed to be the same as for N_2O_5 (H3201, H6300, H7300).

Table 2: Acid-base and other eqilibria

#	labels	reaction	$K_0[M^{m-n}]$	-$\Delta H/R[K]$	reference
EQ21	TrAraMblScScm	$H_2O \rightleftharpoons H^+ + OH^-$	1.0E-16	-6716	Chameides (1984)
EQ30	TrAraMblNScScm	$NH_4^+ \rightleftharpoons H^+ + NH_3$	5.88E-10	-2391	Chameides (1984)
EQ32	TrAraMblNScScm	$HNO_3 \rightleftharpoons H^+ + NO_3^-$	15	8700	Davis and de Bruin (1964)
EQ40	TrAraMblScScm	$CO_2 \rightleftharpoons H^+ + HCO_3^-$	4.3E-7	-913	Chameides (1984)
EQ41	TrAraScScm	$HCOOH \rightleftharpoons H^+ + HCOO^-$	1.8E-4		Weast (1980)
EQ61	TrAraClMblScScm	$HCl \rightleftharpoons H^+ + Cl^-$	1.7E6	6896	Marsh and McElroy (1985)
EQ90	TrAraSMblScScm	$SO_2 \rightleftharpoons H^+ + HSO_3^-$	1.7E-2	2090	Chameides (1984)
EQ91	TrAraSMblScScm	$HSO_3^- \rightleftharpoons H^+ + SO_3^{2-}$	6.0E-8	1120	Chameides (1984)
EQ92	TrAraSMblScScm	$HSO_4^- \rightleftharpoons H^+ + SO_4^{2-}$	1.2E-2	2720	Seinfeld and Pandis (1998)
EQ93	TrAraSMblScScm	$H_2SO_4 \rightleftharpoons H^+ + HSO_4^-$	1.0E3		Seinfeld and Pandis (1998)

*Notes:

EQ82 and EQ83: Thermodynamic calculations on the IBr/ICl equilibrium according to the data tables from Wagman et al. (1982):

ICl	+	Br^-	$\rightleftharpoons$	IBr	+	Cl^-
-17.1		-103.96	=	-4.2		-131.228

$$\frac{\Delta G}{[\text{kJ/mol}]} = -4.2 - 131.228 - (-17.1 - 103.96) = -14.368$$

$$K = \frac{[\text{IBr}] \times [\text{Cl}^-]}{[\text{ICl}] \times [\text{Br}^-]} = \exp\left(\frac{-\Delta G}{RT}\right) = \exp\left(\frac{14368}{8.314 \times 298}\right) = 330$$

This means we have equal amounts of IBr and ICl when the $[Cl^-]/[Br^-]$ ratio equals 330.

Table 3: Aqueous phase reactions

#	labels	reaction	k_0 $[M^{1-n}s^{-1}]$	$-E_a/R[K]$	reference
A9101	TrAraSMblScScm	$SO_3^{2-} + O_3 \rightarrow SO_4^{2-}$	1.5E9	-5300	Hoffmann (1986)
A9206	TrAraSMblScScm	$HSO_3^- + O_3 \rightarrow SO_4^{2-} + H^+$	3.7E5	-5500	Hoffmann (1986)
A9209	TrAraSMblScScm	$HSO_3^- + H_2O_2 \rightarrow SO_4^{2-} + H^+$	5.2E6	-3650	Martin and Damschen (1981)

A6102: Jacobi (1996) found an upper limit of `6E9` and cite an upper limit from another study of `2E9`. Here, we set the rate coefficient to `1E9`.

A6301: There is also an earlier study by Exner et al. (1992) which found a smaller rate coefficient but did not consider the back reaction.

A7400: assumed to be the same as for $Br_2^- + H_2O_2$.

A9106: see also: (Huie and Neta, 1987; Warneck, 1991). If this reaction produces a lot of SO_4^-, it will have an effect. However, we currently assume only the stable $S_2O_8^{2-}$ as product.

A9205: D. Sedlak, pers. comm. (1993)

A9208: D. Sedlak, pers. comm. (1993)

A9105: The rate coefficient for the sum of the paths (leading to either HSO_5^- or SO_4^{2-}) is from Huie and Neta (1987), the ratio 0.28/0.72 is from Deister and Warneck (1990).

A9605: assumed to be the same as for SO_3^{2-} + HOCl.

A9705: assumed to be the same as for SO_3^{2-} + HOBr.

References (SCAV)

Behnke, W., Scheer, V., and Zetzsch, C.: Production of $BrNO_2$, Br_2 and $ClNO_2$ from the reaction between sea spray aerosol and N_2O_5, J. Aerosol Sci., 25, S277–S278, 1994.

Behnke, W., George, C., Scheer, V., and Zetzsch, C.: Production and decay of $ClNO_2$ from the reaction of gaseous N_2O_5 with NaCl solution: Bulk and aerosol experiments, J. Geophys. Res., 102D, 3795–3804, 1997.

Chameides, W. L.: The photochemistry of a remote marine stratiform cloud, J. Geophys. Res., 89D, 4739–4755, 1984.

Davis, Jr., W. and de Bruin, H. J.: New activity coefficients of 0-100 per cent aqueous nitric acid, J. Inorg. Nucl. Chem., 26, 1069–1083, 1964.

Deister, U. and Warneck, P.: Photooxidation of SO_3^{2-} in aqueous solution, J. Phys. Chem., 94, 2191–2198, 1990.

Exner, M., Herrmann, H., and Zellner, R.: Laser-based studies of reactions of the nitrate radical in aqueous solution, Ber. Bunsenges. Phys. Chem., 96, 470–477, 1992.

Hoffmann, M. R.: On the kinetics and mechanism of oxidation of aquated sulfur dioxide by ozone, Atmos. Environ., 20, 1145–1154, 1986.

Huie, R. E. and Neta, P.: Rate constants for some oxidations of S(IV) by radicals in aqueous solutions, Atmos. Environ., 21, 1743–1747, 1987.

Jacobi, H.-W.: Kinetische Untersuchungen und Modellrechnungen zur troposphärischen Chemie von Radikalanionen und Ozon in wäßriger Phase, Ph.D. thesis, Universität GH Essen, FRG, 1996.

Marsh, A. R. W. and McElroy, W. J.: The dissociation constant and Henry's law constant of HCl in aqueous solution, Atmos. Environ., 19, 1075–1080, 1985.

Martin, L. R. and Damschen, D. E.: Aqueous oxidation of sulfur dioxide by hydrogen peroxide at low pH, Atmos. Environ., 15, 1615–1621, 1981.

Seinfeld, J. H. and Pandis, S. N.: Atmospheric Chemistry and Physics, John Wiley & Sons, Inc., 1998.

Wagman, D. D., Evans, W. H., Parker, V. B., Schumm, R. H., Halow, I., Bailey, S. M., Churney, K. L., and Nuttall, R. L.: The NBS tables of chemical thermodynamic properties; Selected values for inorganic and C_1 and C_2 organic substances in SI units, J. Phys. Chem. Ref. Data, 11, suppl. 2, 1982.

Warneck, P.: Chemical reactions in clouds, Fresenius J. Anal. Chem., 340, 585–590, 1991.

Weast, R. C., ed.: CRC Handbook of Chemistry and Physics, 61st Edition, CRC Press, Inc., Boca Raton, FL, 1980.

A.4 Mode assignment of cloud residual aerosol

This section provides a detailed description of the algorithm used in EMAC to assign cloud and precipitation residual aerosol to the MADE3 modes. It was devised and implemented into the MESSy submodel SCAV as part of the present work. The residual assignment is an important process in EMAC as it is not yet possible to track in-cloud or in-precipitation aerosol separately from interstitial aerosol in the model. Hence, this procedure is applied at the end of each time step, regardless of whether a cloud persists or not.

After a brief definition of terminology employed in this section, the assumptions underlying the residual assignment scheme are outlined. Subsequently, the algorithm is described in detail.

A.4.1 Terminology

Whenever the term "cloud particles" is used in the following it refers to both ice crystals and liquid droplets suspended in clouds, as well as to falling snow flakes and rain droplets. The same applies to "cloud residual aerosol", which is meant to also include "precipitation residual aerosol". Finally, the term "evaporation" as used here includes both evaporation of cloud and rain droplets, and sublimation or melting plus subsequent evaporation of ice crystals and snow flakes.

A.4.2 Basic assumptions

1. According to an operator splitting approach, it is assumed that activation of aerosol particles into cloud particles occurs first, and impaction of interstitial aerosol upon the cloud particles follows in an instantaneous manner as a second step. It is acknowledged that this constitutes a strong simplification of the two interdependent processes. When more measurement data on the mixing state of cloud residual aerosol becomes available, the impact of this simplification can be evaluated and the algorithm may then be refined. However, as the influence of cloud particle coagulation on mixing state is not represented in the model code, there will be some inevitable error anyway.

2. It is further assumed that aerosol particles from each mode impact equally frequently on all cloud particles, regardless of their cores. Note that this assumption is alleviated in some cases in order to keep the complexity of the involved equations at a reasonable level. The exceptions are mentioned explicitly in Sect. A.4.3.

3. Aerosol particles from the insoluble modes ("ki", "ai", "ci") cannot be activated into cloud droplets in the present scheme, as they are assumed to be hydrophobic. Nevertheless, they can serve as ice nuclei.

4. The formation of water soluble species within cloud droplets and coagulation between cloud particles lead to accumulation of soluble aerosol components inside cloud particles. To account for such effects it is assumed that all aerosol particles that were incorporated into cloud particles are hydrophilic upon cloud particle evaporation. Hence, no residual aerosol is assigned to the insoluble, hydrophobic modes ("ki", "ai", "ci").

5. Furthermore, it is assumed that—due to collection of other aerosol particles, generation of aerosol mass inside cloud droplets, and coagulation of cloud particles—the aerosol particle cores of the cloud particles will have grown from Aitken to accumulation mode sizes when the cloud particles evaporate. Hence, no residual aerosol is assigned to the Aitken modes ("ks", "km", "ki").

A.4.3 Algorithm for residual assignment

Assignment of aerosol particle number concentrations

Let $\mathfrak{N}_q^{\mathrm{lnu}}$ and $\mathfrak{N}_q^{\mathrm{inu}}$ be the number concentrations of aerosol particles from mode q that were activated to form cloud droplets or ice crystals, respectively, as computed by the nucleation scavenging scheme in SCAV (Sect. 5.6). Before all other calculations the insoluble ice nuclei number concentrations are assigned to the corresponding mixed modes (according to assumption 4 in Sect. A.4.2) and the Aitken mode cloud particle cores to the corresponding accumulation modes (according to assumption 5):

$$N_{\mathrm{as}}^{\mathrm{lnu}} = \mathfrak{N}_{\mathrm{as}}^{\mathrm{lnu}} + \mathfrak{N}_{\mathrm{ks}}^{\mathrm{lnu}}, \qquad N_{\mathrm{cs}}^{\mathrm{lnu}} = \mathfrak{N}_{\mathrm{cs}}^{\mathrm{lnu}}, \tag{A.1a}$$

$$N_{\mathrm{as}}^{\mathrm{inu}} = \mathfrak{N}_{\mathrm{as}}^{\mathrm{inu}} + \mathfrak{N}_{\mathrm{ks}}^{\mathrm{inu}}, \qquad N_{\mathrm{cs}}^{\mathrm{inu}} = \mathfrak{N}_{\mathrm{cs}}^{\mathrm{inu}}, \tag{A.1b}$$

$$N_{\mathrm{am}}^{\mathrm{lnu}} = \mathfrak{N}_{\mathrm{am}}^{\mathrm{lnu}} + \mathfrak{N}_{\mathrm{km}}^{\mathrm{lnu}}, \qquad N_{\mathrm{cm}}^{\mathrm{lnu}} = \mathfrak{N}_{\mathrm{cm}}^{\mathrm{lnu}}, \tag{A.1c}$$

$$N_{\mathrm{am}}^{\mathrm{inu}} = \mathfrak{N}_{\mathrm{am}}^{\mathrm{inu}} + \mathfrak{N}_{\mathrm{ai}}^{\mathrm{inu}} + \mathfrak{N}_{\mathrm{km}}^{\mathrm{inu}} + \mathfrak{N}_{\mathrm{ki}}^{\mathrm{inu}}, \qquad N_{\mathrm{cm}}^{\mathrm{inu}} = \mathfrak{N}_{\mathrm{cm}}^{\mathrm{inu}} + \mathfrak{N}_{\mathrm{ci}}^{\mathrm{inu}}. \tag{A.1d}$$

The N will be the output values of the algorithm. Cloud particle cores now belong to one of the four modes $q = 4, 5, 7, 8$ (corresponding to "as", "am", "cs", and "cm"; cf. Table 3.2), and the symbol

$$N_q^{\mathrm{nuc}} = N_q^{\mathrm{lnu}} + N_q^{\mathrm{inu}} \tag{A.2}$$

is used to represent their cumulative number concentration in mode q. The total number concentration of cloud particles is assumed to remain constant, i.e., $\sum_{q=\{4,5,7,8\}} N_q^{\mathrm{nuc}} = \text{const.}$ during the mode assignment process. In the present setup SCAV later reduces all N_q^{nuc} to 10 % of their values to account for coagulation of cloud particles.

Now, the numbers of cloud particle cores per unit volume that are transferred to different aerosol modes upon evaporation of the cloud particles are calculated. Such transfers are due to impaction scavenging of other aerosol particles. The symbol for the number of cores transferred from mode q to mode r per unit volume shall be N_q^r, the symbol for the total number of interstitial mode q particles per unit volume collected by impaction scavenging (Sect. 5.6) shall be $\mathfrak{N}_q^{\mathrm{imp}}$.

No transfer is required out of mode "cm" as this mode represents the highest degree of aerosol particle mixing and aging. For modes "cs" and "am" the calculation is straightforward, as cores from these modes can only be transferred to mode "cm" (or remain in their respective mode):

$$N_{\mathrm{cs}}^{\mathrm{cm}} = \mathrm{MIN}\left(f_{\mathrm{cs}} \cdot \left[\mathfrak{N}_{\mathrm{km}}^{\mathrm{imp}} + \mathfrak{N}_{\mathrm{ki}}^{\mathrm{imp}} + \mathfrak{N}_{\mathrm{am}}^{\mathrm{imp}} + \mathfrak{N}_{\mathrm{ai}}^{\mathrm{imp}} + \mathfrak{N}_{\mathrm{cm}}^{\mathrm{imp}} + \mathfrak{N}_{\mathrm{ci}}^{\mathrm{imp}}\right],\ N_{\mathrm{cs}}^{\mathrm{nuc}}\right), \tag{A.3}$$

$$N_{\mathrm{am}}^{\mathrm{cm}} = \mathrm{MIN}\left(f_{\mathrm{am}} \cdot \left[\mathfrak{N}_{\mathrm{cs}}^{\mathrm{imp}} + \mathfrak{N}_{\mathrm{cm}}^{\mathrm{imp}} + \mathfrak{N}_{\mathrm{ci}}^{\mathrm{imp}}\right],\ N_{\mathrm{am}}^{\mathrm{nuc}}\right). \tag{A.4}$$

Here,

$$f_q = \frac{N_q^{\mathrm{nuc}}}{\sum_{r=\{4,5,7,8\}} N_r^{\mathrm{nuc}}} \tag{A.5}$$

is the fraction that mode q contributes to the total number concentration of cloud particle cores. The MIN operation is required because cloud particles can collect multiple other particles via impaction scavenging, but their cores can of course only be transferred to mode "cm" once.

The situation is more complicated for the "as" cores, as they can be transferred to modes "am", "cs", and "cm", depending on the aerosol particles taken up by impaction scavenging. Assuming a uniform distribution of collected aerosol particles from each mode over the individual "as" cores (according to assumption 2 in Sect. A.4.2) would require consideration of all "overlaps", i.e., the fractions of cores that have collected aerosol particles from mode q and

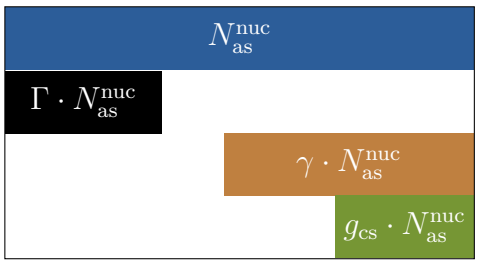

Figure A.2: Illustration of the transfer concept for mode "as" cloud particle cores upon impaction scavenging of particles that induce such transfers. The blue bar represents the number concentration of mode "as" aerosol particles that have nucleated cloud particles, the boxes below it represent the number concentrations of impaction-scavenged aerosol particles from the three considered classes: coarse mode particles that contain insoluble material (black), fine mode particles that contain insoluble material (brown), and soluble coarse mode particles (green). See text for explanation of the symbols.

mode r, but not from mode t, for example. This would lead to very lengthy and complex equations. In order to avoid overly complicated and error-prone formulas, mode transfers of cloud particle cores from mode "as" upon evaporation/sublimation of the cloud particles are therefore prioritized by:

1. maximizing the transfer to mixed modes,
2. maximizing the transfer to coarse modes.

Thus, the amount of aerosol particles transferred to mode "cm" is maximized. This deliberate "overestimation" is motivated by the fact that the general reduction of N_q^{nuc} (to 10 %, see above) does not account for cloud microphysical processes that may transfer further cloud particle cores to the mixed coarse mode. Deviating from assumption 2 in Sect. A.4.2, the prioritization is achieved as follows:

- collected aerosol particles that contain insoluble material are distributed as evenly as possible over the "as" cores,
- fine, i.e., Aitken and accumulation mode particles that contain insoluble material are collected preferentially by cloud particles that have not collected coarse mode particles which contain insoluble material,
- soluble coarse mode particles are collected preferentially by cloud particles that have also collected fine mode particles that contain insoluble material.

Figure A.2 may help the reader visualize these assumptions and the associated transfers described in the following.

It is acknowledged that the presented simplifications are somewhat arbitrary, but judging by previous simulation results—e.g., a relatively small long-term mean effect of cloud processing on aerosol particle aging when compared to condensation of trace gases—the associated error is expected to be tolerable. Nevertheless, different assumptions should be tested in the future in order to explore the sensitivity of the simulation results to this choice.

Following the outlined scheme, the direct transfer of cloud particle cores from mode "as" to mode "cm" by impaction of aerosol particles from modes "cm" and "ci" is considered first. Let

$$\Gamma = \mathrm{MIN}\Big(g_{\mathrm{cm}} + g_{\mathrm{ci}},\ 1\Big) \tag{A.6}$$

be the fraction of mode r cores that has collected aerosol particles from the coarse modes that contain insoluble material (which is actually independent of r). Here,

$$g_q = \frac{f_r \mathfrak{N}_q^{\mathrm{imp}}}{N_r^{\mathrm{nuc}}} = \frac{\mathfrak{N}_q^{\mathrm{imp}}}{\sum_{m=1}^{9} N_m^{\mathrm{nuc}}} \tag{A.7}$$

is the fraction of cores from mode r (or, in fact, from any mode) that has collected aerosol particles from mode q. The number of cores directly transferred from mode "as" to mode "cm" per unit volume can then be written as:

$$N_{\mathrm{as}}^{\mathrm{cm}} = \Gamma \cdot N_{\mathrm{as}}^{\mathrm{nuc}}. \tag{A.8}$$

Subsequently, if any "as" cores remain, transfers from mode "as" to mode "cm" via collection of both fine mode particles that contain insoluble material and soluble coarse mode particles are considered. Let

$$\gamma = \mathrm{MIN}\Big(g_{\mathrm{km}} + g_{\mathrm{ki}} + g_{\mathrm{am}} + g_{\mathrm{ai}},\ 1\Big) \tag{A.9}$$

be the analogue to Γ (Eq. A.6) for collected fine mode particles that contain insoluble material. The expression for the transfer of "as" cores to "cm" via collection of (at least) two aerosol particles per cloud particle then reads:

$$N_{\mathrm{as+2}}^{\mathrm{cm}} = \mathrm{MIN}\Big(\gamma,\ g_{\mathrm{cs}},\ 1-\Gamma\Big) \cdot N_{\mathrm{as}}^{\mathrm{nuc}}. \tag{A.10}$$

Once the terms for transfer to the mixed coarse mode have been established, and in case any "as" cores remain, transfer from "as" to "am" or "cs" without subsequent transfer to "cm" also has to be considered:

$$N_{\mathrm{as}}^{\mathrm{am}} = \mathrm{MAX}\Big(\mathrm{MIN}\Big(\gamma,\ 1-\Gamma\Big) - g_{\mathrm{cs}},\ 0\Big) \cdot N_{\mathrm{as}}^{\mathrm{nuc}}, \tag{A.11}$$

$$N_{\mathrm{as}}^{\mathrm{cs}} = \mathrm{MAX}\Big(\mathrm{MIN}\Big(g_{\mathrm{cs}},\ 1-\Gamma\Big) - \gamma,\ 0\Big) \cdot N_{\mathrm{as}}^{\mathrm{nuc}}. \tag{A.12}$$

After these calculations the N_q^{nuc} are redistributed accordingly (read the arrows as "new value on the left hand side is computed from old values on the right hand side"):

$$N_{\mathrm{as}}^{\mathrm{nuc}} \quad \rightarrow \quad N_{\mathrm{as}}^{\mathrm{nuc}} - N_{\mathrm{as}}^{\mathrm{am}} - N_{\mathrm{as}}^{\mathrm{cs}} - N_{\mathrm{as}}^{\mathrm{cm}} - N_{\mathrm{as+2}}^{\mathrm{cm}}, \tag{A.13a}$$

$$N_{\mathrm{am}}^{\mathrm{nuc}} \quad \rightarrow \quad N_{\mathrm{am}}^{\mathrm{nuc}} + N_{\mathrm{as}}^{\mathrm{am}} - N_{\mathrm{am}}^{\mathrm{cm}}, \tag{A.13b}$$

$$N_{\mathrm{cs}}^{\mathrm{nuc}} \quad \rightarrow \quad N_{\mathrm{cs}}^{\mathrm{nuc}} + N_{\mathrm{as}}^{\mathrm{cs}} - N_{\mathrm{cs}}^{\mathrm{cm}}, \tag{A.13c}$$

$$N_{\mathrm{cm}}^{\mathrm{nuc}} \quad \rightarrow \quad N_{\mathrm{cm}}^{\mathrm{nuc}} + N_{\mathrm{as}}^{\mathrm{cm}} + N_{\mathrm{as+2}}^{\mathrm{cm}} + N_{\mathrm{am}}^{\mathrm{cm}} + N_{\mathrm{cs}}^{\mathrm{cm}}. \tag{A.13d}$$

Assignment of aerosol particle mass concentrations

As for the number concentrations, let $\mathfrak{m}_q^{\mathrm{lnu}}$ and $\mathfrak{m}_q^{\mathrm{inu}}$ be the mass concentrations of aerosol particles from mode q that were activated to form cloud droplets or ice crystals, respectively, as computed by the nucleation scavenging scheme in SCAV (Sect. 5.6). Furthermore, let $\mathfrak{m}_q^{\mathrm{ch}}$ be the aerosol mass per unit volume generated within, or lost from, the cloud particles nucleated by mode q aerosol particles, which is due to cloud phase chemistry.

For consistency with the number treatment the insoluble ice nuclei mass concentrations are first assigned to the corresponding mixed modes and the Aitken mode cloud particle cores to the corresponding accumulation modes:

$$m_{\mathrm{as}}^{\mathrm{lnu}} = \mathfrak{m}_{\mathrm{as}}^{\mathrm{lnu}} + \mathfrak{m}_{\mathrm{ks}}^{\mathrm{lnu}}, \qquad m_{\mathrm{cs}}^{\mathrm{lnu}} = \mathfrak{m}_{\mathrm{cs}}^{\mathrm{lnu}}, \tag{A.14a}$$

$$m_{\mathrm{as}}^{\mathrm{inu}} = \mathfrak{m}_{\mathrm{as}}^{\mathrm{inu}} + \mathfrak{m}_{\mathrm{ks}}^{\mathrm{inu}}, \qquad m_{\mathrm{cs}}^{\mathrm{inu}} = \mathfrak{m}_{\mathrm{cs}}^{\mathrm{inu}}, \tag{A.14b}$$

$$m_{\mathrm{as}}^{\mathrm{ch}} = \mathfrak{m}_{\mathrm{as}}^{\mathrm{ch}} + \mathfrak{m}_{\mathrm{ks}}^{\mathrm{ch}}, \qquad m_{\mathrm{cs}}^{\mathrm{ch}} = \mathfrak{m}_{\mathrm{cs}}^{\mathrm{ch}}, \tag{A.14c}$$

$$m_{\mathrm{am}}^{\mathrm{lnu}} = \mathfrak{m}_{\mathrm{am}}^{\mathrm{lnu}} + \mathfrak{m}_{\mathrm{km}}^{\mathrm{lnu}}, \qquad m_{\mathrm{cm}}^{\mathrm{lnu}} = \mathfrak{m}_{\mathrm{cm}}^{\mathrm{lnu}}, \tag{A.14d}$$

$$m_{\mathrm{am}}^{\mathrm{inu}} = \mathfrak{m}_{\mathrm{am}}^{\mathrm{inu}} + \mathfrak{m}_{\mathrm{ai}}^{\mathrm{inu}} + \mathfrak{m}_{\mathrm{km}}^{\mathrm{inu}} + \mathfrak{m}_{\mathrm{ki}}^{\mathrm{inu}}, \qquad m_{\mathrm{cm}}^{\mathrm{inu}} = \mathfrak{m}_{\mathrm{cm}}^{\mathrm{inu}} + \mathfrak{m}_{\mathrm{ci}}^{\mathrm{inu}}, \tag{A.14e}$$

$$m_{\mathrm{am}}^{\mathrm{ch}} = \mathfrak{m}_{\mathrm{am}}^{\mathrm{ch}} + \mathfrak{m}_{\mathrm{km}}^{\mathrm{ch}}, \qquad m_{\mathrm{cm}}^{\mathrm{ch}} = \mathfrak{m}_{\mathrm{cm}}^{\mathrm{ch}}. \tag{A.14f}$$

As before, the m will be the output values of our algorithm, the $\mathfrak{m}$ are the input values, computed by SCAV using the fractions given in Sect. 5.6. Note that there are no $\mathfrak{m}_{xi}^{\mathrm{ch}}$ ($x \in \{\mathrm{k}, \mathrm{a}, \mathrm{c}\}$) because ice phase chemistry is not considered.

In order to simplify the following expressions the cloud particle core mass concentration m_r^{nuc} for each mode $r = 4, 5, 7, 8$ ("as", "am", "cs", and "cm"; Table 3.2) is defined as the sum of the activated mode r aerosol particle mass per unit volume, the aerosol mass generated per unit volume within or on the cloud particles nucleated by mode r aerosol particles or lost from these cloud particles, and the mass concentration of collected aerosol particles that do not induce transfers of the residual from mode r (let $\mathfrak{m}_q^{\mathrm{imp}}$ be the total mass concentration of mode q particles that are collected by impaction scavenging, Sect. 5.6):

$$m_{\mathrm{as}}^{\mathrm{nuc}} = m_{\mathrm{as}}^{\mathrm{lnu}} + m_{\mathrm{as}}^{\mathrm{inu}} + m_{\mathrm{as}}^{\mathrm{ch}} + f_{\mathrm{as}} \cdot \left[\mathfrak{m}_{\mathrm{ks}}^{\mathrm{imp}} + \mathfrak{m}_{\mathrm{as}}^{\mathrm{imp}}\right], \tag{A.15a}$$

$$m_{\mathrm{am}}^{\mathrm{nuc}} = m_{\mathrm{am}}^{\mathrm{lnu}} + m_{\mathrm{am}}^{\mathrm{inu}} + m_{\mathrm{am}}^{\mathrm{ch}} + f_{\mathrm{am}} \cdot \left[\mathfrak{m}_{\mathrm{ks}}^{\mathrm{imp}} + \mathfrak{m}_{\mathrm{km}}^{\mathrm{imp}} + \mathfrak{m}_{\mathrm{ki}}^{\mathrm{imp}} + \mathfrak{m}_{\mathrm{as}}^{\mathrm{imp}} + \mathfrak{m}_{\mathrm{am}}^{\mathrm{imp}} + \mathfrak{m}_{\mathrm{ai}}^{\mathrm{imp}}\right], \tag{A.15b}$$

$$m_{\mathrm{cs}}^{\mathrm{nuc}} = m_{\mathrm{cs}}^{\mathrm{lnu}} + m_{\mathrm{cs}}^{\mathrm{inu}} + m_{\mathrm{cs}}^{\mathrm{ch}} + f_{\mathrm{cs}} \cdot \left[\mathfrak{m}_{\mathrm{ks}}^{\mathrm{imp}} + \mathfrak{m}_{\mathrm{as}}^{\mathrm{imp}} + \mathfrak{m}_{\mathrm{cs}}^{\mathrm{imp}}\right], \tag{A.15c}$$

$$m_{\mathrm{cm}}^{\mathrm{nuc}} = m_{\mathrm{cm}}^{\mathrm{lnu}} + m_{\mathrm{cm}}^{\mathrm{inu}} + m_{\mathrm{cm}}^{\mathrm{ch}} + f_{\mathrm{cm}} \cdot \sum_{q=1}^{9} \mathfrak{m}_q^{\mathrm{imp}}. \tag{A.15d}$$

Now, the transferred mass concentrations are computed. For each mode $q = 4, 5, 7, 8$ the mass concentrations of particles that induced the transfer and a fraction of the core mass concentration m_q^{nuc} have to be transferred. As mode "cm" is only a target mode for residuals, there is no transfer out of this mode. All the mass that it receives by impaction scavenging stays in mode "cm". For the other three modes of cloud particle cores ("cs", "am", "as") the mass concentrations that have to be transferred are calculated consistently with the number transfers:

$$m_{\mathrm{cs}}^{\mathrm{cm}} = f_{\mathrm{cs}} \cdot \left[\mathfrak{m}_{\mathrm{km}}^{\mathrm{imp}} + \mathfrak{m}_{\mathrm{ki}}^{\mathrm{imp}} + \mathfrak{m}_{\mathrm{am}}^{\mathrm{imp}} + \mathfrak{m}_{\mathrm{ai}}^{\mathrm{imp}} + \mathfrak{m}_{\mathrm{cm}}^{\mathrm{imp}} + \mathfrak{m}_{\mathrm{ci}}^{\mathrm{imp}}\right] + \frac{N_{\mathrm{cs}}^{\mathrm{cm}}}{N_{\mathrm{cs}}^{\mathrm{nuc}}} \cdot m_{\mathrm{cs}}^{\mathrm{nuc}}, \tag{A.16}$$

$$m_{\mathrm{am}}^{\mathrm{cm}} = f_{\mathrm{am}} \cdot \left[\mathfrak{m}_{\mathrm{cs}}^{\mathrm{imp}} + \mathfrak{m}_{\mathrm{cm}}^{\mathrm{imp}} + \mathfrak{m}_{\mathrm{ci}}^{\mathrm{imp}}\right] + \frac{N_{\mathrm{am}}^{\mathrm{cm}}}{N_{\mathrm{am}}^{\mathrm{nuc}}} \cdot m_{\mathrm{am}}^{\mathrm{nuc}}, \tag{A.17}$$

$$\begin{aligned} m_{\mathrm{as}}^{\mathrm{cm}} = {} & f_{\mathrm{as}} \cdot \left[\mathfrak{m}_{\mathrm{cm}}^{\mathrm{imp}} + \mathfrak{m}_{\mathrm{ci}}^{\mathrm{imp}}\right] \\ & + \underbrace{\frac{\mathrm{MAX}\left(\Gamma + \gamma - 1,\ 0\right) \cdot N_{\mathrm{as}}^{\mathrm{nuc}}}{\gamma \cdot N_{\mathrm{as}}^{\mathrm{nuc}}}}_{\text{see note 1}} \cdot f_{\mathrm{as}} \cdot \left[\mathfrak{m}_{\mathrm{km}}^{\mathrm{imp}} + \mathfrak{m}_{\mathrm{ki}}^{\mathrm{imp}} + \mathfrak{m}_{\mathrm{am}}^{\mathrm{imp}} + \mathfrak{m}_{\mathrm{ai}}^{\mathrm{imp}}\right] \\ & + \underbrace{\frac{\mathrm{MAX}\left(\Gamma + g_{\mathrm{cs}} - 1,\ 0\right) \cdot N_{\mathrm{as}}^{\mathrm{nuc}}}{g_{\mathrm{cs}} \cdot N_{\mathrm{as}}^{\mathrm{nuc}}}}_{\text{see note 2}} \cdot f_{\mathrm{as}} \cdot \mathfrak{m}_{\mathrm{cs}}^{\mathrm{imp}} \\ & + \frac{N_{\mathrm{as}}^{\mathrm{cm}}}{N_{\mathrm{as}}^{\mathrm{nuc}}} \cdot m_{\mathrm{as}}^{\mathrm{nuc}}, \end{aligned} \tag{A.18}$$

$$m_{\mathrm{as+2}}^{\mathrm{cm}} = \frac{N_{\mathrm{as+2}}^{\mathrm{cm}}}{\gamma \cdot N_{\mathrm{as}}^{\mathrm{nuc}}} \cdot f_{\mathrm{as}} \cdot \left[\mathfrak{m}_{\mathrm{km}}^{\mathrm{imp}} + \mathfrak{m}_{\mathrm{ki}}^{\mathrm{imp}} + \mathfrak{m}_{\mathrm{am}}^{\mathrm{imp}} + \mathfrak{m}_{\mathrm{ai}}^{\mathrm{imp}}\right] + \frac{N_{\mathrm{as+2}}^{\mathrm{cm}}}{g_{\mathrm{cs}} \cdot N_{\mathrm{as}}^{\mathrm{nuc}}} \cdot f_{\mathrm{as}} \cdot \mathfrak{m}_{\mathrm{cs}}^{\mathrm{imp}} + \frac{N_{\mathrm{as+2}}^{\mathrm{cm}}}{N_{\mathrm{as}}^{\mathrm{nuc}}} \cdot m_{\mathrm{as}}^{\mathrm{nuc}}, \tag{A.19}$$

$$m_{\mathrm{as}}^{\mathrm{am}} = \frac{N_{\mathrm{as}}^{\mathrm{am}}}{\gamma \cdot N_{\mathrm{as}}^{\mathrm{nuc}}} \cdot f_{\mathrm{as}} \cdot \left[\mathfrak{m}_{\mathrm{km}}^{\mathrm{imp}} + \mathfrak{m}_{\mathrm{ki}}^{\mathrm{imp}} + \mathfrak{m}_{\mathrm{am}}^{\mathrm{imp}} + \mathfrak{m}_{\mathrm{ai}}^{\mathrm{imp}}\right] + \frac{N_{\mathrm{as}}^{\mathrm{am}}}{N_{\mathrm{as}}^{\mathrm{nuc}}} \cdot m_{\mathrm{as}}^{\mathrm{nuc}}, \tag{A.20}$$

$$m_{\mathrm{as}}^{\mathrm{cs}} = \frac{N_{\mathrm{as}}^{\mathrm{cs}}}{g_{\mathrm{cs}} \cdot N_{\mathrm{as}}^{\mathrm{nuc}}} \cdot f_{\mathrm{as}} \cdot \mathfrak{m}_{\mathrm{cs}}^{\mathrm{imp}} + \frac{N_{\mathrm{as}}^{\mathrm{cs}}}{N_{\mathrm{as}}^{\mathrm{nuc}}} \cdot m_{\mathrm{as}}^{\mathrm{nuc}}. \tag{A.21}$$

Notes:

1. fraction of collected fine mode particles containing insoluble material that is transferred with $N_{\mathrm{as}}^{\mathrm{cm}}$,
2. fraction of collected soluble coarse mode particles that is transferred with $N_{\mathrm{as}}^{\mathrm{cm}}$.

Similar notes apply to the first terms in Eqs. (A.19)–(A.21). Note also that the terms with denominator $\gamma \cdot N_{\mathrm{as}}^{\mathrm{nuc}}$ add up to 1, and the terms with denominator $g_{\mathrm{cs}} \cdot N_{\mathrm{as}}^{\mathrm{nuc}}$ do so as well. This is due to the limits imposed on the number transfers (see "Assignment of aerosol particle number concentrations").

Finally, the mass concentration assignments are performed in an analogous manner as for the numbers (again, read the arrows as "new value on the left hand side is computed from old values on the right hand side"):

$$
\begin{aligned}
m_{\mathrm{as}}^{\mathrm{nuc}} \quad \rightarrow \quad & m_{\mathrm{as}}^{\mathrm{nuc}} + f_{\mathrm{as}} \cdot \left[\mathfrak{m}_{\mathrm{km}}^{\mathrm{imp}} + \mathfrak{m}_{\mathrm{ki}}^{\mathrm{imp}} + \mathfrak{m}_{\mathrm{am}}^{\mathrm{imp}} + \mathfrak{m}_{\mathrm{ai}}^{\mathrm{imp}} + \mathfrak{m}_{\mathrm{cs}}^{\mathrm{imp}} + \mathfrak{m}_{\mathrm{cm}}^{\mathrm{imp}} + \mathfrak{m}_{\mathrm{ci}}^{\mathrm{imp}} \right] \\
& - m_{\mathrm{as}}^{\mathrm{am}} - m_{\mathrm{as}}^{\mathrm{cs}} - m_{\mathrm{as}}^{\mathrm{cm}} - m_{\mathrm{as+2}}^{\mathrm{cm}} && \text{(A.22a)} \\
& = m_{\mathrm{as}}^{\mathrm{nuc}} \cdot \left(1 - \frac{N_{\mathrm{as}}^{\mathrm{am}}}{N_{\mathrm{as}}^{\mathrm{nuc}}} - \frac{N_{\mathrm{as}}^{\mathrm{cs}}}{N_{\mathrm{as}}^{\mathrm{nuc}}} - \frac{N_{\mathrm{as}}^{\mathrm{cm}}}{N_{\mathrm{as}}^{\mathrm{nuc}}} - \frac{N_{\mathrm{as+2}}^{\mathrm{cm}}}{N_{\mathrm{as}}^{\mathrm{nuc}}} \right), && \text{(A.22b)} \\
m_{\mathrm{am}}^{\mathrm{nuc}} \quad \rightarrow \quad & m_{\mathrm{am}}^{\mathrm{nuc}} + f_{\mathrm{am}} \cdot \left[\mathfrak{m}_{\mathrm{cs}}^{\mathrm{imp}} + \mathfrak{m}_{\mathrm{cm}}^{\mathrm{imp}} + \mathfrak{m}_{\mathrm{ci}}^{\mathrm{imp}} \right] \\
& + m_{\mathrm{as}}^{\mathrm{am}} - m_{\mathrm{am}}^{\mathrm{cm}} && \text{(A.22c)} \\
& = m_{\mathrm{am}}^{\mathrm{nuc}} \cdot \left(1 - \frac{N_{\mathrm{am}}^{\mathrm{cm}}}{N_{\mathrm{am}}^{\mathrm{nuc}}} \right) + m_{\mathrm{as}}^{\mathrm{am}}, && \text{(A.22d)} \\
m_{\mathrm{cs}}^{\mathrm{nuc}} \quad \rightarrow \quad & m_{\mathrm{cs}}^{\mathrm{nuc}} + f_{\mathrm{cs}} \cdot \left[\mathfrak{m}_{\mathrm{km}}^{\mathrm{imp}} + \mathfrak{m}_{\mathrm{ki}}^{\mathrm{imp}} + \mathfrak{m}_{\mathrm{am}}^{\mathrm{imp}} + \mathfrak{m}_{\mathrm{ai}}^{\mathrm{imp}} + \mathfrak{m}_{\mathrm{cm}}^{\mathrm{imp}} + \mathfrak{m}_{\mathrm{ci}}^{\mathrm{imp}} \right] \\
& + m_{\mathrm{as}}^{\mathrm{cs}} - m_{\mathrm{cs}}^{\mathrm{cm}} && \text{(A.22e)} \\
& = m_{\mathrm{cs}}^{\mathrm{nuc}} \cdot \left(1 - \frac{N_{\mathrm{cs}}^{\mathrm{cm}}}{N_{\mathrm{cs}}^{\mathrm{nuc}}} \right) + m_{\mathrm{as}}^{\mathrm{cs}}, && \text{(A.22f)} \\
m_{\mathrm{cm}}^{\mathrm{nuc}} \quad \rightarrow \quad & m_{\mathrm{cm}}^{\mathrm{nuc}} \\
& + m_{\mathrm{as}}^{\mathrm{cm}} + m_{\mathrm{as+2}}^{\mathrm{cm}} + m_{\mathrm{am}}^{\mathrm{cm}} + m_{\mathrm{cs}}^{\mathrm{cm}}. && \text{(A.22g)}
\end{aligned}
$$

A.5 Year 2000 aerosol in EMAC with MADE3

Average aerosol number concentrations and composition from the ten evaluated years of the reference simulation with MADE3 are shown by mode in Figs. A.3– A.11. The emissions dataset was chosen to represent year 2000 conditions, so that these figures show how EMAC represents the year 2000 aerosol when run with MADE3 as its aerosol microphysics submodel.

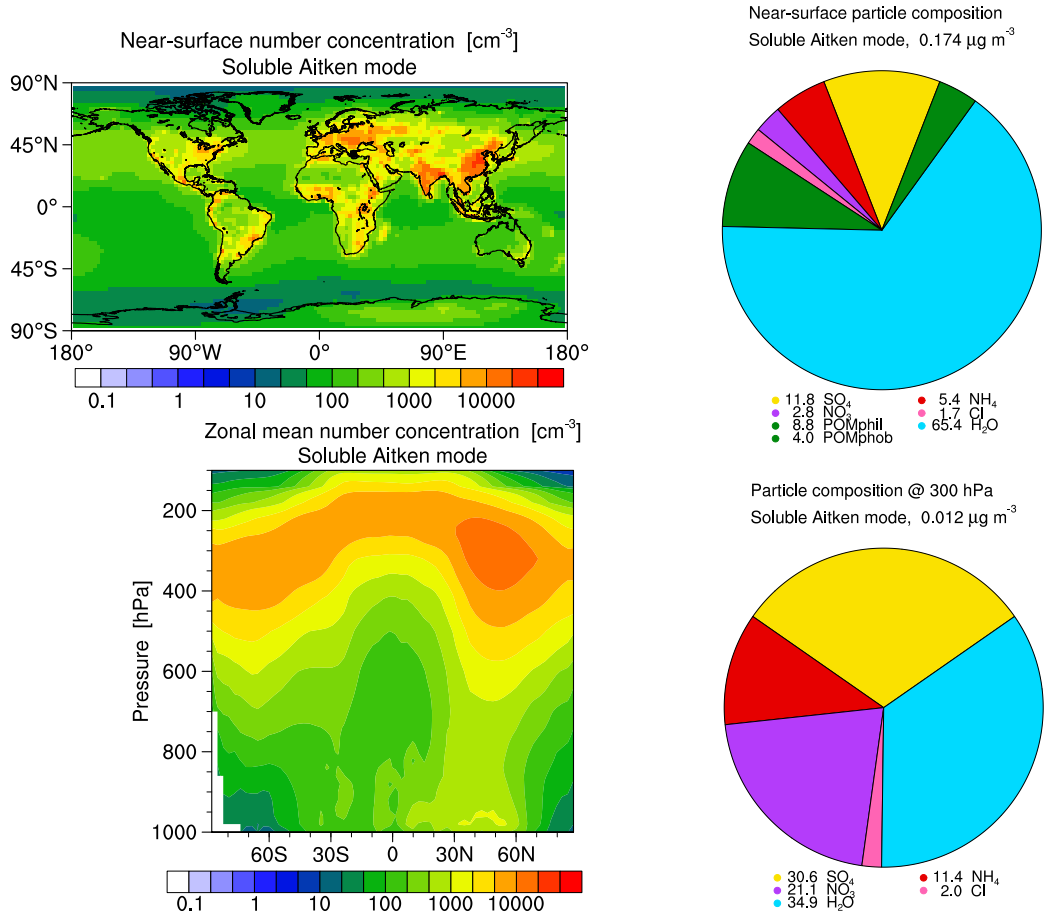

Figure A.3: Ten-year average properties of the soluble Aitken mode ("ks") in the MADE3 reference simulation. The mass concentrations given in the titles of the pie charts include all species. Note that only species whose contributions are greater than 1 % are shown. The white area in the zonal mean plot does not contain any data because average pressure does not reach these values over Antarctica.

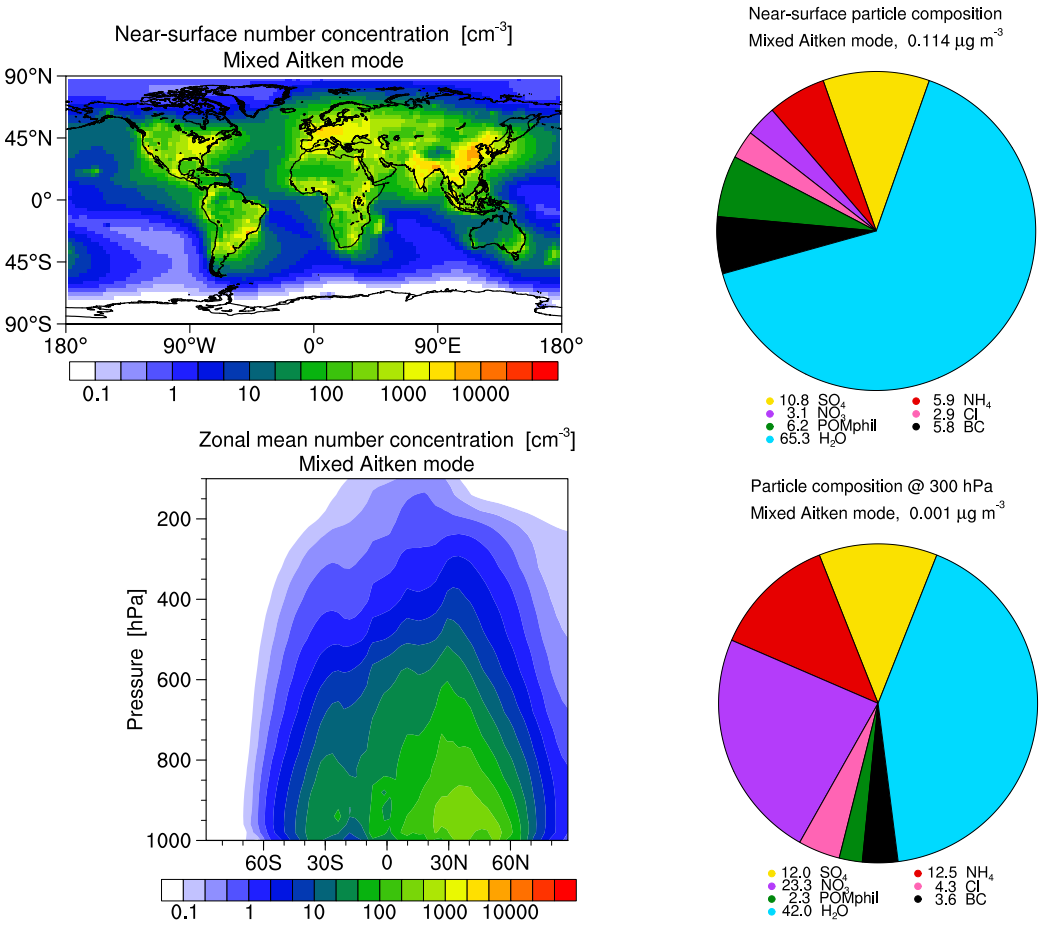

Figure A.4: Same as Fig. A.3, but for the mixed Aitken mode ("km").

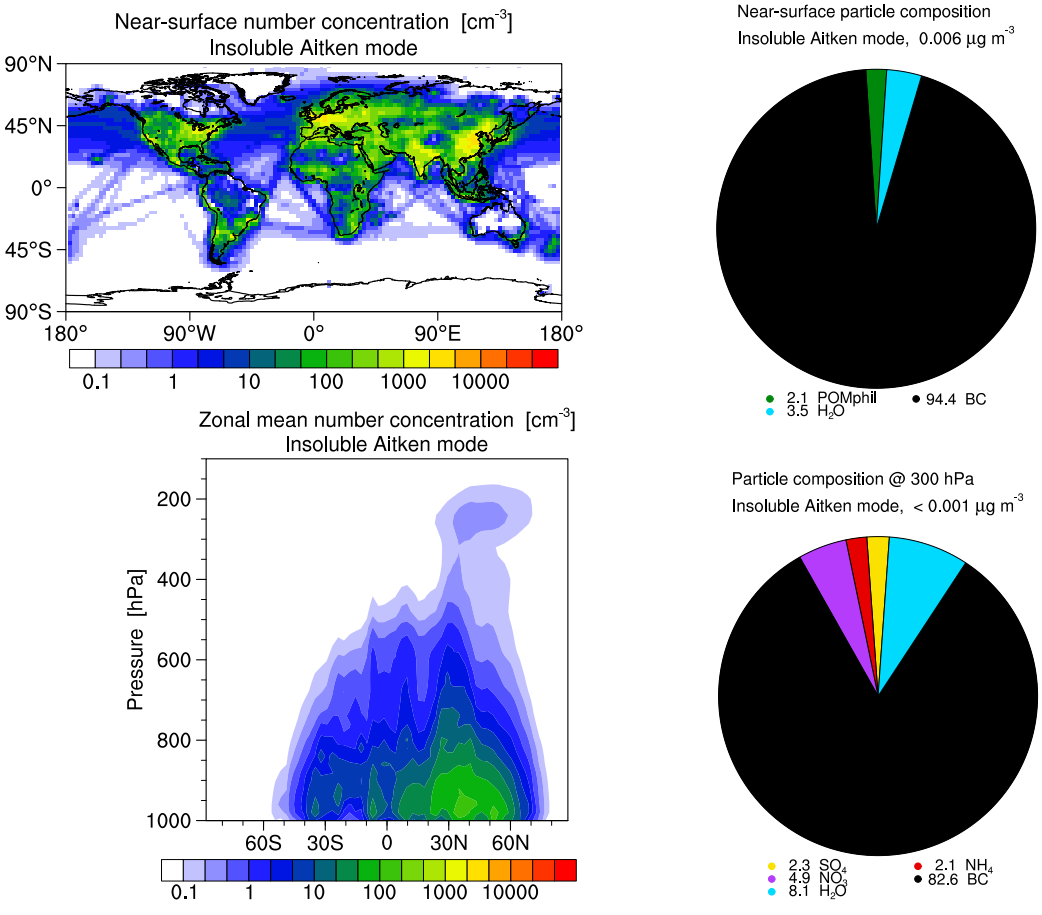

Figure A.5: Same as Fig. A.3, but for the insoluble Aitken mode ("ki").

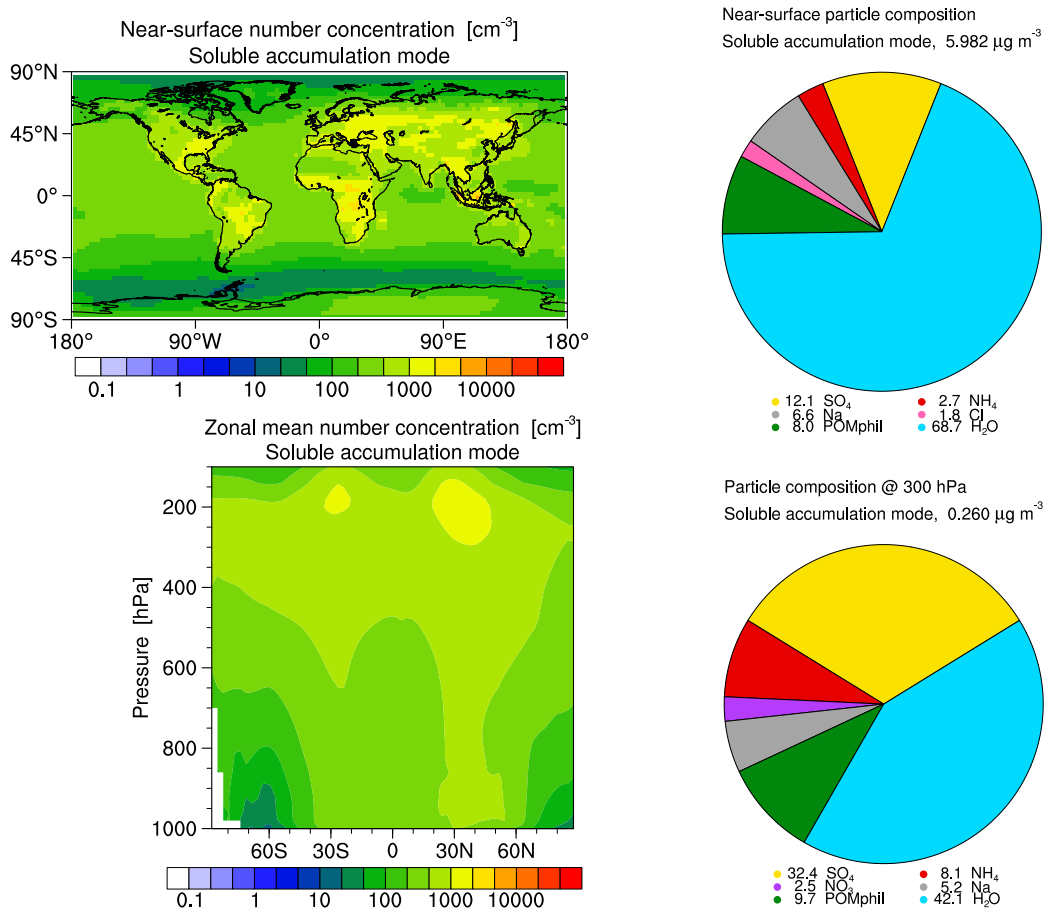

Figure A.6: Same as Fig. A.3, but for the soluble accumulation mode ("as").

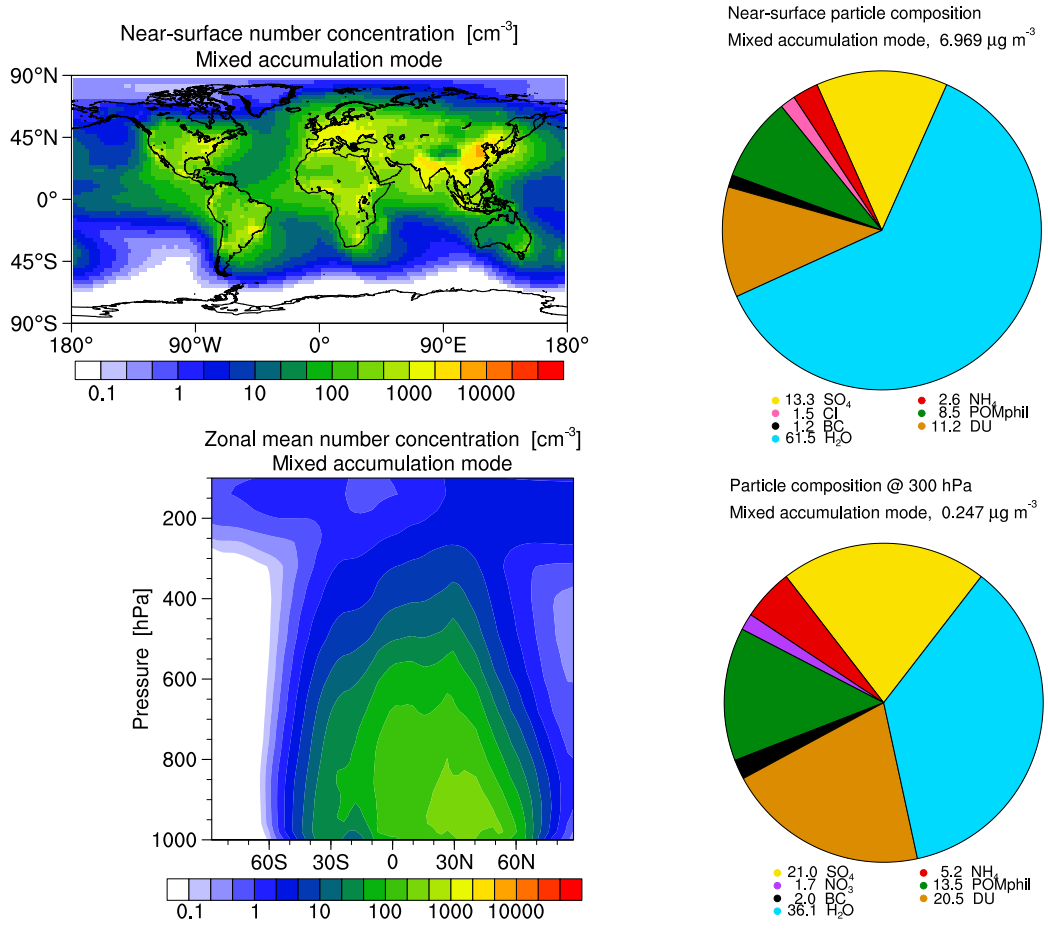

Figure A.7: Same as Fig. A.3, but for the mixed accumulation mode ("am").

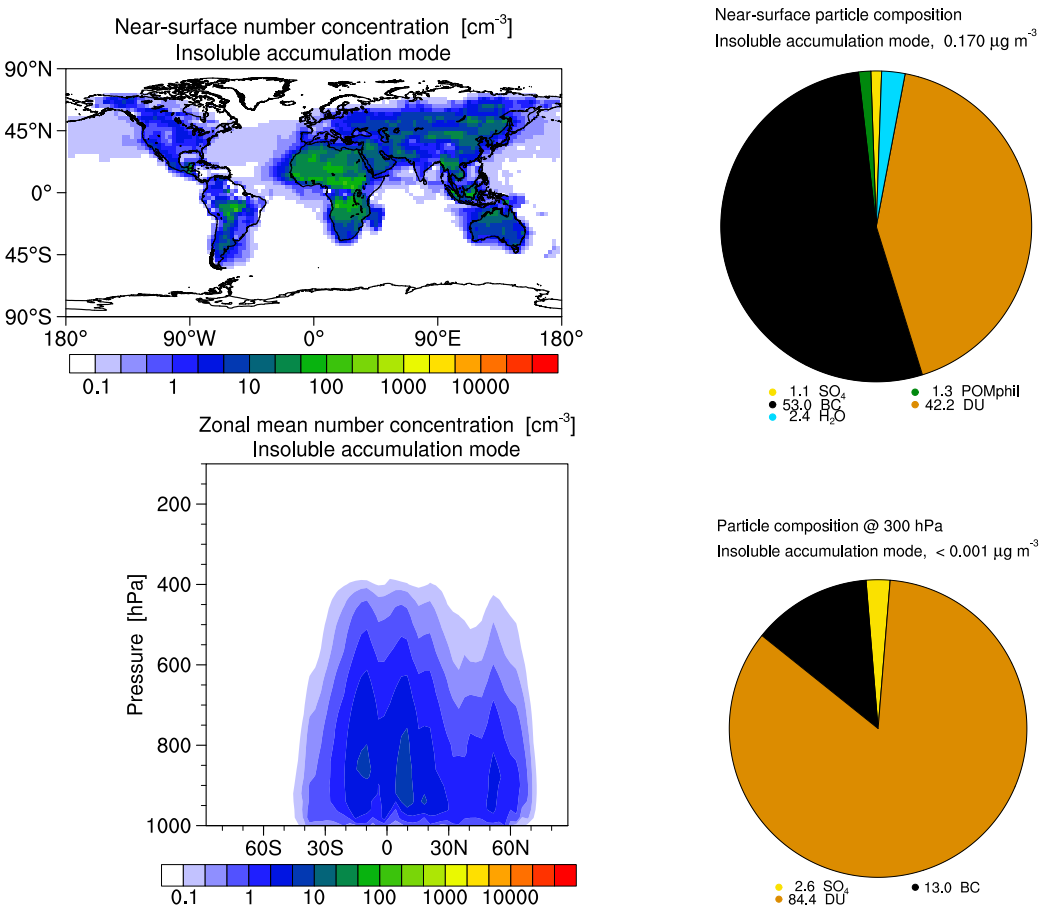

Figure A.8: Same as Fig. A.3, but for the insoluble accumulation mode ("ai").

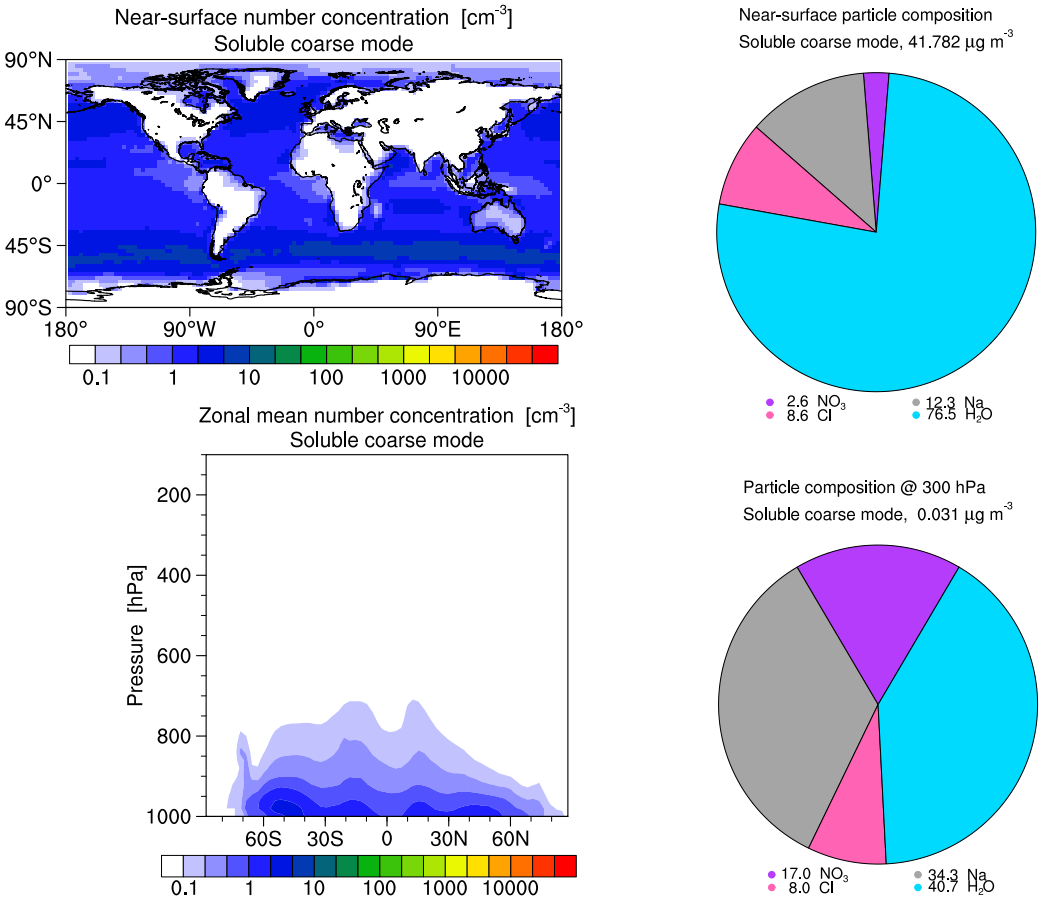

Figure A.9: Same as Fig. A.3, but for the soluble coarse mode ("cs").

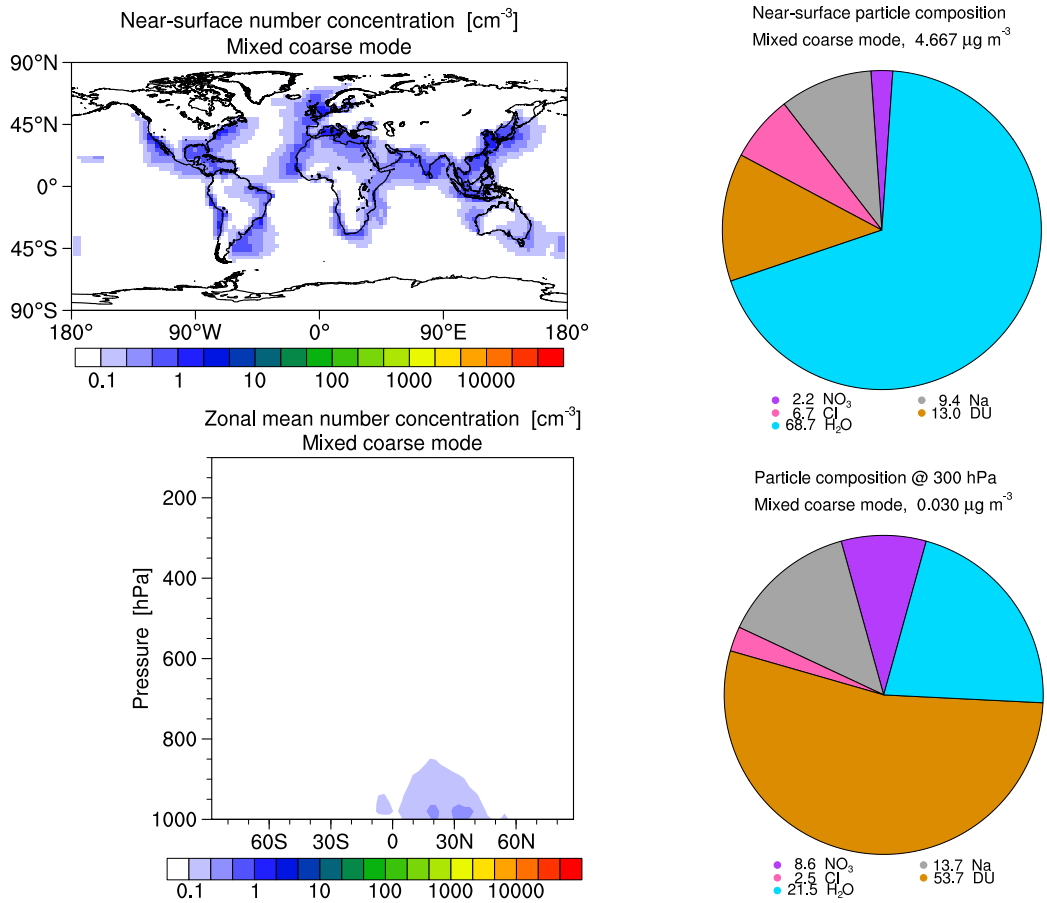

Figure A.10: Same as Fig. A.3, but for the mixed coarse mode ("cm").

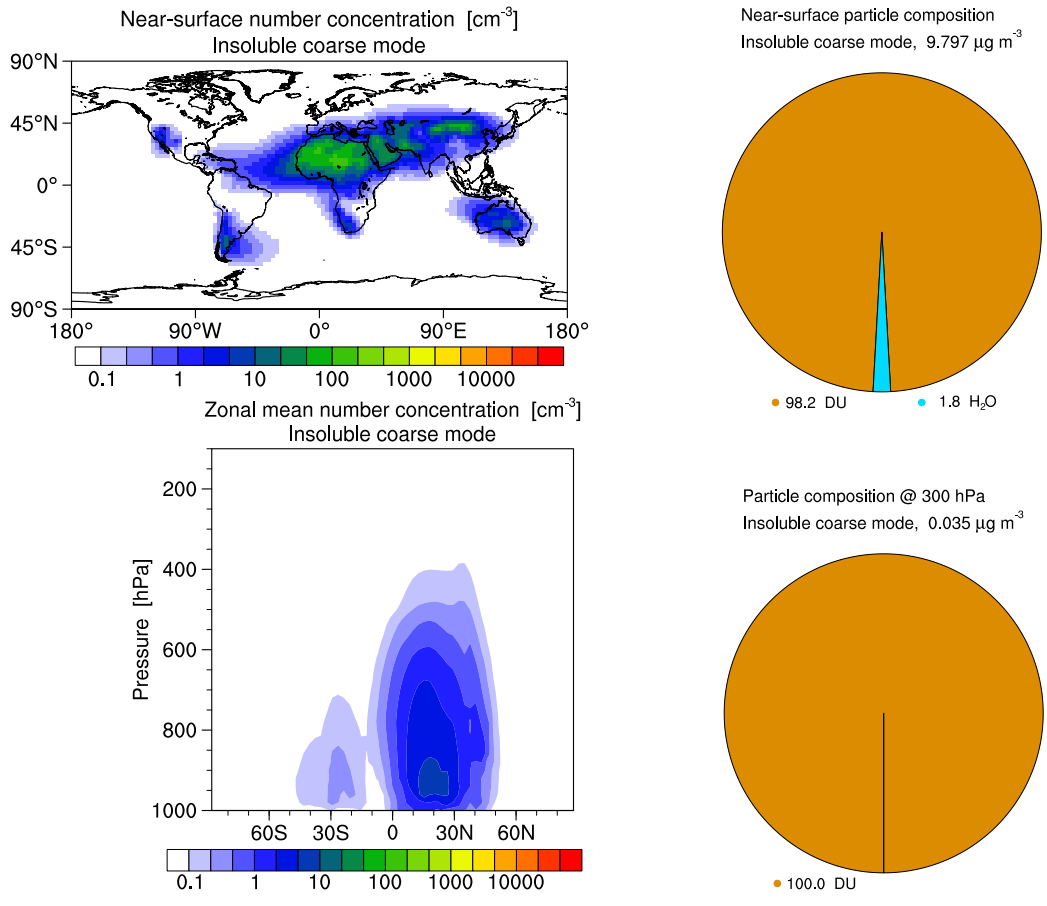

Figure A.11: Same as Fig. A.3, but for the insoluble coarse mode ("ci").

A.6 Near-surface mass concentration evaluation

Figures A.12–A.15 show scatterplots of the data that is summarized in Table 6.1, i.e., monthly mean near-surface concentration values from the reference simulation with MADE3 vs. those from station network observations. The number of comparable tracers varies by network.

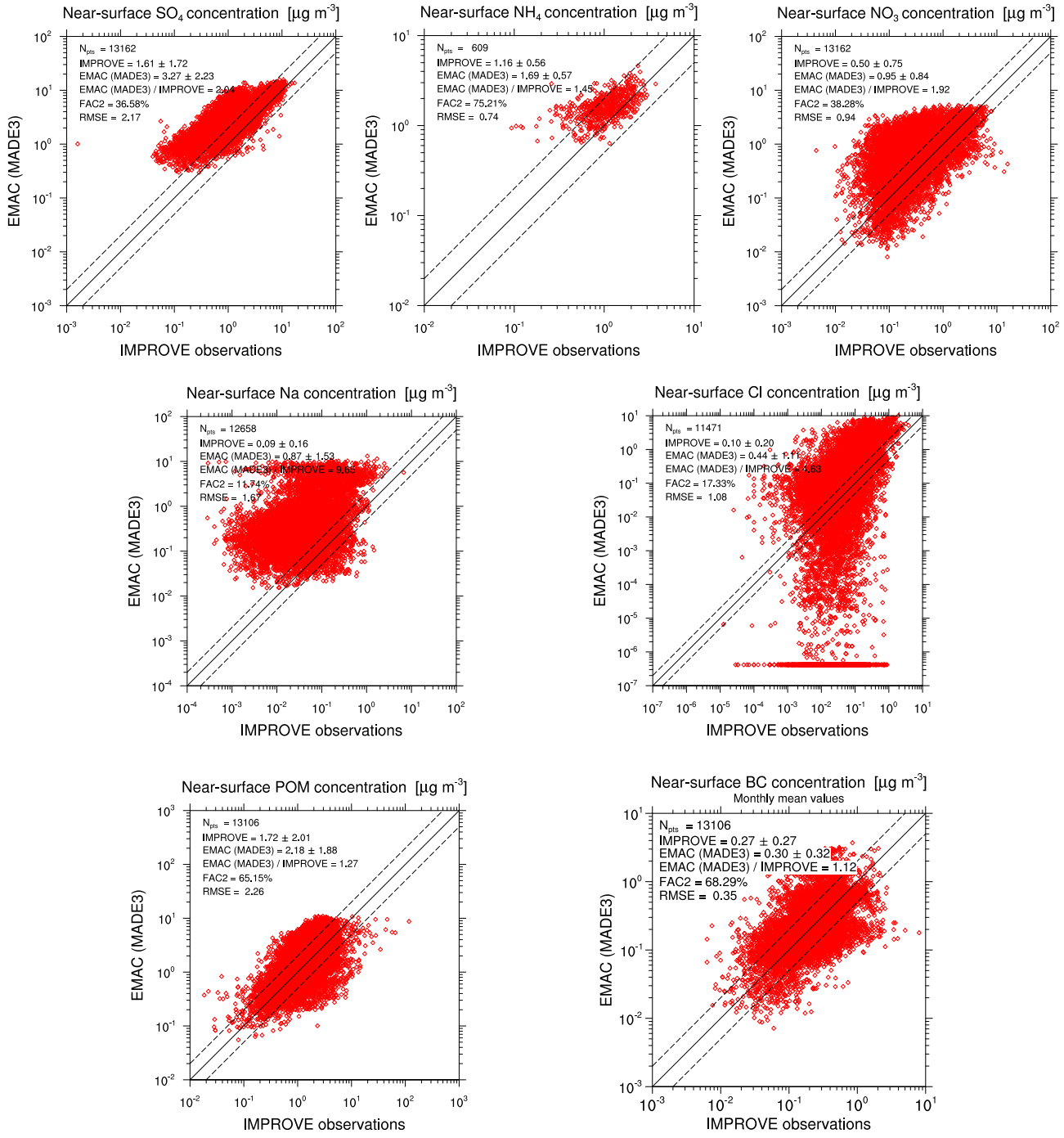

Figure A.12: Monthly mean near-surface aerosol mass concentrations: reference simulation with MADE3 versus observations from the IMPROVE network. N_{pts} stands for the number of compared data points, the next two lines of the legend give the average value plus/minus one standard deviation for the observations and the simulation, respectively, the fourth line gives the ratio of these averages, FAC2 stands for the fraction of simulated data points within a factor of two of the corresponding observed values, and RMSE stands for the root mean squared error of the simulation w.r.t. the observations.

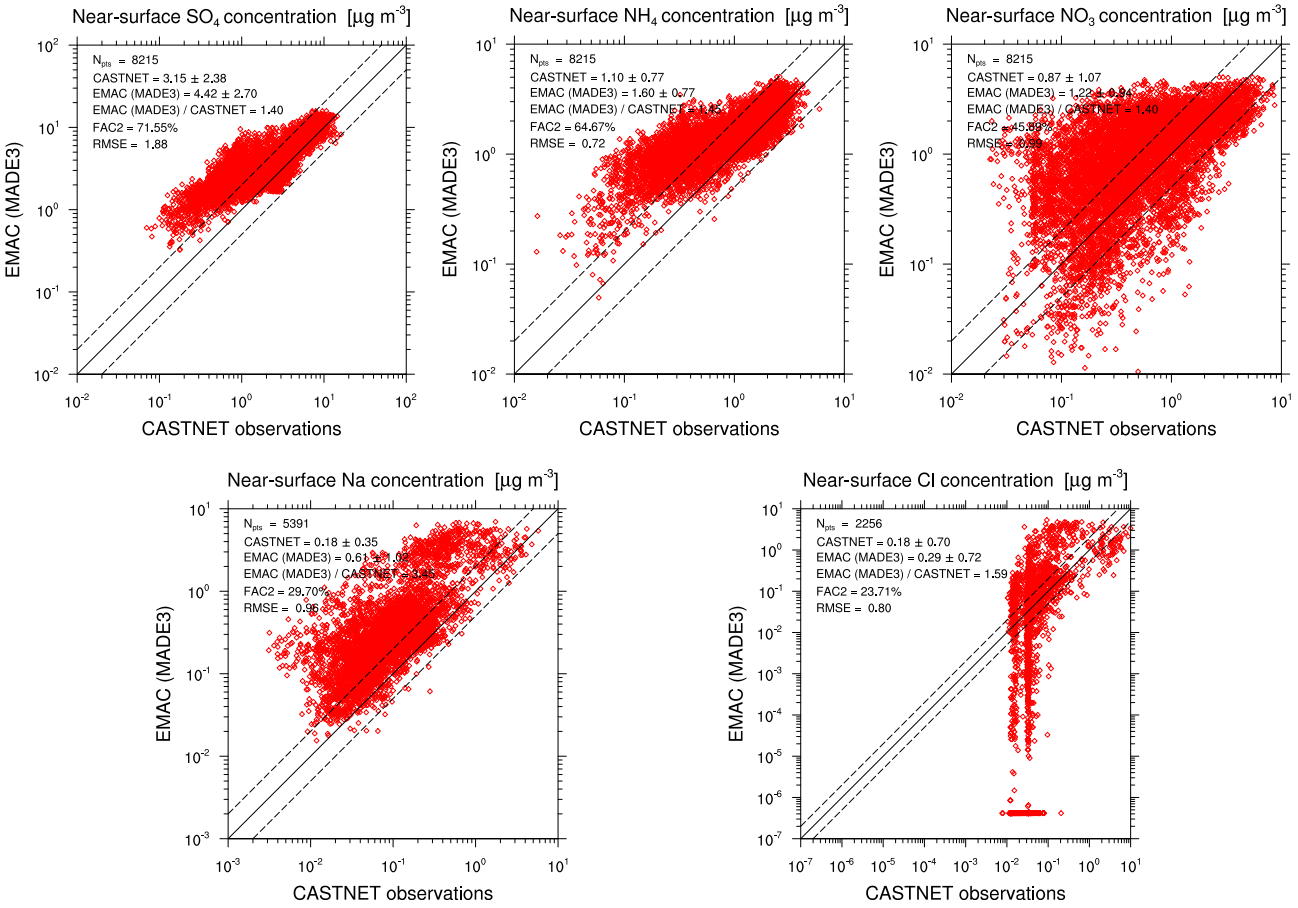

Figure A.13: Same as Fig. A.12, but for CASTNET network.

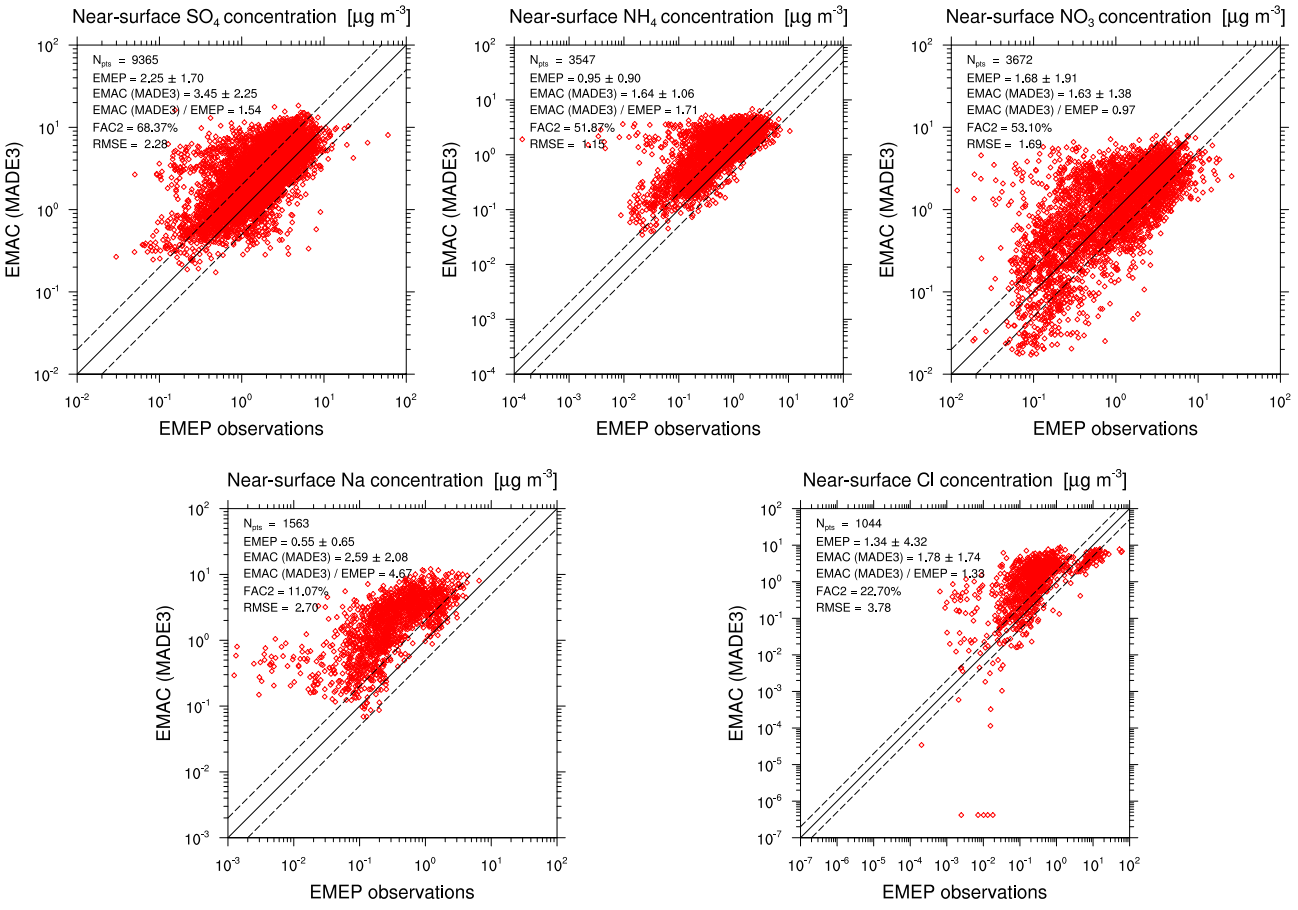

Figure A.14: Same as Fig. A.12, but for EMEP network.

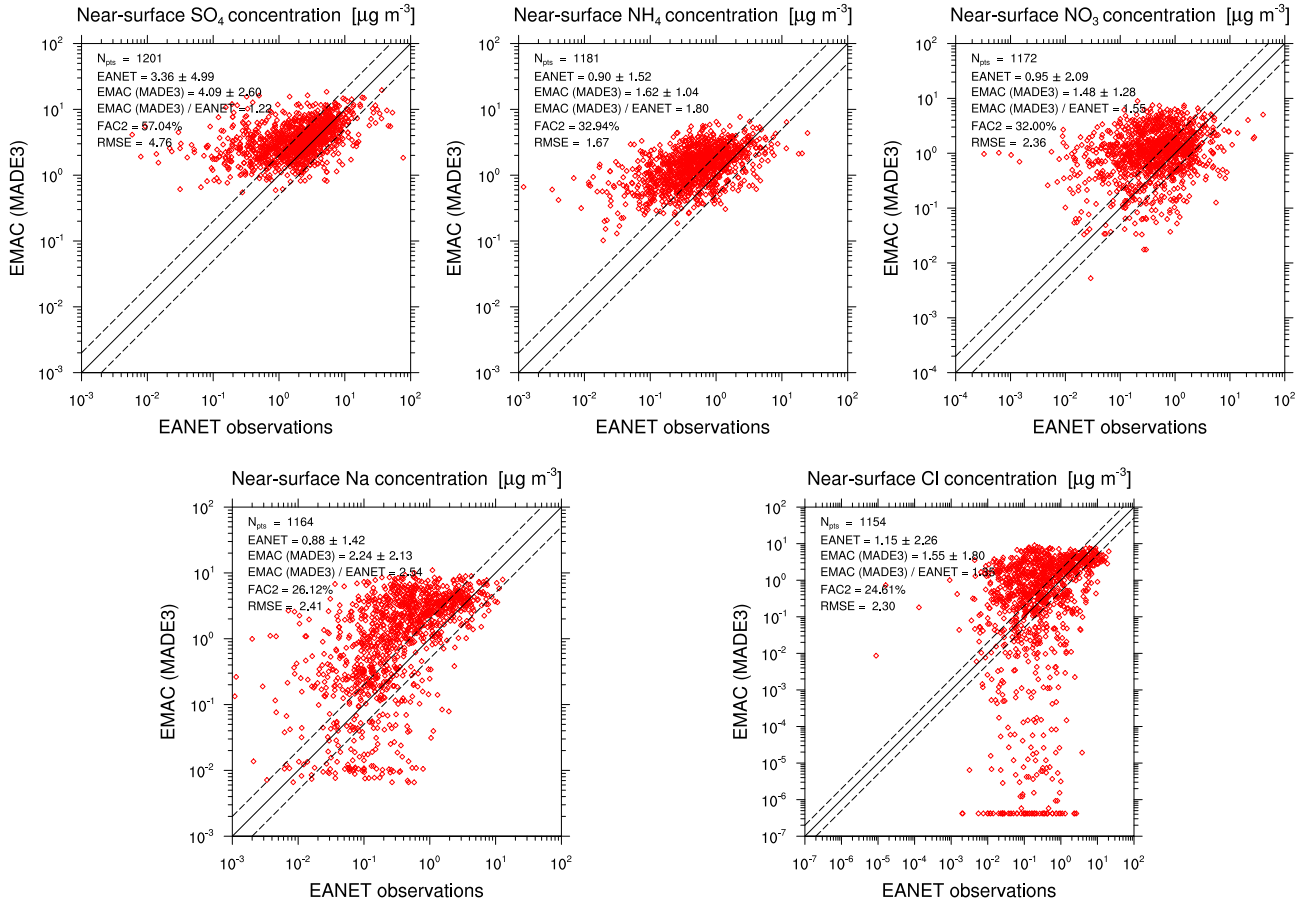

Figure A.15: Same as Fig. A.12, but for EANET network.

References

Aan de Brugh, J. M. J., Ouwersloot, H. G., Vilà-Guerau de Arellano, J., & Krol, M. C. (2013). A large-eddy simulation of the phase transition of ammonium nitrate in a convective boundary layer. *Journal of Geophysical Research: Atmospheres*, 118(2), 826–836. doi:10.1002/jgrd.50161.

Ackerman, T. P. & Toon, O. B. (1981). Absorption of visible radiation in atmosphere containing mixtures of absorbing and nonabsorbing particles. *Applied Optics*, 20(20), 3661–3668. `http://ao.osa.org/abstract.cfm?URI=ao-20-20-3661`.

Ackermann, I. J., Hass, H., Memmesheimer, M., Ebel, A., Binkowski, F. S., & Shankar, U. (1998). Modal aerosol dynamics model for Europe: development and first applications. *Atmospheric Environment*, 32(17), 2981–2999. `http://www.sciencedirect.com/science/article/pii/S1352231098000065`.

Adams, P. J., Seinfeld, J. H., Koch, D., Mickley, L., & Jacob, D. (2001). General circulation model assessment of direct radiative forcing by the sulfate-nitrate-ammonium-water inorganic aerosol system. *Journal of Geophysical Research: Atmospheres*, 106(D1), 1097–1111. doi:10.1029/2000JD900512.

Ahmad, I., Mielonen, T., Grosvenor, D., Portin, H., Arola, A., Mikkonen, S., Kühn, T., Leskinen, A., Juotsensaari, J., Komppula, M., Lehtinen, K., Laaksonen, A., & Romakkaniemi, S. (2013). Long-term measurements of cloud droplet concentrations and aerosol-cloud interactions in continental boundary layer clouds. *Tellus B*, 65(0), 20138. `http://www.tellusb.net/index.php/tellusb/article/view/20138`.

Albani, S., Mahowald, N. M., Perry, A. T., Scanza, R. A., Zender, C. S., Heavens, N. G., Maggi, V., Kok, J. F., & Otto-Bliesner, B. L. (2014). Improved dust representation in the Community Atmosphere Model. *Journal of Advances in Modeling Earth Systems*, 6(3), 541–570. doi:10.1002/2013MS000279.

Allan, J. D., Williams, P. I., Najera, J., Whitehead, J. D., Flynn, M. J., Taylor, J. W., Liu, D., Darbyshire, E., Carpenter, L. J., Chance, R., Andrews, S. J., Hackenberg, S. C., & McFiggans, G. (2015). Iodine observed in new particle formation events in the Arctic atmosphere during ACCACIA. *Atmospheric Chemistry and Physics*, 15(10), 5599–5609. `http://www.atmos-chem-phys.net/15/5599/2015/`.

Allen, R. J. & Landuyt, W. (2014). The vertical distribution of black carbon in CMIP5 models: Comparison to observations and the importance of convective transport. *Journal of Geophysical Research: Atmospheres*, 119(8), 4808–4835. doi:10.1002/2014JD021595.

Almeida, G. P., Brito, J., Morales, C. A., Andrade, M. F., & Artaxo, P. (2014). Measured and modelled cloud condensation nuclei (CCN) concentration in Sáo Paulo, Brazil: the importance of aerosol size-resolved chemical composition on CCN concentration prediction. *Atmospheric Chemistry and Physics*, 14(14), 7559–7572. `http://www.atmos-chem-phys.net/14/7559/2014/`.

Almeida, J., Schobesberger, S., Kürten, A., Ortega, I. K., Kupiainen-Määttä, O., Praplan, A. P., Adamov, A., Amorim, A., Bianchi, F., Breitenlechner, M., David, A., Dommen, J., Donahue, N. M., Downard, A., Dunne, E., Duplissy, J., Ehrhart, S., Flagan, R. C., Franchin, A., Guida, R., Hakala, J., Hansel, A., Heinritzi, M., Henschel, H., Jokinen, T., Junninen, H., Kajos, M., Kangasluoma, J., Keskinen, H., Kupc, A., Kurtén, T., Kvashin, A. N., Laaksonen, A., Lehtipalo, K., Leiminger, M., Leppä, J., Loukonen, V., Makhmutov, V., Mathot, S., McGrath, M. J., Nieminen, T., Olenius, T., Onnela, A., Petäjä, T., Riccobono, F., Riipinen, I., Rissanen, M., Rondo, L., Ruuskanen, T., Santos, F. D., Sarnela, N., Schallhart, S., Schnitzhofer, R., Seinfeld, J. H., Simon, M., Sipilä, M., Stozhkov, Y., Stratmann, F., Tomé, A., Tröstl, J., Tsagkogeorgas, G., Vaattovaara, P., Viisanen, Y., Virtanen, A., Vrtala, A., Wagner, P. E., Weingartner, E., Wex, H., Williamson, C., Wimmer, D., Ye, P., Yli-Juuti, T., Carslaw, K. S., Kulmala, M., Curtius, J., Baltensperger, U., Worsnop, D. R., Vehkamäki, H., & Kirkby, J. (2013). Molecular understanding of sulphuric acid–amine particle nucleation in the atmosphere. *Nature*, 502(7471), 359–363. doi:10.1038/nature12663.

Alterskjær, K. & Kristjánsson, J. E. (2013). The sign of the radiative forcing from marine cloud brightening depends on both particle size and injection amount. *Geophysical Research Letters*, 40(1), 210–215. doi:10.1029/2012GL054286.

AMEC Environment & Infrastructure, Inc. (2015). *Clean Air Status and Trends Network (CASTNET) 2013 Annual Report*. Technical report, U.S. Environmental Protection Agency, Washington, DC, USA. `http://epa.gov/castnet/javaweb/docs/annual_report_2013.pdf`.

Ames, R. B. & Malm, W. C. (2001). Comparison of sulfate and nitrate particle mass concentrations measured by IMPROVE and the CDN. *Atmospheric Environment*, 35(5), 905–916. doi:10.1016/S1352-2310(00)00369-1.

Andreae, M. O. & Merlet, P. (2001). Emission of trace gases and aerosols from biomass burning. *Global Biogeochemical Cycles*, 15(4), 955–966. doi:10.1029/2000GB001382.

Andrejczuk, M., Gadian, A., & Blyth, A. (2014). Numerical simulations of stratocumulus cloud response to aerosol perturbation. *Atmospheric Research*, 140-141, 76–84. doi:10.1016/j.atmosres.2014.01.006.

Andres, R. J. & Kasgnoc, A. D. (1998). A time-averaged inventory of subaerial volcanic sulfur emissions. *Journal of Geophysical Research: Atmospheres*, 103(D19), 25251–25261. doi:10.1029/98JD02091.

Anttila, T., Brus, D., Jaatinen, A., Hyvärinen, A.-P., Kivekäs, N., Romakkaniemi, S., Komppula, M., & Lihavainen, H. (2012). Relationships between particles, cloud condensation nuclei and cloud droplet activation during the third Pallas Cloud Experiment. *Atmospheric Chemistry and Physics*, 12(23), 11435–11450. http://www.atmos-chem-phys.net/12/11435/2012/.

Aquila, V. (2009). *Global model studies on the distribution and composition of potential atmospheric ice nuclei*. PhD thesis, LMU München, Germany. http://elib.dlr.de/61778/1/Aquila-diss-FINAL-20091215.pdf.

Aquila, V., Hendricks, J., Lauer, A., Riemer, N., Vogel, H., Baumgardner, D., Minikin, A., Petzold, A., Schwarz, J. P., Spackman, J. R., Weinzierl, B., Righi, M., & Dall'Amico, M. (2011). MADE-in: a new aerosol microphysics submodel for global simulation of insoluble particles and their mixing state. *Geoscientific Model Development*, 4(2), 325–355. http://www.geosci-model-dev.net/4/325/2011/gmd-4-325-2011.html.

Archer-Nicholls, S., Lowe, D., Utembe, S., Allan, J., Zaveri, R. A., Fast, J. D., Hodnebrog, Ø., Denier van der Gon, H., & McFiggans, G. (2014). Gaseous chemistry and aerosol mechanism developments for version 3.5.1 of the online regional model, WRF-Chem. *Geoscientific Model Development*, 7(6), 2557–2579. http://www.geosci-model-dev.net/7/2557/2014/.

Arden Pope III, C. & Dockery, D. W. (2006). Health Effects of Fine Particulate Air Pollution: Lines that Connect. *Journal of the Air & Waste Management Association*, 56(6), 709–742. doi:10.1080/10473289.2006.10464485.

Athanasopoulou, E., Tombrou, M., Pandis, S. N., & Russell, A. G. (2008). The role of sea-salt emissions and heterogeneous chemistry in the air quality of polluted coastal areas. *Atmospheric Chemistry and Physics*, 8(19), 5755–5769. http://www.atmos-chem-phys.net/8/5755/2008/acp-8-5755-2008.html.

Augustin-Bauditz, S., Wex, H., Kanter, S., Ebert, M., Niedermeier, D., Stolz, F., Prager, A., & Stratmann, F. (2014). The immersion mode ice nucleation behavior of mineral dusts: A comparison of different pure and surface modified dusts. *Geophysical Research Letters*, 41(20), 7375–7382. doi:10.1002/2014GL061317.

Ault, A. P., Moore, M. J., Furutani, H., & Prather, K. A. (2009). Impact of Emissions from the Los Angeles Port Region on San Diego Air Quality during Regional Transport Events. *Environmental Science & Technology*, 43(10), 3500–3506. http://pubs.acs.org/doi/abs/10.1021/es8018918.

Baker, L. H., Collins, W. J., Olivié, D. J. L., Cherian, R., Hodnebrog, Ø., Myhre, G., & Quaas, J. (2015). Climate responses to anthropogenic emissions of short-lived climate pollutants. *Atmospheric Chemistry and Physics*, 15(14), 8201–8216. http://www.atmos-chem-phys.net/15/8201/2015/.

Ban-Weiss, G. A., Cao, L., Bala, G., & Caldeira, K. (2012). Dependence of climate forcing and response on the altitude of black carbon aerosols. *Climate Dynamics*, 38(5-6), 897–911. doi:10.1007/s00382-011-1052-y.

Banzhaf, S., Schaap, M., Wichink Kruit, R. J., Denier van der Gon, H. A. C., Stern, R., & Builtjes, P. J. H. (2013). Impact of emission changes on secondary inorganic aerosol episodes across Germany. *Atmospheric Chemistry and Physics*, 13(23), 11675–11693. http://www.atmos-chem-phys.net/13/11675/2013/.

Bardouki, H., Berresheim, H., Vrekoussis, M., Sciare, J., Kouvarakis, G., Oikonomou, K., Schneider, J., & Mihalopoulos, N. (2003). Gaseous (DMS, MSA, SO_2, H_2SO_4 and DMSO) and particulate (sulfate and methanesulfonate) sulfur species over the northeastern coast of Crete. *Atmospheric Chemistry and Physics*, 3(5), 1871–1886. http://www.atmos-chem-phys.net/3/1871/2003/.

Bates, T. S., Kelly, K. C., Johnson, J. E., & Gammon, R. H. (1995). Regional and seasonal variations in the flux of oceanic carbon monoxide to the atmosphere. *Journal of Geophysical Research: Atmospheres*, 100(D11), 23093–23101. doi:10.1029/95JD02737.

Bauer, S. E. & Menon, S. (2012). Aerosol direct, indirect, semidirect, and surface albedo effects from sector contributions based on the IPCC AR5 emissions for preindustrial and present-day conditions. *Journal of Geophysical Research: Atmospheres*, 117(D1), D01206. doi:10.1029/2011JD016816.

Bauer, S. E., Wright, D. L., Koch, D., Lewis, E. R., McGraw, R., Chang, L. . S., Schwartz, S. E., & Ruedy, R. (2008). MATRIX (Multiconfiguration Aerosol TRacker of mIXing state): an aerosol microphysical module for global atmospheric models. *Atmospheric Chemistry and Physics*, 8(20), 6003–6035. http://www.atmos-chem-phys.net/8/6003/2008/acp-8-6003-2008.html.

Baumgardner, D., Kok, G., Krämer, M., & Weidle, F. (2008). Meridional gradients of light absorbing carbon over northern Europe. *Environmental Research Letters*, 3(2), 025010. http://stacks.iop.org/1748-9326/3/i=2/a=025010.

Bègue, N., Tulet, P., Chaboureau, J.-P., Roberts, G., Gomes, L., & Mallet, M. (2012). Long-range transport of Saharan dust over northwestern Europe during EUCAARI 2008 campaign: Evolution of dust optical properties by scavenging. *Journal of Geophysical Research: Atmospheres*, 117(D17), D17201. doi:10.1029/2012JD017611.

Bellouin, N., Mann, G. W., Woodhouse, M. T., Johnson, C., Carslaw, K. S., & Dalvi, M. (2013a). Impact of the modal aerosol scheme GLOMAP-mode on aerosol forcing in the Hadley Centre Global Environmental Model. *Atmospheric Chemistry and Physics*, 13(6), 3027–3044. http://www.atmos-chem-phys.net/13/3027/2013/.

Bellouin, N., Quaas, J., Morcrette, J.-J., & Boucher, O. (2013b). Estimates of aerosol radiative forcing from the MACC re-analysis. *Atmospheric Chemistry and Physics*, 13(4), 2045–2062. http://www.atmos-chem-phys.net/13/2045/2013/.

Bellouin, N., Rae, J., Jones, A., Johnson, C., Haywood, J., & Boucher, O. (2011). Aerosol forcing in the Climate Model Intercomparison Project (CMIP5) simulations by HadGEM2-ES and the role of ammonium nitrate. *Journal of Geophysical Research: Atmospheres*, 116(D20), D20206. doi:10.1029/2011JD016074.

Berndt, T., Jokinen, T., Sipilä, M., Mauldin III, R. L., Herrmann, H., Stratmann, F., Junninen, H., & Kulmala, M. (2014). H2SO4 formation from the gas-phase reaction of stabilized Criegee Intermediates with SO2: Influence of water vapour content and temperature. *Atmospheric Environment*, 89, 603–612. doi:10.1016/j.atmosenv.2014.02.062.

Bevan, S. L., North, P. R. J., Los, S. O., & Grey, W. M. F. (2012). A global dataset of atmospheric aerosol optical depth and surface reflectance from AATSR. *Remote Sensing of Environment*, 116, 199–210. doi:10.1016/j.rse.2011.05.024.

Bian, Q., Huang, X. H. H., & Yu, J. Z. (2014). One-year observations of size distribution characteristics of major aerosol constituents at a coastal receptor site in Hong Kong – Part 1: Inorganic ions and oxalate. *Atmospheric Chemistry and Physics*, 14(17), 9013–9027. http://www.atmos-chem-phys.net/14/9013/2014/.

Bikkina, S., Kawamura, K., Miyazaki, Y., & Fu, P. (2014). High abundances of oxalic, azelaic, and glyoxylic acids and methylglyoxal in the open ocean with high biological activity: Implication for secondary OA formation from isoprene. *Geophysical Research Letters*, 41(10), 3649–3657. doi:10.1002/2014GL059913.

Binkowski, F. S. & Roselle, S. J. (2003). Models-3 community multiscale air quality (CMAQ) model aerosol component - 1. Model description. *Journal of Geophysical Research: Atmospheres*, 108(D6), 4183. http://onlinelibrary.wiley.com/doi/10.1029/2001JD001409/abstract.

Binkowski, F. S. & Shankar, U. (1995). The Regional Particulate Matter Model: 1. Model description and preliminary results. *Journal of Geophysical Research: Atmospheres*, 100(D12), 26191–26209. doi:10.1029/95JD02093.

Birmili, W., Wiedensohler, A., Heintzenberg, J., & Lehmann, K. (2001). Atmospheric particle number size distribution in central Europe: Statistical relations to air masses and meteorology. *Journal of Geophysical Research: Atmospheres*, 106(D23), 32005–32018. doi:10.1029/2000JD000220.

Bohren, C. F. (1986). Applicability of Effective-Medium Theories to problems of Scattering and Absorption by Nonhomogeneous Atmospheric Particles. *Journal of the Atmospheric Sciences*, 43(5), 468–475. doi:10.1175/1520-0469(1986)043<0468:AOEMTT>2.0.CO;2.

Bond, T. C. & Bergstrom, R. W. (2006). Light absorption by carbonaceous particles: An investigative review. *Aerosol Science and Technology*, 40(1), 27–67. http://www.scopus.com/inward/record.url?eid=2-s2.0-33646400486&partnerID=40&md5=0081751d1d1749d0eb5588abafecd2b0.

Bonn, B., Bourtsoukidis, E., Sun, T. S., Bingemer, H., Rondo, L., Javed, U., Li, J., Axinte, R., Li, X., Brauers, T., Sonderfeld, H., Koppmann, R., Sogachev, A., Jacobi, S., & Spracklen, D. V. (2014). The link between atmospheric radicals and newly formed particles at a spruce forest site in Germany. *Atmospheric Chemistry and Physics*, 14(19), 10823–10843. http://www.atmos-chem-phys.net/14/10823/2014/.

Booth, B. B. B., Dunstone, N. J., Halloran, P. R., Andrews, T., & Bellouin, N. (2012). Aerosols implicated as a prime driver of twentieth-century North Atlantic climate variability. *Nature*, 484(7393), 228–232. doi:10.1038/nature10946.

Boucher, O., Randall, D., Artaxo, P., Bretherton, C., Feingold, G., Forster, P., Kerminen, V.-M., Kondo, Y., Liao, H., Lohmann, U., Rasch, P., Satheesh, S. K., Sherwood, S., Stevens, B., & Zhang, X. Y. (2013). Clouds and Aerosols. In T. F. Stocker, D. Qin, G.-K. Plattner, M. Tignor, S. K. Allen, J. Boschung, A. Nauels, Y. Xia, V. Bex, & P. M. Midgley (Eds.), *Climate Change 2013: The Physical Science Basis. Contribution of Working Group I to the Fifth Assessment Report of the Intergovernmental Panel on Climate Change* chapter 7, (pp. 571–658). Cambridge, United Kingdom and New York, NY, USA: Cambridge University Press. www.climatechange2013.org.

Brinkop, S. & Sausen, R. (1997). A Finite Difference Approximation for Convective Transports which Maintains Positive Tracer Concentrations. *Beiträge zur Physik der Atmosphäre*, 70(3), 245–248. http://elib.dlr.de/32316/1/97-brinkop.pdf.

Buseck, P. R., Adachi, K., Gelencsér, A., Tompa, É., & Pósfai, M. (2012). Are black carbon and soot the same? *Atmospheric Chemistry and Physics Discussions*, 12(9), 24821–24846. http://www.atmos-chem-phys-discuss.net/12/24821/2012/.

Bzdek, B. R., Lawler, M. J., Horan, A. J., Pennington, M. R., DePalma, J. W., Zhao, J., Smith, J. N., & Johnston, M. V. (2014). Molecular constraints on particle growth during new particle formation. *Geophysical Research Letters*, 41(16), 6045–6054. doi:10.1002/2014GL060160.

Capaldo, K., Corbett, J. J., Kasibhatla, P., Fischbeck, P., & Pandis, S. N. (1999). Effects of ship emissions on sulphur cycling and radiative climate forcing over the ocean. *Nature*, 400(6746), 743–746. doi:10.1038/23438.

Capaldo, K. P., Pilinis, C., & Pandis, S. N. (2000). A computationally efficient hybrid approach for dynamic gas/aerosol transfer in air quality models. *Atmospheric Environment*, 34(21), 3617–3627. http://www.sciencedirect.com/science/article/pii/S1352231000000923.

Cappa, C. D., Williams, E. J., Lack, D. A., Buffaloe, G. M., Coffman, D., Hayden, K. L., Herndon, S. C., Lerner, B. M., Li, S.-M., Massoli, P., McLaren, R., Nuaaman, I., Onasch, T. B., & Quinn, P. K. (2014). A case study into the measurement of ship emissions from plume intercepts of the NOAA ship Miller Freeman. *Atmospheric Chemistry and Physics*, 14(3), 1337–1352. http://www.atmos-chem-phys.net/14/1337/2014/.

Carslaw, K. S., Lee, L. A., Reddington, C. L., Mann, G. W., & Pringle, K. J. (2013). The magnitude and sources of uncertainty in global aerosol. *Faraday Discussions*, 165, 495–512. doi:10.1039/C3FD00043E.

Catinon, M., Ayrault, S., Boudouma, O., Bordier, L., Agnello, G., Reynaud, S., & Tissut, M. (2013). Are coarse particles unexpected common reservoirs for some atmospheric anthropogenic trace elements? A case study. *Atmospheric Environment*, 74, 217–226. doi:10.1016/j.atmosenv.2013.03.059.

Cavalli, F., Facchini, M. C., Decesari, S., Mircea, M., Emblico, L., Fuzzi, S., Ceburnis, D., Yoon, Y. J., O'Dowd, C. D., Putaud, J.-P., & Dell'Acqua, A. (2004). Advances in characterization of size-resolved organic matter in marine aerosol over the North Atlantic. *Journal of Geophysical Research: Atmospheres*, 109(D24), D24215. doi:10.1029/2004JD005137.

Chen, J.-P., Tsai, I.-C., & Lin, Y.-C. (2013). A statistical-numerical aerosol parameterization scheme. *Atmospheric Chemistry and Physics*, 13(20), 10483–10504. http://www.atmos-chem-phys.net/13/10483/2013/.

Chen, S.-H., Liu, Y.-C., Nathan, T. R., Davis, C., Torn, R., Sowa, N., Cheng, C.-T., & Chen, J.-P. (2015a). Modeling the Effects of Dust-Radiative Forcing on the Movement of Hurricane Helene (2006). *Quarterly Journal of the Royal Meteorological Society*. doi:10.1002/qj.2542.

Chen, Y.-C., Christensen, M. W., Diner, D. J., & Garay, M. J. (2015b). Aerosol-cloud interactions in ship tracks using Terra MODIS/MISR. *Journal of Geophysical Research: Atmospheres*, 120(7), 2819–2833. doi:10.1002/2014JD022736.

Chen, Y. C., Xue, L., Lebo, Z. J., Wang, H., Rasmussen, R. M., & Seinfeld, J. H. (2011). A comprehensive numerical study of aerosol-cloud-precipitation interactions in marine stratocumulus. *Atmospheric Chemistry and Physics*, 11(18), 9749–9769. `http://www.atmos-chem-phys.net/11/9749/2011/acp-11-9749-2011.html`.

Cherian, R., Quaas, J., Salzmann, M., & Wild, M. (2014). Pollution trends over Europe constrain global aerosol forcing as simulated by climate models. *Geophysical Research Letters*, 41(6), 2176–2181. doi:10.1002/2013GL058715.

Chernoff, D. I. & Bertram, A. K. (2010). Effects of sulfate coatings on the ice nucleation properties of a biological ice nucleus and several types of minerals. *Journal of Geophysical Research: Atmospheres*, 115(D20), D20205. doi:10.1029/2010JD014254.

Ching, J., Riemer, N., & West, M. (2012). Impacts of black carbon mixing state on black carbon nucleation scavenging: Insights from a particle-resolved model. *Journal of Geophysical Research: Atmospheres*, 117(D23), D23209. doi:10.1029/2012JD018269.

Chow, J. C., Watson, J. G., Mauderly, J. L., Costa, D. L., Wyzga, R. E., Vedal, S., Hidy, G. M., Altshuler, S. L., Marrack, D., Heuss, J. M., Wolff, G. T., Arden Pope III, C., & Dockery, D. W. (2006). Health Effects of Fine Particulate Air Pollution: Lines that Connect. *Journal of the Air & Waste Management Association*, 56(10), 1368–1380. doi:10.1080/10473289.2006.10464545.

Christensen, M. W. & Stephens, G. L. (2011). Microphysical and macrophysical responses of marine stratocumulus polluted by underlying ships: Evidence of cloud deepening. *Journal of Geophysical Research: Atmospheres*, 116(D3), D03201. doi:10.1029/2010JD014638.

Christensen, M. W., Suzuki, K., Zambri, B., & Stephens, G. L. (2014). Ship track observations of a reduced shortwave aerosol indirect effect in mixed-phase clouds. *Geophysical Research Letters*, 41(19), 6970–6977. doi:10.1002/2014GL061320.

Christian, T. J., Kleiss, B., Yokelson, R. J., Holzinger, R., Crutzen, P. J., Hao, W. M., Saharjo, B. H., & Ward, D. E. (2003). Comprehensive laboratory measurements of biomass-burning emissions: 1. Emissions from Indonesian, African, and other fuels. *Journal of Geophysical Research: Atmospheres*, 108(D23), 4719. doi:10.1029/2003JD003704.

Clarke, A. D., Davis, D., Kapustin, V. N., Eisele, F., Chen, G., Paluch, I., Lenschow, D., Bandy, A. R., Thornton, D., Moore, K., Mauldin, L., Tanner, D., Litchy, M., Carroll, M. A., Collins, J., & Albercook, G. (1998). Particle Nucleation in the Tropical Boundary Layer and Its Coupling to Marine Sulfur Sources. *Science*, 282(5386), 89–92. `http://www.sciencemag.org/content/282/5386/89.abstract`.

Clarke, A. D., Freitag, S., Simpson, R. M. C., Hudson, J. G., Howell, S. G., Brekhovskikh, V. L., Campos, T., Kapustin, V. N., & Zhou, J. (2013). Free troposphere as a major source of CCN for the equatorial pacific boundary layer: long-range transport and teleconnections. *Atmospheric Chemistry and Physics*, 13(15), 7511–7529. `http://www.atmos-chem-phys.net/13/7511/2013/`.

Clarke, A. D. & Kapustin, V. N. (2002). A Pacific Aerosol Survey. Part I: A Decade of Data on Particle Production, Transport, Evolution, and Mixing in the Troposphere. *Journal of the Atmospheric Sciences*, 59(3), 363–382. doi:10.1175/1520-0469(2002)059<0363:APASPI>2.0.CO;2.

Contini, D., Gambaro, A., Donateo, A., Cescon, P., Cesari, D., Merico, E., Belosi, F., & Citron, M. (2015). Inter-annual trend of the primary contribution of ship emissions to PM2.5 concentrations in Venice (Italy): Efficiency of emissions mitigation strategies. *Atmospheric Environment*, 102, 183–190. doi:10.1016/j.atmosenv.2014.11.065.

Cooke, W. F., Liousse, C., Cachier, H., & Feichter, J. (1999). Construction of a $1^\circ \times 1^\circ$ fossil fuel emission data set for carbonaceous aerosol and implementation and radiative impact in the ECHAM4 model. *Journal of Geophysical Research: Atmospheres*, 104(D18), 22137–22162. doi:10.1029/1999JD900187.

Corbett, J. J., Winebrake, J. J., Green, E. H., Kasibhatla, P., Eyring, V., & Lauer, A. (2007). Mortality from Ship Emissions: A Global Assessment. *Environmental Science & Technology*, 41(24), 8512–8518. doi:10.1021/es071686z.

Costantino, L. & Bréon, F.-M. (2013). Aerosol indirect effect on warm clouds over South-East Atlantic, from co-located MODIS and CALIPSO observations. *Atmospheric Chemistry and Physics*, 13(1), 69–88. http://www.atmos-chem-phys.net/13/69/2013/.

Crippa, M., Canonaco, F., Lanz, V. A., Äijälä, M., Allan, J. D., Carbone, S., Capes, G., Ceburnis, D., Dall'Osto, M., Day, D. A., DeCarlo, P. F., Ehn, M., Eriksson, A., Freney, E., Hildebrandt Ruiz, L., Hillamo, R., Jimenez, J. L., Junninen, H., Kiendler-Scharr, A., Kortelainen, A.-M., Kulmala, M., Laaksonen, A., Mensah, A. A., Mohr, C., Nemitz, E., O'Dowd, C., Ovadnevaite, J., Pandis, S. N., Petäjä, T., Poulain, L., Saarikoski, S., Sellegri, K., Swietlicki, E., Tiitta, P., Worsnop, D. R., Baltensperger, U., & Prévôt, A. S. H. (2014). Organic aerosol components derived from 25 AMS data sets across Europe using a consistent ME-2 based source apportionment approach. *Atmospheric Chemistry and Physics*, 14(12), 6159–6176. http://www.atmos-chem-phys.net/14/6159/2014/.

Crisp, T. A., Lerner, B. M., Williams, E. J., Quinn, P. K., Bates, T. S., & Bertram, T. H. (2014). Observations of gas phase hydrochloric acid in the polluted marine boundary layer. *Journal of Geophysical Research: Atmospheres*, 119(11), 6897–6915. doi:10.1002/2013JD020992.

Croft, B., Pierce, J. R., Martin, R. V., Hoose, C., & Lohmann, U. (2012). Uncertainty associated with convective wet removal of entrained aerosols in a global climate model. *Atmospheric Chemistry and Physics*, 12(22), 10725–10748. http://www.atmos-chem-phys.net/12/10725/2012/.

Crosbie, E., Youn, J.-S., Balch, B., Wonaschütz, A., Shingler, T., Wang, Z., Conant, W. C., Betterton, E. A., & Sorooshian, A. (2015). On the competition among aerosol number, size and composition in predicting CCN variability: a multi-annual field study in an urbanized desert. *Atmospheric Chemistry and Physics*, 15(12), 6943–6958. http://www.atmos-chem-phys.net/15/6943/2015/.

Cruz, C. N., Dassios, K. G., & Pandis, S. N. (2000). The effect of dioctyl phthalate films on the ammonium nitrate aerosol evaporation rate. *Atmospheric Environment*, 34(23), 3897–3905. doi:10.1016/S1352-2310(00)00173-4.

Dalirian, M., Keskinen, H., Ahlm, L., Ylisirniö, A., Romakkaniemi, S., Laaksonen, A., Virtanen, A., & Riipinen, I. (2015). CCN activation of fumed silica aerosols mixed with soluble pollutants. *Atmospheric Chemistry and Physics*, 15(7), 3815–3829. http://www.atmos-chem-phys.net/15/3815/2015/.

D'Andrea, S. D., Häkkinen, S. A. K., Westervelt, D. M., Kuang, C., Levin, E. J. T., Kanawade, V. P., Leaitch, W. R., Spracklen, D. V., Riipinen, I., & Pierce, J. R. (2013). Understanding global secondary organic aerosol amount and size-resolved condensational behavior. *Atmospheric Chemistry and Physics*, 13(22), 11519–11534. http://www.atmos-chem-phys.net/13/11519/2013/.

Dassios, K. G. & Pandis, S. N. (1999). The mass accommodation coefficient of ammonium nitrate aerosol. *Atmospheric Environment*, 33(18), 2993–3003. doi:10.1016/S1352-2310(99)00079-5.

de Leeuw, G., Holzer-Popp, T., Bevan, S., Davies, W. H., Descloitres, J., Grainger, R. G., Griesfeller, J., Heckel, A., Kinne, S., Klüser, L., Kolmonen, P., Litvinov, P., Martynenko, D., North, P., Ovigneur, B., Pascal, N., Poulsen, C., Ramon, D., Schulz, M., Siddans, R., Sogacheva, L., Tanré, D., Thomas, G. E., Virtanen, T. H., von Hoyningen Huene, W., Vountas, M., & Pinnock, S. (2015). Evaluation of seven European aerosol optical depth retrieval algorithms for climate analysis. *Remote Sensing of Environment*, 162, 295–315. doi:10.1016/j.rse.2013.04.023.

DeMott, P. J., Cziczo, D. J., Prenni, A. J., Murphy, D. M., Kreidenweis, S. M., Thomson, D. S., Borys, R., & Rogers, D. C. (2003). Measurements of the concentration and composition of nuclei for cirrus formation. *Proceedings of the National Academy of Sciences*, 100(25), 14655–14660. http://www.pnas.org/content/100/25/14655.abstract.

Dentener, F., Kinne, S., Bond, T., Boucher, O., Cofala, J., Generoso, S., Ginoux, P., Gong, S., Hoelzemann, J. J., Ito, A., Marelli, L., Penner, J. E., Putaud, J.-P., Textor, C., Schulz, M., van der Werf, G. R., & Wilson, J. (2006). Emissions of primary aerosol and precursor gases in the years 2000 and 1750 prescribed data-sets for AeroCom. *Atmospheric Chemistry and Physics*, 6(12), 4321–4344. http://www.atmos-chem-phys.net/6/4321/2006/.

Deshler, T. (2008). A review of global stratospheric aerosol: Measurements, importance, life cycle, and local stratospheric aerosol. *Atmospheric Research*, 90(2–4), 223–232. doi:10.1016/j.atmosres.2008.03.016.

DeVille, R. E. L., Riemer, N., & West, M. (2011). Weighted Flow Algorithms (WFA) for stochastic particle coagulation. *Journal of Computational Physics*, 230(23), 8427–8451. doi:10.1016/j.jcp.2011.07.027.

Ding, A. J., Fu, C. B., Yang, X. Q., Sun, J. N., Petäjä, T., Kerminen, V.-M., Wang, T., Xie, Y., Herrmann, E., Zheng, L. F., Nie, W., Liu, Q., Wei, X. L., & Kulmala, M. (2013). Intense atmospheric pollution modifies weather: a case of mixed biomass burning with fossil fuel combustion pollution in eastern China. *Atmospheric Chemistry and Physics*, 13(20), 10545–10554. `http://www.atmos-chem-phys.net/13/10545/2013/`.

Doherty, O. M. & Evan, A. T. (2014). Identification of a new dust-stratocumulus indirect effect over the tropical North Atlantic. *Geophysical Research Letters*, 41(19), 6935–6942. doi:10.1002/2014GL060897.

Donahue, N. M., Robinson, A. L., & Pandis, S. N. (2009). Atmospheric organic particulate matter: From smoke to secondary organic aerosol. *Atmospheric Environment*, 43(1), 94–106. doi:10.1016/j.atmosenv.2008.09.055.

Dusek, U., Frank, G. P., Hildebrandt, L., Curtius, J., Schneider, J., Walter, S., Chand, D., Drewnick, F., Hings, S., Jung, D., Borrmann, S., & Andreae, M. O. (2006). Size Matters More Than Chemistry for Cloud-Nucleating Ability of Aerosol Particles. *Science*, 312(5778), 1375–1378. `http://www.sciencemag.org/content/312/5778/1375.abstract`.

Easter, R. C., Ghan, S. J., Zhang, Y., Saylor, R. D., Chapman, E. G., Laulainen, N. S., Abdul-Razzak, H., Leung, L. R., Bian, X. D., & Zaveri, R. A. (2004). MIRAGE: Model description and evaluation of aerosols and trace gases. *Journal of Geophysical Research: Atmospheres*, 109(D20), D20210. doi:10.1029/2004JD004571.

Eisele, F. L. & Tanner, D. J. (1993). Measurement of the gas phase concentration of H2SO4 and methane sulfonic acid and estimates of H2SO4 production and loss in the atmosphere. *Journal of Geophysical Research: Atmospheres*, 98(D5), 9001–9010. doi:10.1029/93JD00031.

Ekman, A. M. L. (2014). Do sophisticated parameterizations of aerosol-cloud interactions in CMIP5 models improve the representation of recent observed temperature trends? *Journal of Geophysical Research: Atmospheres*, 119(2), 817–832. doi:10.1002/2013JD020511.

Endresen, Ø., Sørgård, E., Sundet, J. K., Dalsøren, S. B., Isaksen, I. S. A., Berglen, T. F., & Gravir, G. (2003). Emission from international sea transportation and environmental impact. *Journal of Geophysical Research: Atmospheres*, 108(D17), 4560. doi:10.1029/2002JD002898.

Eyring, V., Isaksen, I. S. A., Berntsen, T., Collins, W. J., Corbett, J. J., Endresen, O., Grainger, R. G., Moldanova, J., Schlager, H., & Stevenson, D. S. (2010). Transport impacts on atmosphere and climate: Shipping. *Atmospheric Environment*, 44(37), 4735–4771. doi:10.1016/j.atmosenv.2009.04.059.

Eyring, V., Köhler, H. W., van Aardenne, J., & Lauer, A. (2005). Emissions from international shipping: 1. The last 50 years. *Journal of Geophysical Research: Atmospheres*, 110(D17), D17305. doi:10.1029/2004JD005619.

Eyring, V., Righi, M., Evaldsson, M., Lauer, A., Wenzel, S., Jones, C., Anav, A., Andrews, O., Cionni, I., Davin, E. L., Deser, C., Ehbrecht, C., Friedlingstein, P., Gleckler, P., Gottschaldt, K.-D., Hagemann, S., Juckes, M., Kindermann, S., Krasting, J., Kunert, D., Levine, R., Loew, A., Mäkelä, J., Martin, G., Mason, E., Phillips, A., Read, S., Rio, C., Roehrig, R., Senftleben, D., Sterl, A., van Ulft, L. H., Walton, J., Wang, S., & Williams, K. D. (2015). ESMValTool (v1.0) – a community diagnostic and performance metrics tool for routine evaluation of Earth System Models in CMIP. *Geoscientific Model Development Discussions*, 8(9), 7541–7661. `http://www.geosci-model-dev-discuss.net/8/7541/2015/`.

Eyring, V., Stevenson, D. S., Lauer, A., Dentener, F. J., Butler, T., Collins, W. J., Ellingsen, K., Gauss, M., Hauglustaine, D. A., Isaksen, I. S. A., Lawrence, M. G., Richter, A., Rodriguez, J. M., Sanderson, M., Strahan, S. E., Sudo, K., Szopa, S., van Noije, T. P. C., & Wild, O. (2007). Multi-model simulations of the impact of international shipping on Atmospheric Chemistry and Climate in 2000 and 2030. *Atmospheric Chemistry and Physics*, 7(3), 757–780. `http://www.atmos-chem-phys.net/7/757/2007/`.

Fan, S.-M., Moxim, W. J., & Levy, H. (2006). Aeolian input of bioavailable iron to the ocean. *Geophysical Research Letters*, 33(7), L07602. doi:10.1029/2005GL024852.

Fang, Y., Naik, V., Horowitz, L. W., & Mauzerall, D. L. (2013). Air pollution and associated human mortality: the role of air pollutant emissions, climate change and methane concentration increases from the preindustrial period to present. *Atmospheric Chemistry and Physics*, 13(3), 1377–1394. `http://www.atmos-chem-phys.net/13/1377/2013/`.

Feingold, G., McComiskey, A., Rosenfeld, D., & Sorooshian, A. (2013). On the relationship between cloud contact time and precipitation susceptibility to aerosol. *Journal of Geophysical Research: Atmospheres*, 118(18), 10544–10554. doi:10.1002/jgrd.50819.

Feng, Y. & Penner, J. E. (2007). Global modeling of nitrate and ammonium: Interaction of aerosols and tropospheric chemistry. *Journal of Geophysical Research: Atmospheres*, 112(D1), D01304. doi:10.1029/2005JD006404.

Fiebig, M., Stohl, A., Wendisch, M., Eckhardt, S., & Petzold, A. (2003). Dependence of solar radiative forcing of forest fire aerosol on ageing and state of mixture. *Atmospheric Chemistry and Physics*, 3(3), 881–891. http://www.atmos-chem-phys.net/3/881/2003/.

Fierce, L., Riemer, N., & Bond, T. C. (2013). When is cloud condensation nuclei activity sensitive to particle characteristics at emission? *Journal of Geophysical Research: Atmospheres*, 118(24), 13476–13488. doi:10.1002/2013JD020608.

Fierce, L., Riemer, N., & Bond, T. C. (2015). Explaining variance in black carbon's aging timescale. *Atmospheric Chemistry and Physics*, 15(6), 3173–3191. http://www.atmos-chem-phys.net/15/3173/2015/.

Fitzgerald, E., Ault, A. P., Zauscher, M. D., Mayol-Bracero, O. L., & Prather, K. A. (2015). Comparison of the mixing state of long-range transported Asian and African mineral dust. *Atmospheric Environment*, 115, 19–25. doi:10.1016/j.atmosenv.2015.04.031.

Formenti, P., Caquineau, S., Desboeufs, K., Klaver, A., Chevaillier, S., Journet, E., & Rajot, J. L. (2014). Mapping the physico-chemical properties of mineral dust in western Africa: mineralogical composition. *Atmospheric Chemistry and Physics*, 14(19), 10663–10686. http://www.atmos-chem-phys.net/14/10663/2014/.

Forster, P., Ramaswamy, V., Artaxo, P., Berntsen, T., Betts, R., Fahey, D. W., Haywood, J., Lean, J., Lowe, D. C., Myhre, G., Nganga, J., Prinn, R., Raga, G., Schulz, M., & Van Dorland, R. (2007). Changes in Atmospheric Constituents and in Radiative Forcing. In S. Solomon, D. Qin, M. Manning, Z. Chen, M. Marquis, K. B. Averyt, M. Tignor, & H. L. Miller (Eds.), *Climate Change 2007: The Physical Science Basis. Contribution of Working Group I to the Fourth Assessment Report of the Intergovernmental Panel on Climate Change*. Cambridge, United Kingdom and New York, NY, USA: Cambridge University Press. http://ipcc.ch/publications_and_data/ar4/wg1/en/contents.html.

Fortuin, F. P. J. & Kelder, H. (1998). An ozone climatology based on ozonesonde and satellite measurements. *Journal of Geophysical Research: Atmospheres*, 103(D24), 31709–31734. doi:10.1029/1998JD200008.

Fuglestvedt, J., Berntsen, T., Eyring, V., Isaksen, I., Lee, D. S., & Sausen, R. (2009). Shipping Emissions: From Cooling to Warming of Climate—and Reducing Impacts on Health. *Environmental Science & Technology*, 43(24), 9057–9062. http://pubs.acs.org/doi/abs/10.1021/es901944r.

Fuglestvedt, J., Berntsen, T., Myhre, G., Rypdal, K., & Skeie, R. B. (2008). Climate forcing from the transport sectors. *Proceedings of the National Academy of Sciences*, 105(2), 454–458. http://www.pnas.org/content/105/2/454.abstract.

Fuzzi, S., Baltensperger, U., Carslaw, K., Decesari, S., Denier van der Gon, H., Facchini, M. C., Fowler, D., Koren, I., Langford, B., Lohmann, U., Nemitz, E., Pandis, S., Riipinen, I., Rudich, Y., Schaap, M., Slowik, J. G., Spracklen, D. V., Vignati, E., Wild, M., Williams, M., & Gilardoni, S. (2015). Particulate matter, air quality and climate: lessons learned and future needs. *Atmospheric Chemistry and Physics*, 15(14), 8217–8299. http://www.atmos-chem-phys.net/15/8217/2015/.

Gantt, B. & Meskhidze, N. (2013). The physical and chemical characteristics of marine primary organic aerosol: a review. *Atmospheric Chemistry and Physics*, 13(8), 3979–3996. http://www.atmos-chem-phys.net/13/3979/2013/.

Ghan, S. J., Liu, X., Easter, R. C., Zaveri, R., Rasch, P. J., Yoon, J.-H., & Eaton, B. (2012). Toward a Minimal Representation of Aerosols in Climate Models: Comparative Decomposition of Aerosol Direct, Semidirect, and Indirect Radiative Forcing. *Journal of Climate*, 25(19), 6461–6476. doi:10.1175/JCLI-D-11-00650.1.

Ghan, S. J. & Schwartz, S. E. (2007). Aerosol properties and processes - A path from field and laboratory measurements to global climate models. *Bulletin of the American Meteorological Society*, 88(7), 1059–1083. doi:10.1175/BAMS-88-7-1059.

Ginoux, P., Chin, M., Tegen, I., Prospero, J. M., Holben, B., Dubovik, O., & Lin, S.-J. (2001). Sources and distributions of dust aerosols simulated with the GOCART model. *Journal of Geophysical Research: Atmospheres*, 106(D17), 20255–20273. doi:10.1029/2000JD000053.

Ginoux, P., Prospero, J. M., Torres, O., & Chin, M. (2004). Long-term simulation of global dust distribution with the GOCART model: correlation with North Atlantic Oscillation. *Environmental Modelling & Software*, 19(2), 113–128. doi:10.1016/S1364-8152(03)00114-2.

Giordano, M., Espinoza, C., & Asa-Awuku, A. (2015). Experimentally measured morphology of biomass burning aerosol and its impacts on CCN ability. *Atmospheric Chemistry and Physics*, 15(4), 1807–1821. http://www.atmos-chem-phys.net/15/1807/2015/.

Glaccum, R. A. & Prospero, J. M. (1980). Saharan aerosols over the tropical North Atlantic – Mineralogy. *Marine Geology*, 37(3–4), 295–321. http://www.sciencedirect.com/science/article/pii/0025322780901073.

Gläser, G., Kerkweg, A., & Wernli, H. (2012). The Mineral Dust Cycle in EMAC 2.40: sensitivity to the spectral resolution and the dust emission scheme. *Atmospheric Chemistry and Physics*, 12(3), 1611–1627. http://www.atmos-chem-phys.net/12/1611/2012/.

Glasoe, W. A., Volz, K., Panta, B., Freshour, N., Bachman, R., Hanson, D. R., McMurry, P. H., & Jen, C. (2015). Sulfuric acid nucleation: An experimental study of the effect of seven bases. *Journal of Geophysical Research: Atmospheres*, 120(5), 1933–1950. doi:10.1002/2014JD022730.

Gong, L., Lewicki, R., Griffin, R. J., Tittel, F. K., Lonsdale, C. R., Stevens, R. G., Pierce, J. R., Malloy, Q. G. J., Travis, S. A., Bobmanuel, L. M., Lefer, B. L., & Flynn, J. H. (2013). Role of atmospheric ammonia in particulate matter formation in Houston during summertime. *Atmospheric Environment*, 77, 893–900. doi:10.1016/j.atmosenv.2013.04.079.

Gong, S. L., Lavoué, D., Zhao, T. L., Huang, P., & Kaminski, J. W. (2012). GEM-AQ/EC, an on-line global multi-scale chemical weather modelling system: model development and evaluation of global aerosol climatology. *Atmospheric Chemistry and Physics*, 12(17), 8237–8256. http://www.atmos-chem-phys.net/12/8237/2012/.

Gonser, S. G., Klein, F., Birmili, W., Größ, J., Kulmala, M., Manninen, H. E., Wiedensohler, A., & Held, A. (2014). Ion–particle interactions during particle formation and growth at a coniferous forest site in central Europe. *Atmospheric Chemistry and Physics*, 14(19), 10547–10563. http://www.atmos-chem-phys.net/14/10547/2014/.

González, Y. & Rodríguez, S. (2013). A comparative study on the ultrafine particle episodes induced by vehicle exhaust: A crude oil refinery and ship emissions. *Atmospheric Research*, 120–121, 43–54. http://www.sciencedirect.com/science/article/pii/S0169809512002633.

Goren, T. & Rosenfeld, D. (2012). Satellite observations of ship emission induced transitions from broken to closed cell marine stratocumulus over large areas. *Journal of Geophysical Research: Atmospheres*, 117(D17), D17206. doi:10.1029/2012JD017981.

Goren, T. & Rosenfeld, D. (2014). Decomposing aerosol cloud radiative effects into cloud cover, liquid water path and Twomey components in marine stratocumulus. *Atmospheric Research*, 138, 378–393. doi:10.1016/j.atmosres.2013.12.008.

Grewe, V., Brunner, D., Dameris, M., Grenfell, J. L., Hein, R., Shindell, D., & Staehelin, J. (2001). Origin and variability of upper tropospheric nitrogen oxides and ozone at northern mid-latitudes. *Atmospheric Environment*, 35(20), 3421–3433. doi:10.1016/S1352-2310(01)00134-0.

Guelle, W., Schulz, M., Balkanski, Y., & Dentener, F. (2001). Influence of the source formulation on modeling the atmospheric global distribution of sea salt aerosol. *Journal of Geophysical Research: Atmospheres*, 106(D21), 27509–27524. doi:10.1029/2001JD900249.

Guenther, A., Hewitt, C. N., Erickson, D., Fall, R., Geron, C., Graedel, T., Harley, P., Klinger, L., Lerdau, M., Mckay, W. A., Pierce, T., Scholes, B., Steinbrecher, R., Tallamraju, R., Taylor, J., & Zimmerman, P. (1995). A global model of natural volatile organic compound emissions. *Journal of Geophysical Research: Atmospheres*, 100(D5), 8873–8892. doi:10.1029/94JD02950.

Gupta, D., Kim, H., Park, G., Li, X., Eom, H.-J., & Ro, C.-U. (2015). Hygroscopic properties of NaCl and $NaNO_3$ mixture particles as reacted inorganic sea-salt aerosol surrogates. *Atmospheric Chemistry and Physics*, 15(6), 3379–3393. http://www.atmos-chem-phys.net/15/3379/2015/.

Hale, G. M. & Querry, M. R. (1973). Optical Constants of Water in the 200-nm to 200-μm Wavelength Region. *Applied Optics*, 12(3), 555–563. http://ao.osa.org/abstract.cfm?URI=ao-12-3-555.

Hallquist, M., Wenger, J. C., Baltensperger, U., Rudich, Y., Simpson, D., Claeys, M., Dommen, J., Donahue, N. M., George, C., Goldstein, A. H., Hamilton, J. F., Herrmann, H., Hoffmann, T., Iinuma, Y., Jang, M., Jenkin, M. E., Jimenez, J. L., Kiendler-Scharr, A., Maenhaut, W., McFiggans, G., Mentel, T. F., Monod, A., Prévôt, A. S. H., Seinfeld, J. H., Surratt, J. D., Szmigielski, R., & Wildt, J. (2009). The formation, properties and impact of secondary organic aerosol: current and emerging issues. *Atmospheric Chemistry and Physics*, 9(14), 5155–5236. http://www.atmos-chem-phys.net/9/5155/2009/.

Hand, J. L., Copeland, S. A., Day, D. E., Dillner, A. M., Indresand, H., Malm, W. C., McDade, C. E., Moore, Jr., C. T. T., Pitchford, M. L., Schichtel, B. A., & Watson, J. G. (2011). *Spatial and Seasonal Patterns and Temporal Variability of Haze and its Constituents in the United States – Report V*. Technical report, Cooperative Institute for Research in the Atmosphere, Colorado State University, Fort Collins, CO, USA. http://vista.cira.colostate.edu/improve/Publications/Reports/2011/PDF/IMPROVE_V_FullReport.pdf.

Hand, J. L., Schichtel, B. A., Malm, W. C., Pitchford, M., & Frank, N. H. (2014). Spatial and seasonal patterns in urban influence on regional concentrations of speciated aerosols across the United States. *Journal of Geophysical Research: Atmospheres*, 119(22), 12832–12849. doi:10.1002/2014JD022328.

Hara, K., Nakazawa, F., Fujita, S., Fukui, K., Enomoto, H., & Sugiyama, S. (2014). Horizontal distributions of aerosol constituents and their mixing states in Antarctica during the JASE traverse. *Atmospheric Chemistry and Physics*, 14(18), 10211–10230. http://www.atmos-chem-phys.net/14/10211/2014/.

Hara, K., Osada, K., Hayashi, M., Matsunaga, K., Shibata, T., Iwasaka, Y., & Furuya, K. (1999). Fractionation of inorganic nitrates in winter Arctic troposphere: Coarse aerosol particles containing inorganic nitrates. *Journal of Geophysical Research: Atmospheres*, 104(D19), 23671–23679. doi:10.1029/1999JD900348.

Harris, E., Sinha, B., van Pinxteren, D., Schneider, J., Poulain, L., Collett, J., D'Anna, B., Fahlbusch, B., Foley, S., Fomba, K. W., George, C., Gnauk, T., Henning, S., Lee, T., Mertes, S., Roth, A., Stratmann, F., Borrmann, S., Hoppe, P., & Herrmann, H. (2014). In-cloud sulfate addition to single particles resolved with sulfur isotope analysis during HCCT-2010. *Atmospheric Chemistry and Physics*, 14(8), 4219–4235. http://www.atmos-chem-phys.net/14/4219/2014/.

Hartmann, D. L., Ockert-Bell, M. E., & Michelsen, M. L. (1992). The Effect of Cloud Type on Earth's Energy Balance: Global Analysis. *Journal of Climate*, 5(11), 1281–1304. doi:10.1175/1520-0442(1992)005<1281:TEOCTO>2.0.CO;2.

Hauglustaine, D. A., Balkanski, Y., & Schulz, M. (2014). A global model simulation of present and future nitrate aerosols and their direct radiative forcing of climate. *Atmospheric Chemistry and Physics*, 14(20), 11031–11063. http://www.atmos-chem-phys.net/14/11031/2014/.

He, J. & Zhang, Y. (2014). Improvement and further development in CESM/CAM5: gas-phase chemistry and inorganic aerosol treatments. *Atmospheric Chemistry and Physics*, 14(17), 9171–9200. http://www.atmos-chem-phys.net/14/9171/2014/.

He, J., Zhang, Y., Glotfelty, T., He, R., Bennartz, R., Rausch, J., & Sartelet, K. (2015). Decadal simulation and comprehensive evaluation of CESM/CAM5.1 with advanced chemistry, aerosol microphysics, and aerosol-cloud interactions. *Journal of Advances in Modeling Earth Systems*, 7(1), 110–141. doi:10.1002/2014MS000360.

Heald, C. L., Ridley, D. A., Kroll, J. H., Barrett, S. R. H., Cady-Pereira, K. E., Alvarado, M. J., & Holmes, C. D. (2014). Contrasting the direct radiative effect and direct radiative forcing of aerosols. *Atmospheric Chemistry and Physics*, 14(11), 5513–5527. http://www.atmos-chem-phys.net/14/5513/2014/.

Healy, R. M., Riemer, N., Wenger, J. C., Murphy, M., West, M., Poulain, L., Wiedensohler, A., O'Connor, I. P., McGillicuddy, E., Sodeau, J. R., & Evans, G. J. (2014). Single particle diversity and mixing state measurements. *Atmospheric Chemistry and Physics*, 14(12), 6289–6299. http://www.atmos-chem-phys.net/14/6289/2014/.

Heil, A. (2007). *Indonesian Forest and Peat Fires: Emissions, Air Quality, and Human Health*. PhD thesis, Max-Planck-Institut für Meteorologie, Hamburg, Germany. http://pubman.mpdl.mpg.de/pubman/item/escidoc:994286/component/escidoc:994285/BzE_50.pdf.

Heintzenberg, J., Covert, D., & Van Dingenen, R. (2000). Size distribution and chemical composition of marine aerosols: a compilation and review. *Tellus B*, 52(4), 1104–1122. `http://www.tellusb.net/index.php/tellusb/article/view/17090`.

Hendricks, J., Kärcher, B., & Lohmann, U. (2011). Effects of ice nuclei on cirrus clouds in a global climate model. *Journal of Geophysical Research: Atmospheres*, 116(D18), D18206. doi:10.1029/2010JD015302.

Hendricks, J., Lippert, E., Petry, H., & Ebel, A. (1999). Heterogeneous reactions on and in sulfate aerosols: Implications for the chemistry of the midlatitude tropopause region. *Journal of Geophysical Research: Atmospheres*, 104(D5), 5531–5550. doi:10.1029/1998JD100098.

Hennigan, C. J., Westervelt, D. M., Riipinen, I., Engelhart, G. J., Lee, T., Collett, Jeffrey L., J., Pandis, S. N., Adams, P. J., & Robinson, A. L. (2012). New particle formation and growth in biomass burning plumes: An important source of cloud condensation nuclei. *Geophysical Research Letters*, 39(9), L09805. doi:10.1029/2012GL050930.

Hess, M., Koepke, P., & Schult, I. (1998). Optical Properties of Aerosols and Clouds: The Software Package OPAC. *Bulletin of the American Meteorological Society*, 79(5), 831–844. doi:10.1175/1520-0477(1998)079<0831:OPOAAC>2.0.CO;2.

Hicks, B. B., Baldocchi, D. D., Meyers, T. P., Hosker, R. P., J., & Matt, D. R. (1987). A preliminary multiple resistance routine for deriving dry deposition velocities from measured quantities. *Water, Air, and Soil Pollution*, 36(3–4), 311–330. doi:10.1007/BF00229675.

Hjellbrekke, A.-G. (2014). *Data Report 2012 – Acidifying and eutrophying compounds and particulate matter*. Technical Report EMEP/CCC-Report 3/2014, Norwegian Institute for Air Research, Kjeller, Norway. `http://www.nilu.no/projects/ccc/reports/cccr3-2014.pdf`.

Hobbs, P. V., Garrett, T. J., Ferek, R. J., Strader, S. R., Hegg, D. A., Frick, G. M., Hoppel, W. A., Gasparovic, R. F., Russell, L. M., Johnson, D. W., O'Dowd, C., Durkee, P. A., Nielsen, K. E., & Innis, G. (2000). Emissions from Ships with respect to Their Effects on Clouds. *Journal of the Atmospheric Sciences*, 57(16), 2570–2590. doi:10.1175/1520-0469(2000)057<2570:EFSWRT>2.0.CO;2.

Hodas, N., Zuend, A., Mui, W., Flagan, R. C., & Seinfeld, J. H. (2015). Influence of particle-phase state on the hygroscopic behavior of mixed organic–inorganic aerosols. *Atmospheric Chemistry and Physics*, 15(9), 5027–5045. `http://www.atmos-chem-phys.net/15/5027/2015/`.

Holben, B. N., Eck, T. F., Slutsker, I., Tanré, D., Buis, J. P., Setzer, A., Vermote, E., Reagan, J. A., Kaufman, Y. J., Nakajima, T., Lavenu, F., Jankowiak, I., & Smirnov, A. (1998). AERONET–A Federated Instrument Network and Data Archive for Aerosol Characterization. *Remote Sensing of Environment*, 66(1), 1–16. doi:10.1016/S0034-4257(98)00031-5.

Holben, B. N., Tanré, D., Smirnov, A., Eck, T. F., Slutsker, I., Abuhassan, N., Newcomb, W. W., Schafer, J. S., Chatenet, B., Lavenu, F., Kaufman, Y. J., Castle, J. V., Setzer, A., Markham, B., Clark, D., Frouin, R., Halthore, R., Karneli, A., O'Neill, N. T., Pietras, C., Pinker, R. T., Voss, K., & Zibordi, G. (2001). An emerging ground-based aerosol climatology: Aerosol optical depth from AERONET. *Journal of Geophysical Research: Atmospheres*, 106(D11), 12067–12097. doi:10.1029/2001JD900014.

Holzer-Popp, T., de Leeuw, G., Griesfeller, J., Martynenko, D., Klüser, L., Bevan, S., Davies, W., Ducos, F., Deuzé, J. L., Graigner, R. G., Heckel, A., von Hoyningen-Hüne, W., Kolmonen, P., Litvinov, P., North, P., Poulsen, C. A., Ramon, D., Siddans, R., Sogacheva, L., Tanre, D., Thomas, G. E., Vountas, M., Descloitres, J., Griesfeller, J., Kinne, S., Schulz, M., & Pinnock, S. (2013). Aerosol retrieval experiments in the ESA Aerosol_cci project. *Atmospheric Measurement Techniques*, 6(8), 1919–1957. `http://www.atmos-meas-tech.net/6/1919/2013/`.

Hsieh, W.-C., Collins, W. D., Liu, Y., Chiang, J. C. H., Shie, C.-L., Caldeira, K., & Cao, L. (2013). Climate response due to carbonaceous aerosols and aerosol-induced SST effects in NCAR community atmospheric model CAM3.5. *Atmospheric Chemistry and Physics*, 13(15), 7489–7510. `http://www.atmos-chem-phys.net/13/7489/2013/`.

Huang, X., Song, Y., Zhao, C., Li, M., Zhu, T., Zhang, Q., & Zhang, X. (2014). Pathways of sulfate enhancement by natural and anthropogenic mineral aerosols in China. *Journal of Geophysical Research: Atmospheres*, 119(24), 14165–14179. doi:10.1002/2014JD022301.

Huneeus, N., Schulz, M., Balkanski, Y., Griesfeller, J., Prospero, J., Kinne, S., Bauer, S., Boucher, O., Chin, M., Dentener, F., Diehl, T., Easter, R., Fillmore, D., Ghan, S., Ginoux, P., Grini, A., Horowitz, L., Koch, D., Krol, M. C., Landing, W., Liu, X., Mahowald, N., Miller, R., Morcrette, J.-J., Myhre, G., Penner, J., Perlwitz, J., Stier, P., Takemura, T., & Zender, C. S. (2011). Global dust model intercomparison in AeroCom phase I. *Atmospheric Chemistry and Physics*, 11(15), 7781–7816. http://www.atmos-chem-phys.net/11/7781/2011/.

Im, U. (2013). Impact of sea-salt emissions on the model performance and aerosol chemical composition and deposition in the East Mediterranean coastal regions. *Atmospheric Environment*, 75, 329–340. doi:10.1016/j.atmosenv.2013.04.034.

IMO (2011). *MARPOL Consolidated Edition 2011: Articles, Protocols, Annexes, Unified Interpretations of the International Convention for the Prevention of Pollution from Ships, 1973, as Modified by the 1978 and 1997 Protocols*. IMO Publication. International Maritime Organization.

IMPROVE (1995). *IMPROVE Data Guide*. Technical report, University of California Davis. http://vista.cira.colostate.edu/IMPROVE/Publications/OtherDocs/IMPROVEDataGuide/IMPROVEDataGuide.pdf.

Jacob, D. J., Field, B. D., Li, Q., Blake, D. R., de Gouw, J., Warneke, C., Hansel, A., Wisthaler, A., Singh, H. B., & Guenther, A. (2005). Global budget of methanol: Constraints from atmospheric observations. *Journal of Geophysical Research: Atmospheres*, 110(D8), D08303. doi:10.1029/2004JD005172.

Jacobson, M. Z. (2000). A physically-based treatment of elemental carbon optics: Implications for global direct forcing of aerosols. *Geophysical Research Letters*, 27(2), 217–220. doi:10.1029/1999GL010968.

Jacobson, M. Z. (2005). A solution to the problem of nonequilibrium acid/base gas-particle transfer at long time step. *Aerosol Science and Technology*, 39(2), 92–103. doi:10.1080/027868290904546.

Jaeglé, L., Quinn, P. K., Bates, T. S., Alexander, B., & Lin, J. . T. (2011). Global distribution of sea salt aerosols: new constraints from in situ and remote sensing observations. *Atmospheric Chemistry and Physics*, 11(7), 3137–3157. http://www.atmos-chem-phys.net/11/3137/2011/acp-11-3137-2011.html.

Jefferson, A., Eisele, F. L., Ziemann, P. J., Weber, R. J., Marti, J. J., & McMurry, P. H. (1997). Measurements of the H2SO4 mass accommodation coefficient onto polydisperse aerosol. *Journal of Geophysical Research: Atmospheres*, 102(D15), 19021–19028. doi:10.1029/97JD01152.

Jenkins, A. K. L., Forster, P. M., & Jackson, L. S. (2013). The effects of timing and rate of marine cloud brightening aerosol injection on albedo changes during the diurnal cycle of marine stratocumulus clouds. *Atmospheric Chemistry and Physics*, 13(3), 1659–1673. http://www.atmos-chem-phys.net/13/1659/2013/.

Jeong, G. Y., Kim, J. Y., Seo, J., Kim, G. M., Jin, H. C., & Chun, Y. (2014). Long-range transport of giant particles in Asian dust identified by physical, mineralogical, and meteorological analysis. *Atmospheric Chemistry and Physics*, 14(1), 505–521. http://www.atmos-chem-phys.net/14/505/2014/.

Jeuken, A. B. M., Siegmund, P. C., Heijboer, L. C., Feichter, J., & Bengtsson, L. (1996). On the potential of assimilating meteorological analyses in a global climate model for the purpose of model validation. *Journal of Geophysical Research: Atmospheres*, 101(D12), 16939–16950. doi:10.1029/96JD01218.

Jöckel, P., Kerkweg, A., Pozzer, A., Sander, R., Tost, H., Riede, H., Baumgaertner, A., Gromov, S., & Kern, B. (2010). Development cycle 2 of the Modular Earth Submodel System (MESSy2). *Geoscientific Model Development*, 3(2), 717–752. http://www.geosci-model-dev.net/3/717/2010/gmd-3-717-2010.html.

Jöckel, P., Sander, R., Kerkweg, A., Tost, H., & Lelieveld, J. (2005). Technical Note: The Modular Earth Submodel System (MESSy) - a new approach towards Earth System Modeling. *Atmospheric Chemistry and Physics*, 5(2), 433–444. http://www.atmos-chem-phys.net/5/433/2005/.

Jöckel, P., Tost, H., Pozzer, A., Brühl, C., Buchholz, J., Ganzeveld, L., Hoor, P., Kerkweg, A., Lawrence, M. G., Sander, R., Steil, B., Stiller, G., Tanarhte, M., Taraborrelli, D., van Aardenne, J., & Lelieveld, J. (2006). The atmospheric chemistry general circulation model ECHAM5/MESSy1: consistent simulation of ozone from the surface to the mesosphere. *Atmospheric Chemistry and Physics*, 6(12), 5067–5104. http://www.atmos-chem-phys.net/6/5067/2006/.

Jöckel, P., Tost, H., Pozzer, A., Kunze, M., Kirner, O., Brenninkmeijer, C. A. M., Brinkop, S., Cai, D. S., Dyroff, C., Eckstein, J., Frank, F., Garny, H., Gottschaldt, K.-D., Graf, P., Grewe, V., Kerkweg, A., Kern, B., Matthes, S., Mertens, M., Meul, S., Neumaier, M., Nützel, M., Oberländer-Hayn, S., Ruhnke, R., Runde, T., Sander, R., Scharffe, D., , & Zahn, A. (2015). Earth System Chemistry Integrated Modelling (ESCiMo) with the Modular Earth Submodel System (MESSy, version 2.51). *Geoscientific Model Development Discussions*, 8, 8635–8750. http://www.geosci-model-dev-discuss.net/gmd-2015-165/.

Johansson, L., Jalkanen, J.-P., Kalli, J., & Kukkonen, J. (2013). The evolution of shipping emissions and the costs of regulation changes in the northern EU area. *Atmospheric Chemistry and Physics*, 13(22), 11375–11389. http://www.atmos-chem-phys.net/13/11375/2013/.

Johnson, M. S., Meskhidze, N., & Praju Kiliyanpilakkil, V. (2012). A global comparison of GEOS-Chem-predicted and remotely-sensed mineral dust aerosol optical depth and extinction profiles. *Journal of Advances in Modeling Earth Systems*, 4, M07001. doi:10.1029/2011MS000109.

Jones, A., Haywood, J., & Boucher, O. (2009). Climate impacts of geoengineering marine stratocumulus clouds. *Journal of Geophysical Research: Atmospheres*, 114(D10), D10106. doi:10.1029/2008JD011450.

Jones, A. & Haywood, J. M. (2012). Sea-spray geoengineering in the HadGEM2-ES earth-system model: radiative impact and climate response. *Atmospheric Chemistry and Physics*, 12(22), 10887–10898. http://www.atmos-chem-phys.net/12/10887/2012/.

Jonson, J. E., Jalkanen, J. P., Johansson, L., Gauss, M., & Denier van der Gon, H. A. C. (2015). Model calculations of the effects of present and future emissions of air pollutants from shipping in the Baltic Sea and the North Sea. *Atmospheric Chemistry and Physics*, 15(2), 783–798. http://www.atmos-chem-phys.net/15/783/2015/.

Jurkat, T., Voigt, C., Arnold, F., Schlager, H., Kleffmann, J., Aufmhoff, H., Schäuble, D., Schaefer, M., & Schumann, U. (2011). Measurements of HONO, NO, NOy and SO2 in aircraft exhaust plumes at cruise. *Geophysical Research Letters*, 38(10), L10807. doi:10.1029/2011GL046884.

Kaiser, J. C., Hendricks, J., Righi, M., Riemer, N., Zaveri, R. A., Metzger, S., & Aquila, V. (2014). The MESSy aerosol submodel MADE3 (v2.0b): description and a box model test. *Geoscientific Model Development*, 7(3), 1137–1157. http://www.geosci-model-dev.net/7/1137/2014/.

Kaiser, J. C., Riemer, N., & Knopf, D. A. (2011). Detailed heterogeneous oxidation of soot surfaces in a particle-resolved aerosol model. *Atmospheric Chemistry and Physics*, 11(9), 4505–4520. http://www.atmos-chem-phys.net/11/4505/2011/.

Kajino, M. (2011). MADMS: Modal Aerosol Dynamics model for multiple Modes and fractal Shapes in the free-molecular and near-continuum regimes. *Journal of Aerosol Science*, 42(4), 224–248. doi:10.1016/j.jaerosci.2011.01.005.

Kajino, M., Inomata, Y., Sato, K., Ueda, H., Han, Z., An, J., Katata, G., Deushi, M., Maki, T., Oshima, N., Kurokawa, J., Ohara, T., Takami, A., & Hatakeyama, S. (2012). Development of the RAQM2 aerosol chemical transport model and predictions of the Northeast Asian aerosol mass, size, chemistry, and mixing type. *Atmospheric Chemistry and Physics*, 12(24), 11833–11856. http://www.atmos-chem-phys.net/12/11833/2012/.

Kandler, K., Lieke, K., Benker, N., Emmel, C., Küpper, M., Müller-Ebert, D., Ebert, M., Scheuvens, D., Schladitz, A., Schütz, L., & Weinbruch, S. (2011). Electron microscopy of particles collected at Praia, Cape Verde, during the Saharan Mineral Dust Experiment: particle chemistry, shape, mixing state and complex refractive index. *Tellus B*, 63(4), 475–496. http://www.tellusb.net/index.php/tellusb/article/view/16241.

Kandler, K., Schütz, L., Deutscher, C., Ebert, M., Hofmann, H., Jäckel, S., Jaenicke, R., Knippertz, P., Lieke, K., Massling, A., Petzold, A., Schladitz, A., Weinzierl, B., Wiedensohler, A., Zorn, S., & Weinbruch, S. (2009). Size distribution, mass concentration, chemical and mineralogical composition and derived optical parameters of the boundary layer aerosol at Tinfou, Morocco, during SAMUM 2006. *Tellus B*, 61(1), 32–50. http://www.tellusb.net/index.php/tellusb/article/view/16798.

Kärcher, B., Möhler, O., DeMott, P. J., Pechtl, S., & Yu, F. (2007). Insights into the role of soot aerosols in cirrus cloud formation. *Atmospheric Chemistry and Physics*, 7(16), 4203–4227. http://www.atmos-chem-phys.net/7/4203/2007/.

Kärcher, B. & Solomon, S. (1999). On the composition and optical extinction of particles in the tropopause region. *Journal of Geophysical Research: Atmospheres*, 104(D22), 27441–27459. doi:10.1029/1999JD900838.

Karl, M., Leck, C., Gross, A., & Pirjola, L. (2012). A study of new particle formation in the marine boundary layer over the central Arctic Ocean using a flexible multicomponent aerosol dynamic model. *Tellus B*, 64(0), 17158. http://www.tellusb.net/index.php/tellusb/article/view/17158.

Kasischke, E. S., Hyer, E. J., Novelli, P. C., Bruhwiler, L. P., French, N. H. F., Sukhinin, A. I., Hewson, J. H., & Stocks, B. J. (2005). Influences of boreal fire emissions on Northern Hemisphere atmospheric carbon and carbon monoxide. *Global Biogeochemical Cycles*, 19(1), GB1012. doi:10.1029/2004GB002300.

Kazil, J., Stier, P., Zhang, K., Quaas, J., Kinne, S., O'Donnell, D., Rast, S., Esch, M., Ferrachat, S., Lohmann, U., & Feichter, J. (2010). Aerosol nucleation and its role for clouds and Earth's radiative forcing in the aerosol-climate model ECHAM5-HAM. *Atmospheric Chemistry and Physics*, 10(22), 10733–10752. http://www.atmos-chem-phys.net/10/10733/2010/.

Kelly, J. T. & Wexler, A. S. (2005). Thermodynamics of carbonates and hydrates related to heterogeneous reactions involving mineral aerosol. *Journal of Geophysical Research: Atmospheres*, 110(D11), D11201. doi:10.1029/2004JD005583.

Kerkweg, A., Buchholz, J., Ganzeveld, L., Pozzer, A., Tost, H., & Jöckel, P. (2006a). Technical Note: An implementation of the dry removal processes DRY DEPosition and SEDImentation in the Modular Earth Submodel System (MESSy). *Atmospheric Chemistry and Physics*, 6(12), 4617–4632. http://www.atmos-chem-phys.net/6/4617/2006/.

Kerkweg, A., Buchholz, J., Ganzeveld, L., Pozzer, A., Tost, H., & Jöckel, P. (2009). Corrigendum to "Technical Note: An implementation of the dry removal processes DRY DEPosition and SEDImentation in the Modular Earth Submodel System (MESSy)" published in Atmos. Chem. Phys., 6, 4617–4632, 2006. *Atmospheric Chemistry and Physics*, 9(24), 9569–9569. http://www.atmos-chem-phys.net/9/9569/2009/.

Kerkweg, A., Sander, R., Tost, H., & Joeckel, P. (2006b). Technical note: Implementation of prescribed (OFFLEM), calculated (ONLEM), and pseudo-emissions (TNUDGE) of chemical species in the Modular Earth Submodel System (MESSy). *Atmospheric Chemistry and Physics*, 6(11), 3603–3609. http://www.atmos-chem-phys.net/6/3603/2006/.

Kerminen, V. M., Pakkanen, T. A., & Hillamo, R. E. (1997). Interactions between inorganic trace gases and supermicrometer particles at a coastal site. *Atmospheric Environment*, 31(17), 2753–2765. doi:10.1016/S1352-2310(97)00092-7.

Kerminen, V.-M. & Wexler, A. S. (1995). Enhanced formation and development of sulfate particles due to marine boundary layer circulation. *Journal of Geophysical Research: Atmospheres*, 100(D11), 23051–23062. doi:10.1029/95JD02365.

Kesselmeier, J., Bode, K., Gerlach, C., & Jork, E.-M. (1998). Exchange of atmospheric formic and acetic acids with trees and crop plants under controlled chamber and purified air conditions. *Atmospheric Environment*, 32(10), 1765–1775. doi:10.1016/S1352-2310(97)00465-2.

Kettle, A. J., Andreae, M. O., Amouroux, D., Andreae, T. W., Bates, T. S., Berresheim, H., Bingemer, H., Boniforti, R., Curran, M. A. J., DiTullio, G. R., Helas, G., Jones, G. B., Keller, M. D., Kiene, R. P., Leck, C., Levasseur, M., Malin, G., Maspero, M., Matrai, P., McTaggart, A. R., Mihalopoulos, N., Nguyen, B. C., Novo, A., Putaud, J. P., Rapsomanikis, S., Roberts, G., Schebeske, G., Sharma, S., Simó, R., Staubes, R., Turner, S., & Uher, G. (1999). A global database of sea surface dimethylsulfide (DMS) measurements and a procedure to predict sea surface DMS as a function of latitude, longitude, and month. *Global Biogeochemical Cycles*, 13(2), 399–444. doi:10.1029/1999GB900004.

Khairoutdinov, M. F. & Yang, C.-E. (2013). Cloud-resolving modelling of aerosol indirect effects in idealised radiative-convective equilibrium with interactive and fixed sea surface temperature. *Atmospheric Chemistry and Physics*, 13(8), 4133–4144. http://www.atmos-chem-phys.net/13/4133/2013/.

Kharol, S. K., Martin, R. V., Philip, S., Vogel, S., Henze, D. K., Chen, D., Wang, Y., Zhang, Q., & Heald, C. L. (2013). Persistent sensitivity of Asian aerosol to emissions of nitrogen oxides. *Geophysical Research Letters*, 40(5), 1021–1026. doi:10.1002/grl.50234.

Kinne, S., Schulz, M., Litvinov, P., & Stebel, K. (2015). *ATSR Climate Data Record Evaluations.* Technical report, ESA Climate Change Initiative aerosol_cci. http://www.esa-aerosol-cci.org/?q=webfm_send/836.

Kipling, Z., Stier, P., Schwarz, J. P., Perring, A. E., Spackman, J. R., Mann, G. W., Johnson, C. E., & Telford, P. J. (2013). Constraints on aerosol processes in climate models from vertically-resolved aircraft observations of black carbon. *Atmospheric Chemistry and Physics*, 13(12), 5969–5986. http://www.atmos-chem-phys.net/13/5969/2013/.

Kirchstetter, T. W., Novakov, T., & Hobbs, P. V. (2004). Evidence that the spectral dependence of light absorption by aerosols is affected by organic carbon. *Journal of Geophysical Research: Atmospheres*, 109(D21), D21208. doi:10.1029/2004JD004999.

Kirkevåg, A., Iversen, T., Seland, Ø., Hoose, C., Kristjánsson, J. E., Struthers, H., Ekman, A. M. L., Ghan, S., Griesfeller, J., Nilsson, E. D., & Schulz, M. (2013). Aerosol–climate interactions in the Norwegian Earth System Model – NorESM1-M. *Geoscientific Model Development*, 6(1), 207–244. http://www.geosci-model-dev.net/6/207/2013/.

Kivekäs, N., Massling, A., Grythe, H., Lange, R., Rusnak, V., Carreno, S., Skov, H., Swietlicki, E., Nguyen, Q. T., Glasius, M., & Kristensson, A. (2014). Contribution of ship traffic to aerosol particle concentrations downwind of a major shipping lane. *Atmospheric Chemistry and Physics*, 14(16), 8255–8267. http://www.atmos-chem-phys.net/14/8255/2014/.

Klingmüller, K., Steil, B., Brühl, C., Tost, H., & Lelieveld, J. (2014). Sensitivity of aerosol radiative effects to different mixing assumptions in the AEROPT 1.0 submodel of the EMAC atmospheric-chemistry–climate model. *Geoscientific Model Development*, 7(5), 2503–2516. http://www.geosci-model-dev.net/7/2503/2014/.

Knopf, D. A., Alpert, P. A., Wang, B., & Aller, J. Y. (2011). Stimulation of ice nucleation by marine diatoms. *Nature Geoscience*, 4(2), 88–90. doi:10.1038/ngeo1037.

Koch, D., Schulz, M., Kinne, S., McNaughton, C., Spackman, J. R., Balkanski, Y., Bauer, S., Berntsen, T., Bond, T. C., Boucher, O., Chin, M., Clarke, A., De Luca, N., Dentener, F., Diehl, T., Dubovik, O., Easter, R., Fahey, D. W., Feichter, J., Fillmore, D., Freitag, S., Ghan, S., Ginoux, P., Gong, S., Horowitz, L., Iversen, T., Kirkevåg, A., Klimont, Z., Kondo, Y., Krol, M., Liu, X., Miller, R., Montanaro, V., Moteki, N., Myhre, G., Penner, J. E., Perlwitz, J., Pitari, G., Reddy, S., Sahu, L., Sakamoto, H., Schuster, G., Schwarz, J. P., Seland, Ø., Stier, P., Takegawa, N., Takemura, T., Textor, C., van Aardenne, J. A., & Zhao, Y. (2009). Evaluation of black carbon estimations in global aerosol models. *Atmospheric Chemistry and Physics*, 9(22), 9001–9026. http://www.atmos-chem-phys.net/9/9001/2009/.

Koch, D., Schulz, M., Kinne, S., McNaughton, C., Spackman, J. R., Balkanski, Y., Bauer, S., Berntsen, T., Bond, T. C., Boucher, O., Chin, M., Clarke, A., De Luca, N., Dentener, F., Diehl, T., Dubovik, O., Easter, R., Fahey, D. W., Feichter, J., Fillmore, D., Freitag, S., Ghan, S., Ginoux, P., Gong, S., Horowitz, L., Iversen, T., Kirkevåg, A., Klimont, Z., Kondo, Y., Krol, M., Liu, X., Miller, R., Montanaro, V., Moteki, N., Myhre, G., Penner, J. E., Perlwitz, J., Pitari, G., Reddy, S., Sahu, L., Sakamoto, H., Schuster, G., Schwarz, J. P., Seland, Ø., Stier, P., Takegawa, N., Takemura, T., Textor, C., van Aardenne, J. A., & Zhao, Y. (2010). Corrigendum to "Evaluation of black carbon estimations in global aerosol models" published in Atmos. Chem. Phys., 9, 9001-9026, 2009. *Atmospheric Chemistry and Physics*, 10(1), 79–81. http://www.atmos-chem-phys.net/10/79/2010/.

Kompalli, S. K., Moorthy, K. K., & Babu, S. S. (2014). Rapid response of atmospheric BC to anthropogenic sources: observational evidence. *Atmospheric Science Letters*, 15(3), 166–171. doi:10.1002/asl2.483.

Koo, B., Gaydos, T. M., & Pandis, S. N. (2003). Evaluation of the equilibrium, dynamic, and hybrid aerosol modeling approaches. *Aerosol Science and Technology*, 37(1), 53–64. doi:10.1080/02786820300893.

Kotchenruther, R. A. (2013). A regional assessment of marine vessel PM2.5 impacts in the U.S. Pacific Northwest using a receptor-based source apportionment method. *Atmospheric Environment*, 68, 103–111. doi:10.1016/j.atmosenv.2012.11.067.

Kotchenruther, R. A. (2015). The effects of marine vessel fuel sulfur regulations on ambient PM2.5 along the west coast of the U.S. *Atmospheric Environment*, 103, 121–128. doi:10.1016/j.atmosenv.2014.12.040.

Kulmala, M. & Kerminen, V.-M. (2008). On the formation and growth of atmospheric nanoparticles. *Atmospheric Research*, 90(2–4), 132–150. doi:10.1016/j.atmosres.2008.01.005.

Kulmala, M., Vehkamäki, H., Petäjä, T., Maso, M. D., Lauri, A., Kerminen, V.-M., Birmili, W., & McMurry, P. H. (2004). Formation and growth rates of ultrafine atmospheric particles: a review of observations. *Journal of Aerosol Science*, 35(2), 143–176. doi:10.1016/j.jaerosci.2003.10.003.

Lack, D. A., Corbett, J. J., Onasch, T., Lerner, B., Massoli, P., Quinn, P. K., Bates, T. S., Covert, D. S., Coffman, D., Sierau, B., Herndon, S., Allan, J., Baynard, T., Lovejoy, E., Ravishankara, A. R., & Williams, E. (2009). Particulate emissions from commercial shipping: Chemical, physical, and optical properties. *Journal of Geophysical Research: Atmospheres*, 114(D7), D00F04. doi:10.1029/2008JD011300.

Lamarque, J.-F., Bond, T. C., Eyring, V., Granier, C., Heil, A., Klimont, Z., Lee, D., Liousse, C., Mieville, A., Owen, B., Schultz, M. G., Shindell, D., Smith, S. J., Stehfest, E., Van Aardenne, J., Cooper, O. R., Kainuma, M., Mahowald, N., McConnell, J. R., Naik, V., Riahi, K., & van Vuuren, D. P. (2010). Historical (1850-2000) gridded anthropogenic and biomass burning emissions of reactive gases and aerosols: methodology and application. *Atmospheric Chemistry and Physics*, 10(15), 7017–7039. http://www.atmos-chem-phys.net/10/7017/2010/.

Lana, A., Bell, T. G., Simo, R., Vallina, S. M., Ballabrera-Poy, J., Kettle, A. J., Dachs, J., Bopp, L., Saltzman, E. S., Stefels, J., Johnson, J. E., & Liss, P. S. (2011). An updated climatology of surface dimethlysulfide concentrations and emission fluxes in the global ocean. *Global Biogeochemical Cycles*, 25(1), GB1004. doi:10.1029/2010GB003850.

Landi, T. C., Curci, G., Carbone, C., Menut, L., Bessagnet, B., Giulianelli, L., Paglione, M., & Facchini, M. C. (2013). Simulation of size-segregated aerosol chemical composition over northern Italy in clear sky and wind calm conditions. *Atmospheric Research*, 125–126, 1–11. doi:10.1016/j.atmosres.2013.01.009.

Laskin, A., Moffet, R. C., Gilles, M. K., Fast, J. D., Zaveri, R. A., Wang, B., Nigge, P., & Shutthanandan, J. (2012). Tropospheric chemistry of internally mixed sea salt and organic particles: Surprising reactivity of NaCl with weak organic acids. *Journal of Geophysical Research: Atmospheres*, 117(D15), D15302. doi:10.1029/2012JD017743.

Lauer, A. (2004). *Untersuchung von Größenverteilung und Zusammensetzung des troposphärischen Aerosols mit einem globalen Zirkulationsmodell*. PhD thesis, FU Berlin, Germany.

Lauer, A., Eyring, V., Corbett, J. J., Wang, C., & Winebrake, J. J. (2009). Assessment of Near-Future Policy Instruments for Oceangoing Shipping: Impact on Atmospheric Aerosol Burdens and the Earth's Radiation Budget. *Environmental Science & Technology*, 43(15), 5592–5598. http://pubs.acs.org/doi/abs/10.1021/es900922h.

Lauer, A., Eyring, V., Hendricks, J., Jöckel, P., & Lohmann, U. (2007). Global model simulations of the impact of ocean-going ships on aerosols, clouds, and the radiation budget. *Atmospheric Chemistry and Physics*, 7(19), 5061–5079. http://www.atmos-chem-phys.net/7/5061/2007/.

Lauer, A. & Hendricks, J. (2006). Simulating aerosol microphysics with the ECHAM4/MADE GCM – Part II: Results from a first multiannual simulation of the submicrometer aerosol. *Atmospheric Chemistry and Physics*, 6(12), 5495–5513. http://www.atmos-chem-phys.net/6/5495/2006/.

Lauer, A., Hendricks, J., Ackermann, I., Schell, B., Hass, H., & Metzger, S. (2005). Simulating aerosol microphysics with the ECHAM/MADE GCM - Part I: Model description and comparison with observations. *Atmospheric Chemistry and Physics*, 5(12), 3251–3276. http://www.atmos-chem-phys.net/5/3251/2005/.

Lee, D. S., Pitari, G., Grewe, V., Gierens, K., Penner, J. E., Petzold, A., Prather, M. J., Schumann, U., Bais, A., Berntsen, T., Iachetti, D., Lim, L. L., & Sausen, R. (2010). Transport impacts on atmosphere and climate: Aviation. *Atmospheric Environment*, 44(37), 4678–4734. doi:10.1016/j.atmosenv.2009.06.005.

Lee, L. A., Pringle, K. J., Reddington, C. L., Mann, G. W., Stier, P., Spracklen, D. V., Pierce, J. R., & Carslaw, K. S. (2013a). Corrigendum to "The magnitude and causes of uncertainty in global model simulations of cloud condensation nuclei" published in Atmos. Chem. Phys., 13, 8879–8914, 2013. *Atmospheric Chemistry and Physics*, 13(18), 9375–9377. http://www.atmos-chem-phys.net/13/9375/2013/.

Lee, L. A., Pringle, K. J., Reddington, C. L., Mann, G. W., Stier, P., Spracklen, D. V., Pierce, J. R., & Carslaw, K. S. (2013b). The magnitude and causes of uncertainty in global model simulations of cloud condensation nuclei. *Atmospheric Chemistry and Physics*, 13(17), 8879–8914. http://www.atmos-chem-phys.net/13/8879/2013/.

Lee, T., Yu, X.-Y., Ayres, B., Kreidenweis, S. M., Malm, W. C., & Collett, Jeffrey L., J. (2008). Observations of fine and coarse particle nitrate at several rural locations in the United States. *Atmospheric Environment*, 42(11), 2720–2732. doi:10.1016/j.atmosenv.2007.05.016.

Lee, Y. H., Adams, P. J., & Shindell, D. T. (2015). Evaluation of the global aerosol microphysical ModelE2-TOMAS model against satellite and ground-based observations. *Geoscientific Model Development*, 8(3), 631–667. `http://www.geosci-model-dev.net/8/631/2015/`.

Lee, Y. H., Chen, K., & Adams, P. J. (2009). Development of a global model of mineral dust aerosol microphysics. *Atmospheric Chemistry and Physics*, 9(7), 2441–2458. `http://www.atmos-chem-phys.net/9/2441/2009/acp-9-2441-2009.html`.

Lee, Y. H., Pierce, J. R., & Adams, P. J. (2013c). Representation of nucleation mode microphysics in a global aerosol model with sectional microphysics. *Geoscientific Model Development*, 6(4), 1221–1232. `http://www.geosci-model-dev.net/6/1221/2013/`.

Lee, Y.-N., Springston, S., Jayne, J., Wang, J., Hubbe, J., Senum, G., Kleinman, L., & Daum, P. H. (2014). Chemical composition and sources of coastal marine aerosol particles during the 2008 VOCALS-REx campaign. *Atmospheric Chemistry and Physics*, 14(10), 5057–5072. `http://www.atmos-chem-phys.net/14/5057/2014/`.

Levy, H., Horowitz, L. W., Schwarzkopf, M. D., Ming, Y., Golaz, J.-C., Naik, V., & Ramaswamy, V. (2013). The roles of aerosol direct and indirect effects in past and future climate change. *Journal of Geophysical Research: Atmospheres*, 118(10), 4521–4532. doi:10.1002/jgrd.50192.

Li, J., Han, Z., & Zhang, R. (2014). Influence of aerosol hygroscopic growth parameterization on aerosol optical depth and direct radiative forcing over East Asia. *Atmospheric Research*, 140–141, 14–27. doi:10.1016/j.atmosres.2014.01.013.

Li, X., Wang, L., Ji, D., Wen, T., Pan, Y., Sun, Y., & Wang, Y. (2013). Characterization of the size-segregated water-soluble inorganic ions in the Jing-Jin-Ji urban agglomeration: Spatial/temporal variability, size distribution and sources. *Atmospheric Environment*, 77, 250–259. doi:10.1016/j.atmosenv.2013.03.042.

Lin, C. T., Baker, A. R., Jickells, T. D., Kelly, S., & Lesworth, T. (2012). An assessment of the significance of sulphate sources over the Atlantic Ocean based on sulphur isotope data. *Atmospheric Environment*, 62, 615–621. doi:10.1016/j.atmosenv.2012.08.052.

Lin, S.-J. & Rood, R. B. (1996). Multidimensional Flux-Form Semi-Lagrangian Transport Schemes. *Monthly Weather Review*, 124(9), 2046–2070. doi:10.1175/1520-0493(1996)124<2046:MFFSLT>2.0.CO;2.

Liss, P. S. & Merlivat, L. (1986). Air-Sea Gas Exchange Rates: Introduction and Synthesis. In P. Buat-Ménard (Ed.), *The Role of Air-Sea Exchange in Geochemical Cycling*, volume 185 of *NATO ASI Series* (pp. 113–127). Springer Netherlands. doi:10.1007/978-94-009-4738-2_5.

Liu, D., Allan, J., Whitehead, J., Young, D., Flynn, M., Coe, H., McFiggans, G., Fleming, Z. L., & Bandy, B. (2013). Ambient black carbon particle hygroscopic properties controlled by mixing state and composition. *Atmospheric Chemistry and Physics*, 13(4), 2015–2029. `http://www.atmos-chem-phys.net/13/2015/2013/`.

Liu, H. J., Zhao, C. S., Nekat, B., Ma, N., Wiedensohler, A., van Pinxteren, D., Spindler, G., Müller, K., & Herrmann, H. (2014). Aerosol hygroscopicity derived from size-segregated chemical composition and its parameterization in the North China Plain. *Atmospheric Chemistry and Physics*, 14(5), 2525–2539. `http://www.atmos-chem-phys.net/14/2525/2014/`.

Liu, J., Fan, S., Horowitz, L. W., & Levy, H. (2011). Evaluation of factors controlling long-range transport of black carbon to the Arctic. *Journal of Geophysical Research: Atmospheres*, 116(D4), D04307. doi:10.1029/2010JD015145.

Liu, X., Penner, J. E., & Herzog, M. (2005). Global modeling of aerosol dynamics: Model description, evaluation, and interactions between sulfate and nonsulfate aerosols. *Journal of Geophysical Research: Atmospheres*, 110(D18), D18206. doi:10.1029/2004JD005674.

Loeb, N. G. & Manalo-Smith, N. (2005). Top-of-Atmosphere Direct Radiative Effect of Aerosols over Global Oceans from Merged CERES and MODIS Observations. *Journal of Climate*, 18(17), 3506–3526. doi:10.1175/JCLI3504.1.

Lohmann, U., Feichter, J., Chuang, C. C., & Penner, J. E. (1999). Prediction of the number of cloud droplets in the ECHAM GCM. *Journal of Geophysical Research: Atmospheres*, 104(D8), 9169–9198. doi:10.1029/1999JD900046.

Lohmann, U. & Hoose, C. (2009). Sensitivity studies of different aerosol indirect effects in mixed-phase clouds. *Atmospheric Chemistry and Physics*, 9(22), 8917–8934. http://www.atmos-chem-phys.net/9/8917/2009/.

Lohmann, U., Stier, P., Hoose, C., Ferrachat, S., Kloster, S., Roeckner, E., & Zhang, J. (2007). Cloud microphysics and aerosol indirect effects in the global climate model ECHAM5-HAM. *Atmospheric Chemistry and Physics*, 7(13), 3425–3446. http://www.atmos-chem-phys.net/7/3425/2007/.

Lu, M.-L., Conant, W. C., Jonsson, H. H., Varutbangkul, V., Flagan, R. C., & Seinfeld, J. H. (2007). The Marine Stratus/Stratocumulus Experiment (MASE): Aerosol-cloud relationships in marine stratocumulus. *Journal of Geophysical Research: Atmospheres*, 112(D10), D10209. doi:10.1029/2006JD007985.

Lu, M. L., Sorooshian, A., Jonsson, H. H., Feingold, G., Flagan, R. C., & Seinfeld, J. H. (2009). Marine stratocumulus aerosol-cloud relationships in the MASE-II experiment: Precipitation susceptibility in eastern Pacific marine stratocumulus. *Journal of Geophysical Research: Atmospheres*, 114(D24), D24203. doi:10.1029/2009JD012774.

Lu, Q., Zheng, J., Ye, S., Shen, X., Yuan, Z., & Yin, S. (2013). Emission trends and source characteristics of SO2, NOx, PM10 and VOCs in the Pearl River Delta region from 2000 to 2009. *Atmospheric Environment*, 76, 11–20. doi:10.1016/j.atmosenv.2012.10.062.

Lund, M. T. & Berntsen, T. (2012). Parameterization of black carbon aging in the OsloCTM2 and implications for regional transport to the Arctic. *Atmospheric Chemistry and Physics*, 12(15), 6999–7014. http://www.atmos-chem-phys.net/12/6999/2012/.

Luo, C., Zender, C. S., Bian, H., & Metzger, S. (2007). Role of ammonia chemistry and coarse mode aerosols in global climatological inorganic aerosol distributions. *Atmospheric Environment*, 41(12), 2510–2533. doi:10.1016/j.atmosenv.2006.11.030.

Ma, X., Yu, F., & Quaas, J. (2014). Reassessment of satellite-based estimate of aerosol climate forcing. *Journal of Geophysical Research: Atmospheres*, 119(17), 10394–10409. doi:10.1002/2014JD021670.

Mahajan, A. S., Fadnavis, S., Thomas, M. A., Pozzoli, L., Gupta, S., Royer, S.-J., Saiz-Lopez, A., & Simó, R. (2015). Quantifying the impacts of an updated global dimethyl sulfide climatology on cloud microphysics and aerosol radiative forcing. *Journal of Geophysical Research: Atmospheres*, 120(6), 2524–2536. doi:10.1002/2014JD022687.

Mahowald, N., Albani, S., Kok, J. F., Engelstaeder, S., Scanza, R., Ward, D. S., & Flanner, M. G. (2014). The size distribution of desert dust aerosols and its impact on the Earth system. *Aeolian Research*, 15, 53–71. doi:10.1016/j.aeolia.2013.09.002.

Makar, P., Gong, W., Milbrandt, J., Hogrefe, C., Zhang, Y., Curci, G., Žabkar, R., Im, U., Balzarini, A., Baró, R., Bianconi, R., Cheung, P., Forkel, R., Gravel, S., Hirtl, M., Honzak, L., Hou, A., Jiménez-Guerrero, P., Langer, M., Moran, M., Pabla, B., Pérez, J., Pirovano, G., José, R. S., Tuccella, P., Werhahn, J., Zhang, J., & Galmarini, S. (2015). Feedbacks between air pollution and weather, Part 1: Effects on weather. *Atmospheric Environment*, 115, 442–469. doi:10.1016/j.atmosenv.2014.12.003.

Makkonen, R., Asmi, A., Korhonen, H., Kokkola, H., Järvenoja, S., Räisänen, P., Lehtinen, K. E. J., Laaksonen, A., Kerminen, V.-M., Järvinen, H., Lohmann, U., Bennartz, R., Feichter, J., & Kulmala, M. (2009). Sensitivity of aerosol concentrations and cloud properties to nucleation and secondary organic distribution in ECHAM5-HAM global circulation model. *Atmospheric Chemistry and Physics*, 9(5), 1747–1766. http://www.atmos-chem-phys.net/9/1747/2009/.

Makkonen, R., Seland, Ø., Kirkevåg, A., Iversen, T., & Kristjánsson, J. E. (2014). Evaluation of aerosol number concentrations in NorESM with improved nucleation parameterization. *Atmospheric Chemistry and Physics*, 14(10), 5127–5152. http://www.atmos-chem-phys.net/14/5127/2014/.

Makkonen, U., Virkkula, A., Mäntykenttä, J., Hakola, H., Keronen, P., Vakkari, V., & Aalto, P. P. (2012). Semi-continuous gas and inorganic aerosol measurements at a Finnish urban site: comparisons with filters, nitrogen in aerosol and gas phases, and aerosol acidity. *Atmospheric Chemistry and Physics*, 12(12), 5617–5631. http://www.atmos-chem-phys.net/12/5617/2012/.

Mann, G. W., Carslaw, K. S., Reddington, C. L., Pringle, K. J., Schulz, M., Asmi, A., Spracklen, D. V., Ridley, D. A., Woodhouse, M. T., Lee, L. A., Zhang, K., Ghan, S. J., Easter, R. C., Liu, X., Stier, P., Lee, Y. H., Adams, P. J., Tost, H., Lelieveld, J., Bauer, S. E., Tsigaridis, K., van Noije, T. P. C., Strunk, A., Vignati, E., Bellouin, N., Dalvi, M., Johnson, C. E., Bergman, T., Kokkola, H., von Salzen, K., Yu, F., Luo, G., Petzold, A., Heintzenberg, J., Clarke, A., Ogren, J. A., Gras, J., Baltensperger, U., Kaminski, U., Jennings, S. G., O'Dowd, C. D., Harrison, R. M., Beddows, D. C. S., Kulmala, M., Viisanen, Y., Ulevicius, V., Mihalopoulos, N., Zdimal, V., Fiebig, M., Hansson, H.-C., Swietlicki, E., & Henzing, J. S. (2014). Intercomparison and evaluation of global aerosol microphysical properties among AeroCom models of a range of complexity. *Atmospheric Chemistry and Physics*, 14(9), 4679–4713. http://www.atmos-chem-phys.net/14/4679/2014/.

Mann, G. W., Carslaw, K. S., Ridley, D. A., Spracklen, D. V., Pringle, K. J., Merikanto, J., Korhonen, H., Schwarz, J. P., Lee, L. A., Manktelow, P. T., Woodhouse, M. T., Schmidt, A., Breider, T. J., Emmerson, K. M., Reddington, C. L., Chipperfield, M. P., & Pickering, S. J. (2012). Intercomparison of modal and sectional aerosol microphysics representations within the same 3-D global chemical transport model. *Atmospheric Chemistry and Physics*, 12(10), 4449–4476. http://www.atmos-chem-phys.net/12/4449/2012/.

Mann, G. W., Carslaw, K. S., Spracklen, D. V., Ridley, D. A., Manktelow, P. T., Chipperfield, M. P., Pickering, S. J., & Johnson, C. E. (2010). Description and evaluation of GLOMAP-mode: a modal global aerosol microphysics model for the UKCA composition-climate model. *Geoscientific Model Development*, 3(2), 519–551. doi:10.5194/gmd-3-519-2010.

Massling, A., Nielsen, I. E., Kristensen, D., Christensen, J. H., Sørensen, L. L., Jensen, B., Nguyen, Q. T., Nøjgaard, J. K., Glasius, M., & Skov, H. (2015). Atmospheric black carbon and sulfate concentrations in Northeast Greenland. *Atmospheric Chemistry and Physics*, 15(16), 9681–9692. http://www.atmos-chem-phys.net/15/9681/2015/.

Matsui, H., Koike, M., Kondo, Y., Moteki, N., Fast, J. D., & Zaveri, R. A. (2013). Development and validation of a black carbon mixing state resolved three-dimensional model: Aging processes and radiative impact. *Journal of Geophysical Research: Atmospheres*, 118(5), 2304–2326. doi:10.1029/2012JD018446.

Mayer, B. & Kylling, A. (2005). Technical note: The libRadtran software package for radiative transfer calculations - description and examples of use. *Atmospheric Chemistry and Physics*, 5(7), 1855–1877. http://www.atmos-chem-phys.net/5/1855/2005/.

McInnes, L. M., Covert, D. S., Quinn, P. K., & Germani, M. S. (1994). Measurements of chloride depletion and sulfur enrichment in individual sea-salt particles collected from the remote marine boundary layer. *Journal of Geophysical Research: Atmospheres*, 99(D4), 8257–8268. doi:10.1029/93JD03453.

Metzger, S., Dentener, F., Pandis, S., & Lelieveld, J. (2002). Gas/aerosol partitioning: 1. A computationally efficient model. *Journal of Geophysical Research: Atmospheres*, 107(D16), 4312. doi:10.1029/2001JD001102.

Metzger, S., Mihalopoulos, N., & Lelieveld, J. (2006). Importance of mineral cations and organics in gas-aerosol partitioning of reactive nitrogen compounds: case study based on MINOS results. *Atmospheric Chemistry and Physics*, 6(9), 2549–2567. http://www.atmos-chem-phys.net/6/2549/2006/.

Meng, Z. Y. & Seinfeld, J. H. (1996). Time scales to achieve atmospheric gas-aerosol equilibrium for volatile species. *Atmospheric Environment*, 30(16), 2889–2900. doi:10.1016/1352-2310(95)00493-9.

Merikanto, J., Spracklen, D. V., Mann, G. W., Pickering, S. J., & Carslaw, K. S. (2009). Impact of nucleation on global CCN. *Atmospheric Chemistry and Physics*, 9(21), 8601–8616. http://www.atmos-chem-phys.net/9/8601/2009/.

Meskhidze, N., Xu, J., Gantt, B., Zhang, Y., Nenes, A., Ghan, S. J., Liu, X., Easter, R., & Zaveri, R. (2011). Global distribution and climate forcing of marine organic aerosol: 1. Model improvements and evaluation. *Atmospheric Chemistry and Physics*, 11(22), 11689–11705. http://www.atmos-chem-phys.net/11/11689/2011/acp-11-11689-2011.html.

Meyer, K., Platnick, S., Oreopoulos, L., & Lee, D. (2013). Estimating the direct radiative effect of absorbing aerosols overlying marine boundary layer clouds in the southeast Atlantic using MODIS and CALIOP. *Journal of Geophysical Research: Atmospheres*, 118(10), 4801–4815. doi:10.1002/jgrd.50449.

Michou, M., Nabat, P., & Saint-Martin, D. (2015). Development and basic evaluation of a prognostic aerosol scheme (v1) in the CNRM Climate Model CNRM-CM6. *Geoscientific Model Development*, 8(3), 501–531. http://www.geosci-model-dev.net/8/501/2015/.

Miñambres, L., Méndez, E., Sánchez, M. N., Castaño, F., & Basterretxea, F. J. (2014). The effect of low solubility organic acids on the hygroscopicity of sodium halide aerosols. *Atmospheric Chemistry and Physics*, 14(20), 11409–11425. http://www.atmos-chem-phys.net/14/11409/2014/.

Minikin, A., Petzold, A., Strom, J., Krejci, R., Seifert, M., van Velthoven, P., Schlager, H., & Schumann, U. (2003). Aircraft observations of the upper tropospheric fine particle aerosol in the Northern and Southern Hemispheres at midlatitudes. *Geophysical Research Letters*, 30(10), 1503. doi:10.1029/2002GL016458.

Monahan, E. C., Spiel, D. E., & Davidson, K. L. (1986). A Model of Marine Aerosol Generation Via Whitecaps and Wave Disruption. In E. C. Monahan & G. Mac Niocaill (Eds.), *Oceanic Whitecaps*, volume 2 of *Oceanographic Sciences Library* (pp. 167–174). Springer Netherlands. doi:10.1007/978-94-009-4668-2_16.

Moteki, N., Kondo, Y., & Adachi, K. (2014). Identification by single-particle soot photometer of black carbon particles attached to other particles: Laboratory experiments and ground observations in Tokyo. *Journal of Geophysical Research: Atmospheres*, 119(2), 1031–1043. doi:10.1002/2013JD020655.

Moteki, N., Kondo, Y., Oshima, N., Takegawa, N., Koike, M., Kita, K., Matsui, H., & Kajino, M. (2012). Size dependence of wet removal of black carbon aerosols during transport from the boundary layer to the free troposphere. *Geophysical Research Letters*, 39(13), L13802. doi:10.1029/2012GL052034.

Moya, M., Pandis, S. N., & Jacobson, M. Z. (2002). Is the size distribution of urban aerosols determined by thermodynamic equilibrium? An application to Southern California. *Atmospheric Environment*, 36(14), 2349–2365. doi:10.1016/S1352-2310(01)00549-0.

Murphy, B. N., Donahue, N. M., Robinson, A. L., & Pandis, S. N. (2014a). A naming convention for atmospheric organic aerosol. *Atmospheric Chemistry and Physics*, 14(11), 5825–5839. http://www.atmos-chem-phys.net/14/5825/2014/.

Murphy, D. M., Cziczo, D. J., Froyd, K. D., Hudson, P. K., Matthew, B. M., Middlebrook, A. M., Peltier, R. E., Sullivan, A., Thomson, D. S., & Weber, R. J. (2006). Single-particle mass spectrometry of tropospheric aerosol particles. *Journal of Geophysical Research: Atmospheres*, 111(D23), D23S32. doi:10.1029/2006JD007340.

Murphy, D. M., Froyd, K. D., Schwarz, J. P., & Wilson, J. C. (2014b). Observations of the chemical composition of stratospheric aerosol particles. *Quarterly Journal of the Royal Meteorological Society*, 140(681), 1269–1278. doi:10.1002/qj.2213.

Murray, B. J., O'Sullivan, D., Atkinson, J. D., & Webb, M. E. (2012). Ice nucleation by particles immersed in supercooled cloud droplets. *Chemical Society Reviews*, 41(19), 6519–6554. doi:10.1039/C2CS35200A.

Myhre, G., Samset, B. H., Schulz, M., Balkanski, Y., Bauer, S., Berntsen, T. K., Bian, H., Bellouin, N., Chin, M., Diehl, T., Easter, R. C., Feichter, J., Ghan, S. J., Hauglustaine, D., Iversen, T., Kinne, S., Kirkevåg, A., Lamarque, J.-F., Lin, G., Liu, X., Lund, M. T., Luo, G., Ma, X., van Noije, T., Penner, J. E., Rasch, P. J., Ruiz, A., Seland, Ø., Skeie, R. B., Stier, P., Takemura, T., Tsigaridis, K., Wang, P., Wang, Z., Xu, L., Yu, H., Yu, F., Yoon, J.-H., Zhang, K., Zhang, H., & Zhou, C. (2013a). Radiative forcing of the direct aerosol effect from AeroCom Phase II simulations. *Atmospheric Chemistry and Physics*, 13(4), 1853–1877. http://www.atmos-chem-phys.net/13/1853/2013/.

Myhre, G., Shindell, D., Bréon, F.-M., Collins, W., Fuglestvedt, J., Huang, J., Koch, D., Lamarque, J.-F., Lee, D., Mendoza, B., Nakajima, T., Robock, A., Stephens, G., Takemura, T., & Zhang, H. (2013b). Anthropogenic and Natural Radiative Forcing. In T. F. Stocker, D. Qin, G.-K. Plattner, M. Tignor, S. K. Allen, J. Boschung, A. Nauels, Y. Xia, V. Bex, & P. M. Midgley (Eds.), *Climate Change 2013: The Physical Science Basis. Contribution of Working Group I to the Fifth Assessment Report of the Intergovernmental Panel on Climate Change* chapter 8, (pp. 659–740). Cambridge, United Kingdom and New York, NY, USA: Cambridge University Press. www.climatechange2013.org.

Nabat, P., Solmon, F., Mallet, M., Kok, J. F., & Somot, S. (2012). Dust emission size distribution impact on aerosol budget and radiative forcing over the Mediterranean region: a regional climate model approach. *Atmospheric Chemistry and Physics*, 12(21), 10545–10567. http://www.atmos-chem-phys.net/12/10545/2012/.

Naik, V., Horowitz, L. W., Fiore, A. M., Ginoux, P., Mao, J., Aghedo, A. M., & Levy, H. (2013). Impact of preindustrial to present-day changes in short-lived pollutant emissions on atmospheric composition and climate forcing. *Journal of Geophysical Research: Atmospheres*, 118(14), 8086–8110. doi:10.1002/jgrd.50608.

Nair, P. V. N. & Vohra, K. G. (1975). Growth of aqueous sulphuric acid droplets as a function of relative humidity. *Journal of Aerosol Science*, 6(3–4), 265–271. doi:10.1016/0021-8502(75)90094-4.

Napier, W. J., Ensberg, J. J., & Seinfeld, J. H. (2014). Insight into the numerical challenges of implementing 2-dimensional SOA models in atmospheric chemical transport models. *Atmospheric Environment*, 96, 331–344. doi:10.1016/j.atmosenv.2014.07.048.

Neitola, K., Brus, D., Makkonen, U., Sipilä, M., Lihavainen, H., & Kulmala, M. (2014). Effect of addition of four base compounds on sulphuric-acid-water new-particle formation: a laboratory study. *Boreal Environment Research*, 19(suppl. B), 257–274. `http://www.borenv.net/BER/pdfs/ber19/ber19B-257.pdf`.

Network Center for EANET (2014). *Data Report on the Acid Deposition in the East Asian Region 2013*. Technical report, Asia Center for Air Pollution Research (ACAP), Niigata-shi, Japan. `http://www.eanet.asia/product/datarep/datarep13/datarep13.pdf`.

Nie, W., Wang, T., Wang, W., Wei, X., & Liu, Q. (2013). Atmospheric concentrations of particulate sulfate and nitrate in Hong Kong during 1995–2008: Impact of local emission and super-regional transport. *Atmospheric Environment*, 76, 43–51. doi:10.1016/j.atmosenv.2012.07.001.

Niemi, J. V., Tervahattu, H., Virkkula, A., Hillamo, R., Teinilä, K., Koponen, I. K., & Kulmala, M. (2005). Continental impact on marine boundary layer coarse particles over the Atlantic Ocean between Europe and Antarctica. *Atmospheric Research*, 75(4), 301–321. doi:10.1016/j.atmosres.2005.01.005.

Nolte, C. G., Bhave, P. V., Arnold, J. R., Dennis, R. L., Zhang, K. M., & Wexler, A. S. (2008). Modeling urban and regional aerosols - Application of the CMAQ-UCD Aerosol Model to Tampa, a coastal urban site. *Atmospheric Environment*, 42(13), 3179–3191. doi:10.1016/j.atmosenv.2007.12.059.

Noone, K. J., Öström, E., Ferek, R. J., Garrett, T., Hobbs, P. V., Johnson, D. W., Taylor, J. P., Russell, L. M., Flagan, R. C., Seinfeld, J. H., O'Dowd, C. D., Smith, M. H., Durkee, P. A., Nielsen, K., Hudson, J. G., Pockalny, R. A., De Bock, L., Van Grieken, R. E., Gasparovic, R. F., & Brooks, I. (2000). A Case Study of Ships Forming and Not Forming Tracks in Moderately Polluted Clouds. *Journal of the Atmospheric Sciences*, 57(16), 2729–2747. doi:10.1175/1520-0469(2000)057<2729:ACSOSF>2.0.CO;2.

Nordeng, T. E. (1994). *Extended versions of the convective parameterization scheme at ECMWF and their impact on the mean and transient activity of the model in the tropics*. Technical Memorandum 206, European Centre for Medium-Range Weather Forecasts, Reading, UK. `http://old.ecmwf.int/publications/library/ecpublications/_pdf/tm/001-300/tm206.pdf`.

North, P., Briggs, S. A., Plummer, S. E., & Settle, J. J. (1999). Retrieval of land surface bidirectional reflectance and aerosol opacity from ATSR-2 multiangle imagery. *IEEE Transactions on Geoscience and Remote Sensing*, 37(1), 526–537. doi:10.1109/36.739106.

Ochoa, C., Baumgardner, D., Grutter, M., Allan, J., Fast, J., & Rappenglueck, B. (2012). Physical and chemical properties of the regional mixed layer of Mexico's Megapolis Part II: evaluation of measured and modeled trace gases and particle size distributions. *Atmospheric Chemistry and Physics*, 12(21), 10161–10179. `http://www.atmos-chem-phys.net/12/10161/2012/`.

Ocko, I. B., Ramaswamy, V., Ginoux, P., Ming, Y., & Horowitz, L. W. (2012). Sensitivity of scattering and absorbing aerosol direct radiative forcing to physical climate factors. *Journal of Geophysical Research: Atmospheres*, 117(D20), D20203. doi:10.1029/2012JD018019.

O'Dowd, C. D., Facchini, M. C., Cavalli, F., Ceburnis, D., Mircea, M., Decesari, S., Fuzzi, S., Yoon, Y. J., & Putaud, J.-P. (2004). Biogenically driven organic contribution to marine aerosol. *Nature*, 431(7009), 676–680. doi:10.1038/nature02959.

Olin, M., Rönkkö, T., & Dal Maso, M. (2015). CFD modeling of a vehicle exhaust laboratory sampling system: sulfur-driven nucleation and growth in diluting diesel exhaust. *Atmospheric Chemistry and Physics*, 15(9), 5305–5323. `http://www.atmos-chem-phys.net/15/5305/2015/`.

Olivié, D. J. L., Cariolle, D., Teyssèdre, H., Salas, D., Voldoire, A., Clark, H., Saint-Martin, D., Michou, M., Karcher, F., Balkanski, Y., Gauss, M., Dessens, O., Koffi, B., & Sausen, R. (2012). Modeling the climate impact of road transport, maritime shipping and aviation over the period 1860–2100 with an AOGCM. *Atmospheric Chemistry and Physics*, 12(3), 1449–1480. `http://www.atmos-chem-phys.net/12/1449/2012/`.

Oshima, N. & Koike, M. (2013). Development of a parameterization of black carbon aging for use in general circulation models. *Geoscientific Model Development*, 6(2), 263–282. http://www.geosci-model-dev.net/6/263/2013/.

Öström, E., Noone, K. J., & Pockalny, R. A. (2000). Cloud Droplet Residual Particle Microphysics in Marine Stratocumulus Clouds Observed during the Monterey Area Ship Track Experiment. *Journal of the Atmospheric Sciences*, 57(16), 2671–2683. doi:10.1175/1520-0469(2000)057<2671:CDRPMI>2.0.CO;2.

Ouimette, J. R. & Flagan, R. C. (1982). The extinction coefficient of multicomponent aerosols. *Atmospheric Environment*, 16(10), 2405–2419. doi:10.1016/0004-6981(82)90131-7.

Ouwersloot, H. G., Pozzer, A., Steil, B., Tost, H., & Lelieveld, J. (2015). Revision of the convective transport module CVTRANS 2.4 in the EMAC atmospheric chemistry–climate model. *Geoscientific Model Development*, 8(8), 2435–2445. http://www.geosci-model-dev.net/8/2435/2015/.

Partanen, A. I., Laakso, A., Schmidt, A., Kokkola, H., Kuokkanen, T., Pietikäinen, J.-P., Kerminen, V.-M., Lehtinen, K. E. J., Laakso, L., & Korhonen, H. (2013). Climate and air quality trade-offs in altering ship fuel sulfur content. *Atmospheric Chemistry and Physics*, 13(23), 12059–12071. http://www.atmos-chem-phys.net/13/12059/2013/.

Patoulias, D., Fountoukis, C., Riipinen, I., & Pandis, S. N. (2015). The role of organic condensation on ultrafine particle growth during nucleation events. *Atmospheric Chemistry and Physics*, 15(11), 6337–6350. http://www.atmos-chem-phys.net/15/6337/2015/.

Peng, Y., von Salzen, K., & Li, J. (2012). Simulation of mineral dust aerosol with Piecewise Log-normal Approximation (PLA) in CanAM4-PAM. *Atmospheric Chemistry and Physics*, 12(15), 6891–6914. http://www.atmos-chem-phys.net/12/6891/2012/.

Péré, J. C., Colette, A., Dubuisson, P., Bessagnet, B., Mallet, M., & Pont, V. (2012). Impacts of future air pollution mitigation strategies on the aerosol direct radiative forcing over Europe. *Atmospheric Environment*, 62, 451–460. doi:10.1016/j.atmosenv.2012.08.046.

Peters, K., Stier, P., Quaas, J., & Graßl, H. (2012). Aerosol indirect effects from shipping emissions: sensitivity studies with the global aerosol-climate model ECHAM-HAM. *Atmospheric Chemistry and Physics*, 12(13), 5985–6007. http://www.atmos-chem-phys.net/12/5985/2012/.

Peters, K., Stier, P., Quaas, J., & Graßl, H. (2013). Corrigendum to "Aerosol indirect effects from shipping emissions: sensitivity studies with the global aerosol-climate model ECHAM-HAM" published in Atmos. Chem. Phys., 12, 5985–6007, 2012. *Atmospheric Chemistry and Physics*, 13(13), 6429–6430. http://www.atmos-chem-phys.net/13/6429/2013/.

Petters, M. D. & Kreidenweis, S. M. (2007). A single parameter representation of hygroscopic growth and cloud condensation nucleus activity. *Atmospheric Chemistry and Physics*, 7(8), 1961–1971. http://www.atmos-chem-phys.net/7/1961/2007/.

Petzold, A., Döpelheuer, A., Brock, C. A., & Schröder, F. (1999). In situ observations and model calculations of black carbon emission by aircraft at cruise altitude. *Journal of Geophysical Research: Atmospheres*, 104(D18), 22171–22181. doi:10.1029/1999JD900460.

Petzold, A., Fiebig, M., Flentje, H., Keil, A., Leiterer, U., Schröder, F., Stifter, A., Wendisch, M., & Wendling, P. (2002). Vertical variability of aerosol properties observed at a continental site during the Lindenberg Aerosol Characterization Experiment (LACE 98). *Journal of Geophysical Research: Atmospheres*, 107(D21), 8128. doi:10.1029/2001JD001043.

Petzold, A., Gysel, M., Vancassel, X., Hitzenberger, R., Puxbaum, H., Vrochticky, S., Weingartner, E., Baltensperger, U., & Mirabel, P. (2005). On the effects of organic matter and sulphur-containing compounds on the CCN activation of combustion particles. *Atmospheric Chemistry and Physics*, 5(12), 3187–3203. http://www.atmos-chem-phys.net/5/3187/2005/.

Petzold, A., Hasselbach, J., Lauer, P., Baumann, R., Franke, K., Gurk, C., Schlager, H., & Weingartner, E. (2008). Experimental studies on particle emissions from cruising ship, their characteristic properties, transformation and atmospheric lifetime in the marine boundary layer. *Atmospheric Chemistry and Physics*, 8(9), 2387–2403. http://www.atmos-chem-phys.net/8/2387/2008/.

Petzold, A., Ogren, J. A., Fiebig, M., Laj, P., Li, S.-M., Baltensperger, U., Holzer-Popp, T., Kinne, S., Pappalardo, G., Sugimoto, N., Wehrli, C., Wiedensohler, A., & Zhang, X.-Y. (2013). Recommendations for reporting "black carbon" measurements. *Atmospheric Chemistry and Physics*, 13(16), 8365–8379. http://www.atmos-chem-phys.net/13/8365/2013/.

Petzold, A., Ström, J., Ohlsson, S., & Schröder, F. (1998). Elemental composition and morphology of ice-crystal residual particles in cirrus clouds and contrails. *Atmospheric Research*, 49(1), 21–34. doi:10.1016/S0169-8095(97)00083-5.

Pierce, J. R., Croft, B., Kodros, J. K., D'Andrea, S. D., & Martin, R. V. (2015). The importance of interstitial particle scavenging by cloud droplets in shaping the remote aerosol size distribution and global aerosol-climate effects. *Atmospheric Chemistry and Physics*, 15(11), 6147–6158. http://www.atmos-chem-phys.net/15/6147/2015/.

Pierce, J. R., Evans, M. J., Scott, C. E., D'Andrea, S. D., Farmer, D. K., Swietlicki, E., & Spracklen, D. V. (2013). Weak global sensitivity of cloud condensation nuclei and the aerosol indirect effect to Criegee + SO_2 chemistry. *Atmospheric Chemistry and Physics*, 13(6), 3163–3176. http://www.atmos-chem-phys.net/13/3163/2013/.

Pietikäinen, J.-P., Kupiainen, K., Klimont, Z., Makkonen, R., Korhonen, H., Karinkanta, R., Hyvärinen, A.-P., Karvosenoja, N., Laaksonen, A., Lihavainen, H., & Kerminen, V.-M. (2015). Impacts of emission reductions on aerosol radiative effects. *Atmospheric Chemistry and Physics*, 15(10), 5501–5519. http://www.atmos-chem-phys.net/15/5501/2015/.

Pietikäinen, J.-P., Mikkonen, S., Hamed, A., Hienola, A. I., Birmili, W., Kulmala, M., & Laaksonen, A. (2014). Analysis of nucleation events in the European boundary layer using the regional aerosol–climate model REMO-HAM with a solar radiation-driven OH-proxy. *Atmospheric Chemistry and Physics*, 14(21), 11711–11729. http://www.atmos-chem-phys.net/14/11711/2014/.

Pilinis, C., Capaldo, K. P., Nenes, A., & Pandis, S. N. (2000). MADM - A new multicomponent aerosol dynamics model. *Aerosol Science and Technology*, 32(5), 482–502. doi:10.1080/027868200303597.

Popovicheva, O. B., DeMott, P. J., Koehler, K. A., Kreidenweis, S. M., Petters, M. D., Carrico, C. M., Shonija, N., & Kireeva, E. (2010). Ice nucleation on soot in contrails and cirrus: Laboratory view. In R. Sausen, P. F. J. van Velthoven, C. Brüning, & A. Blum (Eds.), *Proceedings of the 2nd International Conference on Transport, Atmosphere and Climate (TAC-2)*, volume 2010-10 of *Forschungsbericht* (pp. 51–56). DLR. http://www.scopus.com/inward/record.url?eid=2-s2.0-77956562607&partnerID=40&md5=0c50a85215cf76fa7e348f055894910d.

Popovicheva, O. B., Persiantseva, N. M., Kireeva, E. D., Khokhlova, T. D., & Shonija, N. K. (2011). Quantification of the Hygroscopic Effect of Soot Aging in the Atmosphere: Laboratory Simulations. *The Journal of Physical Chemistry A*, 115(3), 298–306. http://pubs.acs.org/doi/abs/10.1021/jp109238x.

Pöschl, U. (2005). Atmospheric Aerosols: Composition, Transformation, Climate and Health Effects. *Angewandte Chemie International Edition*, 44(46), 7520–7540. doi:10.1002/anie.200501122.

Pozzer, A., de Meij, A., Pringle, K. J., Tost, H., Doering, U. M., van Aardenne, J., & Lelieveld, J. (2012). Distributions and regional budgets of aerosols and their precursors simulated with the EMAC chemistry-climate model. *Atmospheric Chemistry and Physics*, 12(2), 961–987. http://www.atmos-chem-phys.net/12/961/2012/.

Pozzer, A., de Meij, A., Yoon, J., Tost, H., Georgoulias, A. K., & Astitha, M. (2015). AOD trends during 2001–2010 from observations and model simulations. *Atmospheric Chemistry and Physics*, 15(10), 5521–5535. http://www.atmos-chem-phys.net/15/5521/2015/.

Pozzer, A., Jöckel, P., & Van Aardenne, J. (2009). The influence of the vertical distribution of emissions on tropospheric chemistry. *Atmospheric Chemistry and Physics*, 9(24), 9417–9432. http://www.atmos-chem-phys.net/9/9417/2009/.

Prabhakar, G., Ervens, B., Wang, Z., Maudlin, L. C., Coggon, M. M., Jonsson, H. H., Seinfeld, J. H., & Sorooshian, A. (2014). Sources of nitrate in stratocumulus cloud water: Airborne measurements during the 2011 E-PEACE and 2013 NiCE studies. *Atmospheric Environment*, 97, 166–173. doi:10.1016/j.atmosenv.2014.08.019.

Pratt, K. A., DeMott, P. J., French, J. R., Wang, Z., Westphal, D. L., Heymsfield, A. J., Twohy, C. H., Prenni, A. J., & Prather, K. A. (2009). In situ detection of biological particles in cloud ice-crystals. *Nature Geoscience*, 2(6), 398–401. doi:10.1038/ngeo521.

Pringle, K. J., Tost, H., Message, S., Steil, B., Giannadaki, D., Nenes, A., Fountoukis, C., Stier, P., Vignati, E., & Lelieveld, J. (2010a). Description and evaluation of GMXe: a new aerosol submodel for global simulations (v1). *Geoscientific Model Development*, 3(2), 391–412. http://www.geosci-model-dev.net/3/391/2010/gmd-3-391-2010.html.

Pringle, K. J., Tost, H., Metzger, S., Steil, B., Giannadaki, D., Nenes, A., Fountoukis, C., Stier, P., Vignati, E., & Lelieveld, J. (2010b). Corrigendum to "Description and evaluation of GMXe: a new aerosol submodel for global simulations (v1)" published in Geosci. Model Dev., 3, 391-412, 2010. *Geoscientific Model Development*, 3(2), 413–413. http://www.geosci-model-dev.net/3/413/2010/.

Pruppacher, H. R. & Klett, J. D. (1997). *Microphysics of Clouds and Precipitation*. Atmospheric and Oceanographic Sciences Library. Dordrecht, The Netherlands: Kluwer Academic Publishers, second edition.

Putaud, J.-P., Van Dingenen, R., Alastuey, A., Bauer, H., Birmili, W., Cyrys, J., Flentje, H., Fuzzi, S., Gehrig, R., Hansson, H. C., Harrison, R. M., Herrmann, H., Hitzenberger, R., Hüglin, C., Jones, A. M., Kasper-Giebl, A., Kiss, G., Kousa, A., Kuhlbusch, T. A. J., Löschau, G., Maenhaut, W., Molnar, A., Moreno, T., Pekkanen, J., Perrino, C., Pitz, M., Puxbaum, H., Querol, X., Rodriguez, S., Salma, I., Schwarz, J., Smolik, J., Schneider, J., Spindler, G., ten Brink, H., Tursic, J., Viana, M., Wiedensohler, A., & Raes, F. (2010). A European aerosol phenomenology - 3: Physical and chemical characteristics of particulate matter from 60 rural, urban, and kerbside sites across Europe. *Atmospheric Environment*, 44(10), 1308–1320. doi:10.1016/j.atmosenv.2009.12.011.

Putaud, J.-P., Van Dingenen, R., Baltensperger, U., Brüggemann, E., Charron, A., Facchini, M., Decesari, S., Fuzzi, S., Gehrig, R., Hansson, H.-C., Harrison, R., Jones, A., Laj, P., Lorbeer, G., Maenhaut, W., Mihalopoulos, N., Müller, K., Palmgren, F., Querol, X., Rodriguez, S., Schneider, J., Spindler, G., ten Brink, H., Tunved, P., Tørseth, K., Wehner, B., Weingartner, E., Wiedensohler, A., Wåhlin, P., & Raes, F. (2003). *A European Aerosol Phenomenology*. Technical Report EUR 20411 EN, European Commission, Joint Research Centre, Institute for Environment and Sustainability, Ispra, Italy. http://ccaqu.jrc.ec.europa.eu/Publication/Phenomenology.pdf.

Raes, F., Van Dingenen, R., Vignati, E., Wilson, J., Putaud, J. P., Seinfeld, J. H., & Adams, P. (2000). Formation and cycling of aerosols in the global troposphere. *Atmospheric Environment*, 34(25), 4215–4240. doi:10.1016/S1352-2310(00)00239-9.

Räisänen, P., Haapanala, P., Chung, C. E., Kahnert, M., Makkonen, R., Tonttila, J., & Nousiainen, T. (2013). Impact of dust particle non-sphericity on climate simulations. *Quarterly Journal of the Royal Meteorological Society*, 139(677), 2222–2232. doi:10.1002/qj.2084.

Randles, C. A., Colarco, P. R., & da Silva, A. (2013). Direct and semi-direct aerosol effects in the NASA GEOS-5 AGCM: aerosol-climate interactions due to prognostic versus prescribed aerosols. *Journal of Geophysical Research: Atmospheres*, 118(1), 149–169. doi:10.1029/2012JD018388.

Rap, A., Scott, C. E., Spracklen, D. V., Bellouin, N., Forster, P. M., Carslaw, K. S., Schmidt, A., & Mann, G. (2013). Natural aerosol direct and indirect radiative effects. *Geophysical Research Letters*, 40(12), 3297–3301. doi:10.1002/grl.50441.

Rastak, N., Silvergren, S., Zieger, P., Wideqvist, U., Ström, J., Svenningsson, B., Maturilli, M., Tesche, M., Ekman, A. M. L., Tunved, P., & Riipinen, I. (2014). Seasonal variation of aerosol water uptake and its impact on the direct radiative effect at Ny-Ålesund, Svalbard. *Atmospheric Chemistry and Physics*, 14(14), 7445–7460. http://www.atmos-chem-phys.net/14/7445/2014/.

Riccobono, F., Schobesberger, S., Scott, C. E., Dommen, J., Ortega, I. K., Rondo, L., Almeida, J., Amorim, A., Bianchi, F., Breitenlechner, M., David, A., Downard, A., Dunne, E. M., Duplissy, J., Ehrhart, S., Flagan, R. C., Franchin, A., Hansel, A., Junninen, H., Kajos, M., Keskinen, H., Kupc, A., Kürten, A., Kvashin, A. N., Laaksonen, A., Lehtipalo, K., Makhmutov, V., Mathot, S., Nieminen, T., Onnela, A., Petäjä, T., Praplan, A. P., Santos, F. D., Schallhart, S., Seinfeld, J. H., Sipilä, M., Spracklen, D. V., Stozhkov, Y., Stratmann, F., Tomé, A., Tsagkogeorgas, G., Vaattovaara, P., Viisanen, Y., Vrtala, A., Wagner, P. E., Weingartner, E., Wex, H., Wimmer, D., Carslaw, K. S., Curtius, J., Donahue, N. M., Kirkby, J., Kulmala, M., Worsnop, D. R., & Baltensperger, U. (2014). Oxidation Products of Biogenic Emissions Contribute to Nucleation of Atmospheric Particles. *Science*, 344(6185), 717–721. http://www.sciencemag.org/content/344/6185/717.abstract.

Ridley, D. A., Heald, C. L., Pierce, J. R., & Evans, M. J. (2013). Toward resolution-independent dust emissions in global models: Impacts on the seasonal and spatial distribution of dust. *Geophysical Research Letters*, 40(11), 2873–2877. doi:10.1002/grl.50409.

Riemer, N., West, M., Zaveri, R. A., & Easter, R. C. (2009). Simulating the evolution of soot mixing state with a particle-resolved aerosol model. *Journal of Geophysical Research: Atmospheres*, 114(D9), D09202. doi:10.1029/2008JD011073.

Righi, M., Hendricks, J., & Sausen, R. (2013). The global impact of the transport sectors on atmospheric aerosol: simulations for year 2000 emissions. *Atmospheric Chemistry and Physics*, 13(19), 9939–9970. http://www.atmos-chem-phys.net/13/9939/2013/.

Righi, M., Hendricks, J., & Sausen, R. (2015). The global impact of the transport sectors on atmospheric aerosol in 2030 – Part 1: Land transport and shipping. *Atmospheric Chemistry and Physics*, 15(2), 633–651. http://www.atmos-chem-phys.net/15/633/2015/.

Righi, M., Klinger, C., Eyring, V., Hendricks, J., Lauer, A., & Petzold, A. (2011). Climate Impact of Biofuels in Shipping: Global Model Studies of the Aerosol Indirect Effect. *Environmental Science & Technology*, 45(8), 3519–3525. http://pubs.acs.org/doi/abs/10.1021/es1036157.

Roeckner, E., Bäuml, G., Bonaventura, L., Brokopf, R., Esch, M., Giorgetta, M., Hagemann, S., Kirchner, I., Kornblueh, L., Manzini, E., Rhodin, A., Schlese, U., Schulzweida, U., & Tompkins, A. (2003). *The atmospheric general circulation model ECHAM 5. PART I: Model description.* Technical Report 349, Max-Planck-Institut für Meteorologie, Hamburg, Germany. http://www.mpimet.mpg.de/fileadmin/publikationen/Reports/max_scirep_349.pdf.

Roeckner, E., Bengtsson, L., Feichter, J., Lelieveld, J., & Rodhe, H. (1999). Transient Climate Change Simulations with a Coupled Atmosphere-Ocean GCM Including the Tropospheric Sulfur Cycle. *Journal of Climate*, 12(10), 3004–3032. doi:10.1175/1520-0442(1999)012<3004:TCCSWA>2.0.CO;2.

Roeckner, E., Brokopf, R., Esch, M., Giorgetta, M., Hagemann, S., Kornblueh, L., Manzini, E., Schlese, U., & Schulzweida, U. (2006). Sensitivity of Simulated Climate to Horizontal and Vertical Resolution in the ECHAM5 Atmosphere Model. *Journal of Climate*, 19(16), 3771–3791. doi:10.1175/JCLI3824.1.

Romakkaniemi, S., Kokkola, H., & Laaksonen, A. (2005). Parameterization of the nitric acid effect on CCN activation. *Atmospheric Chemistry and Physics*, 5(4), 879–885. http://www.atmos-chem-phys.net/5/879/2005/.

Rose, C., Sellegri, K., Asmi, E., Hervo, M., Freney, E., Colomb, A., Junninen, H., Duplissy, J., Sipilä, M., Kontkanen, J., Lehtipalo, K., & Kulmala, M. (2015). Major contribution of neutral clusters to new particle formation at the interface between the boundary layer and the free troposphere. *Atmospheric Chemistry and Physics*, 15(6), 3413–3428. http://www.atmos-chem-phys.net/15/3413/2015/.

Russell, J. M., Gordley, L. L., Park, J. H., Drayson, S. R., Hesketh, W. D., Cicerone, R. J., Tuck, A. F., Frederick, J. E., Harries, J. E., & Crutzen, P. J. (1993). The Halogen Occultation Experiment. *Journal of Geophysical Research: Atmospheres*, 98(D6), 10777–10797. doi:10.1029/93JD00799.

Sakai, T., Orikasa, N., Nagai, T., Murakami, M., Tajiri, T., Saito, A., Yamashita, K., & Hashimoto, A. (2014). Balloon-borne and Raman lidar observations of Asian dust and cirrus cloud properties over Tsukuba, Japan. *Journal of Geophysical Research: Atmospheres*, 119(6), 3295–3308. doi:10.1002/2013JD020987.

Salzmann, M., Weser, H., & Cherian, R. (2014). Robust response of Asian summer monsoon to anthropogenic aerosols in CMIP5 models. *Journal of Geophysical Research: Atmospheres*, 119(19), 11321–11337. doi:10.1002/2014JD021783.

Sand, M., Berntsen, T. K., Kay, J. E., Lamarque, J. F., Seland, Ø., & Kirkevåg, A. (2013). The Arctic response to remote and local forcing of black carbon. *Atmospheric Chemistry and Physics*, 13(1), 211–224. http://www.atmos-chem-phys.net/13/211/2013/.

Sander, R., Baumgaertner, A., Gromov, S., Harder, H., Jöckel, P., Kerkweg, A., Kubistin, D., Regelin, E., Riede, H., Sandu, A., Taraborrelli, D., Tost, H., & Xie, Z.-Q. (2011). The atmospheric chemistry box model CAABA/MECCA-3.0. *Geoscientific Model Development*, 4(2), 373–380. http://www.geosci-model-dev.net/4/373/2011/.

Sander, R., Jöckel, P., Kirner, O., Kunert, A. T., Landgraf, J., & Pozzer, A. (2014). The photolysis module JVAL-14, compatible with the MESSy standard, and the JVal PreProcessor (JVPP). *Geoscientific Model Development*, 7(6), 2653–2662. http://www.geosci-model-dev.net/7/2653/2014/.

Scanza, R. A., Mahowald, N., Ghan, S., Zender, C. S., Kok, J. F., Liu, X., Zhang, Y., & Albani, S. (2015). Modeling dust as component minerals in the Community Atmosphere Model: development of framework and impact on radiative forcing. *Atmospheric Chemistry and Physics*, 15(1), 537–561. http://www.atmos-chem-phys.net/15/537/2015/.

Scarnato, B. V., China, S., Nielsen, K., & Mazzoleni, C. (2015). Perturbations of the optical properties of mineral dust particles by mixing with black carbon: a numerical simulation study. *Atmospheric Chemistry and Physics*, 15(12), 6913–6928. http://www.atmos-chem-phys.net/15/6913/2015/.

Schembari, C., Cavalli, F., Cuccia, E., Hjorth, J., Calzolai, G., Pérez, N., Pey, J., Prati, P., & Raes, F. (2012). Impact of a European directive on ship emissions on air quality in Mediterranean harbours. *Atmospheric Environment*, 61, 661–669. doi:10.1016/j.atmosenv.2012.06.047.

Scheuvens, D., Schütz, L., Kandler, K., Ebert, M., & Weinbruch, S. (2013). Bulk composition of northern African dust and its source sediments – A compilation. *Earth-Science Reviews*, 116, 170–194. http://www.sciencedirect.com/science/article/pii/S001282521200102X.

Schmale, J., Schneider, J., Nemitz, E., Tang, Y. S., Dragosits, U., Blackall, T. D., Trathan, P. N., Phillips, G. J., Sutton, M., & Braban, C. F. (2013). Sub-Antarctic marine aerosol: dominant contributions from biogenic sources. *Atmospheric Chemistry and Physics*, 13(17), 8669–8694. http://www.atmos-chem-phys.net/13/8669/2013/.

Schobesberger, S., Franchin, A., Bianchi, F., Rondo, L., Duplissy, J., Kürten, A., Ortega, I. K., Metzger, A., Schnitzhofer, R., Almeida, J., Amorim, A., Dommen, J., Dunne, E. M., Ehn, M., Gagné, S., Ickes, L., Junninen, H., Hansel, A., Kerminen, V.-M., Kirkby, J., Kupc, A., Laaksonen, A., Lehtipalo, K., Mathot, S., Onnela, A., Petäjä, T., Riccobono, F., Santos, F. D., Sipilä, M., Tomé, A., Tsagkogeorgas, G., Viisanen, Y., Wagner, P. E., Wimmer, D., Curtius, J., Donahue, N. M., Baltensperger, U., Kulmala, M., & Worsnop, D. R. (2015). On the composition of ammonia–sulfuric-acid ion clusters during aerosol particle formation. *Atmospheric Chemistry and Physics*, 15(1), 55–78. http://www.atmos-chem-phys.net/15/55/2015/.

Schroder, J. C., Hanna, S. J., Modini, R. L., Corrigan, A. L., Kreidenweis, S. M., Macdonald, A. M., Noone, K. J., Russell, L. M., Leaitch, W. R., & Bertram, A. K. (2015a). Corrigendum to "Size-resolved observations of refractory black carbon particles in cloud droplets at a marine boundary layer site" published in Atmos. Chem. Phys., 15, 1367–1383, 2015. *Atmospheric Chemistry and Physics*, 15(3), 1487–1487. http://www.atmos-chem-phys.net/15/1487/2015/.

Schroder, J. C., Hanna, S. J., Modini, R. L., Corrigan, A. L., Kreidenweis, S. M., Macdonald, A. M., Noone, K. J., Russell, L. M., Leaitch, W. R., & Bertram, A. K. (2015b). Size-resolved observations of refractory black carbon particles in cloud droplets at a marine boundary layer site. *Atmospheric Chemistry and Physics*, 15(3), 1367–1383. http://www.atmos-chem-phys.net/15/1367/2015/.

Schwarz, J. P., Gao, R. S., Fahey, D. W., Thomson, D. S., Watts, L. A., Wilson, J. C., Reeves, J. M., Darbeheshti, M., Baumgardner, D. G., Kok, G. L., Chung, S. H., Schulz, M., Hendricks, J., Lauer, A., Kärcher, B., Slowik, J. G., Rosenlof, K. H., Thompson, T. L., Langford, A. O., Loewenstein, M., & Aikin, K. C. (2006). Single-particle measurements of midlatitude black carbon and light-scattering aerosols from the boundary layer to the lower stratosphere. *Journal of Geophysical Research: Atmospheres*, 111(D16), D16207. doi:10.1029/2006JD007076.

Schwarz, J. P., Samset, B. H., Perring, A. E., Spackman, J. R., Gao, R. S., Stier, P., Schulz, M., Moore, F. L., Ray, E. A., & Fahey, D. W. (2013). Global-scale seasonally resolved black carbon vertical profiles over the Pacific. *Geophysical Research Letters*, 40(20), 5542–5547. doi:10.1002/2013GL057775.

Schwarz, J. P., Spackman, J. R., Fahey, D. W., Gao, R. S., Lohmann, U., Stier, P., Watts, L. A., Thomson, D. S., Lack, D. A., Pfister, L., Mahoney, M. J., Baumgardner, D., Wilson, J. C., & Reeves, J. M. (2008). Coatings and their enhancement of black carbon light absorption in the tropical atmosphere. *Journal of Geophysical Research: Atmospheres*, 113(D3), D03203. doi:10.1029/2007JD009042.

Seinfeld, J. H. & Pandis, S. N. (2006). *Atmospheric chemistry and physics: from air pollution to climate change*. Hoboken, NJ: Wiley, second edition.

Semeniuk, T. A., Bruintjes, R. T., Salazar, V., Breed, D. W., Jensen, T. L., & Buseck, P. R. (2014). Individual aerosol particles in ambient and updraft conditions below convective cloud bases in the Oman mountain region. *Journal of Geophysical Research: Atmospheres*, 119(5), 2511–2528. doi:10.1002/2013JD021165.

Serra, N., Martínez Avellaneda, N., & Stammer, D. (2014). Large-scale impact of Saharan dust on the North Atlantic Ocean circulation. *Journal of Geophysical Research: Oceans*, 119(2), 704–730. doi:10.1002/2013JC009274.

Shen, Z., Liu, J., Horowitz, L. W., Henze, D. K., Fan, S., H., L. I., Mauzerall, D. L., Lin, J.-T., & Tao, S. (2014). Analysis of transpacific transport of black carbon during HIPPO-3: implications for black carbon aging. *Atmospheric Chemistry and Physics*, 14(12), 6315–6327. `http://www.atmos-chem-phys.net/14/6315/2014/`.

Shettle, E. P. & Fenn, R. W. (1979). *Models for the Aerosols of the Lower Atmosphere and the Effects of Humidity Variations on their Optical Properties.* Technical Report ADA085951, Air Force Geophysics Lab Hanscom AFB MA. `http://www.dtic.mil/cgi-bin/GetTRDoc?Location=U2&doc=GetTRDoc.pdf&AD=ADA085951`.

Shi, Z., Zhang, D., Hayashi, M., Ogata, H., Ji, H., & Fujiie, W. (2008). Influences of sulfate and nitrate on the hygroscopic behaviour of coarse dust particles. *Atmospheric Environment*, 42(4), 822–827. `http://www.sciencedirect.com/science/article/pii/S135223100700948X`.

Shrivastava, M., Berg, L. K., Fast, J. D., Easter, R. C., Laskin, A., Chapman, E. G., Gustafson, W. I., Liu, Y., & Berkowitz, C. M. (2013). Modeling aerosols and their interactions with shallow cumuli during the 2007 CHAPS field study. *Journal of Geophysical Research: Atmospheres*, 118(3), 1343–1360. doi:10.1029/2012JD018218.

Sigma Aldrich (2014). Sea Salt S9883. `http://www.sigmaaldrich.com/catalog/product/sigma/s9883?lang=de&region=DE`, accessed on 2014-07-22.

Sillmann, J., Pozzoli, L., Vignati, E., Kloster, S., & Feichter, J. (2013). Aerosol effect on climate extremes in Europe under different future scenarios. *Geophysical Research Letters*, 40(10), 2290–2295. doi:10.1002/grl.50459.

Simpson, R. M. C., Howell, S. G., Blomquist, B. W., Clarke, A. D., & Huebert, B. J. (2014). Dimethyl sulfide: Less important than long-range transport as a source of sulfate to the remote tropical Pacific marine boundary layer. *Journal of Geophysical Research: Atmospheres*, 119(14), 9142–9167. doi:10.1002/2014JD021643.

Slinn, W. G. N. (1984). Precipitation Scavenging. In D. Randerson (Ed.), *Atmospheric science and power production* chapter 11, (pp. 466–532). U.S.: Department of Energy. `http://www.osti.gov/scitech/servlets/purl/6503687`.

Smith, M. H. & Harrison, N. M. (1998). The sea spray generation function. *Journal of Aerosol Science*, 29, Supplement 1, S189–S190. doi:10.1016/S0021-8502(98)00280-8.

Smith, S. J. & Bond, T. C. (2014). Two hundred fifty years of aerosols and climate: the end of the age of aerosols. *Atmospheric Chemistry and Physics*, 14(2), 537–549. `http://www.atmos-chem-phys.net/14/537/2014/`.

Sorooshian, A., Prabhakar, G., Jonsson, H., Woods, R. K., Flagan, R. C., & Seinfeld, J. H. (2015). On the presence of giant particles downwind of ships in the marine boundary layer. *Geophysical Research Letters*, 42(6), 2024–2030. doi:10.1002/2015GL063179.

Sorribas, M., Olmo, F. J., Quirantes, A., Lyamani, H., Gil-Ojeda, M., Alados-Arboledas, L., & Horvath, H. (2015). Role of spheroids particles on closure studies for aerosol microphysical-optical properties. *Quarterly Journal of the Royal Meteorological Society.* doi:10.1002/qj.2557.

Spackman, J. R., Gao, R. S., Schwarz, J. P., Watts, L. A., Fahey, D. W., Pfister, L., & Bui, T. P. (2011). Seasonal variability of black carbon mass in the tropical tropopause layer. *Geophysical Research Letters*, 38(9), L09803. doi:10.1029/2010GL046343.

Spada, M., Jorba, O., Pérez García-Pando, C., Janjic, Z., & M. Baldasano, J. (2013). Modeling and evaluation of the global sea-salt aerosol distribution: sensitivity to emission schemes and resolution effects at coastal/orographic sites. *Atmospheric Chemistry and Physics*, 13(23), 11735–11755. `http://www.atmos-chem-phys.net/13/11735/2013/`.

Spiro, P. A., Jacob, D. J., & Logan, J. A. (1992). Global inventory of sulfur emissions with 1°x1° resolution. *Journal of Geophysical Research: Atmospheres*, 97(D5), 6023–6036. doi:10.1029/91JD03139.

Spracklen, D. V., Carslaw, K. S., Kulmala, M., Kerminen, V.-M., Mann, G. W., & Sihto, S.-L. (2006). The contribution of boundary layer nucleation events to total particle concentrations on regional and global scales. *Atmospheric Chemistry and Physics*, 6(12), 5631–5648. http://www.atmos-chem-phys.net/6/5631/2006/.

Squizzato, S., Masiol, M., Brunelli, A., Pistollato, S., Tarabotti, E., Rampazzo, G., & Pavoni, B. (2013). Factors determining the formation of secondary inorganic aerosol: a case study in the Po Valley (Italy). *Atmospheric Chemistry and Physics*, 13(4), 1927–1939. http://www.atmos-chem-phys.net/13/1927/2013/.

Stier, P., Feichter, J., Kinne, S., Kloster, S., Vignati, E., Wilson, J., Ganzeveld, L., Tegen, I., Werner, M., Balkanski, Y., Schulz, M., Boucher, O., Minikin, A., & Petzold, A. (2005). The aerosol-climate model ECHAM5-HAM. *Atmospheric Chemistry and Physics*, 5(4), 1125–1156. http://www.atmos-chem-phys.net/5/1125/2005/.

Sullivan, R. C., Guazzotti, S. A., Sodeman, D. A., & Prather, K. A. (2007). Direct observations of the atmospheric processing of Asian mineral dust. *Atmospheric Chemistry and Physics*, 7(5), 1213–1236. http://www.atmos-chem-phys.net/7/1213/2007/.

Sullivan, R. C., Moore, M. J. K., Petters, M. D., Kreidenweis, S. M., Roberts, G. C., & Prather, K. A. (2009). Effect of chemical mixing state on the hygroscopicity and cloud nucleation properties of calcium mineral dust particles. *Atmospheric Chemistry and Physics*, 9(10), 3303–3316. http://www.atmos-chem-phys.net/9/3303/2009/.

Sullivan, R. C., Petters, M. D., DeMott, P. J., Kreidenweis, S. M., Wex, H., Niedermeier, D., Hartmann, S., Clauss, T., Stratmann, F., Reitz, P., Schneider, J., & Sierau, B. (2010). Irreversible loss of ice nucleation active sites in mineral dust particles caused by sulphuric acid condensation. *Atmospheric Chemistry and Physics*, 10(23), 11471–11487. http://www.atmos-chem-phys.net/10/11471/2010/.

Sundqvist, H., Berge, E., & Kristjánsson, J. E. (1989). Condensation and Cloud Parameterization Studies with a Mesoscale Numerical Weather Prediction Model. *Monthly Weather Review*, 117(8), 1641–1657. doi:10.1175/1520-0493(1989)117<1641:CACPSW>2.0.CO;2.

Sundström, A.-M., Arola, A., Kolmonen, P., Xue, Y., de Leeuw, G., & Kulmala, M. (2015). On the use of a satellite remote-sensing-based approach for determining aerosol direct radiative effect over land: a case study over China. *Atmospheric Chemistry and Physics*, 15(1), 505–518. http://www.atmos-chem-phys.net/15/505/2015/.

Sutherland, R. A. & Khanna, R. K. (1991). Optical Properties of Organic-based Aerosols Produced by Burning Vegetation. *Aerosol Science and Technology*, 14(3), 331–342. doi:10.1080/02786829108959495.

Takemura, T. (2012). Distributions and climate effects of atmospheric aerosols from the preindustrial era to 2100 along Representative Concentration Pathways (RCPs) simulated using the global aerosol model SPRINTARS. *Atmospheric Chemistry and Physics*, 12(23), 11555–11572. http://www.atmos-chem-phys.net/12/11555/2012/.

Tan, I., Storelvmo, T., & Choi, Y.-S. (2014). Spaceborne lidar observations of the ice-nucleating potential of dust, polluted dust, and smoke aerosols in mixed-phase clouds. *Journal of Geophysical Research: Atmospheres*, 119(11), 6653–6665. doi:10.1002/2013JD021333.

Tanré, D., Geleyn, J.-F., & Slingo, J. (1984). First results of the introduction of an advanced aerosol-radiation interaction in the ECMWF low resolution global model. In H. E. Gerber & A. Deepak (Eds.), *Aerosols and their Climatic Effects* (pp. 133–177). Hampton, VA: A. Deepak Publishing.

Taylor, J. W., Allan, J. D., Allen, G., Coe, H., Williams, P. I., Flynn, M. J., Le Breton, M., Muller, J. B. A., Percival, C. J., Oram, D., Forster, G., Lee, J. D., Rickard, A. R., Parrington, M., & Palmer, P. I. (2014). Size-dependent wet removal of black carbon in Canadian biomass burning plumes. *Atmospheric Chemistry and Physics*, 14(24), 13755–13771. http://www.atmos-chem-phys.net/14/13755/2014/.

Teinilä, K., Frey, A., Hillamo, R., Tülp, H. C., & Weller, R. (2014). A study of the sea-salt chemistry using size-segregated aerosol measurements at coastal Antarctic station Neumayer. *Atmospheric Environment*, 96, 11–19. doi:10.1016/j.atmosenv.2014.07.025.

Telford, P., Braesicke, P., Morgenstern, O., & Pyle, J. (2009). Reassessment of causes of ozone column variability following the eruption of Mount Pinatubo using a nudged CCM. *Atmospheric Chemistry and Physics*, 9(13), 4251–4260. http://www.atmos-chem-phys.net/9/4251/2009/.

Textor, C., Schulz, M., Guibert, S., Kinne, S., Balkanski, Y., Bauer, S., Berntsen, T., Berglen, T., Boucher, O., Chin, M., Dentener, F., Diehl, T., Easter, R., Feichter, H., Fillmore, D., Ghan, S., Ginoux, P., Gong, S., Grini, A., Hendricks, J., Horowitz, L., Huang, P., Isaksen, I., Iversen, I., Kloster, S., Koch, D., Kirkevåg, A., Kristjansson, J. E., Krol, M., Lauer, A., Lamarque, J. F., Liu, X., Montanaro, V., Myhre, G., Penner, J., Pitari, G., Reddy, S., Seland, Ø., Stier, P., Takemura, T., & Tie, X. (2006). Analysis and quantification of the diversities of aerosol life cycles within AeroCom. *Atmospheric Chemistry and Physics*, 6(7), 1777–1813. http://www.atmos-chem-phys.net/6/1777/2006/.

Tian, J., Riemer, N., West, M., Pfaffenberger, L., Schlager, H., & Petzold, A. (2014). Modeling the evolution of aerosol particles in a ship plume using PartMC-MOSAIC. *Atmospheric Chemistry and Physics*, 14(11), 5327–5347. http://www.atmos-chem-phys.net/14/5327/2014/.

Tiedtke, M. (1989). A Comprehensive Mass Flux Scheme for Cumulus Parameterization in Large-Scale Models. *Monthly Weather Review*, 117(8), 1779–1800. doi:10.1175/1520-0493(1989)117<1779:ACMFSF>2.0.CO;2.

Tobo, Y., Zhang, D., Matsuki, A., & Iwasaka, Y. (2010). Asian dust particles converted into aqueous droplets under remote marine atmospheric conditions. *Proceedings of the National Academy of Sciences*, 107(42), 17905–17910. http://www.pnas.org/content/107/42/17905.abstract.

Tompkins, A. M. (2002). A Prognostic Parameterization for the Subgrid-Scale Variability of Water Vapor and Clouds in Large-Scale Models and Its Use to Diagnose Cloud Cover. *Journal of the Atmospheric Sciences*, 59(12), 1917–1942. doi:10.1175/1520-0469(2002)059<1917:APPFTS>2.0.CO;2.

Tosca, M. G., Randerson, J. T., & Zender, C. S. (2013). Global impact of smoke aerosols from landscape fires on climate and the Hadley circulation. *Atmospheric Chemistry and Physics*, 13(10), 5227–5241. http://www.atmos-chem-phys.net/13/5227/2013/.

Tost, H. (2006). *Global Modelling of Cloud, Convection and Precipitation Influences on Trace Gases and Aerosols*. PhD thesis, University of Bonn, Germany. http://hss.ulb.uni-bonn.de/2006/0731/0731.pdf.

Tost, H., Jöckel, P., Kerkweg, A., Sander, R., & Lelieveld, J. (2006a). Technical note: A new comprehensive SCAVenging submodel for global atmospheric chemistry modelling. *Atmospheric Chemistry and Physics*, 6(3), 565–574. http://www.atmos-chem-phys.net/6/565/2006/.

Tost, H., Jöckel, P., & Lelieveld, J. (2006b). Influence of different convection parameterisations in a GCM. *Atmospheric Chemistry and Physics*, 6(12), 5475–5493. http://www.atmos-chem-phys.net/6/5475/2006/.

Tost, H., Jöckel, P., & Lelieveld, J. (2007). Lightning and convection parameterisations – uncertainties in global modelling. *Atmospheric Chemistry and Physics*, 7(17), 4553–4568. http://www.atmos-chem-phys.net/7/4553/2007/.

Tost, H. & Pringle, K. J. (2012). Improvements of organic aerosol representations and their effects in large-scale atmospheric models. *Atmospheric Chemistry and Physics*, 12(18), 8687–8709. http://www.atmos-chem-phys.net/12/8687/2012/.

Tronstad Lund, M., Eyring, V., Fuglestvedt, J., Hendricks, J., Lauer, A., Lee, D., & Righi, M. (2012). Global-Mean Temperature Change from Shipping toward 2050: Improved Representation of the Indirect Aerosol Effect in Simple Climate Models. *Environmental Science & Technology*, 46(16), 8868–8877. doi:10.1021/es301166e.

Trump, E. R., Fountoukis, C., Donahue, N. M., & Pandis, S. N. (2015). Improvement of simulation of fine inorganic PM levels through better descriptions of coarse particle chemistry. *Atmospheric Environment*, 102, 274–281. doi:10.1016/j.atmosenv.2014.11.059.

Tsigaridis, K. & Kanakidou, M. (2003). Global modelling of secondary organic aerosol in the troposphere: a sensitivity analysis. *Atmospheric Chemistry and Physics*, 3(5), 1849–1869. http://www.atmos-chem-phys.net/3/1849/2003/.

Twohy, C. H. & Anderson, J. R. (2008). Droplet nuclei in non-precipitating clouds: composition and size matter. *Environmental Research Letters*, 3(4), 045002. http://stacks.iop.org/1748-9326/3/i=4/a=045002.

Twohy, C. H., Anderson, J. R., Toohey, D. W., Andrejczuk, M., Adams, A., Lytle, M., George, R. C., Wood, R., Saide, P., Spak, S., Zuidema, P., & Leon, D. (2013). Impacts of aerosol particles on the microphysical and radiative properties of stratocumulus clouds over the southeast Pacific Ocean. *Atmospheric Chemistry and Physics*, 13(5), 2541–2562. http://www.atmos-chem-phys.net/13/2541/2013/.

Twomey, S. (1977). The Influence of Pollution on the Shortwave Albedo of Clouds. *Journal of the Atmospheric Sciences*, 34(7), 1149–1152. doi:10.1175/1520-0469(1977)034<1149:TIOPOT>2.0.CO;2.

Ueda, S., Hirose, Y., Miura, K., & Okochi, H. (2014). Individual aerosol particles in and below clouds along a Mt. Fuji slope: Modification of sea-salt-containing particles by in-cloud processing. *Atmospheric Research*, 137, 216–227. doi:10.1016/j.atmosres.2013.10.011.

van der Werf, G. R., Randerson, J. T., Giglio, L., Collatz, G. J., Kasibhatla, P. S., & Arellano Jr., A. F. (2006). Interannual variability in global biomass burning emissions from 1997 to 2004. *Atmospheric Chemistry and Physics*, 6(11), 3423–3441. http://www.atmos-chem-phys.net/6/3423/2006/.

Van Dingenen, R. & Raes, F. (1991). Determination of the Condensation Accommodation Coefficient of Sulfuric Acid on Water-Sulfuric Acid Aerosol. *Aerosol Science and Technology*, 15(2), 93–106. http://www.tandfonline.com/doi/abs/10.1080/02786829108959516.

van Noije, T. P. C., Le Sager, P., Segers, A. J., van Velthoven, P. F. J., Krol, M. C., Hazeleger, W., Williams, A. G., & Chambers, S. D. (2014). Simulation of tropospheric chemistry and aerosols with the climate model EC-Earth. *Geoscientific Model Development*, 7(5), 2435–2475. http://www.geosci-model-dev.net/7/2435/2014/.

Vaughan, N. E. & Lenton, T. M. (2011). A review of climate geoengineering proposals. *Climatic Change*, 109(3–4), 745–790. doi:10.1007/s10584-011-0027-7.

Vehkamäki, H., Kulmala, M., Napari, I., Lehtinen, K. E. J., Timmreck, C., Noppel, M., & Laaksonen, A. (2002). An improved parameterization for sulfuric acid-water nucleation rates for tropospheric and stratospheric conditions. *Journal of Geophysical Research: Atmospheres*, 107(D22), 4622–4631. doi:10.1029/2002JD002184.

Vehkamäki, H., Kulmala, M., Napari, I., Lehtinen, K. E. J., Timmreck, C., Noppel, M., & Laaksonen, A. (2013). Correction to "An improved parameterization for sulfuric acid/water nucleation rates for tropospheric and stratospheric conditions". *Journal of Geophysical Research: Atmospheres*, 118(16), 9330–9330. doi:10.1002/jgrd.50603.

Viana, M., Hammingh, P., Colette, A., Querol, X., Degraeuwe, B., de Vlieger, I., & van Aardenne, J. (2014). Impact of maritime transport emissions on coastal air quality in Europe. *Atmospheric Environment*, 90, 96–105. doi:10.1016/j.atmosenv.2014.03.046.

Vignati, E., Karl, M., Krol, M., Wilson, J., Stier, P., & Cavalli, F. (2010). Sources of uncertainties in modelling black carbon at the global scale. *Atmospheric Chemistry and Physics*, 10(6), 2595–2611. http://www.atmos-chem-phys.net/10/2595/2010/.

Vignati, E., Wilson, J., & Stier, P. (2004). M7: An efficient size-resolved aerosol microphysics module for large-scale aerosol transport models. *Journal of Geophysical Research: Atmospheres*, 109(D22), D22202. doi:10.1029/2003JD004485.

Vuolo, M. R., Schulz, M., Balkanski, Y., & Takemura, T. (2014). A new method for evaluating the impact of vertical distribution on aerosol radiative forcing in general circulation models. *Atmospheric Chemistry and Physics*, 14(2), 877–897. http://www.atmos-chem-phys.net/14/877/2014/.

Wan, H., Rasch, P. J., Zhang, K., Kazil, J., & Leung, L. R. (2013). Numerical issues associated with compensating and competing processes in climate models: an example from ECHAM-HAM. *Geoscientific Model Development*, 6(3), 861–874. http://www.geosci-model-dev.net/6/861/2013/.

Wang, C., Corbett, J. J., & Firestone, J. (2008). Improving Spatial Representation of Global Ship Emissions Inventories. *Environmental Science & Technology*, 42(1), 193–199. doi:10.1021/es0700799.

Wang, H., Easter, R. C., Rasch, P. J., Wang, M., Liu, X., Ghan, S. J., Qian, Y., Yoon, J.-H., Ma, P.-L., & Vinoj, V. (2013a). Sensitivity of remote aerosol distributions to representation of cloud-aerosol interactions in a global climate model. *Geoscientific Model Development*, 6(3), 765–782. http://www.geosci-model-dev.net/6/765/2013/.

Wang, M., Ghan, S., Liu, X., L'Ecuyer, T. S., Zhang, K., Morrison, H., Ovchinnikov, M., Easter, R., Marchand, R., Chand, D., Qian, Y., & Penner, J. E. (2012). Constraining cloud lifetime effects of aerosols using A-Train satellite observations. *Geophysical Research Letters*, 39(15), L15709. doi:10.1029/2012GL052204.

Wang, M., Penner, J. E., & Liu, X. (2009). Coupled IMPACT aerosol and NCAR CAM3 model: Evaluation of predicted aerosol number and size distribution. *Journal of Geophysical Research: Atmospheres*, 114(D6), D06302. doi:10.1029/2008JD010459.

Wang, X., Zhang, L., & Moran, M. D. (2010). Uncertainty assessment of current size-resolved parameterizations for below-cloud particle scavenging by rain. *Atmospheric Chemistry and Physics*, 10(12), 5685–5705. http://www.atmos-chem-phys.net/10/5685/2010/.

Wang, Z., Zhang, H., Li, J., Jing, X., & Lu, P. (2013b). Radiative forcing and climate response due to the presence of black carbon in cloud droplets. *Journal of Geophysical Research: Atmospheres*, 118(9), 3662–3675. doi:10.1002/jgrd.50312.

Wang, Z. B., Hu, M., Pei, X. Y., Zhang, R. Y., Paasonen, P., Zheng, J., Yue, D. L., Wu, Z. J., Boy, M., & Wiedensohler, A. (2015). Connection of organics to atmospheric new particle formation and growth at an urban site of Beijing. *Atmospheric Environment*, 103, 7–17. doi:10.1016/j.atmosenv.2014.11.069.

Warren, S. G., Hahn, C. J., London, J., Chervin, R. M., & Jenne, R. L. (1988). *Global distribution of total cloud cover and cloud type amounts over the ocean.* Technical Report DOE/ER-0406; NCAR/TN–317-STR, USDOE Office of Energy Research, Washington, DC (USA). Carbon Dioxide Research Div.; National Center for Atmospheric Research, Boulder, CO (USA). http://www.osti.gov/scitech/servlets/purl/5415329.

Warren, S. G. & Wiscombe, W. J. (1980). A Model for the Spectral Albedo of Snow. II: Snow Containing Atmospheric Aerosols. *Journal of the Atmospheric Sciences*, 37(12), 2734–2745. doi:10.1175/1520-0469(1980)037<2734:AMFTSA>2.0.CO;2.

Werner, F., Ditas, F., Siebert, H., Simmel, M., Wehner, B., Pilewskie, P., Schmeissner, T., Shaw, R. A., Hartmann, S., Wex, H., Roberts, G. C., & Wendisch, M. (2014). Twomey effect observed from collocated microphysical and remote sensing measurements over shallow cumulus. *Journal of Geophysical Research: Atmospheres*, 119(3), 1534–1545. doi:10.1002/2013JD020131.

Westervelt, D. M., Pierce, J. R., & Adams, P. J. (2014). Analysis of feedbacks between nucleation rate, survival probability and cloud condensation nuclei formation. *Atmospheric Chemistry and Physics*, 14(11), 5577–5597. http://www.atmos-chem-phys.net/14/5577/2014/.

Westervelt, D. M., Pierce, J. R., Riipinen, I., Trivitayanurak, W., Hamed, A., Kulmala, M., Laaksonen, A., Decesari, S., & Adams, P. J. (2013). Formation and growth of nucleated particles into cloud condensation nuclei: model-measurement comparison. *Atmospheric Chemistry and Physics*, 13(15), 7645–7663. http://www.atmos-chem-phys.net/13/7645/2013/.

Wex, H., DeMott, P. J., Tobo, Y., Hartmann, S., Rösch, M., Clauss, T., Tomsche, L., Niedermeier, D., & Stratmann, F. (2014). Kaolinite particles as ice nuclei: learning from the use of different kaolinite samples and different coatings. *Atmospheric Chemistry and Physics*, 14(11), 5529–5546. http://www.atmos-chem-phys.net/14/5529/2014/.

Wexler, A. S. & Seinfeld, J. H. (1990). The distribution of ammonium salts among a size and composition dispersed aerosol. *Atmospheric Environment. Part A. General Topics*, 24(5), 1231–1246. http://www.sciencedirect.com/science/article/pii/0960168690900885.

Wexler, A. S. & Seinfeld, J. H. (1992). Analysis of aerosol ammonium nitrate: Departures from equilibrium during SCAQS. *Atmospheric Environment. Part A. General Topics*, 26(4), 579–591. http://www.sciencedirect.com/science/article/pii/096016869290171G.

Whitby, E. R. & McMurry, P. H. (1997). Modal aerosol dynamics modeling. *Aerosol Science and Technology*, 27(6), 673–688. doi:10.1080/02786829708965504.

Whitby, E. R., McMurry, P. H., Shankar, U., & Binkowski, F. S. (1991). *Modal aerosol dynamics modeling.* Technical Report EPA-68-01-7365, U.S. Environmental Protection Agency, Office of Research and Development, Atmospheric Research and Exposure Assessment Laboratory, Research Triangle Park, N.C. http://nepis.epa.gov/Exe/ZyPURL.cgi?Dockey=9100J9A0.txt.

Winebrake, J. J., Corbett, J. J., Green, E. H., Lauer, A., & Eyring, V. (2009). Mitigating the Health Impacts of Pollution from Oceangoing Shipping: An Assessment of Low-Sulfur Fuel Mandates. *Environmental Science & Technology*, 43(13), 4776–4782. doi:10.1021/es803224q.

Wong, J. P. S., Liggio, J., Li, S.-M., Nenes, A., & Abbatt, J. P. D. (2014). Suppression in droplet growth kinetics by the addition of organics to sulfate particles. *Journal of Geophysical Research: Atmospheres*, 119(21), 12222–12232. doi:10.1002/2014JD021689.

Wood, R., Leon, D., Lebsock, M., Snider, J., & Clarke, A. D. (2012). Precipitation driving of droplet concentration variability in marine low clouds. *Journal of Geophysical Research: Atmospheres*, 117(D19), D19210. doi:10.1029/2012JD018305.

Wu, Z. J., Poulain, L., Henning, S., Dieckmann, K., Birmili, W., Merkel, M., van Pinxteren, D., Spindler, G., Müller, K., Stratmann, F., Herrmann, H., & Wiedensohler, A. (2013). Relating particle hygroscopicity and CCN activity to chemical composition during the HCCT-2010 field campaign. *Atmospheric Chemistry and Physics*, 13(16), 7983–7996. http://www.atmos-chem-phys.net/13/7983/2013/.

Wyant, M. C., Bretherton, C. S., Wood, R., Carmichael, G. R., Clarke, A., Fast, J., George, R., Gustafson Jr., W. I., Hannay, C., Lauer, A., Lin, Y., Morcrette, J.-J., Mulcahy, J., Saide, P. E., Spak, S. N., & Yang, Q. (2015). Global and regional modeling of clouds and aerosols in the marine boundary layer during VOCALS: the VOCA intercomparison. *Atmospheric Chemistry and Physics*, 15(1), 153–172. http://www.atmos-chem-phys.net/15/153/2015/.

Xiao, H., Yin, Y., Jin, L., Chen, Q., & Chen, J. (2014). Simulation of aerosol effects on orographic clouds and precipitation using WRF model with a detailed bin microphysics scheme. *Atmospheric Science Letters*, 15(2), 134–139. doi:10.1002/asl2.480.

Xu, J., Wang, Z., Yu, G., Qin, X., Ren, J., & Qin, D. (2014). Characteristics of water soluble ionic species in fine particles from a high altitude site on the northern boundary of Tibetan Plateau: Mixture of mineral dust and anthropogenic aerosol. *Atmospheric Research*, 143, 43–56. doi:10.1016/j.atmosres.2014.01.018.

Yao, X. H. & Zhang, L. (2012). Supermicron modes of ammonium ions related to fog in rural atmosphere. *Atmospheric Chemistry and Physics*, 12(22), 11165–11178. http://www.atmos-chem-phys.net/12/11165/2012/.

Yau, P. S., Lee, S. C., Cheng, Y., Huang, Y., Lai, S. C., & Xu, X. H. (2013). Contribution of ship emissions to the fine particulate in the community near an international port in Hong Kong. *Atmospheric Research*, 124, 61–72. doi:10.1016/j.atmosres.2012.12.009.

Yeatman, S. G., Spokes, L. J., & Jickells, T. D. (2001). Comparisons of coarse-mode aerosol nitrate and ammonium at two polluted coastal sites. *Atmospheric Environment*, 35(7), 1321–1335. doi:10.1016/S1352-2310(00)00452-0.

Yoon, J., Burrows, J. P., Vountas, M., von Hoyningen-Huene, W., Chang, D. Y., Richter, A., & Hilboll, A. (2014). Changes in atmospheric aerosol loading retrieved from space-based measurements during the past decade. *Atmospheric Chemistry and Physics*, 14(13), 6881–6902. http://www.atmos-chem-phys.net/14/6881/2014/.

Yu, F., Luo, G., Liu, X., Easter, R. C., Ma, X., & Ghan, S. J. (2012). Indirect radiative forcing by ion-mediated nucleation of aerosol. *Atmospheric Chemistry and Physics*, 12(23), 11451–11463. http://www.atmos-chem-phys.net/12/11451/2012/.

Yu, H., Chin, M., Yuan, T., Bian, H., Remer, L. A., Prospero, J. M., Omar, A., Winker, D., Yang, Y., Zhang, Y., Zhang, Z., & Zhao, C. (2015). The fertilizing role of African dust in the Amazon rainforest: A first multiyear assessment based on data from Cloud-Aerosol Lidar and Infrared Pathfinder Satellite Observations. *Geophysical Research Letters*, 42(6), 1984–1991. doi:10.1002/2015GL063040.

Yu, S., Kasibhatla, P. S., Wright, D. L., Schwartz, S. E., McGraw, R., & Deng, A. (2003). Moment-based simulation of microphysical properties of sulfate aerosols in the eastern United States: Model description, evaluation, and regional analysis. *Journal of Geophysical Research: Atmospheres*, 108(D12), 4353. doi:10.1029/2002JD002890.

Yuan, T., Remer, L. A., Bian, H., Ziemke, J. R., Albrecht, R., Pickering, K. E., Oreopoulos, L., Goodman, S. J., Yu, H., & Allen, D. J. (2012). Aerosol indirect effect on tropospheric ozone via lightning. *Journal of Geophysical Research: Atmospheres*, 117(D18), D18213. doi:10.1029/2012JD017723.

Yun, Y. & Penner, J. E. (2013). An evaluation of the potential radiative forcing and climatic impact of marine organic aerosols as heterogeneous ice nuclei. *Geophysical Research Letters*, 40(15), 4121–4126. doi:10.1002/grl.50794.

Yun, Y., Penner, J. E., & Popovicheva, O. (2013). The effects of hygroscopicity on ice nucleation of fossil fuel combustion aerosols in mixed-phase clouds. *Atmospheric Chemistry and Physics*, 13(8), 4339–4348. http://www.atmos-chem-phys.net/13/4339/2013/.

Zare, A., Christensen, J. H., Gross, A., Irannejad, P., Glasius, M., & Brandt, J. (2014). Quantifying the contributions of natural emissions to ozone and total fine PM concentrations in the Northern Hemisphere. *Atmospheric Chemistry and Physics*, 14(6), 2735–2756. http://www.atmos-chem-phys.net/14/2735/2014/.

Zaveri, R. A., Easter, R. C., Fast, J. D., & Peters, L. K. (2008). Model for Simulating Aerosol Interactions and Chemistry (MOSAIC). *Journal of Geophysical Research: Atmospheres*, 113(D13), D13204. doi:10.1029/2007JD008782.

Zaveri, R. A., Easter, R. C., & Peters, L. K. (2005a). A computationally efficient Multicomponent Equilibrium Solver for Aerosols (MESA). *Journal of Geophysical Research: Atmospheres*, 110(D24), D24203. doi:10.1029/2004JD005618.

Zaveri, R. A., Easter, R. C., & Wexler, A. S. (2005b). A new method for multicomponent activity coefficients of electrolytes in aqueous atmospheric aerosols. *Journal of Geophysical Research: Atmospheres*, 110(D2), D02201. doi:10.1029/2004JD004681.

Zelinka, M. D., Andrews, T., Forster, P. M., & Taylor, K. E. (2014). Quantifying components of aerosol-cloud-radiation interactions in climate models. *Journal of Geophysical Research: Atmospheres*, 119(12), 7599–7615. doi:10.1002/2014JD021710.

Zhang, D., Liu, D., Luo, T., Wang, Z., & Yin, Y. (2015). Aerosol impacts on cloud thermodynamic phase change over East Asia observed with CALIPSO and CloudSat measurements. *Journal of Geophysical Research: Atmospheres*, 120(4), 1490–1501. doi:10.1002/2014JD022630.

Zhang, F., Li, Y., Li, Z., Sun, L., Li, R., Zhao, C., Wang, P., Sun, Y., Liu, X., Li, J., Li, P., Ren, G., & Fan, T. (2014a). Aerosol hygroscopicity and cloud condensation nuclei activity during the AC^{3}Exp campaign: implications for cloud condensation nuclei parameterization. *Atmospheric Chemistry and Physics*, 14(24), 13423–13437. http://www.atmos-chem-phys.net/14/13423/2014/.

Zhang, H., DeNero, S. P., Joe, D. K., Lee, H.-H., Chen, S.-H., Michalakes, J., & Kleeman, M. J. (2014b). Development of a source oriented version of the WRF/Chem model and its application to the California regional PM_{10} / $PM_{2.5}$ air quality study. *Atmospheric Chemistry and Physics*, 14(1), 485–503. http://www.atmos-chem-phys.net/14/485/2014/.

Zhang, K., O'Donnell, D., Kazil, J., Stier, P., Kinne, S., Lohmann, U., Ferrachat, S., Croft, B., Quaas, J., Wan, H., Rast, S., & Feichter, J. (2012). The global aerosol-climate model ECHAM-HAM, version 2: sensitivity to improvements in process representations. *Atmospheric Chemistry and Physics*, 12(19), 8911–8949. http://www.atmos-chem-phys.net/12/8911/2012/.

Zhao, C., Chen, S., Leung, L. R., Qian, Y., Kok, J. F., Zaveri, R. A., & Huang, J. (2013a). Uncertainty in modeling dust mass balance and radiative forcing from size parameterization. *Atmospheric Chemistry and Physics*, 13(21), 10733–10753. http://www.atmos-chem-phys.net/13/10733/2013/.

Zhao, C., Ruby Leung, L., Easter, R., Hand, J., & Avise, J. (2013b). Characterization of speciated aerosol direct radiative forcing over California. *Journal of Geophysical Research: Atmospheres*, 118(5), 2372–2388. doi:10.1029/2012JD018364.

Zhao, M., Zhang, Y., Ma, W., Fu, Q., Yang, X., Li, C., Zhou, B., Yu, Q., & Chen, L. (2013c). Characteristics and ship traffic source identification of air pollutants in China's largest port. *Atmospheric Environment*, 64, 277–286. doi:10.1016/j.atmosenv.2012.10.007.

Zhou, C.-H., Gong, S., Zhang, X.-Y., Liu, H.-L., Xue, M., Cao, G.-L., An, X.-Q., Che, H.-Z., Zhang, Y.-M., & Niu, T. (2012). Towards the improvements of simulating the chemical and optical properties of Chinese aerosols using an online coupled model – CUACE/Aero. *Tellus B*, 64(0), 18965. http://www.tellusb.net/index.php/tellusb/article/view/18965.

Zhou, Y. & Savijärvi, H. (2014). The effect of aerosols on long wave radiation and global warming. *Atmospheric Research*, 135-136, 102–111. doi:10.1016/j.atmosres.2013.08.009.

Zhuang, H., Chan, C. K., Fang, M., & Wexler, A. S. (1999). Formation of nitrate and non-sea-salt sulfate on coarse particles. *Atmospheric Environment*, 33(26), 4223–4233. doi:10.1016/S1352-2310(99)00186-7.

Acronyms, symbols, and species names

Acronyms

AC-GCM . . . Atmospheric chemistry general circulation model

AIR . . . . . Aircraft

ANT . . . . . Anthropogenic non-traffic

AOD . . . . . Aerosol optical depth

AWB . . . . . Agricultural waste burning

BB . . . . . Biomass burning

CCN . . . . . Cloud condensation nuclei

CDNC . . . . Cloud droplet number concentration

ESM . . . . . Earth system model

GHG . . . . . Greenhouse gas

IN . . . . . Ice nuclei

LAND . . . . Land transport

MBL . . . . . Marine boundary layer

NPF . . . . . New particle formation

OA . . . . . Organic aerosol

OC . . . . . Organic carbon

RE . . . . . Radiative effect

RF . . . . . Radiative forcing

RH . . . . . Relative humidity

SHIP . . . . . Shipping

SST . . . . . Sea surface temperature

VOC . . . . . Volatile organic compound

Symbols

A . . . . . Number of considered aerosol components

B . . . . . Constant in atmospheric dynamic viscosity parameterization

C_{ext} . . . . . Extinction cross section

D . . . . . Aerosol particle diameter

$\tilde{D}$ . . . . . Aerosol particle diameter, dimensionless after division by $1\,\mu$m

$\tilde{D}_{\text{g},k}$ . . . . . Mode k median aerosol particle diameter, dimensionless after division by $1\,\mu$m

E . . . . . Collision efficiency

F . . . . . Mass flux per unit area and time

$F_{\text{dep},a}$ . . . . . Sum of deposition fluxes for aerosol species a

G . . . . . Correction factor in continuum regime Brownian coagulation kernel

GF . . . . . Hygroscopic growth factor

J . . . . . Rate constant in aerosol nucleation parameterization

K . . . . . Number of aerosol modes

L_X . . . . . Loss rate coefficient for species X

M_j . . . . . The j^{th} moment of the aerosol particle size distribution

M_X . . . . . Molar mass of species X

N . . . . . Cumulative aerosol particle number concentration

N_k . . . . . Aerosol particle number concentration in mode k

P_X . . . . . Mass concentration production rate of species X

R . . . . . Universal gas constant; if subscripted: “resistance” term for dry deposition

S . . . . . Constant in atmospheric dynamic viscosity parameterization

T . . . . . Ambient temperature (absolute)

T_0 . . . . . Reference temperature in mean free path of air parameterization

V_k . . . . . Aerosol particle volume concentration in mode k

V_{p} . . . . . Volume of one aerosol particle

W . . . . . Weighting factor

$\dot{Y}_{\text{emi},k}$ . . . . . Placeholder for aerosol number or mass emission rate to mode k

Y_k . . . . . Placeholder for aerosol number or mass concentration in mode k

a_{lm}^k . . . . . Rate coefficient for mode l and m particle coagulation forming mode k particles

$c_{a,k}$ . . . . . Mass concentration of aerosol component a in mode k

g . . . . . Earth's gravitational acceleration

g_X . . . . . Mass concentration of gas species X

$g_{X,\mathrm{s}}$ . . . . . Mass concentration of gas species X close to a particle's surface

$g_{X,\infty}$ . . . . . Mass concentration of gas species X far away from a particle's surface

k . . . . . Aerosol mode index

k_B . . . . . Boltzmann's constant

m . . . . . Aerosol particle mass size distribution function

m_p . . . . . Mass of one aerosol particle

$m_{\mathrm{tot},a}$ . . . . . Atmospheric burden of aerosol species a

n . . . . . Aerosol particle number size distribution function (of mode k, if subscripted)

$\dot{n}$ . . . . . Aerosol particle number production rate

p . . . . . Ambient pressure

p_0 . . . . . Reference pressure in mean free path of air parameterization

q . . . . . Exponent in aerosol nucleation parameterization

r_cld . . . . . Effective cloud droplet radius

r_r . . . . . Rain droplet radius

s_k . . . . . Slip correction factor for aerosol particles in mode k

t . . . . . Time

$t_{\mathrm{res},a}$ . . . . . Tropospheric residence time of aerosol species a

$\vec{v}$ . . . . . Wind vector

$v_{\mathrm{d},k}$ . . . . . Placeholder for dry deposition velocity for mode k aerosol number or mass

$v_{\mathrm{s},k}$ . . . . . Placeholder for sedimentation velocity for mode k aerosol number or mass

y_k . . . . . Mie size parameter for aerosol particles in mode k

z . . . . . Vertical spatial coordinate

Δt . . . . . Model time step duration

Δ_X . . . . . Diffusivity of X (gas species or mode k aerosol particle ($X = \mathrm{p}, k$)) in air

Λ . . . . . Constant in mean free path of air parameterization

α_X . . . . . Mass accommodation coefficient of gas species X on aerosol particles

β . . . . . Brownian motion coagulation kernel function

γ_{asy} . . . . . Asymmetry parameter

δ . . . . . Kronecker symbol

ε . . . . . Complex refractive index

η . . . . . Scavenging rate

κ . . . . . Hygroscopicity parameter

λ . . . . . Wavelength (of radiation)

λ_X . . . . . Mean free path of X (gas species or aerosol particle ($X = \text{p}$)) in air

ν . . . . . Atmospheric dynamic viscosity

ρ . . . . . Average aerosol particle density

ρ_a . . . . . Density of aerosol particle component a

ρ_k . . . . . Density of aerosol particles in mode k

σ . . . . . Standard deviation (arithmetic)

σ_k . . . . . Geometric standard deviation of aerosol mode k

τ . . . . . Coagulation assignment matrix

ζ . . . . . Diffusion coefficient

ω . . . . . Single scattering albedo

ω_X . . . . . Thermal speed of molecules of gas species X

Tracers and chemical species

BC . . . . . Black carbon

Ca . . . . . Calcium

$CaCO_3$ . . . . Calcium carbonate

CH_4 . . . . . Methane

Cl . . . . . Chloride

CO . . . . . Carbon monoxide

CO_2 . . . . . Carbon dioxide

CO_3 . . . . . Carbonate

DMS . . . . . Dimethyl sulfide

DU . . . . . Mineral dust

H_2O . . . . . Water

H_2O_2 . . . . . Hydrogen peroxide

H_2SO_4 . . . . Sulfuric acid

HCl . . . . . Hydrochloric acid

HNO_3 . . . . . Nitric acid

HO_2 . . . . . Hydroperoxy

HO_x . . . . . Reactive hydrogen oxides

K . . . . . Potassium

Mg . . . . . Magnesium

N_2O . . . . . Nitrous oxide

N_2O_5 . . . . . Dinitrogen pentoxide

Na . . . . . Sodium

Na_2SO_4 . . . . Sodium sulfate

NaCl . . . . . Sodium chloride

$NaNO_3$ . . . . Sodium nitrate

NH_3 . . . . . Ammonia

NH_4 . . . . . Ammonium

$(NH_4)_2SO_4$ . . Ammonium sulfate

$(NH_4)_3H(SO_4)_2$ Letovicite

NH_4Cl . . . . Ammonium chloride

NH_4HSO_4 . . Ammonium hydrogen sulfate

NH_4NO_3 . . . Ammonium nitrate

NO . . . . . Nitrogen oxide

NO_3 . . . . . Nitrate

NO_x . . . . . Reactive nitrogen oxides

O_3 . . . . . Ozone

OH . . . . . Hydroxyl

POM . . . . . Particulate organic matter

SO_2 . . . . . Sulfur dioxide

SO_4 . . . . . Sulfate

SOA . . . . . Secondary organic aerosol

SS . . . . . Sea spray

Danksagung

Ich danke meinem Doktorvater, Robert Sausen, für das Ermöglichen der vorliegenden Arbeit sowie für hilfreiche Diskussionen und Hinweise während ihrer Erstellung. Auch bei meinem Zweitgutachter, George Craig, möchte ich mich an dieser Stelle bedanken.

Zu besonderem Dank bin ich meinem Betreuer Johannes Hendricks verpflichtet. Die jederzeit offene Tür und die damit verbundene Bereitschaft zu Beratung und Diskussionen betrachte ich nicht als selbstverständlich. Erfahren habe ich sie aber ebenso von Mattia Righi, bei dem ich mich speziell für die Bereitstellung seiner Werkzeuge für die Datenaufbereitung bedanke. In puncto Datenerzeugung danke ich Patrick Jöckel für die große Geduld und die immer freundliche Hilfestellung bei Problemen mit MESSy, Fortran und den Supercomputern. Das Verständnis und die Ermunterung, die ich von Euch erfahren habe, haben mir besonders während der "Durststrecken" der Doktorarbeit geholfen. Auch den anderen Kollegen der Abteilung Erdsystemmodellierung des Instituts für Physik der Atmosphäre bin ich dankbar für die offenen Ohren und hilfreiche Tipps. Namentlich erwähnt sei an dieser Stelle noch mein Büronachbar Michael Ponater, der nicht nur sein fachliches Wissen, sondern auch die Süßigkeiten, die er von seinen diversen Reisen mitbrachte, mit mir geteilt hat.

Weiterhin danke ich meinen Koautoren bei der Publikation, die im Rahmen meiner Doktorarbeit entstanden ist: Johannes und Mattia (s. o.); Valentina Aquila, für die Entwicklung des MADE3-Vorgängers MADE-in; Nicole Riemer, für die Bereitstellung von PartMC und die Hilfe beim Aufsetzen einer mit MADE- und MADE3-Simulationen vergleichbaren PartMC-MOSAIC-Simulation; Swen Metzger, für Hilfe bei der Erweiterung seines Gas-Aerosol-Partitionierungs-Codes für MADE3; und Rahul Zaveri, für die Bereitstellung von MOSAIC. In diesem Zusammenhang bedanke ich mich auch bei Bernd Kärcher für die nützlichen Kommentare zu dem Manuskript.

Holger Tost danke ich für hilfreiche Hinweise zur Anpassung des Submodells SCAV an die MADE3-Bedürfnisse. Bei Andrea Pozzer und Laurens Ganzeveld bedanke ich mich für ihre Hinweise bezüglich Emissionsdaten und Randbedingungen für meine Simulationen, sowie zu den zugehörigen Literaturstellen.

Der Vergleich mit den größenaufgelösten Daten zur Aerosolzusammensetzung wäre ohne Konrad Kandlers Einsatz nicht möglich gewesen. Ich bedanke mich sehr für diese Zusammenarbeit, die mir aufgezeigt hat wie unterschiedlich die Sichtweisen von Experimentalisten und Modellierern auf das atmosphärische Aerosol sein können. Im Zusammenhang mit der Evaluierung des Modells danke ich außerdem den Entwicklern des ESMValTools unter Leitung von Veronika Eyring und ganz besonders all den Wissenschaftlern und anderen Beteiligten, die ihre Messdaten zugänglich gemacht haben.

Zuguterletzt bedanke ich mich bei meiner Familie, insbesondere bei meiner Frau. Die Aufmunterung und Unterstützung, gelegentlich einfach in Form von Toleranz, die ich erfahren habe, waren wohl die wertvollsten Begleiter während der Erstellung dieser Arbeit.

Die hier ausgewerteten Simulationen habe ich auf dem Hochleistungsrechnersystem für die Erdsystemforschung II ("Blizzard") am Deutschen Klimarechenzentrum (DKRZ) durchgeführt. Für einige Testsimulationen stand mir außerdem Rechenzeit auf dem Supercomputer SuperMUC des Leibniz-Rechenzentrums der Bayerischen Akademie der Wissenschaften (LRZ) zur Verfügung. Für die Datenaufbereitung kamen Gnuplot, Python mit NumPy, SciPy und matplotlib sowie vielfach die NCAR Command Language (NCL) zum Einsatz.